

## Investigation of limestone-calcined clay-based cementitious materials for sustainable 3d concrete printing

Chen, Y.

**DOI**

[10.4233/uuid:a0d9289b-9f24-4805-86ab-09f12714a946](https://doi.org/10.4233/uuid:a0d9289b-9f24-4805-86ab-09f12714a946)

**Publication date**

2021

**Document Version**

Final published version

**Citation (APA)**

Chen, Y. (2021). *Investigation of limestone-calcined clay-based cementitious materials for sustainable 3d concrete printing*. [Dissertation (TU Delft), Delft University of Technology].  
<https://doi.org/10.4233/uuid:a0d9289b-9f24-4805-86ab-09f12714a946>

**Important note**


To cite this publication, please use the final published version (if applicable).  
Please check the document version above.

**Copyright**

Other than for strictly personal use, it is not permitted to download, forward or distribute the text or part of it, without the consent of the author(s) and/or copyright holder(s), unless the work is under an open content license such as Creative Commons.

**Takedown policy**

Please contact us and provide details if you believe this document breaches copyrights.  
We will remove access to the work immediately and investigate your claim.



Investigation of limestone-calcined clay-based  
cementitious materials for  
sustainable 3D concrete printing

Yu CHEN  
陈宇

**INVESTIGATION OF LIMESTONE-CALCINED CLAY-BASED  
CEMENTITIOUS MATERIALS FOR SUSTAINABLE 3D  
CONCRETE PRINTING**





**INVESTIGATION OF LIMESTONE-CALCINED CLAY-BASED  
CEMENTITIOUS MATERIALS FOR SUSTAINABLE 3D  
CONCRETE PRINTING**

**Dissertation**

for the purpose of obtaining the degree of doctor  
at Delft University of Technology  
by the authority of the Rector Magnificus Prof.dr.ir. T.H.J.J. van der Hagen  
chair of the Board for Doctorates  
to be defended publicly on  
Thursday 15 July 2021 at 12:30 o'clock

by

**Yu CHEN**

Master of Architecture in Design,  
University of Nottingham, the United Kingdom,  
born in Jilin, China.

This dissertation has been approved by the promotor.

Composition of the doctoral committee:

Rector Magnificus,	chairperson
Prof.dr.ir. E. Schlangen	Delft University of Technology, promotor
Dr.ir. F.A. Veer	Delft University of Technology, promotor
Dr. O. Çopuroğlu	Delft University of Technology, copromotor

*Independent Members:*

Prof.dr. Y. Zhang	Southeast University, China
Prof.dr.ir. T.A.M. Salet	Eindhoven University of Technology
Prof.dr.ir. L.J. Sluys	Delft University of Technology
Prof.dr.-ing. U. Knaack	Delft University of Technology



*Keywords:* 3D concrete printing, Limestone, Calcined clay, Sustainability, Viscosity modifying admixture, Fresh properties, Hydration kinetic, Mechanical performance, Interlayer bonding, Air void

*Printed by:* Ipskamp Printing, the Netherlands

*Cover design:* Yu Chen

Copyright © 2021 by Y. Chen

All rights reserved. This copy of the thesis has been supplied on condition that anyone who consults it is understood to recognize that its copyright rests with its author and that no quotation from the thesis and no information derived from it may be published without the author's prior consent.

ISBN 978-94-6421-404-8

An electronic version of this dissertation is available at  
<http://repository.tudelft.nl/>.

*"I think of the past and the future as well as the present to determine where I am, and I move on while thinking of these things."*

Tadao Ando



# CONTENTS

<b>List of Figures</b>	<b>xi</b>
<b>List of Tables</b>	<b>xix</b>
<b>Summary</b>	<b>xxi</b>
<b>Samenvatting</b>	<b>xxiii</b>
<b>I General Introduction</b>	<b>1</b>
<b>1 Introduction</b>	<b>3</b>
1.1 Introduction . . . . .	4
1.2 Research aim and objectives . . . . .	6
1.3 Research scope . . . . .	7
1.4 Strategy of this research . . . . .	8
1.5 Thesis outline . . . . .	8
References . . . . .	10
<b>2 Literature review</b>	<b>15</b>
2.1 Introduction . . . . .	16
2.2 Extrusion-based 3D concrete printing strategy . . . . .	16
2.3 SCM-based cementitious materials for 3DCP . . . . .	20
2.3.1 Effect of common SCMs on fresh properties . . . . .	20
2.3.2 Effect of limestone and calcined clay on fresh properties . . . . .	23
2.4 Characterization methods of fresh-state and interlayer behaviors . . . . .	28
2.4.1 Fresh properties and test methods . . . . .	28
2.4.2 Interlayer behaviors and test methods . . . . .	44
2.5 Summary and perspectives . . . . .	48
References . . . . .	49
<b>II Experimental Investigation</b>	<b>65</b>
<b>3 Effect of Portland cement substitutions by calcined clay and limestone on 3D printability, stiffness evolution and early-age hydration</b>	<b>67</b>
3.1 Introduction . . . . .	68
3.2 Materials and methods . . . . .	68
3.2.1 Raw materials and mix designs . . . . .	68
3.2.2 Lab-scale 3D concrete printing setup . . . . .	69
3.2.3 Formulation of printable mix designs . . . . .	70
3.2.4 Evaluation of 3D printability . . . . .	71
3.2.5 Characterization of early-age hydration . . . . .	75



3.3	Results . . . . .	78
3.3.1	Mix designs and fresh properties . . . . .	78
3.3.2	3D printability . . . . .	81
3.3.3	Stiffness development and early-age hydration . . . . .	86
3.4	Discussion . . . . .	93
3.4.1	Effect of increasing LGCC and LF content on flowability and 3D printability. . . . .	93
3.4.2	Effect of increasing LGCC and LF content on stiffness evolution with time. . . . .	94
3.4.3	Effect of increasing LGCC and LF content on the main hydration peak . . . . .	96
3.5	Conclusion . . . . .	97
	References . . . . .	98
<b>4</b>	<b>Effect of viscosity modifying admixture on fresh-state behaviors and hardened properties</b>	<b>103</b>
4.1	Introduction . . . . .	104
4.2	Materials and methods . . . . .	104
4.2.1	Raw materials and mix designs. . . . .	104
4.2.2	Flowability test. . . . .	105
4.2.3	Evaluation of 3D printability . . . . .	105
4.2.4	Green strength test. . . . .	106
4.2.5	Isothermal calorimetry test . . . . .	107
4.2.6	Compressive strength test . . . . .	107
4.2.7	X-ray computed tomography scanning . . . . .	107
4.3	Results and discussion . . . . .	108
4.3.1	Flowability . . . . .	108
4.3.2	3D printability . . . . .	108
4.3.3	Green strength . . . . .	113
4.3.4	Isothermal calorimetry. . . . .	114
4.3.5	Compressive strength . . . . .	115
4.3.6	Air void content and distribution . . . . .	116
4.4	Conclusion . . . . .	120
	References . . . . .	121
<b>5</b>	<b>Effect of different grade levels of calcined clays on fresh and hardened properties</b>	<b>125</b>
5.1	Introduction . . . . .	126
5.2	Materials and methods . . . . .	126
5.2.1	Raw materials and mix designs. . . . .	126
5.2.2	Ram extrusion test . . . . .	127
5.2.3	3D printing test . . . . .	129
5.2.4	Compressive strength test . . . . .	131
5.2.5	Air void analysis . . . . .	133
5.2.6	Isothermal calorimetry test and thermogravimetric analysis. . . . .	133

5.3	Results	134
5.3.1	Ram extrusion rheology	134
5.3.2	Evaluation of 3D printability	134
5.3.3	Compressive strength	138
5.3.4	Air void content and distribution	140
5.3.5	Hydration kinetics	141
5.4	Discussion	144
5.4.1	Effect of increasing HGCC content on 3D printability	144
5.4.2	Effect of increasing HGCC content on hydration kinetics	148
5.4.3	Effect of increasing HGCC content on compressive strength	150
5.5	Conclusion	152
	References	153
<b>6</b>	<b>Characterization of air-void systems in 3D printed cementitious materials using optical image scanning and X-ray computed tomography</b>	<b>157</b>
6.1	Introduction	158
6.2	Materials and methods	159
6.2.1	Printable mixture design	159
6.2.2	Sample preparation	159
6.2.3	Image acquisition and segmentation	160
6.2.4	Air void characterization	161
6.3	Results and discussion	164
6.3.1	Air void content and distribution	164
6.3.2	Air void size distribution	165
6.3.3	Air void shape property	167
6.3.4	Perspective and limitations	172
6.4	Conclusion	180
	References	181
<b>7</b>	<b>Effect of printing parameters on interlayer bond strength of 3D printed limestone-calcined clay-based cementitious materials</b>	<b>185</b>
7.1	Introduction	186
7.2	Materials	186
7.3	Experimental tests	186
7.3.1	Sample preparation	186
7.3.2	Uniaxial tensile test	187
7.3.3	X-ray computed tomography	190
7.4	Modeling	191
7.5	Results and discussion	194
7.5.1	Uniaxial tensile strength	194
7.5.2	Air void content and distribution	194
7.5.3	Modeling results	198
7.6	Conclusion	206
	References	207

<b>III Discussion and Conclusion</b>	<b>211</b>
<b>8 Challenges and opportunities for implementing 3D concrete printing in building construction</b>	<b>213</b>
8.1 Introduction . . . . .	214
8.2 Technical challenges . . . . .	214
8.2.1 On-site printing . . . . .	214
8.2.2 Reinforcement placement . . . . .	215
8.2.3 Standardization . . . . .	217
8.2.4 Durability . . . . .	217
8.3 Environmental and economic potentials . . . . .	220
8.3.1 Flash calcination of clay . . . . .	220
8.3.2 Print in a smart and efficient way . . . . .	221
8.4 Conclusion . . . . .	224
References . . . . .	226
<b>9 Conclusions and recommendations</b>	<b>231</b>
9.1 Retrospection . . . . .	232
9.2 Conclusions. . . . .	233
9.2.1 General principles of 3D concrete printing. . . . .	233
9.2.2 Main conclusions of the thesis . . . . .	234
9.3 Recommendations for further study . . . . .	235
<b>Acknowledgments</b>	<b>239</b>
<b>Curriculum Vitae</b>	<b>241</b>
<b>List of Publications</b>	<b>243</b>

# LIST OF FIGURES

1.1	Portland cement production worldwide from 1990 to 2050, adapted from [9]. . . . .	4
1.2	Quantities of common supplementary cementing materials (SCMs), adapted from [26]. . . . .	5
1.3	Outline of the thesis. . . . .	9
2.1	Typical 3DCP experimental setups. (a) 4-axis gantry-based system, multiple batches (material preparation), and rotor-stator-based pump, adapted from [14]; (b) 6-axis robotic arm, continuous mixing (material preparation), and rotor-stator-based pump, adapted from [15]. . . . .	18
2.2	(a) Diagram of set-on-demand printing system, adapted from [16]; (b) Photographs of the set-on-demand printing system and printed columns at ETH Zürich, adapted from [17]. . . . .	19
2.3	3DCP experimental setup at TU Dresden: 4-axis gantry-based system, multiple batches, and screw extruder, adapted from [18]. . . . .	19
2.4	Literature survey of OPC content and aggregate to binder mass ratio in different 3D printable mortars. Data from Refs: [1, 2, 9, 29–40]. . . . .	21
2.5	Diagram showing the structure of muscovite, kaolinite, and montmorillonite, adapted from [108]. . . . .	27
2.6	Clay phases transformation at different calcined temperatures, adapted from [98]. . . . .	27
2.7	(a) Scheme of the ram extrusion setup; (b) Illustration of the orifice entrance flow region based on a spherical coordinate system; (c) An example of test results and the fitted curve (Basterfield et al. model). Adapted from [135]. . . . .	31
2.8	An example of the open time measurement. The width of the nozzle opening used in this test is 30 mm. Adapted from [7]. . . . .	33
2.9	An example of the buildability test, adapted from [149]. . . . .	34
2.10	(a) Diagram showing two failure modes of a wall; (b) Elastic buckling of a large square wall (wall width: 500 mm); (c) Plastic collapse of a small square wall (wall width: 250 mm). Adapted from [152]. . . . .	35
2.11	(a) Illustration of green strength test setup (Left) and a cylindrical sample (Right); (b) Typical failures observed in green strength tests at different material ages; (c) Typical stress-strain relations in green strength tests. Adapted from [151]. . . . .	37
2.12	Schematic illustration of different penetrometer tips, modified from [160]. . . . .	39

2.13 (a) Fast penetration test at different times (using conical tip); (b) The evolution of penetration force and yield stress obtained by using different approaches. Both (a) and (b) adapted from [17]. . . . .	40
2.14 CSR test of cement paste (W/C=0.4)-the relationship between shear strain and shear stress. (a) Shear strain from 0% to 15%; (b) Shear strain from 0% to 0.4%. Adapted from [178]. . . . .	41
2.15 (a) A hysteresis loop test protocol; (b) A typical result of the hysteresis loop test. Adapted from [37]. . . . .	42
2.16 Uniaxial tensile test setup with rotating loading plates (Left) and non-rotating loading plates (Right). . . . .	47
3.1 Particle size distribution of PC, LGCC, LP and sand used in this chapter. . .	71
3.2 Electron micrograph of (a) LGCC and (b) LP under secondary electron mode (Left: magnification of $\times 6,000$ ; Right: magnification of $\times 20,000$ ). . .	72
3.3 XRD analysis results: (a) LP; (b) PC; (c) LGCC. M-mullite, Q-quartz, K-kaolinite, G-gypsum, $C_3S$ -alite, $C_3A$ -tricalcium aluminate, C-calcite. . .	73
3.4 A lab-scale 3DCP configuration at TU Delft: (a) 3D CNC table and material conveying pump; (b) Down-flow nozzle with a round opening ( $\varnothing 15$ mm). . .	74
3.5 (a) Illustration of the section of material conveying pump; (b) Measurements of material flow rate and increased temperature ( $T=T_2-T_1$ ). . .	76
3.6 Example of the buildability test process. . . . .	77
3.7 Slump and slump-flow test results of mixtures with different SP dosages: (a) Height (before table drops), the height smaller than 20 mm is recorded as 0 mm; (b) Spread diameter (after 25 times of table drops). . . . .	79
3.8 Slump and slump-flow test results of mixtures with different dosages of SP and VMA: (a) Height (before table drops); (b) Spread diameter (after 25 times of table drops). . . . .	80
3.9 Water retention of fresh mixtures with different dosages of SP and VMA. . .	81
3.10 (a) Material flow rates of different mixtures at various material ages; (b) Test results of extrudability and operation windows; (c) Increased temperatures (after extrusion) of different mixtures at various material ages; (d) Correlation between material flow rates and increased temperatures after extrusion. . . . .	82
3.11 Buildability tests of mixtures (a) B45-1; (b) B75-1; (c) B75-2; (d) B90-1; (e) B90-2. . . . .	84
3.12 Buildability test results of different mixtures. The measured maximum height of printed structure before collapse. . . . .	85
3.13 Illustration of the increased nozzle standoff distances and the expected cross-section of printed structure during printing. . . . .	86
3.14 The linear correlation between: (a) Measured sample height in slump test and measured printed structure height in buildability test; (b) Measured spread sample diameter in slump-flow test (after 25 times of table drops) and material flow rate (under 58-60 rpm) at 15 min in extrudability window test. . . . .	87
3.15 Results of the initial setting time. . . . .	88



3.16 (a) $SSA_{total}$ of different paste mixtures at the material ages of 1 h and 3 h; (b) Growth rate of $SSA_{total}$ of different paste mixtures between 1 h and 3 h.	89
3.17 Test results of isothermal calorimetry: (a) Normalized heat flow by mass of paste with time (7 days); (b) Normalized cumulative heat by mass of paste with time (7 days); (c) Normalized heat flow by mass of Portland cement with time (7 days); (d) Normalized heat flow by mass of Portland cement with time (4 days).	91
3.18 (a) Compressive strength of different mixtures at 1, 3, 7, and 28 days. (b) The linear relationship between compressive strength and normalized cumulative heat by mass of paste at 1, 3, and 7 days (excluding any heat within the first 2 h after mixing).	92
3.19 (a) Packing density and $SSA_0$ ; (b) Water film thickness of cementitious systems containing different contents of limestone and calcined clay.	95
3.20 Correlation between: Water film thickness and measured sample height in slump test; Water film thickness and measured sample diameter in slump flow test.	96
3.21 The time to the main hydration peak (mixtures B0-1, B45-1, B75-1 and B90-1) and reactive aluminate to Portland cement mass ratio varying with different calcined clay and limestone contents and reactive aluminate dosages (sourced from calcined clay).	97
4.1 Schematic section of the hybrid back- and down-flow nozzle.	105
4.2 Stages of a typical trial for printing a single filament.	106
4.3 Schematic diagram of loading directions for performing the compressive strength test on printed samples.	108
4.4 The slump flow test results of mixture Ref.	109
4.5 Flowability test results of mixtures with different VMA contents: (a) Height (before dropping the table) and (b) Spread diameters (after dropping the table for 25 times) of demolded samples varied with different material ages.	109
4.6 The extrudability test results for mixtures 1.2VMA, 2VMA, and 4VMA. 1 bar = 0.1 MPa.	110
4.7 Open time test results: (1) Mixture 1.2VMA; (2) Mixture 2VMA; (3) Mixture 4VMA.	111
4.8 Shape retention ratios of mixtures 1.2VMA, 2VMA, and 4VMA at different ages.	112
4.9 The stiff material got stuck in the nozzle during the waiting period of the open time test, which is one of the reasons to restrict the printed amount.	112
4.10 Buildability tests of mixtures 1.2VMA, 2VMA, and 4VMA.	113
4.11 Shape stability ratio of mixtures with different VMA contents (measured at 45 min of the resting time).	114
4.12 (a) The stress/strain curve of mixture 1.2VMA; (b) The stress/strain curve of mixture 2VMA; (c) The stress/strain curve of mixture 4VMA. The black dashed lines indicate the individual test results, and the red curves represent the average stress and strain relation. (d) Comparison of green strength development of mixtures 1.2VMA, 2VMA, and 4VMA.	115

4.13	Damaged samples of mixture 2VMA at different material ages. . . . .	116
4.14	Isothermal calorimetry test results: (a) Normalized heat flow with time, and (b) Normalized cumulative heat with time. . . . .	117
4.15	(a) Extracted areas from the printed samples for performing compressive strength tests. (b) Compressive strength at the age of 7 days. . . . .	118
4.16	(a) The grayscale images of the cross-section from the front view, the interface from the top view, and the layer from the top view: (1) Sample 1.2VMA; (2) Sample 2VMA; (3) Sample 4VMA. (b) 2D void content (porosity) from top to bottom of ROI; (c) The average air void diameter of the interface and layer. . . . .	119
4.17	Schematic of the laminar flow based printing (Left). Formation of the lubrication layer in the material hose/pipe (Middle). Section of two printed layers (Right). . . . .	121
5.1	XRD patterns (Cu-K $\alpha$ radiation) of LGCC and HGCC. Q-quartz (SiO <sub>2</sub> ), M-mullite (3Al <sub>2</sub> O <sub>3</sub> 2SiO <sub>2</sub> ), and K-kaolinite (Al <sub>2</sub> O <sub>3</sub> 2SiO <sub>2</sub> 2H <sub>2</sub> O). . . . .	128
5.2	The particle size distribution of PC, LGCC, HGCC, LP and sand. The grain size of sand was measured by using a sieving machine. All other dry components were determined by laser diffractometry. . . . .	129
5.3	Electron micrographs (secondary electron mode) of LGCC (Left) and HGCC (Right). . . . .	129
5.4	(a) Schematic drawing of the ram extruder; (b) Diagram of the orifice entrance flow region in a spherical coordinate system, according to [2, 4]; (c) A typical trial of the ram extrusion test - predefined piston moving speed vs. displacement. . . . .	130
5.5	Schematic diagram of buildability test: (a) Method 1 (by using nozzle 1); (b) Method 2 (by using nozzle 2). . . . .	132
5.6	(a) A typical plot of the ram extrusion test; (b) Experimental results of extrusion pressure with different material flow rates at the orifice and fitted curves via using Basterfield et al. model (Eq 2.6); (c) Computed rheological parameters: shear yield stress $\tau_0$ , and flow consistency $k$ of mixtures LCC, MCC, and HCC. . . . .	135
5.7	Open time various with the HGCC substitution in calcined clay. . . . .	136
5.8	Buildability test results of Method 1: (a) Buildability performance of mixtures LCC, MCC, and HCC; (b) Height and layer number of the printed object by using different mixtures (mixtures LCC and MCC: data recorded before collapse; mixture HCC: data recorded after the 21 <sup>st</sup> layer). . . . .	137
5.9	Method 1-possible reasons for collapse of the rising structure. . . . .	138
5.10	Buildability test results of Method 2: (a) Buildability performance of mixtures LCC, MCC, and HCC; (b) Height and layer number of the printed object by using different mixtures (mixtures LCC and MCC: the maximum height before collapse; mixture HCC: data recorded after the 18 <sup>th</sup> layer). . . . .	139
5.11	Method 2-possible reasons for collapse of the rising structure. . . . .	140

5.12	Cross-sections of printed samples by using nozzle 1 (Left) and nozzle 2 (Right). The dashed line represents the contact area between two adjacent layers. . . . .	141
5.13	Compressive strength of both cast and printed samples from different mixtures at the age of 7 days. For test directions X, Y, and Z, the reader is referred to Figure 4.3. . . . .	142
5.14	(a) 2D air void content analysis; (b) Average air void diameter analysis; (c) Air void content in the interface and layer zones; Interface zone: 5-8 mm in height of the sample. Layer zone: 0-5 mm and 8-13 mm in height of the sample. . . . .	143
5.15	Grayscale images of different samples acquired from CT scanning. . . . .	144
5.16	Isothermal calorimetry test results of (a) Normalized heat flow with time (4 days). (I)-main hydration peak, (II)-aluminat peak, (III)-AFm reaction peak; and (b) Normalized cumulative heat with time (7 days). . . . .	145
5.17	TGA at 1, 2, 3, and 7 days: (a) A typical example of TG and DTG curves (mixture HCC); (b) The normalized amount of hydrate water (H) relative to the dry sample weight at 600 °C; (c) The normalized amount of calcium hydroxide (CH) relative to the dry sample weight at 600 °C. . . . .	146
5.18	Relationship between: (a) Mean interparticle distance and total SSA of solid; (b) Mean interparticle distance and shear yield stress as well as flow consistency obtained in ram extrusion test. . . . .	149
5.19	Slope value of the acceleration period as a function of the mean interparticle distance. . . . .	150
5.20	The linear relationship between: (a) 7 days compressive strength and normalized cumulative heat at 7 days (excluding any heat within the first 12 h after mixing) obtained from isothermal calorimetry test; (b) 7 days compressive strength and hydrate water (H) content at 7 days obtained from TGA. . . . .	151
6.1	Illustration of sample preparation for thin section analysis, and X-ray computed tomography. . . . .	160
6.2	ROI of the thin section and TWS segmentation process. . . . .	161
6.3	CT-TP and CT-LP GSV images extracted from the reconstructed 3D volume. . . . .	162
6.4	An example of air void segmentation of GSV image. . . . .	162
6.5	Illustration of the horizontal width and vertical height of the air void. . . . .	164
6.6	Local porosity vs. sample height of samples M1 and M2 based on 40 CT-LP images: (a) Result of sample M1; (b) Result of sample M2. The gray line is the computed result of each slice, and the black curve means the average result from 40 slices. . . . .	165
6.7	Local porosity vs. sample height of samples M1 and M2: (a) Average result of CT-LP images; (b) Result of TS images; (c) Result of CT-TP images. . . . .	166
6.8	Total air void content $V_{lp}$ from TS images (Left); Total air void content $V_{lp}$ from CT-LP images (Middle); Total air void content $V_{lp}$ from CT-TP images (Right). . . . .	167

6.9	3D visualization of the air voids in the prism ROI. A-A section: interface region of sample M1 (thickness: 2 mm); B-B section: interface region of sample M2 (thickness: 2 mm). Small and medium air voids: 10-1000 $\mu\text{m}$ ; Large air voids: 1000-6000 $\mu\text{m}$ . . . . .	168
6.10	Pore size distribution of samples M1 and M2: (a) $d_{2D}$ from TS images; (b) $d_{2D}$ from CT-LP images; (c) $d_{3D}$ from CT-TP images. . . . .	169
6.11	Pore size distribution of samples M1 and M2-characterized into three pore size groups. . . . .	170
6.12	Relative frequency of air voids in three pore size groups characterized by analyzing TS, CT-LP and CT-TP images: (a) Sample M1; (b) Sample M2. . .	171
6.13	(a) The average pore diameter of air voids in each CT-TP image from the bottom to the top of the sample; (b) The average circularity of air voids in each CT-TP image from the bottom to the top of the sample. . . . .	171
6.14	3D configuration of the interlayer region in sample M1 (volume: $10 \times 10 \times 2 \text{ mm}^3$ ). . . . .	172
6.15	Photomicrograph of the interlayer region in sample M1 (under PPL mode). Yellow areas represent the air bubbles. Image fields: $8.95 \times 6.69 \text{ mm}^2$ . . . .	173
6.16	(a) Photomicrograph of the large air void (part) in the interface (under XPL mode). Image fields: $0.70 \times 0.53 \text{ mm}^2$ ; (b) Photomicrograph of the medium air void (under XPL mode). Image fields: $0.70 \times 0.53 \text{ mm}^2$ ; (c) Photomicrograph of the small air void (under XPL mode). Image fields: $0.35 \times 0.27 \text{ mm}^2$ ; (d) Photomicrograph of the small air void (detail) (under XPL mode). Image fields: $0.18 \times 0.14 \text{ mm}^2$ . . . . .	174
6.17	Circularity distribution of air voids measured by: (a) TS images; (b) CT-LP images. . . . .	175
6.18	Correlation between average circularity and pore size of samples M1 and M2: (a) TS images; (b) CT-LP images. . . . .	176
6.19	The aspect ratio of air void along with the sample height: (a) TS images; (b) CT-LP images. . . . .	177
6.20	The aspect ratio distribution of air voids measured by using TS and CT-LP images: (a) Sample M1; (b) Sample M2. . . . .	177
6.21	Correlation between average aspect ratio and pore size of samples M1 and M2: (a) TS images; (b) CT-LP images. . . . .	178
6.22	Schematic description of the cross-sections of the sphere (Left) and spheroid (Right). For the spherical voids, only once the slice from the center plane of the sphere (TP and LP-1), the acquired 2D area (diameter) can represent the size of the corresponding air void. For the other anisotropic shapes, like spheroid, all acquired 2D areas can not indicate the real size of the air void. . . . .	180
7.1	(a) Three scenarios: i. A small object with 1200 mm of path length for each layer (Time interval-20 s); ii. A medium object with 3600 mm of path length for each layer (Time interval-1 min); iii. A large object with 36000 mm of path length for each layer (Time interval-10 min). (b) Schematic diagram of the printing process by different time intervals between two layers. . . .	188

7.2	(a) Increasing the nozzle standoff distance $h$ could lead to the inaccurate layer deposition; (b) Schematic diagram of the printing process by different nozzle standoff distances between two layers. . . . .	189
7.3	(a) Extracting the specimen from the printed sample; (b) Illustration of the specimen for performing uniaxial tensile test; (c) A photograph of the uniaxial tensile test setup. . . . .	190
7.4	Extracting specimens from the printed sample (Left); A photograph of the cored specimen for CT scanning (Right). . . . .	191
7.5	The process of acquiring GSV based images for air void analysis and modeling. . . . .	191
7.6	Schematic explanation of the approach used to segment the air voids. . . . .	192
7.7	The notched digital specimen (cast specimen) used for the fracture and deformation analysis. . . . .	192
7.8	Schematic illustration of the 2D mesh generation. . . . .	193
7.9	The boundary condition of the computational uniaxial tension test. . . . .	193
7.10	An example: (a) A typical load and displacement curve of the uniaxial tensile test; (b) The corresponding DIC analysis of the specimen. . . . .	195
7.11	Load vs. displacement curves of uniaxial tensile tests at the material age of 7 days: (a) Time interval-20 s; (b) Time interval-1 min (also known as nozzle standoff distance-0 mm); (c) Time interval-10 min; (d) Nozzle standoff distance-5 mm; (e) Nozzle standoff distance-10 mm; (f) Cast. . . . .	196
7.12	Uniaxial tensile strength results at the material age of 7 days: (a) Different time intervals; (b) Different nozzle standoff distances. . . . .	197
7.13	Air void content and distribution (local porosity) of different samples made with various printing parameters. The gray line represents the individual computed result. The black line indicates the average relation. . . . .	198
7.14	(a) Total porosity in the interlayer zone; (b) The maximum value of local porosity in the interlayer zone. Interlayer zone: 10.5–13.5 mm in the height of the sample. . . . .	199
7.15	Illustration of the influences of extending the time interval on air void formation at the interface. . . . .	200
7.16	(a) Illustration of pore width determination; (b) Pore width distribution of different samples (results of 40 cross-sections for each sample were plotted) in the interlayer zone (10.5-13.5 mm in height). . . . .	201
7.17	(a) The simulated load vs. displacement curves of the cast specimens; (b) The simulated crack pattern (Left: initial specimen; Right: fractured specimen). Pink area-cementitious material; White area-air void; Black area-crack opening. . . . .	202
7.18	Simulated load vs. displacement curves of uniaxial tension tests: (a) Time interval-20 s; (b) Time interval-1 min (also known as nozzle standoff distance-0 mm); (c) Time interval-10 min; (d) Nozzle standoff distance-5 mm; (e) Nozzle standoff distance-10 mm. . . . .	203



7.19	The simulated fracture patterns for different printed specimens (Left: initial specimen; Right: fractured specimen): (a) Time interval-20 s; (b) Time interval-1 min (also known as nozzle standoff distance-0 mm); (c) Time interval-10 min. Pink area-cementitious material; White area-air void; Black area-crack opening. . . . .	204
7.20	The simulated fracture patterns for different printed specimens (Left: initial specimen; Right: fractured specimen): (a) Nozzle standoff distance-5 mm; (b) Nozzle standoff distance-10 mm. Pink area-cementitious material; White area-air void; Black area-crack opening. . . . .	205
7.21	Comparison between the modeling and experimental results. . . . .	206
8.1	A lab-scale prototype was fabricated by using a limestone-calcined clay-based cementitious material developed in this thesis. . . . .	214
8.2	Drying plastic shrinkage induced cracks on the printed cementitious materials, adapted from [3]. . . . .	215
8.3	(a) Steel reinforcement and 3D printed concrete formwork by Winsun, adapted from [32]; (b) External steel reinforcement system connected with 3D printed concrete segments, adapted from [13]; (c) Pre-installed mesh reinforcement method by Huashang Tengda ltd, adapted from [14]; (d) Mesh insertion and embedment method, adapted from [14]. . . . .	218
8.4	(a) 3D printed cementitious materials with fiber reinforcement, adapted from [17]; (b) 3D printed cementitious materials with cable reinforcement, adapted from [33]; (c) Illustration of screw reinforcement for 3D printed cementitious materials, adapted from [34]; (d) 3D printed cementitious materials reinforced by penetrated steel rebars, adapted from [31]. . . . .	219
8.5	The test setup for large-scale 3D printed structural elements in TU Eindhoven, adapted from [38]. . . . .	220
8.6	Illustration of the working mechanism of a flash calciner, adapted from [43]. . . . .	221
8.7	In both graphs, the dashed and solid curves represent digital fabrication and conventional construction, respectively. Top: Unit cost vs. complexity of building component. After the break-even point, using additive manufacturing shows great economic potential. Under the driving force of research, the break-even point can be shifted to the left. Bottom: Market volume vs. complexity of building component. With the development of digital fabrication, the demand for higher complexities is increasing. Adapted from [40]. . . . .	222
8.8	A lab-scale 3D printed and post-tensioned concrete girder constructed at Ghent University, adapted from [51, 52]. . . . .	223
8.9	Illustration of the working mechanism of FDM, adapted from [53]. . . . .	223
8.10	Examples of using the temporary support material during printing: (a) A normal trial; (b) A failed trial. Adapted from [38]. . . . .	224
8.11	(a) 3D printed domes (Left: constant layer thickness; Right: variable layer thickness); (b) An example of a 3D printed Nubian vault. Adapted from [57]. . . . .	225

# LIST OF TABLES

2.1	Material characteristics of different SCMs [47, 53, 78, 79]. . . . .	24
3.1	Physical properties and XRF composition of PC, LP and LGCC. . . . .	70
3.2	Preliminary mix composition of cementitious materials excluding admixtures (% of the binder mass). . . . .	70
3.3	Mixing protocol for the fresh paste/mortar preparation. . . . .	71
3.4	Amounts of admixtures for acceptable printing performance of the binders formulating the printable cementitious materials. . . . .	80
3.5	Printing parameters for performing buildability test. . . . .	85
4.1	Mix designs of cementitious materials (% of the binder mass). . . . .	105
4.2	Open time of different mixtures. . . . .	111
5.1	Physical characteristics and oxide composition from XRF of dry components in binders. . . . .	127
5.2	Reactive content of two different calcined clays (LGCC and HGCC). . . . .	127
5.3	Mix designs of cementitious materials prepared in this study (% of the binder mass). . . . .	128
5.4	$SSA_{total}$ and $\phi$ of different binders. . . . .	131
5.5	Piston moving velocity $V_0$ and material flow velocity $V$ at the orifice. . . . .	131
5.6	Printing parameters for buildability test. . . . .	133
5.7	TG test results-the normalized amount of calcium hydroxide (CH) and hydrate water (H) at 1, 2, 3, and 7 days. . . . .	147
6.1	Mixture proportions of printable cementitious materials (% of the binder mass). . . . .	159
6.2	Printing parameters. . . . .	160
6.3	Overview of approaches for characterizing the air void system. . . . .	164
6.4	Comparative study of different approaches for characterizing air voids. . . . .	179
7.1	Mixture proportions of printable cementitious materials (% of the binder mass). . . . .	186
8.1	A summary of the available reinforcement approaches for 3DCP. . . . .	217
8.2	Comparison between rotary kiln and flash calcination processes [43, 47]. . . . .	221



# SUMMARY

Extrusion-based 3D concrete printing (3DCP), as one of the emerging techniques, has received considerable attention from both academia and industry, due to its numerous benefits for concrete construction, through enhancing the freedom of architectural design, eliminating formwork, optimizing material use, and decreasing wastes, labors and costs. However, in most of proposed 3D printable cementitious materials, ordinary Portland cement (PC) still occupies a relatively high content, which partially neutralizes the sustainable benefits of 3DCP in aspects of formwork free and material-efficient designs. To date, considerable attempts have been made to develop sustainable cementitious materials in the context of 3DCP. Common supplementary cementitious materials (SCMs), i.e., fly ash, silica fume, and slag, are utilized as an ingredient of the binder in 3D printable cementitious materials, which is the most generic and applicable strategy for reducing the use of PC. Nevertheless, these common SCMs, which belong to industrial by-products, are gradually being depleted. For longer-term development, limestone and calcined clay appear to be suitable alternatives to SCMs, considered the worldwide abundance of raw materials and low CO<sub>2</sub> footprint in the material production.

The main goal of this thesis is to develop limestone-calcined clay-based cementitious materials for 3DCP. In order to develop such printable mixtures, investigations about the effect of different material and printing parameters on fresh and hardened properties were conducted.

In Chapter 1, the subject of this research, including background, motivation, objectives, scope and strategy, was clarified. Chapter 2 provided a systematic review of the available printing strategies, sustainable cementitious materials, and characterization methods for 3DCP. The influences of different contents of limestone and calcined clay, different dosages of viscosity modifying admixture (VMA) and different grade levels of calcined clays on fresh-state behaviors, 3D printability, stiffness evolution, hydration, compressive strength, and interlayer properties of limestone-calcined clay-based cementitious materials were investigated in Chapters 3, 4 and 5. For the 3D printed cementitious materials, air voids may play a dominant role in the interlayer bond strength. In Chapter 6, the typical air void system of 3D printed cementitious materials was characterized via digital image analysis. In addition to the thixotropy of printable mixtures, printing parameters also strongly affect the interlayer bond strength. Chapter 7 investigated the effect of two printing parameters, i.e., time gaps and nozzle standoff distances, on interlayer bond strength of limestone-calcined clay-based 3D printed cementitious materials. Since most of the techniques related to 3DCP are currently under development, it may still be a long way to widely use the proposed materials in practice. Chapter 8 discussed the concerns, barriers, state-of-the-art solutions, economic and sustainability potentials for using 3DCP in building and infrastructure construction. The last chapter included retrospection,

conclusions, and recommendations for further work.

The main findings of a series of experimental studies were summarized as follows:

Increasing the content of calcined clay and limestone from 0 wt.% to 90 wt.% in binder can reduce the slump, flowability, initial material flow rate, extrudability window, and initial setting time, improve the buildability, and accelerate the growth of the total specific surface area within the first 3 h. Such effects can link to the decrease of water film thickness and consumption of superplasticizer, which may be attributed to calcined clay's layered structure, high content of reactive aluminate, and high specific surface area. Besides, the high PC replacements led to severe dilution effects on hydration and compressive strength.

Increasing the dosage of VMA from 0.14% to 0.48% of the binder mass (binder: 40 wt.% calcined clay, 20 wt.% limestone, 40 wt.% PC) can increase the extrusion pressure, buildability, and green strength within the first 2.5 h, reduce the slump, flowability and open time, and delay the cement hydration. The mixture containing 0.24% of VMA showed satisfactory 3D printability, and optimal mechanical performance.

Increasing the high-grade calcined clay (HGCC) content from 0 wt.% to 50 wt.% in calcined clay (binder: 40 wt.% calcined clay, 20 wt.% limestone, 40 wt.% PC) can increase the extrusion pressure and flow consistency, improve the buildability, reduce the open time, and accelerate the cement hydration. However, increasing HGCC% led to an increase of air void content in the interface region of the printed sample, which weakened the compressive strength of the printed sample at 7 days. Blending HGCC in the mixture may contribute to enhancing particle flocculation and increasing water adsorption induced by the fine grain size, and high specific surface area.

In 3D printed cementitious materials (developed in this project), most of the air voids with the diameter in the range of 10-1000  $\mu\text{m}$  were distributed evenly in the layer region. Large air voids (1000-6000  $\mu\text{m}$ ) were enclosed mainly between the printed filaments (interface region), which resulted in the relatively higher local porosity than that of layer region. Additionally, the majority of air voids displayed irregular and elongated shapes, which could be due to the extrusion and layer-wise manufacturing processes in 3D printing.

Extending the time interval between two layers decreased the bond strength. In contrast, only increasing the nozzle standoff distance exhibited limited effects on that. The weak bond strength could be ascribed to the high local porosity at the interface of the specimen.



# SAMENVATTING

3D betonprinten op basis van extrusie (3DCP) heeft aanzienlijke aandacht ontvangen van zowel de academische wereld als de industrie. Dit is te danken aan de talloze voordelen die het heeft voor betonconstructies, zoals toename in ontwerprijheid, het niet nodig hebben van bekisting, optimalisatie van materiaalgebruik en vermindering van kosten, manuren en afval. Het leeuwendeel van de beschikbare 3D printbare cementgebonden materialen bestaat echter voor een groot deel uit Portlandcement (PC), wat de duurzaamheids-voordelen van 3DCP betreffende afwezigheid van bekisting en materiaal-efficiënt ontwerp teniet kan doen. Tot op heden zijn aanzienlijke pogingen gedaan om een duurzaam cementgebonden materiaal te ontwikkelen binnen de context van 3DCP. De meest gebruikte strategie voor het verminderen van de toepassing van PC is het toepassen van veelvoorkomende aanvullende cementgebonden materialen (SCMs) zoals vliegas, microsilica en hoogovenslak, die worden gebruikt als ingrediënt voor het bindmiddel in 3D printbare cementgebonden materialen. Deze veel toegepaste SCMs zijn een bijproduct van industriële processen, en waarvan de bronmaterialen uiteindelijk uitgeput zullen raken. Voor de lange termijn-ontwikkeling lijken kalksteen en gecalcineerde klei een geschikt alternatief voor deze SCMs, gezien de wereldwijde overvloed van de ruwe basismaterialen en de lage CO<sub>2</sub> voetafdruk bij de productie van deze materialen.

Het hoofddoel van deze dissertatie is het ontwikkelen van een cementgebonden materiaal voor 3DCP gebaseerd op kalksteen en gecalcineerde klei. Hiertoe is onderzoek uitgevoerd naar de invloed van verschillende materiaal- en print-parameters op verse en uitgeharde eigenschappen van het beton, teneinde een printbare mix te kunnen ontwikkelen.

In hoofdstuk 1 wordt het onderwerp van dit onderzoek, inclusief achtergrond, motivatie, doelen en omvang en strategie van het onderzoek verduidelijkt. Hoofdstuk 2 verschaft een gestructureerd overzicht van de beschikbare print strategieën, duurzame cementgebonden materialen en de karakterisering methodes voor 3DCP. De invloeden van verschillende hoeveelheden kalksteen en gecalcineerde klei, variërende dosissen viscositeit modifierend middel (VMA) en verschillende graadniveaus van het gecalcineerde klei op het gedrag van de verse mix, waaronder 3D printbaarheid, stijfheid evolutie over tijd, hydratatie, druksterkte en aanhechtingseigenschappen van kalksteen en gecalcineerde klei bevattende cementgebonden materialen zijn onderzocht in Hoofdstuk 3, 4 en 5. Voor 3D geprint cementgebonden materiaal kunnen luchtbellen een dominante rol spelen voor de aanhechting tussen de lagen. Hoofdstuk 6 karakteriseert de typische luchtbellenstructuur van 3D geprint cementgebonden materiaal door middel van digitale beeldanalyse. Naast de invloed op de thixotropie van printbare materialen hebben printparameters ook een sterk effect op de laagaaanhechting. Hoofdstuk 7 onderzoekt het effect van twee printparameters, te weten tijdsinterval tussen de lagen en de printkopafstand, op de hechtingssterkte tussen de

lagen van kalksteen en gecalcineerde klei bevattend cementgebonden materialen. Omdat de meeste technieken met betrekking tot 3DCP op het moment van schrijven onder ontwikkeling zijn, is er mogelijk nog een lange weg te gaan voordat de voorgestelde materialen toegepast worden in de praktijk. Hoofdstuk 8 beprekt de bedenkingen, barrières, ultramoderne oplossingen en het economisch en duurzaam potentieel voor het gebruik van 3DCP in gebouwen en infrastructurele constructies. Het laatste hoofdstuk bevat reflectie, conclusies en aanbevelingen voor toekomstig onderzoek.

De hoofdconclusies van een serie experimentele onderzoeken zijn als volgt samengevat:

Het verhogen van het aandeel gecalcineerd klei en kalksteen in het bindmiddel van 0 wt.% naar 90 wt.% kan de Zetmaat, verwerkbaarheid, initiële vloeibaarheid van het materiaal, periode waarbinnen extrusie mogelijk is en initiële uithardingstijd doen afnemen, de bouwbaarheid doen toenemen en groei van het totale specifieke oppervlak in de eerste drie uur doen versnellen. Dergelijke effecten kunnen gelinkt worden aan de afname van de dikte van de vloeistoffilm en het gebruik van superplastificeerder, wat toegeschreven kan worden aan de gelaagde structuur van gecalcineerde klei, de aanwezigheid van een grote hoeveelheid reactief aluminaat en een hoog specifiek oppervlak. De grote hoeveelheid PC-vertrengers zorgde daarnaast ook voor hevige afname van hydratatie en van druksterkte.

Het verhogen van de dosering van VMA van 0.14% tot 0.48% van de bindmiddelmassa (bindmiddel: 40 wt.% gecalcineerde klei, 20 wt.% kalksteen, 40 wt.% PC) kan de druk waarbij extrusie plaatsvindt, de bouwbaarheid en de verse druksterkte binnen de eerste 2.5 uur verhogen, de vloeibaarheid en de open tijd verminderen, en de cementhydratatie vertragen. De mix met 0.24% VMA vertoonde een bevredigende 3D-printbaarheid en optimale mechanische prestaties. Verhoging van het HGCC-gehalte (hoogwaardige gecalcineerde klei) van 0 tot 50 wt.% in gecalcineerde klei (bindmiddel: 40 wt.% gecalcineerde klei, 20 wt.% kalksteen, 40 wt.% PC) kan de druk waarbij extrusie plaatsvindt en de viscositeit verhogen, de bouwbaarheid verbeteren, de open tijd verkorten en de cementhydratatie versnellen. Het verhogen van het HGCC-gehalte leidde echter tot een toename van het gehalte aan luchtballen in het grensvlak van het geprinte proefstuk, waardoor de druksterkte van het geprinte proefstuk na 7 dagen afnam. Het bijmengen van HGCC in de mix kan bijdragen tot het verbeteren van de flocculatie en het verhogen van de wateradsorptie door de fijne korrelgrootte en het hoge specifieke oppervlak.

In de in dit project ontwikkelde 3D geprint cementgebonden materialen zijn veel luchtballen met een diameter van 10-1000  $\mu\text{m}$  gelijkwaardig verdeeld over de printlaag. Grote luchtballen (1000-6000  $\mu\text{m}$ ) zijn te vinden tussen de opeenvolgende printlagen (aanhechtingsgebied), wat resulteert in een relatief hoger lokale porositeit dan die in de printlaag. Daarnaast vertoont het gros van de luchtballen onregelmatige en langwerpige vormen, wat het gevolg kan zijn van het fabricageproces van het stapelen van meerdere printlagen doormiddel van extrusie.

Het verlengen van het tijdsinterval tussen twee na elkaar geprinte lagen verlaagde de hechtsterkte van deze lagen. Daarentegen heeft het vergroten van de printkop afstand slechts beperkte invloed op deze aanhechtsterkte. Een zwakke aanhechting kan

worden toegeschreven aan de hoge lokale porositeit in het aanhechtingsgebied van het testspecimen.



# I

## GENERAL INTRODUCTION



# 1

## INTRODUCTION

*This chapter presents the background and motivation of the current thesis. After that, the objectives, scope and strategy of the research are illustrated. Finally, a summary of the thesis outline is given.*

---

Parts of this chapter were published in Heron **62**, 167 (2017) and Cement and Concrete Research **132**, 106040 (2020) [1, 2].

## 1.1. INTRODUCTION

CONCRETE is volumetrically the most widely used human-made construction material throughout the world. There are many advantages to using concrete for the construction of buildings and other types of structures. First, concrete is typically preferred for its low cost, high strength, as well as exceptional durability [3–5]. The second reason is that the raw materials for concrete can be obtained practically anywhere in the world. Furthermore, concrete is also a flexible material giving considerable design freedom to architects [6]. The world consumption of concrete is close to 25 billion tons each year. This means globally more than 3.8 tons of concrete is used per person each single year [7]. The massive production and consumption of concrete generates a substantial burden on our living environment. The manufacturing processes of Portland cement consume large quantities of energy and emit massive amounts of greenhouse gases [5]. According to Dong et al. [8], the cement industry is currently responsible for 5-7% of the global total CO<sub>2</sub> emissions. As a primary construction material, concrete will continue to be in demand far into the future (see Figure 1.1) [9]. It is necessary to improve the sustainability of concrete structures to make sure that concrete will still be a competitive construction material [10]. Moreover, labor safety is an increasing concern for in-situ concrete manufacturing. Skilled workmanship is required in the processes of placing and connecting the reinforcement, and erecting the formwork, especially for casting customized geometries [11]. The workers are continuously threatened by work-related injuries and illnesses [12, 13].

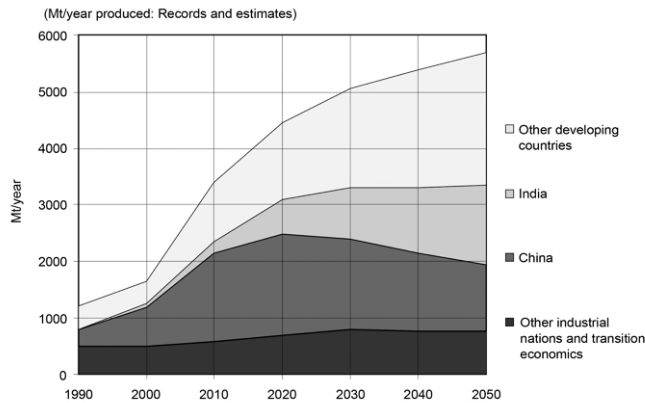


Figure 1.1: Portland cement production worldwide from 1990 to 2050, adapted from [9].

Additive manufacturing (AM) appears to be a viable solution to address the challenges of current concrete industry described above. AM has been developing rapidly in different fields of science and engineering in the past few decades [14, 15]. American Society for Testing and Materials [16] defines AM as “a layer-based process of joining materials to fabricate objects based on 3D model data”. AM technologies have become a daily routine in many industries [14, 17], e.g., aerospace, biomedical, and



food [17]. In the construction industry, AM of concrete is a natural choice since concrete is the most widely used construction material worldwide. 3D concrete printing, or digital concrete construction, has been under development for the past 20 years with an increasing rate of research and application [18]. Currently, two major printing technologies are under development: extrusion-based and selective binding methods [19]. This thesis focuses on extrusion-based 3D concrete printing (3DCP). Many companies, such as Contour Crafting, XtreeE, CyBe, Apis Cor, WinSun, and others, attempted to implement 3DCP in practice [20], showing the potential of this technology.

Development of 3DCP could bring massive benefits to building and construction projects. As illustrated by [18, 21, 22], 3DCP can eliminate the need for formwork, reduce the required cost and time of construction, increase the safety of construction site and flexibility of architectural design. However, as mentioned by Wangler et al. [23], a relatively high cement content in the mix design of digital concrete is needed to satisfy the rheological requirements during the manufacturing process, neutralizes the benefit of material-efficient designs. For 3DCP, most proposed mixtures contain larger quantities of Portland cement than typical conventionally cast concrete [24] with similar mechanical performance. It is clear that for 3DCP techniques to become an alternative to current practices, sustainable binders must be developed that are technically capable yet do not compromise sustainability. As the technology matures, researchers now need to develop sustainable cementitious materials by replacing part of Portland cement with supplementary cementitious materials (SCMs) for 3DCP. Common SCMs, such as fly ash, silica fume, and blast-furnace slag, have been involved in many sustainable and 3D printable concrete proposals (see [20–22, 25]). However, limitations may appear using these common SCMs as the main ingredients of 3D printable cementitious materials for a long-term application. As shown in Figure 1.2, the main problem for silica fume and slag is the limited quantity of their production [6, 26]. The amount of fly ash is relatively higher, whereas more than 66% of available fly ash is not suitable for blending with cement due to quality reasons [27].

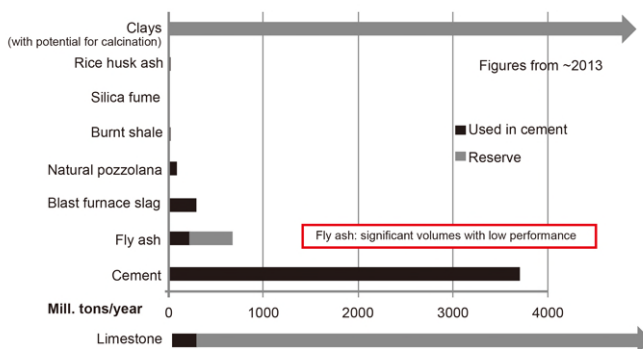


Figure 1.2: Quantities of common supplementary cementing materials (SCMs), adapted from [26].

Scrivener et al. [26] pointed out that limestone and calcined clay cement is an

appropriate solution for developing sustainable concrete in the longer term. Using calcined clay, especially when clays with a lower kaolinite content are used, in concrete shows remarkable advantages, including: (1) lower CO<sub>2</sub> emissions during the production of calcined clay [26, 28]; (2) worldwide abundance (see Figure 1.2) [26, 29, 30]; (3) comparable early-age strength [31–33]; (4) capillary porosity refinement due to the pozzolanic reaction [26, 29, 30, 34, 35]; (5) lower cost [28, 36]. Note that, at present, the benefits of using calcined clay in printable concrete might not be that significant since 3DCP is not widely used yet. Nevertheless, given the potential of 3DCP technology, it is worthwhile to provide a more sustainable and economical option. However, a systematic investigation of developing limestone and calcined clay-based cementitious materials for 3DCP has not been conducted to date.

## 1.2. RESEARCH AIM AND OBJECTIVES

**T**HIS thesis aims to develop sustainable cementitious materials for 3DCP by using limestone and calcined clay as the substitutions of Portland cement. For developing such materials, studies and understanding about the effects of different parameters on their fresh-state behaviors and hardened properties are essential. To reach this goal, the following tasks are required:

- Owing to the material features of calcined clay, i.e., high content of reactive aluminate, fine particle size, high specific surface area (SSA), and layered particle structure, increasing the content of calcined clay may enhance the static yield stress and structural build-up (potentially improve the buildability), reduce the workability, and consequently increase the demand of water and superplasticizer (may adversely affect the extrudability). The compressive strength and cement hydration appear to be decreased by increasing the content of calcined clay and limestone. Thus, the first objective is to investigate the effect of different replacement levels of Portland cement on fresh and hardened properties of limestone-calcined clay-based cementitious materials for 3DCP.
- Utilizing a combination of cellulose-derivative viscosity modifying admixture (VMA) and superplasticizer is a strategy to develop 3D printable cementitious materials. The competitive effects between VMA and superplasticizer in a suspension can increase the yield stress and viscosity, which may be suitable for buildability. However, this effect will significantly increase extrusion pressure, adversely affecting extrudability. The dosage of VMA becomes very critical. Therefore, the effect of different dosages of VMA on fresh and hardened properties of a 3D printable limestone-calcined clay-based cementitious material needs to be explored. The optimal dosage of VMA should be determined.
- Calcined clays that are sourced from different suppliers may exhibit different chemical compositions (especially metakaolin contents and secondary phases), and physical properties, i.e., fineness, morphology, SSA, and density. These differences may bring substantial influences on the rheology and thixotropy of fresh mixtures. The term of different-grade was used to represent various metakaolin contents in calcined clays. Thus, the third objective is to investigate

the effect of different grade levels of calcined clays on fresh and hardened properties of limestone-calcined clay-based cementitious materials for 3DCP.

- For many 3D printed cementitious materials, air voids may play a dominant role in the interlayer bond strength. However, there is still a lack of research to reveal the air void characteristics in 3D printed cementitious materials. The fourth objective is to systematically characterize the typical air void system of 3D printed cementitious materials.
- The interlayer bonding between two layers appears to be influenced by not only the thixotropy of printable mixtures but also the printing parameters. The effect of different printing parameters (time gaps, and nozzle standoff distances) on interlayer bond strength of 3D printed cementitious materials needs to be investigated.

### 1.3. RESEARCH SCOPE

**E**XTRUSION of sufficiently stiff materials that is one of the printing approaches summarized by Mechtcherine et al. [37] is the main printing strategy in this thesis. The extrusion force was only provided by the rotor and stator-based conveying pump. The developed fresh mixtures should exhibit proper flow consistency during printing, and high stiffness and near-zero slump after deposition.

Rheology and thixotropy of cementitious materials depend on the mix design, which is related to volumetric and compositional features (presence of cement, filler, and SCMs) of the binder system, particle shape, content and gradation of the aggregate, the water to binder ratio, as well as type and dosage of the admixture. In the development of limestone and calcined clay-based 3D printable cementitious materials, it would be too complicated to study all parameters. Therefore, in the material aspect, variations of the following parameters were considered:

- Different replacement levels of Portland cement by limestone and calcined clay.
- Different dosages of viscosity-modifying admixture additions.
- Different grade levels of calcined clays.

Note that raw materials, i.e., CEM I 52.5R Portland cement, limestone powder (CALCITEC 2001M, Carmeuse), polycarboxylate ether-based superplasticizers (MasterGlenium®51, BASF), hydroxypropyl methylcellulose-based viscosity-modifying admixture (Powder type, Shanghai Ying Jia Industrial Development Co., Ltd), and quartz sand (0.125-2 mm) were used throughout the study. Two types of calcined clay were employed. A low-grade calcined clay (LGCC), which contained about 50 wt.% of metakaolin, was purchased from Argeco, France. The other one, with nearly 95 wt.% of metakaolin, was regarded as a high-grade calcined clay (HGCC) supplied by Burgess, USA. The same sand gradation, water to binder (0.3), and sand to binder (1.5) mass ratios were employed throughout the thesis. The experimental findings presented in the current thesis should only be considered concerning the materials and methods used in this study.

In contrast, hardened properties of 3D printed cementitious materials do not only rely on the mix design but also on the printing parameters, i.e., printing speeds, nozzle types, time intervals between layers, nozzle standoff distances, printing environments, curing conditions, and others. Not all these parameters showed significant impacts on interface adhesion from literature. This study concentrates on time intervals between layers and nozzle standoff distances.

#### 1.4. STRATEGY OF THIS RESEARCH

To achieve the objectives of this thesis, the strategies are presented as follows:

- First, extrudability and very early-age strength had to be emphasized as two major constraints of developing printable cementitious materials. Experimental tests, i.e., slump, slump flow, ram extrusion and green strength tests, were employed to quantify such fresh state behaviors of developed limestone and calcined clay-based cementitious materials for 3DCP.
- Second, for characterizing the 3D printability of developed limestone and calcined clay-based cementitious materials, extrudability, open time and buildability tests were proposed and performed on the basis of a lab-scale 3DCP setup.
- Third, the compressive strength of 3D printed limestone and calcined clay-based cementitious materials were examined to determine the anisotropic behaviors, as well as influences of the different replacement levels of Portland cement, different dosages of viscosity-modifying admixture, and different grade levels of calcined clays on material strength, respectively. Additionally, for investigating the effect of different printing parameters, the uniaxial tensile test was employed to quantify the interface adhesion of printed specimens.
- Fourth, X-ray computed tomography, and optical image scanning were employed to acquire the micrographs for characterizing the typical air void system of 3D printed cementitious materials.
- Fifth, isothermal calorimetry was used to study the influences of different material parameters on hydration kinetics. Thermogravimetric analysis was carried out for assessing phase assemblages of the studied mixtures at various ages. Brunauer-Emmett-Telle specific surface area of hydrated cementitious materials at the material age of 1 h and 3 h were quantified by liquid nitrogen adsorption method for studying the very early-age cement hydration.

#### 1.5. THESIS OUTLINE

The thesis comprises 9 chapters and is divided into three parts: general introduction, experimental investigation, and discussion and conclusion. An illustration of the thesis outline is given in Figure 1.3.

The current chapter introduces the research background, motivation, scope, objective, and corresponding methodology.

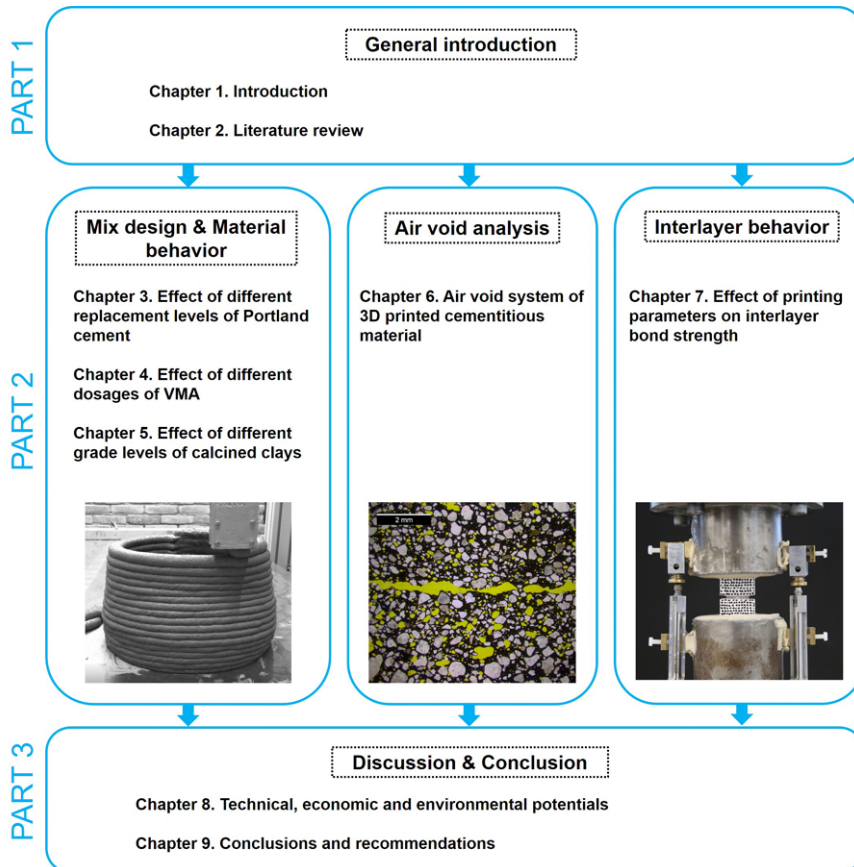


Figure 1.3: Outline of the thesis.

**Chapter 2** is reserved for literature review. A systematic review of the available printing strategies, sustainable cementitious materials and characterization methods of fresh properties and interlayer behaviors for printable cementitious materials is given.

**Chapter 3** studies the effect of different replacement levels of Portland cement by limestone and calcined clay on slump and slump flow, 3D printability, stiffness evolution, compressive strength, and early-age hydration.

**Chapter 4** evaluates the fresh and hardened properties of limestone-calcined clay-based 3D printable cementitious materials. The effect of different dosages of VMA on flowability, green strength development, 3D printability, compressive strength, air void content and distribution, and hydration is studied.

**Chapter 5** investigates the effect of different grade levels of calcined clays on ram extrusion rheology, 3D printability, compressive strength, air void content and distribution, and hydration.

**Chapter 6** attempts to systematically characterize the typical air void system of limestone-calcined clay-based 3D printed cementitious materials via image acquisition and analysis techniques.

**Chapter 7** investigates the effect of different printing parameters (time gaps, and nozzle standoff distance) on interlayer bond strength of limestone-calcined clay-based 3D printed cementitious materials.

**Chapter 8** discusses the challenges and opportunities of implementing 3DCP in building and infrastructure construction, considering its technical, sustainable, and economic potentials.

**Chapter 9** contains conclusions and recommendations.

## REFERENCES

- [1] Y. Chen, F. Veer, and O. Çopuroğlu, *A critical review of 3D concrete printing as a low CO<sub>2</sub> concrete approach*, *Heron* **62**, 167 (2017).
- [2] Y. Chen, S. Chaves Figueiredo, Z. Li, Z. Chang, K. Jansen, O. Çopuroğlu, and E. Schlangen, *Improving printability of limestone-calcined clay-based cementitious materials by using viscosity-modifying admixture*, *Cement and Concrete Research* **132**, 106040 (2020).
- [3] A. P. Gursel and C. Ostertag, *Comparative life-cycle impact assessment of concrete manufacturing in Singapore*, *International Journal of Life Cycle Assessment* **22**, 237 (2017).
- [4] K. Mehta and P. J. M. Monteiro, *Concrete: Microstructure, Properties, and Materials*, (McGraw-Hill, New York, 2006) 3rd ed.
- [5] C. Meyer, *The greening of the concrete industry*, *Cement and Concrete Composites* **31**, 601 (2009).
- [6] M. Glavind, *Sustainability of cement, concrete and cement replacement materials in construction*, in *Sustainability of Construction Materials* (Woodhead Publishing Limited, 2009) pp. 120–147.

- [7] A. Petek Gursel, E. Masanet, A. Horvath, and A. Stadel, *Life-cycle inventory analysis of concrete production: A critical review*, *Cement and Concrete Composites* **51**, 38 (2014).
- [8] Y. H. Dong, S. T. Ng, A. H. Kwan, and S. K. Wu, *Substituting local data for overseas life cycle inventories - A case study of concrete products in Hong Kong*, *Journal of Cleaner Production* **87**, 414 (2015).
- [9] M. S. Imbabi, C. Carrigan, and S. McKenna, *Trends and developments in green cement and concrete technology*, *International Journal of Sustainable Built Environment* **1**, 194 (2012).
- [10] T. Proske, S. Hainer, M. Rezvani, and C. A. Graubner, *Eco-friendly concretes with reduced water and cement contents - Mix design principles and laboratory tests*, *Cement and Concrete Research* **51**, 38 (2013).
- [11] F. Bos, R. Wolfs, Z. Ahmed, and T. Salet, *Additive manufacturing of concrete in construction: Potentials and challenges of 3D concrete printing*, *Virtual and Physical Prototyping* **11**, 209 (2016).
- [12] N. K. Kittusamy and B. Buchholz, *Whole-body vibration and postural stress among operators of construction equipment: A literature review*, *Journal of Safety Research* **35**, 255 (2004).
- [13] Y. W. D. Tay, B. Panda, S. C. Paul, N. A. Noor Mohamed, M. J. Tan, and K. F. Leong, *3D printing trends in building and construction industry: a review*, *Virtual and Physical Prototyping* **12**, 261 (2017).
- [14] G. De Schutter, K. Lesage, V. Mechtcherine, V. N. Nerella, G. Habert, and I. Agusti-Juan, *Vision of 3D printing with concrete — Technical, economic and environmental potentials*, *Cement and Concrete Research* **112**, 25 (2018).
- [15] J. Schwartz, *Graphic statics and their potential for digital design and fabrication with concrete*, *Cement and Concrete Research* **112**, 122 (2018).
- [16] ASTM F2792-10, *Standard Terminology for Additive Manufacturing Technologies*, (2010).
- [17] J. G. Sanjayan, B. Nematollahi, M. Xia, and T. Marchment, *Effect of surface moisture on inter-layer strength of 3D printed concrete*, *Construction and Building Materials* **172**, 468 (2018).
- [18] R. A. Buswell, W. R. Leal de Silva, S. Z. Jones, and J. Dirrenberger, *3D printing using concrete extrusion: A roadmap for research*, *Cement and Concrete Research* **112**, 37 (2018).
- [19] V. N. Nerella and V. Mechtcherine, *Studying the printability of fresh concrete for formwork-free concrete onsite 3D printing technology (CONPrint3D)*, in *3D Concrete Printing Technology* (Elsevier Inc., 2019) pp. 333–347.



- [20] S. Chaves Figueiredo, C. Romero Rodríguez, Z. Y. Ahmed, D. H. Bos, Y. Xu, T. M. Salet, O. Çopuroğlu, E. Schlangen, and F. P. Bos, *An approach to develop printable strain hardening cementitious composites*, *Materials and Design* **169**, 107651 (2019).
- [21] T. T. Le, S. A. Austin, S. Lim, R. A. Buswell, A. G. Gibb, and T. Thorpe, *Mix design and fresh properties for high-performance printing concrete*, *Materials and Structures/Materiaux et Constructions* **45**, 1221 (2012).
- [22] V. Nerella, M. Näther, A. Iqbal, M. Butler, and V. Mechtcherine, *Inline quantification of extrudability of cementitious materials for digital construction*, *Cement and Concrete Composites* **95**, 260 (2019).
- [23] T. Wangler, N. Roussel, F. P. Bos, T. A. Salet, and R. J. Flatt, *Digital concrete: A review*, *Cement and Concrete Research* **123**, 105780 (2019).
- [24] B. Panda, C. Unluer, and M. J. Tan, *Investigation of the rheology and strength of geopolymer mixtures for extrusion-based 3D printing*, *Cement and Concrete Composites* **94**, 307 (2018).
- [25] G. Ma, Z. Li, and L. Wang, *Printable properties of cementitious material containing copper tailings for extrusion based 3D printing*, *Construction and Building Materials* **162**, 613 (2018).
- [26] K. Scrivener, F. Martirena, S. Bishnoi, and S. Maity, *Calcined clay limestone cements (LC3)*, *Cement and Concrete Research* **114**, 49 (2018).
- [27] R. Snellings, *Assessing, understanding and unlocking supplementary cementitious materials*, *RILEM Technical Letters* **1**, 50 (2016).
- [28] W. Huang, H. Kazemi-Kamyab, W. Sun, and K. Scrivener, *Effect of replacement of silica fume with calcined clay on the hydration and microstructural development of eco-UHPFRC*, *Materials and Design* **121**, 36 (2017).
- [29] M. Antoni, J. Rossen, F. Martirena, and K. Scrivener, *Cement substitution by a combination of metakaolin and limestone*, *Cement and Concrete Research* **42**, 1579 (2012).
- [30] Y. Dhandapani, T. Sakthivel, M. Santhanam, R. Gettu, and R. G. Pillai, *Mechanical properties and durability performance of concretes with Limestone Calcined Clay Cement (LC 3)*, *Cement and Concrete Research* **107**, 136 (2018).
- [31] G. L. Alvarez, A. Nazari, A. Bagheri, J. G. Sanjayan, and C. De Lange, *Microstructure, electrical and mechanical properties of steel fibres reinforced cement mortars with partial metakaolin and limestone addition*, *Construction and Building Materials* **135**, 8 (2017).
- [32] Y. Chen, Z. Li, S. Chaves Figueiredo, O. Çopuroğlu, F. Veer, and E. Schlangen, *Limestone and calcined clay-based sustainable cementitious materials for 3D concrete printing: A fundamental study of extrudability and early-age strength development*, *Applied Sciences* **9**, 1809 (2019).



- [33] A. Tironi, A. N. Scian, and E. F. Irassar, *Blended cements with limestone filler and kaolinitic calcined clay: Filler and pozzolanic effects*, *Journal of Materials in Civil Engineering* **29**, 040171116 (2017).
- [34] F. Avet, R. Snellings, A. Alujas Diaz, M. Ben Haha, and K. Scrivener, *Development of a new rapid, relevant and reliable (R3) test method to evaluate the pozzolanic reactivity of calcined kaolinitic clays*, *Cement and Concrete Research* **85**, 1 (2016).
- [35] Y. Dhandapani and M. Santhanam, *Assessment of pore structure evolution in the limestone calcined clay cementitious system and its implications for performance*, *Cement and Concrete Composites* **84**, 36 (2017).
- [36] F. Avet and K. Scrivener, *Investigation of the calcined kaolinite content on the hydration of Limestone Calcined Clay Cement (LC3)*, *Cement and Concrete Research* **107**, 124 (2018).
- [37] V. Mechtcherine, F. Bos, A. Perrot, W. L. da Silva, V. Nerella, S. Fataei, R. Wolfs, M. Sonebi, and N. Roussel, *Extrusion-based additive manufacturing with cement-based materials – Production steps, processes, and their underlying physics: A review*, *Cement and Concrete Research* **132**, 106037 (2020).



# 2

## LITERATURE REVIEW

*This chapter aims to provide a systematical review of the available printing strategies, sustainable cementitious materials and characterization methods for extrusion-based 3D concrete printing (3DCP). The printing strategies, consisting of printing setup, process, and material requirements, were summarized initially. In the material aspect, the high ordinary Portland cement (OPC) content in most printable mixtures is still a major issue that impedes the sustainability of 3DCP. This can be resolved by partially substituting OPC with supplementary cementitious materials (SCMs). In this review, the effect of different SCMs on fresh-state behaviors and 3D printing of cementitious materials was comprehensively discussed. Finally, a series of test methods for quantitatively characterizing fresh properties, 3D printability and interlayer behaviors were summarized and reviewed.*

## 2.1. INTRODUCTION

MANY recent studies attempted to develop sustainable cementitious materials for extrusion-based 3D concrete printing (3DCP) by employing different approaches, for instance, partially replacing ordinary Portland cement (OPC) by supplementary cementitious materials (SCMs) [1, 2], partially substituting natural aggregate by recycled aggregate [3–5], or with other industrial wastes [6, 7]. However, to date, the way to enhance the sustainability of 3DCP, especially within the context of using low OPC (SCMs-based) binders in printable cementitious materials, has not been adequately summarized. Additionally, there is lack of a comprehensive review about the influences of different SCMs on the rheology and 3D printability of fresh cementitious materials.

Compared with conventional concrete, many distinct fresh-state behaviors, e.g., pumpability, extrudability, and buildability, are required in 3DCP [8, 9]. These material behaviors are primarily constrained by the printing strategy, i.e., the printing system and process. Generally, 3D printable cementitious materials should be formulated compatible with the printing strategy. In addition, the methods for investigating the fresh and hardened properties of conventional cementitious materials do not satisfy the demands for quantifying and developing 3D printable cementitious materials. Many modified or novel methods that were proposed in this context were, therefore, need to be summarized. For a comprehensive demonstration of state-of-the-art review on 3D printable cementitious materials, all the above-mentioned aspects should be taken into consideration.

The goal of this study is to systematically review and discuss the printing strategies, sustainable cementitious materials, and characterization methods for 3DCP. Therefore, this chapter was organized into three distinct parts, the first of which was to explore the available 3DCP strategies, including the printing system and process, as well as the requirements of material behaviors. In the second part, a comprehensive review of SCMs-based binders used in the available 3D printable cementitious materials was presented. The influences of different SCMs on the rheology and 3D printing of fresh mixtures were highlighted and discussed. Finally, the test methods for characterizing the fresh properties and interlayer behaviors of 3D printed cementitious materials were summarized.

## 2.2. EXTRUSION-BASED 3D CONCRETE PRINTING STRATEGY

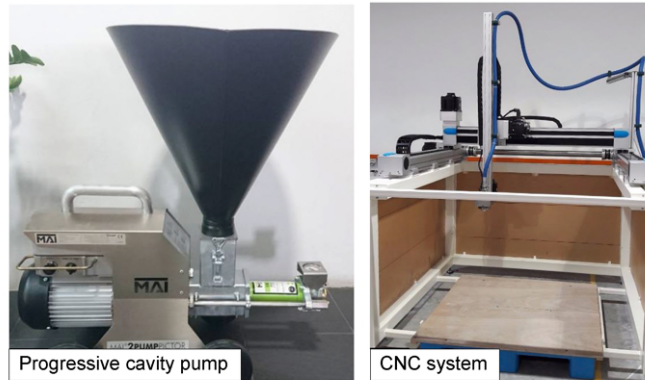
MOST of the 3DCP systems being used in both academic institutes and construction industry consist of three primary units: a deposition setup, a control unit, and a material conveying system. Both 3- or 4-axis gantry-based and 6-axis robotic deposition setups were implemented. The deposition setup is controlled by the control unit to fulfill a predefined printing path that is programmed by the operator. The material conveying system may comprise a series of components, i.e., a mixing machine, a pump, a printhead, and others, for preparing, pumping, and extruding the fresh mixtures.

In material preparation, there are two main strategies, as mentioned by Wolfs [10]. First, the fresh mixture is mixed in multiple batches and hereafter delivered manually or automated to the hopper of the progressive cavity pump (see Figure 2.1(a)). This

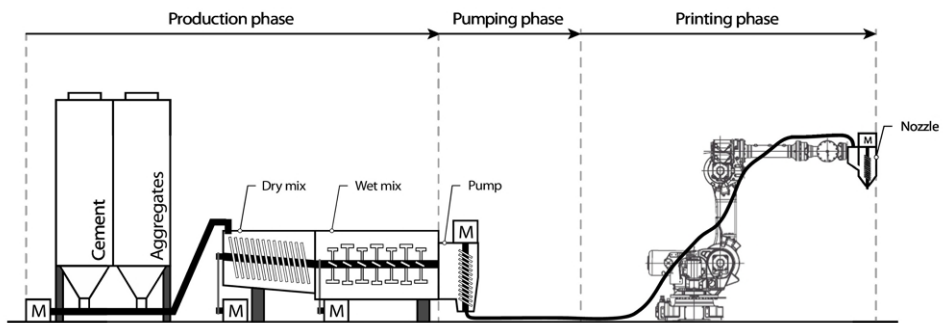
approach is mainly preferred in a small-scale application, e.g., printable material development and other experimental activities. Second, a continuous system, such as an inline mixing machine that works with the pump synchronously (see Figure 2.1(b)), is required for large-scale construction. The various mixing strategies may lead to different demands on fresh mixtures. For example, the former may require fresh mixtures with a relatively longer open time/printability window than the latter. However, it also depends on the hose length and material flow rate. Due to the short and intense mixing procedures, the inline mixing approach may not be a proper way for preparing certain fresh mixtures, which contained a high dosage of fibers and/or exhibited high yield stress and viscosity during the mixing process. There is still some discussion concerning which strategy would be the most appropriate. In different cases, the size of each batch and the mixing strategy are primarily dependent on factors, e.g., the geometry of printed component, volume deposition rate (material flow rate), and open time of the printing material [11].

In many cases, the pumping and extrusion forces are generally supplied by a ram extruder or a material conveying pump on the basis of a rotor-stator configuration (see Figure 2.1(a)). The printhead could be a simple nozzle that has the rectangle opening (most time) with or without a geometric reduction. Roussel [12] mentioned that the shear force between fresh mixtures and the inner wall of hose and nozzle is concentrated at the interface that is also regarded as the lubrication layer. The ability to form the lubrication layer of fresh mixtures becomes critical to evaluate its pumpability and extrudability. During the pumping and extrusion process, a plug zone might exist where the material may already be flocculated and exhibited a certain yield stress. Therefore, the material showed high/sufficient stiffness and near zero-slump after deposition from the nozzle. This strategy is classified as the extrusion of high or sufficiently stiff materials in Mechtcherine et al. [13].

However, it should be noted that the pumping distance (hose length) for extrusion of stiff materials is limited due to the high pumping pressure induced by the high yield stress and plastic viscosity (leading to a significant increase of material temperature and a short initial setting time). Thus, the extrusion of flowable material is proposed as a superior strategy for 3DCP. The material exhibits exceptionally high fluidity, requiring significantly lower pump pressure and energy input than the high/sufficiently stiff material during the mixing, pumping, and extrusion processes. However, once the flowable material is deposited from the nozzle, it should reach sufficient stiffness rapidly. Enhancing the stiffness of the flowable mixture within a short time is quite critical in this context. Rheology-/hydration-control (or set on-demand) as a proper way is therefore proposed by many researchers [15, 19–21]. Accelerating the stiffness of material during and after deposition is the main idea of this strategy. As mentioned by Mechtcherine et al. [13], the principle of this strategy is to mix “active agent”, which could be a chemical accelerator, an organic rheology modifier, or a kind of fast-set cement slurry (such as aluminate-based cement [22]), with the fresh mixture in the printhead (see Figure 2.2). To achieve the goal of this strategy, it largely depends on the dispersion/mixing of “active agent” and the design of the printhead. Earlier attempts of this strategy were made by [15, 23–25]. On the other hand, the pumping process may be excluded in several 3DCP systems, which only consist of a large volume of V-shape



(a)



(b)

Figure 2.1: Typical 3DCP experimental setups. (a) 4-axis gantry-based system, multiple batches (material preparation), and rotor-stator-based pump, adapted from [14]; (b) 6-axis robotic arm, continuous mixing (material preparation), and rotor-stator-based pump, adapted from [15].

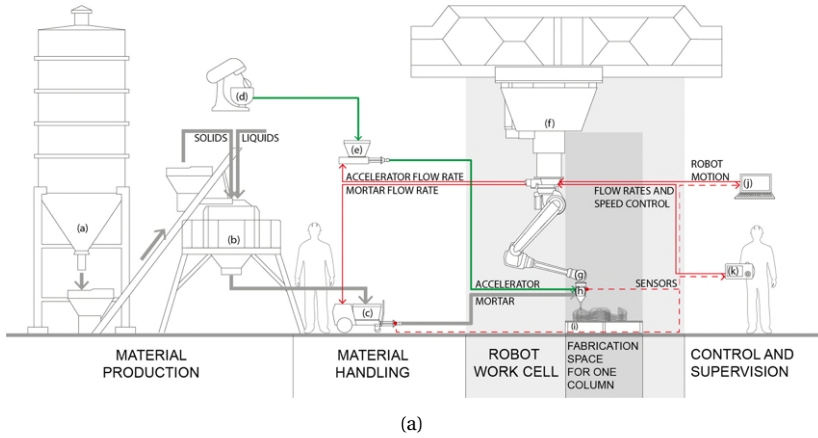


Figure 2.2: (a) Diagram of set-on-demand printing system, adapted from [16]; (b) Photographs of the set-on-demand printing system and printed columns at ETH Zürich, adapted from [17].

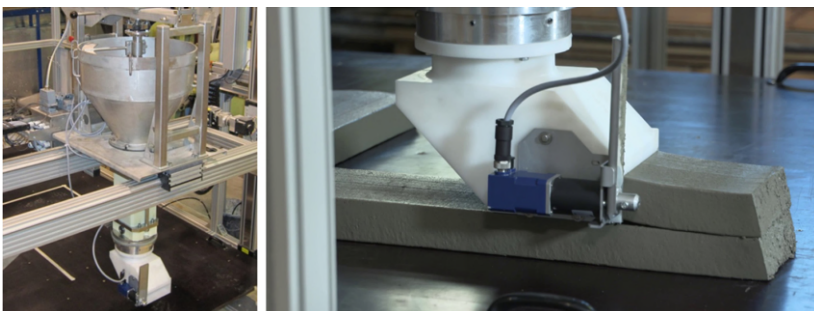


Figure 2.3: 3DCP experimental setup at TU Dresden: 4-axis gantry-based system, multiple batches, and screw extruder, adapted from [18].

material hopper and a screw extruder (see Figure 2.3). The prepared fresh mixture is poured into the hopper directly. Dependent on the gravitational flow with or without the additional energy input (which depends on the fluidity of fresh mixtures), the material is transported to the bottom of the hopper, where the screw extruder is positioned.

2

### 2.3. SCM-BASED CEMENTITIOUS MATERIALS FOR 3DCP

TECHNICALLY, most available 3D printable cementitious materials are designed in the form of grout and mortar as typically fine aggregate of smaller than 2 mm is employed. 3D printable cementitious materials in this study are mainly referred to as printable mortars, which primarily contain three components: binder, fine aggregate, and water. Compared to mold-cast concrete, 3D printable cementitious materials may require a much higher amount of OPC. As shown in Figure 2.4, the proportion of OPC in most of the 3D printable cementitious materials is more than 20 wt.%. Assuming a typical concrete mixture's unit weight is  $2200 \text{ kg/m}^3$ , the majority of printable mixtures would contain at least  $330 \text{ kg/m}^3$  of OPC. In Figure 2.4, the aggregate to binder mass ratio (A/B) is smaller than 2 in most of printable mixtures, whereas the A/B is of the order 3-3.5 in high strength mold-cast concrete (equal or greater than 60 MPa of compressive strength at 28 days), and more than 5 in moderate strength mold-cast concrete (about 30 MPa of compressive strength at 28 days) [26].

There are two strategies for developing low OPC-content cementitious materials in the field of 3DCP: (1) Use supplementary cementitious materials (SCMs) or other types of low carbon cement to substitute a high volume of OPC; (2) Reduce the binder content by increasing the proportion of aggregate (the binder composition is fixed). This study focuses on the cement replacement strategy, while the reader could refer to works [9, 27, 28] for the A/B modification strategy.

#### 2.3.1. EFFECT OF COMMON SCMS ON FRESH PROPERTIES

Common SCMs, including fly ash, blast furnace slag, and silica fume, were used as a partial replacement of OPC/clinker in 3D printable cementitious materials [41–43]. The initial idea of using such SCMs in printable mixtures was to improve the packing density, cohesion, and flow consistency. The addition of SCMs could significantly influence the rheological behavior of fresh mixtures. However, for different SCMs, the impacts on fresh properties may not be the same, as shown in Table 2.1.

Depending on the coal composition, fly ash can be distinguished as siliceous (Class F) and calcareous (Class C) types [44]. Compared to siliceous fly ash, calcareous fly ash contains a much higher content of reactive CaO, which could enable self-cementitious properties [44–46]. In this study, fly ash (FA) is referred to as siliceous/Class F fly ash as it was mainly used in the available printable cementitious materials. For example, Panda et al. [1, 33, 39, 40] proposed many 3D printable cementitious materials containing a high volume of FA. Up to 80% of OPC in the binder mass was replaced by FA in their study [33]. FA particles having high sphericity and smooth surface texture improve the flowability of self-compacting concrete [47, 48]. Due to the “ball bearing effect”, replacing a high amount of OPC by FA may reduce the yield stress and plastic



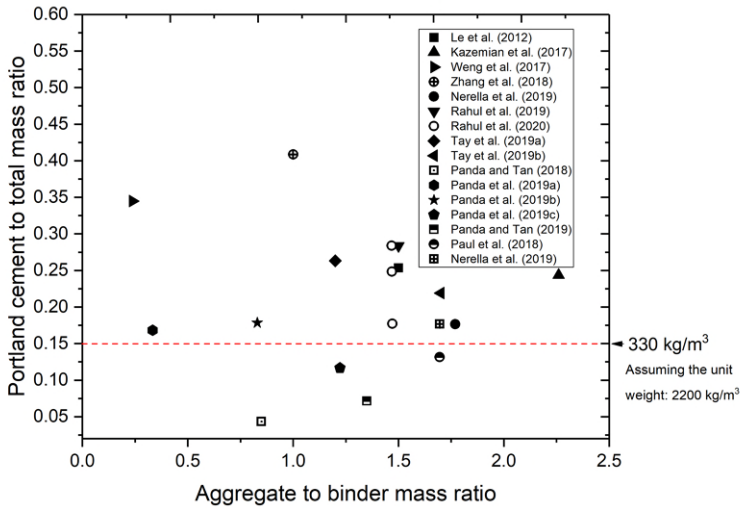


Figure 2.4: Literature survey of OPC content and aggregate to binder mass ratio in different 3D printable mortars. Data from Refs: [1, 2, 9, 29–40].

viscosity [47, 49], which could contribute to the pumpability of fresh mixtures. However, the unburnt coal in FA could adsorb superplasticizer or the mixing water, which may affect the workability of fresh mixtures [47]. On the other hand, FA showed similar or relatively coarser particle size and smaller density than OPC. Using a high volume of FA in the binding material could result in a significant dilution effect, i.e., reducing the number of cement particle flocs, adversely affecting structural build-up, delaying the initial setting and early hydration [47]. For improving the structural build-up of such blended mixtures, other SCMs, like silica fume/micro-silica [2, 9, 29, 30, 32, 50, 51], could be used to formulate the ternary binder system (cement-FA-silica fume) for 3DCP. Additionally, admixture, e.g., nano attapulgite clay, and methyl cellulose-based viscosity modifying admixture (VMA), is also feasible to enhance the robustness and thixotropy of such high volume of FA based printable cementitious materials [1, 36, 40, 52]. Besides, it should be noted that replacing OPC with a very high volume of FA (more than 50 wt.% of binder) may require alkalization for the setting and hardening process. The general approaches for activating FA-based binders included: grinding FA (for increasing specific surface area and reducing fineness), introducing a small content of highly reactive materials (e.g., silica fume), and adding a proper dosage of chemical activator [44]. Panda et al. [39, 40] added about 3 wt.% (of binder) sodium sulfate as the activating agent for enhancing the early strength of their high-volume FA based printable cementitious materials.

Granulated blast furnace slag (GBFS) is also a very commonly used and valuable SCM. For achieving good reactivity, slag is further ground to a fineness comparable to cement particles [53, 54]. Due to its latent hydraulic property, the ground granulated

blast furnace slag (GGBS) can replace up to 95% of clinker in European CEM III /C cement, according to EN 197-1 [55]. Due to the micro-filling effect, the workability may be improved by increasing OPC substitution using GGBS [44, 47, 54]. However, the effect of GGBS on the rheology of fresh mixtures is mostly dependent on its physical and chemical properties. Compared to OPC, the GGBS with smooth particle surface and low reactivity could improve workability, resulting in decreased plastic viscosity and/or yield stress (see [56, 57]). In contrast, the water and superplasticizer demands are increased by using the GGBS that has a relatively high specific surface area (SSA) and chemical reactivity [47]. Currently, there are only a few attempts to develop GGBS-based cementitious materials for 3DCP. Panda et al. [34] investigated the rheology, 3D printability, and compressive strength of ternary blends containing GGBS, cement, and lime. Their work confirmed that it is possible to employ a high volume of slag (70-85 wt.% of binder) in 3D printable cementitious materials. Rahul et al. [31] studied desorptivity of a GGBS-based cementitious material (50% of GGBS in binder) for 3DCP. Chaves Figueiredo et al. [52] developed a series of printable strain-hardening cementitious composites that comprised GGBS, OPC, and limestone. Nevertheless, most of the studies [58–64] in literature focused on developing alkali-activated slag- or slag and fly ash-based geopolymer materials for 3D printing, which is beyond the scope of this study, and therefore, is not discussed.

Silica fume (SF) can fill the space between other cementitious particles to increase the packing density and improve the cohesion due to its ultrafine particle size, round shape, and extremely high SSA. The water and superplasticizer demand and inner particle friction are increased by using SF as the constituent of binder [47, 65–68]. Many studies [47, 69–72] showed that both yield stress and plastic viscosity are increased upon addition of SF, whereas the opposite results (decrease in yield stress and/or plastic viscosity) were observed in cases [57, 73, 74]. According to [47, 72, 75], this is primarily due to the different physical characteristics (e.g., surface properties, density, and morphology) and volume fraction of SF in different studies. Besides, the effect of SF on rheology is also related to the different water to binder ratios and different types of superplasticizers. The ternary blend appears very frequent in the available mix designs for 3DCP. Such ternary blends may comprise OPC, one of SCMs with moderate particle size (FA, GGBS, or limestone powder), and one of the ultrafine materials, i.e., SF, or other inorganic fines. Examples of these ternary blend systems can be found in [9, 32, 36, 37, 72, 76]. SF was used as an SCM addition with up to 20% of binder mass [32] in 3D printable cementitious materials. In this context, SF can improve the flow consistency of fresh mixture for extrusion and enhance the buildability and structural build-up at rest, attributed to the filler effect. As stated by Lothenbach et al. [77], more nucleation sites for the hydration products of cement phases are provided by the fine SCMs, like SF and metakaolin.

For a long-term application, the main challenge with respect to the utilization of common SCMs (FA, GGBS, and SF) is their gradually reducing production and availability [78]. As shown in Table 2.1, the total amount of SF is only 1-2.5 Mt/year. The quantity of slag is much higher than SF, whereas it is about 5-10% of OPC. Under the environmental pressures, the amount of slag is severely affected by the decrease in iron production due to the wide application of recycled steel. The estimated annual

production of FA is 700-1100 Mt. However, not all FA is suitable for the use in cement due to quality reasons [78]. Additionally, the supply chain of FA is threatened by reasons such as retirement or elimination of coal-fired power plants in many countries (e.g., the USA, the UK, and the Netherlands) [53]. Finding alternative SCMs appears to be a critical task in order to ensure uninterrupted supply of SCMs-based cementitious materials. Owing to the abundant availability worldwide, (calcined) clay and limestone stand out as the ideal alternatives.

### 2.3.2. EFFECT OF LIMESTONE AND CALCINED CLAY ON FRESH PROPERTIES

Limestone powder is utilized as a kind of filler component in the binding material. Similar to the SCMs mentioned earlier, the effect of limestone on rheology is linked to the physical properties of limestone particles, i.e., fineness and roughness of the surface. These material characteristics strongly affect the packing density and the demand for water and superplasticizer [47]. In the case of limestone powder with similar or coarser fineness compared to that of cement, the addition of limestone may improve the workability by reducing yield stress and plastic viscosity [80]. In contrast, such parameters can be increased by using the ultrafine limestone [81] due to the high adsorption of water and superplasticizer, as well as the enhancement of inner particle friction. Also, the cement flocculation may be enhanced and accelerated by decreasing the particle size of limestone (for the fixed limestone proportion) [82] or increasing the volume of limestone (for the fixed fineness of limestone) [71]. Filler effect can be regarded as the main influence of limestone addition on cement hydration, which may relate to two mechanisms: the dilution of cement, and the increase of nucleation sites provided by the limestone surface, as stated by Berodier and Scrivener [83]. Replacing a partial amount of OPC by limestone could accelerate the early age hydration, especially when the average particle size of limestone is very fine, because of the increase of nucleation sites [83]. However, it may affect the mechanical performance and increase the porosity of hardened cementitious materials when the substitution of OPC by limestone alone is higher than 10% in binder [78, 84]. This is attributed to the dilution effect of limestone filler. There are only a few examples [85, 86] of using limestone as the main substitute of OPC for formatting the binary binder system for 3DCP. Many 3D printable cementitious materials employed a blend of limestone and one or two of SCMs, e.g., GGBS [52, 87], SF [23, 88], or fly ash [52, 87] as the OPC replacement.

The utilization of calcined clay as an SCM for concrete has attracted much attention in the past decade. The advantages of using calcined clay as the OPC substitute can be summarized as follows.

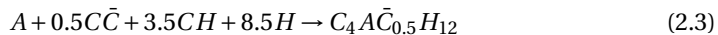
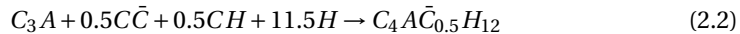
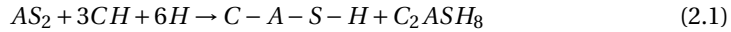
- (1) The raw materials (clays) are vastly abundant worldwide. As the most suitable type, kaolinitic clay is rich in tropical and subtropical environments, especially in India and Southeast Asia [89].
- (2) The calcination process requires fewer fuels and emits much less CO<sub>2</sub> compared with that of clinker production. The burning temperature is about 700-850 °C for manufacturing calcined clay (around 1450 °C for clinker) [78, 90]. The heating time could be controlled as short as a few tenths of a second using flash calcination units [91]. As reported by Huang et al. [92], only 0.25-0.37 kg of CO<sub>2</sub> is emitted by

Table 2.1: Material characteristics of different SCMs [47, 53, 78, 79].

	Fly ash (siliceous)	Silica fume	Granulated blast furnace slag	Limestone	Calcined clay (Metakaolin as the main phase)
Material type	By-product.	By-product.	By-product.	Natural material.	Calcined natural SCMs.
Morphology	Round particle and smooth surface.	Round particle.	Finely granular particle and smooth surface.	Irregular shape and rough surface.	Layered structure and rough surface.
Fineness [ $\mu\text{m}$ ]	10-150 (may coarser than cement particles).	0.01-0.5.	3-100 (close to cement particles).	Close to/finer than that of cement particles.	Generally, finer than other SCMs except for SE.
Specific gravity [g/cm <sup>3</sup> ]	2.1.	2.2.	2.9.	2.7.	2.1-2.5.
Phase compositions	Si-Al-O.	Si-O.	Ca-Si-Al-Mg-O.	CaCO <sub>3</sub> .	Si-Al-O.
The main effect on rheological behaviors	1) The ball-bearing effect could improve flowability and reduce yield stress and plastic viscosity. 2) Dilution effect on cement flocculation (high volume replacement).	1) Generally, it could increase the yield stress and plastic viscosity. 2) It could enhance the flocculation of cement particles, resulting in improved buildability and structural build-up of fresh mixtures.	1) GGBS with a smooth particle surface and low reactivity can improve the workability, and reduce plastic viscosity and/or yield stress. 2) Workability may be negatively affected by the GGBS with high SSA and reactivity.	1) Limestone with coarser or similar particle size compared to cement could reduce the yield stress and plastic viscosity for improving workability. 2) The opposite effect can be obtained by using ultrafine limestone.	1) Generally, it could reduce the workability and increase the yield stress and plastic viscosity. 2) The structural build-up/thixotropic behaviors can be enhanced.
The main effect on hydration	Pozzolanic.	Filler effect and pozzolanic.	Latent hydraulic.	Filler effect.	Filler effect (may be for small metakaolin replacement) and pozzolanic.
Estimated total amount [Mt/year]	700-1100.	1-2.5.	300-360.	Abundant accessible reserves.	Abundant accessible reserves.

producing 1 kg of calcined clay, which is much less than that of producing 1 kg of OPC (about 0.9 kg of CO<sub>2</sub>).

- (3) The ternary blends, containing limestone, calcined clay, and clinker (referred to LC3), were studied by many researchers [93–95]. The most typical one, LC3-50, comprises 50% clinker, 15% limestone, 30% calcined clay, and 5% gypsum. Metakaolin, as the primary reactive phase in calcined clay, is the calcined product of high purity kaolinitic clays. Metakaolin, at a relatively high price (near three times of cement), is generally used in other industries, including paper, ceramics, and refractory [78]. According to [96, 97], using the calcined low-grade kaolinitic clay (containing 40% of metakaolin) in LC3-50 cement could reach compressive strength comparable to that of plain OPC from 7 days. Such low-grade kaolinitic clays were also the low-cost raw material for producing cement and probably available around quarries of cement plants [78].
- (4) The amorphous aluminosilicate in metakaolin (AS<sub>2</sub>) could react with the calcium hydroxide (CH) for forming aluminate hydrates and C-(A)-S-H (see Eq 2.1). Besides, the calcite (C $\bar{C}$ ) from limestone can react with alumina species (C<sub>3</sub>A and A from AS<sub>2</sub>) in the pore solution to generate hemi/mono-carboaluminate (C<sub>4</sub>A $\bar{C}$ <sub>0.5</sub>H<sub>12</sub>) (see Eq 2.2 and 2.3) for inhibiting the formation of ettringite [78, 84, 90, 95, 98]. All the aforementioned products could refill the pores and reduce the total porosity, contributing to enhancing the strength and durability of hardened cementitious materials [78, 90, 99]. Using LC3 could improve the durability of hardened concrete, for example, the excellent chloride resistance [100–103], proper performance under the sulfates attack [104, 105], and mitigation of the alkali-silica reaction [78, 104, 106].



As shown in Figure 2.5, clays, without calcination, were categorized according to the way that tetrahedral (Al<sup>3+</sup> for Si<sup>4+</sup>) and octahedral (Fe<sup>3+</sup>, Fe<sup>2+</sup>, or Mg<sup>2+</sup> for Al<sup>3+</sup>) sheets are combined into layered structures. The clay is referred to the 1:1 or t-o clay if only one tetrahedral and one octahedral sheet are available in each layer. The layers are linked by hydrogen bonds. In contrast, the 2:1 or t-o-t clay contains two tetrahedral sheets positioned at both sides of one octahedral sheet. The interlayer electrostatic forces and cations bond the layers in this case [107, 108]. Different amounts of water molecules and various types of ions can be hosted at the large interlayer. Induced by the changes of relative humidity, the 2:1 clay may easily swell and shrink. Kaolinite is a typical non-swelling 1:1 clay. For those 2:1 clays, muscovite is a non-swelling clay (in the group of illites), whereas montmorillonite belongs to a swelling clay (in the group of smectites) [108]. Polycarboxylate ethers (PCEs), as the most common superplasticizer,

can be significantly adsorbed on the swelling clays, which strongly affects or even nullifies the dispersion of PCEs. Consequently, the other fines in the mixture could not get enough PCEs for achieving the designed workability. However, this is not a critical issue for non-swelling clays [108, 109]. The possible mechanisms of PCEs adsorption by swelling clays were explained elsewhere [21]. As mentioned earlier, low-grade kaolinitic clay is recommended to be used for producing LC3. Except for metakaolin, the calcined low-grade kaolinitic clay may contain quartz, limestone, iron-bearing phases, and other calcined/uncalcined clay minerals. Therefore, the characterization of crystalline phases in calcined clay appears to be essential, especially to determine if swelling clays are present. The phase transformation of natural clay under different temperatures is illustrated in Figure 2.6. At a relatively low temperature, water from the interlayers of clays is removed. After that, a progressive dehydroxylation process results in removing hydroxyl groups, and layers collapse with increased temperature. The amorphous structure that shows the highest pozzolanic reactivity is formed at this stage. Nevertheless, if exceeding this temperature (850 °C for the kaolinitic clay), the amorphous structure is transformed into a crystalline or glass formation [98]. After calcination under 850 °C, kaolinitic clay transforms into the amorphous phase (metakaolin), whereas 2:1 clays, including illite and montmorillonite, could keep a layered crystalline structure (cause the required temperature for 2:1 clays is much higher than 850 °C) [110].

The addition of calcined clay could generally reduce the workability of fresh cementitious materials [80, 110], which resulted in high water and superplasticizer demands [111–113]. However, these impacts on the rheology of fresh mixtures may vary depending on the type of calcined clay used. Calcined clays provided by different suppliers may exhibit various chemical and physical characteristics [103], for example, the different metakaolin content (40–90%), secondary phase (quartz, limestone, clays, and others), fineness, SSA, morphology, and density. These differences may be induced by different raw materials (2:1 or 1:1 clay), calcination methods (temperatures and devices), cooling, and grinding processes. Ferreiro et al. [114] compared the workability and strength of two calcined clays (calcined 2:1 and 1:1 clays). They reported that adding calcined 1:1 clay (the 1:1 clay contains 92% kaolinite) in mixtures increases the water demand compared with that of calcined 2:1 clay (the 2:1 clay consists of 68% montmorillonite) for archiving the same flowability at a fixed PCE dosage. Studies [110, 115] pointed out that the calcined clay containing quartz (even a small amount) could reduce the demands of water and PCEs. Sposito et al. [110] also reported that the SSA, zeta potential, and water demand of calcined clay (except for metamuscovite) could be used to indicate the demand for superplasticizer. In their study, the required dosage of superplasticizer significantly increased with increasing these three indicators' value. The calcination and grinding methods may influence the morphology of calcined clay. The spherical metakaolin particle that was manufactured using a flash calcination method proposed by Claverie et al. [116] could primarily enhance the workability of fresh cementitious materials. In addition, Akhlaghi et al. [117] introduced a modified PCE-based superplasticizer that could efficiently disperse mixtures containing a high content of calcined clay and a high concentration of sulfate ions. This superplasticizer may be an ideal option for LC3 or other multi-component cement systems.

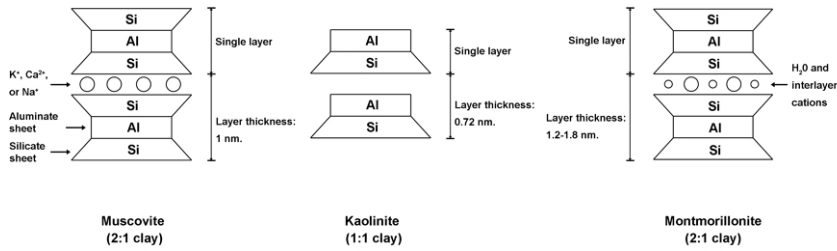


Figure 2.5: Diagram showing the structure of muscovite, kaolinite, and montmorillonite, adapted from [108].

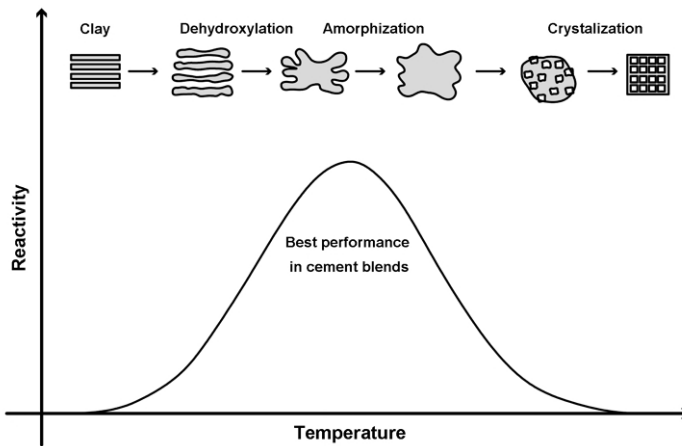


Figure 2.6: Clay phases transformation at different calcined temperatures, adapted from [98].

Calcined clay is also a good ingredient to improve the structural build-up of fresh mixtures at rest, which could be regarded as an advantage of developing calcined clay-based cementitious materials for 3DCP. According to Muzenda et al. [118], the addition of calcined clay could increase the rheological parameters, i.e., thixotropic index, apparent viscosity, cohesion, static and dynamic yield stresses of fresh pastes. Beigh et al. [119] characterized the static yield stress of LC3 paste at different resting times (23-120 min). They found that the structuration rate of LC3 paste is much higher than that of the reference OPC paste. The enhancement of structural build-up may be attributed to the high SSA and layered particle structure of calcined clay [118]. However, as mentioned earlier, using different calcined clays may result in the various structural build-up of fresh mixtures. For example, Aramburo et al. [120] found that the structuration rate of the fresh mixture can be enhanced using the calcined clay with a high content of reactive aluminate. Besides, the presence of uncalcined kaolinite may also affect the structural build-up of fresh LC3 pastes [121].

To date, the implementation of using calcined clay or metakaolin as the cement substitute in 3D printable cementitious materials is still limited. Only a few attempts are available. For instance, small dosages of metakaolin (0-5%) were employed in [88, 122] for modifying the thixotropy of the developed 3D printable cementitious pastes. Bohuchval et al. [123] studied the effects of different proportions of metakaolin (6%, 12%, and 20% of binder mass) on the rheology and printability of fresh mortars. The blend of 24% fly ash and 6% or 12% metakaolin was suggested as an optimal cement replacement for increasing the yield stress and cohesiveness, as well as enhancing printability and reducing water drainage of the developed fresh mixture.

## 2.4. CHARACTERIZATION METHODS OF FRESH-STATE AND INTERLAYER BEHAVIORS

### 2.4.1. FRESH PROPERTIES AND TEST METHODS

#### FLOWABILITY

THE flowability test is a common and straightforward assessment for studying the rheology of fresh cementitious materials. Many conventional methods, e.g., slump and slump flow tests, V-funnel test, and L-box test, show the potential to evaluate the flowability of printable mixtures [7, 124]. Among them, slump and slump flow tests might be the most appropriate tests to effectively indicate the printability of studied mixtures. Tay et al. [14] mentioned that the slump value (slump test) is dominated by the solid-state physical properties of microstructure and the static yield stress of the printable mixture, which may indicate the buildability in 3DCP. As mentioned earlier, most of the printable cementitious materials from literature belong to mortar technically. Thus, a mini-slump cone with the dimension of 50 mm top diameter, 100 mm base diameter, and 150 mm height [7] for mortar or 19 mm top diameter, 38 mm base diameter, and 57 mm height [125] for cement paste is appropriate to be used for the measurement of slump value. Hägermann cone (70 mm top diameter, 100 mm base diameter, and 60 mm height) is also employed in many earlier studies [14, 126] for determining the shape retention of fresh cementitious materials. Besides, a cylindrical mold could be applied for the slump test to indicate the buildability of printable



cementitious materials (see [28]). According to Flatt et al. [127], for the very low spread, the yield stress  $\tau_0$  of studied mixtures can be obtained using the modified model (Eq 2.4) of Murata approach.

$$\tau_0 = \frac{\rho g H}{\sqrt{3}} \quad (2.4)$$

where  $\rho$  is the unit of weight of the mixture.  $g$  is the gravity constant, and  $H$  is the height of the demolded sample. This model may only be valid once the ratio between the initial height and radius is in the range of 0.8-2.

Hägermann cone is primarily used for performing the slump-flow test (also known as jump table test) of mortar composites. The test procedure could refer to ASTM C1437-15 [128]. The spread diameter is measured to quantify the flowability of studied mixtures and is related to the dynamic yield stress, which may influence the pumpability and extrudability of studied mixtures in 3DCP. Tay et al. [14] found that the fresh mixtures with a slump value within the range of 4-8 mm (Hägermann cone), and a spread diameter between 150 mm and 190 mm showed the optimal printing quality and buildability using their 3DCP setup. In contrast, Ma et al. [7] performed the slump flow test with different material ages and attempted to find the correlation between the flowability and printability window. In their study, the recommended ranges of the slump value and spread diameter for 3DCP are 32-88 mm (mini-slump cone for mortar), and 174-210 mm, respectively. The various findings between different studies may be due to the differences in 3DCP setup and slump cone in the slump test.

#### RAM EXTRUSION

A schematic diagram of ram extruder is shown in Figure 2.7(a). The fresh mixture is filled in the barrel, and then the ram is driven by a compression device to push the material towards an abruptly constricted or gradually narrowing die [129]. Ram extrusion is used as a tool in the laboratory for investigating the extrusion flow, describing rheological properties, and examining the extrudability of materials [129-132]. Studies from [2, 133] determined the extrudability of their mixtures by measuring the extrusion force. Additionally, ram extrusion is also feasible to characterize rheological and tribological behaviors of stiff cementitious materials that cannot be conducted using a rotational rheometer [52, 129, 134, 135]. The model proposed by Benbow and Bridgwater [136] that employs a plasticity approach is commonly used to analyze the experimental results (extrusion rheology data) from ram extrusion tests. Benbow-Bridgwater equation is expressed as Eq 2.5 when a sharp-edged orifice equips the ram extruder.

$$P = 2(\sigma_0 + \alpha V^n) \ln \frac{D_0}{D} \quad (2.5)$$

where  $P$  denotes the extrusion pressure.  $\sigma_0$  is the elongational yield stress, and  $\alpha$  and  $n$  are the fitting parameters.  $D_0$  and  $D$  are the inner diameter of the barrel and die.  $V$  is the material flow rate. For studying the ram extrusion rheology of printable cementitious materials, Benbow-Bridgwater model was employed by [52, 60, 88, 137].

Basterfield et al. [138] pointed out that the fitting parameters  $\alpha$  and  $n$  in Benbow-Bridgwater equation are non-intrinsic material factors that do not have any

physical meaning. The authors proposed a modified model (Basterfield et al model, see Eq 2.6) that is adapted from the Gibson equation (without the end effect) for characterizing rigid-viscoplastic materials. This model assumes a spherically convergent flow and neglects the shear stress in the barrel. The detailed derivation process was reported by [135, 138].

$$P = 2\sigma_0 \ln \frac{D_0}{D} + \frac{2}{3n} k (\sin(\theta_{max})(1 + \cos(\theta_{max}))^n (1 - (\frac{D}{D_0})^{3n}) (\frac{2V}{D})^n \quad (2.6)$$

where  $k$  and  $n$  mean flow consistency and flow index, respectively.  $\theta_{max}$  denotes the angle of the maximum convergent flow (see Figure 2.7(b)). For most of the paste-like materials, the value of  $\theta_{max}$  is of the order of 45 degrees (in the range of 40-60 degrees). The obtained elongational yield stress  $\sigma_0$  can be used to compute the related shear yield stress  $\tau_1$ , since the cementitious materials are considered to follow the Von-Mises criterion [132, 138].

$$\tau_1 = \frac{\sigma_0}{\sqrt{3}} \quad (2.7)$$

Zhou et al. [135] investigated the rheological properties of discrete short fiber-reinforced semi-solid cementitious materials by using this model (Eq 2.6). Based on Basterfield et al. model, Perrot et al. [132] added the contribution of shear stress on the tapered surface and studied the rheological and tribological behaviors of cementitious materials.

Nevertheless, it must be noted that many factors may influence the experimental results of the ram extrusion test. First, the friction between the piston and the inner surface of the barrel is not taken into consideration in many cases. As mentioned by [41, 139], applying silicone release or other types of compounds on the surface of these components is one way to minimize such friction, whereas it is impossible to eliminate this wall friction. Second, a dead/static zone may exist near the die (see Figure 2.7(b)). The test results from [2, 132, 133] revealed that the extrusion force increased irrationally when the piston approached the orifice. Thus, it requires the computation of the maximum length of the dead zone ( $L_{dz}$ ) via Eq 2.8 before performing tests.

$$L_{dz} = \frac{D_0 - D}{2 \tan \theta_{max}} \quad (2.8)$$

The maximum value of  $L_{dz}$  is obtained when  $\theta_{max}$  equals 40 degree. The sufficient distance between the ram and dead zone should be left to minimize the influence of the dead zone, which can be predefined in the experimental program. Third, the fresh cementitious materials are assumed as rigid-viscoplastic materials to be incompressible during the ram extrusion process. The material flow rate  $V$  that is not measured directly is calculated by using the predefined ram speed  $V_0$  [135].

#### PUMPABILITY, EXTRUDABILITY AND OPEN TIME TESTS

Pumpability is a primary criterion to assess the fresh properties of some cementitious materials, including self-compacting concrete, shotcrete, and 3D printable cementitious materials. In 3DCP, the term of pumpability is specifically used to indicate the ease with which fresh cementitious materials are delivered from the pump to the

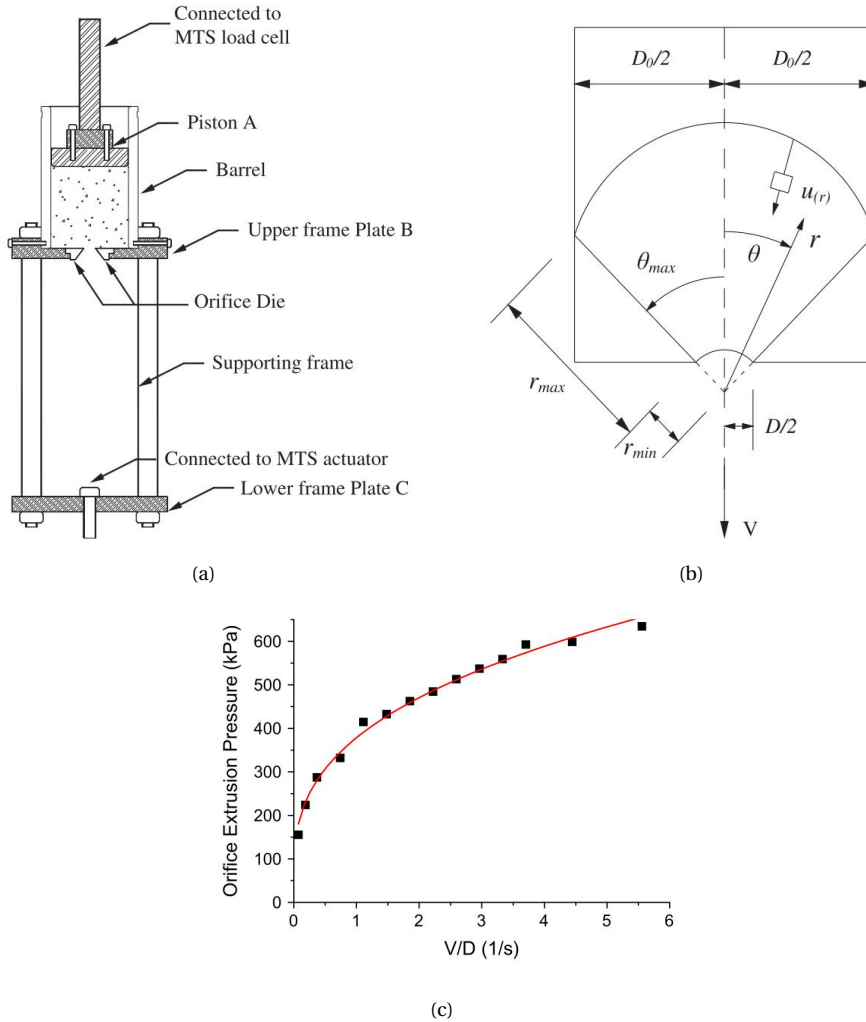


Figure 2.7: (a) Scheme of the ram extrusion setup; (b) Illustration of the orifice entrance flow region based on a spherical coordinate system; (c) An example of test results and the fitted curve (Basterfield et al. model). Adapted from [135].

printhead (nozzle) [8, 9, 11]. During the pumping process, problems like the blockage of the hose, extremely high pumping pressure, material bleeding, and particle segregation may be induced by the improper mix designs and pumping rates, which are possibly determined using the pumpability test. However, until now, a standard test protocol and setup for evaluating the pumpability of 3D printable cementitious materials are not available. Many researchers proposed trial-based methods by using their material pumping setups. For instance, Chaves Figueiredo et al. [52] examined the pumpability of different fresh mixtures that showed various shear and bulk yield stresses using a rotor and stator-based pump under the identical pumping rate with or without a hose of 5 m. A similar approach was also occupied by Tay et al. [14].

The pumpability of cementitious materials can be evaluated by the pumping pressure ( $P$ ) under a specific pumping flow rate ( $Q$ ) related to Bingham parameters. Eq 2.9 is used to describe this relation [37, 140].

$$P = \left( \frac{8\tau_d}{3R} + \frac{8k}{\pi R^4} Q \right) L \quad (2.9)$$

where  $R$  and  $L$  are the radius and length of the hose/pipe, respectively.  $\tau_d$  and  $k$  stand for the dynamic yield stress and plastic viscosity. Since  $R$  usually is smaller than 1 m,  $\tau_d$  and  $k$  dominate the pumping pressure for a specific pumping system under a fixed pumping flow rate. Nevertheless, the quantification of pumpability for printable cementitious materials is still an opened research field. Techniques, like Sliding Pipe Rheometer [141, 142] and other visco-/tribo-meters [143], have shown feasibility to characterize the pumpability of ordinary concrete [144]. Further investigation about using these potential techniques for quantifying the pumpability of printable cementitious materials is needed.

Extrudability is used to describe the ability to continuously print the material through a (round or rectangle opening) nozzle with an acceptable printing quality (minimum degree of tearing/splitting of extruded filament) [9, 11, 35, 145]. The extrudability test in this study means the inline measurement<sup>1</sup> of the extrudability of 3D printable cementitious materials by using a 3DCP setup as an experimental device. Most of the extrudability measurements belonged to the qualitative characterization [18]. Visual inspections were applied to evaluate the printing quality of deposited filaments, i.e., surface quality and dimensional consistency. Kazemian et al. [35] stated their evaluation criteria of printing quality: (1) no surface defects, (2) visible layer edge, (3) dimension conformity. The authors measured the width of the single printed filament at different positions for checking the printing consistency. Similar approaches were adopted in [61, 63, 146]. As mentioned by [2, 30], the filament dimension consistency depends on not only the fresh-state behaviors of materials but also the relation between the linear flow rate of material ( $V_m$ ) and nozzle moving speed ( $V_n$ ). If  $V_m > V_n$ , the 'buckled' layer could be observed. In contrast, if  $V_m < V_n$ , it could result in the width reduction or even discontinuity in the extruded filament. Generally,  $V_m$  should be equal to  $V_n$  during the printing process. Additionally, Nerella et al. [2] introduced an inline and quantitative method for characterizing the extrudability of 3D printable cementitious materials. Under a specific material flow rate, the required

<sup>1</sup>Inline test/measurement/method in this thesis represents 3D printing test conducted using a 3DCP setup.

energy (electric power) for extruding the fresh mixture was measured and recorded as the corresponding extrudability index-unit extrusion energy ( $UEE$ ) [ $\text{J}/\text{cm}^3$ ]. For achieving a similar printing quality, the material with a smaller value of  $UEE$  is more extrudable.

Due to cement hydration increased yield stress with time, pumping and extrusion operation windows should be determined to ensure the acceptable printing quality and avoid nozzle blockage [8, 11, 147]. Open time, also known as the printability window, is defined as the operation window for extrusion of a given volume (batch) of printable cementitious materials. It is to be noted that the open time is only significant for the printing process with multiple batches of material preparation. The volume of each batch is relatively large, such as 45-60 L, and the required time for completely extruding one batch of material is 30-60 min (material flow rate: 1-1.5 L/min). In this case, only the printable material with a minimum open time of 30 min is allowed. Inline measurement of open time was proposed by [7]. At a predefined printing speed, a filament with the designed dimension is extruded from the 3DCP setup at different material ages. The width of the filament is measured at different positions to evaluate the dimensional consistency of printing. The time gap between the two subsequent filaments is 5-10 min and the test is terminated once the filament disruption occurred. The test time is referred to the open time of the tested material (see Figure 2.8).

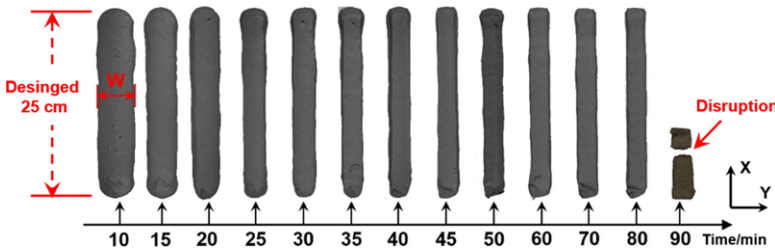


Figure 2.8: An example of the open time measurement. The width of the nozzle opening used in this test is 30 mm. Adapted from [7].

### BUILDABILITY

Buildability is used to indicate the shape retention property of deposited material under the gradually increasing load induced by the subsequent upper layers [8]. Generally, the buildability is characterized as the maximum layer number that could be built up by using a fresh mixture [9, 14, 148]. In many cases, the height of the deposited layers is measured to quantify the material plastic deformation to evaluate the buildability [7, 35, 76, 149] (see Figure 2.9). It must be noted that the printing parameters, i.e., the geometry and length of printing/nozzle path (shape of the designed object for printing), nozzle variables (shape, dimension, and flow direction), the time intervals between two subsequent layers (also known as cycle time [11]), nozzle standoff distances and printing speeds, may significantly influence the buildability assessment.

Extending the time interval between successive layers could improve the buildability of printable cementitious material since the stiffness and rigidity of the deposited layer develop with time, which is related to the flocculation and nucleation

between cement particles at rest [12]. For a non-stop test process, the time interval is primarily dependent on the printing path length and printing speed. As mentioned by Wolfs et al. [150], two failure modes can be observed during the buildability test: material plastic collapse and elastic buckling failure (see Figure 2.10). Material failure is induced by the exceeded load on the deposited layer, leading to yielding and flow out. In contrast, the local or global instability of layered structure can result in the uncontrolled deformation [13, 150]. The former one appears to be mainly dominated by the static yield stress/green strength of printable cementitious material. The resistance of material failure can be improved by enhancing and accelerating the yield stress development of deposited materials at rest [15]. From the material perspective, a possible solution is to reach setting by accelerating very early-age hydration via physical and/or chemical approaches (see [15, 20, 21]). However, elastic buckling failure can be attributed to material behavior and process variations. Most local instability may occur induced by the changes in boundary and geometry conditions during the printing process [10, 13, 150]. The geometry of the printing path is critical in this context. For instance, printing a straight and long wall may fail relatively easily compared to a curved wall with the same path length because the curvature of the wall would likely increase the structural stability [13].

In the buildability test, the local instability of a printed structure could cause stress concentrations resulting in material failure. In many cases, it is hard to determine the dominant source of test failure. Process monitoring techniques appear to be very useful for a better inspection and understanding of the failure during the buildability test [149]. The gradually increased layer deformation can be measured using optical sensors [140] or analyzing the images recorded during the test process [151].

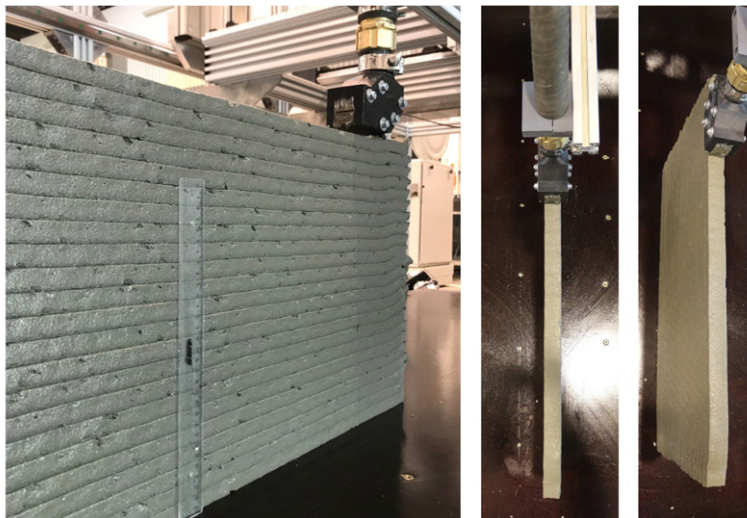
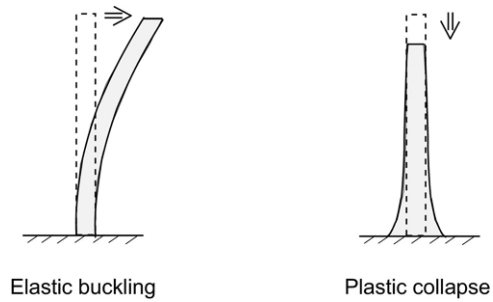
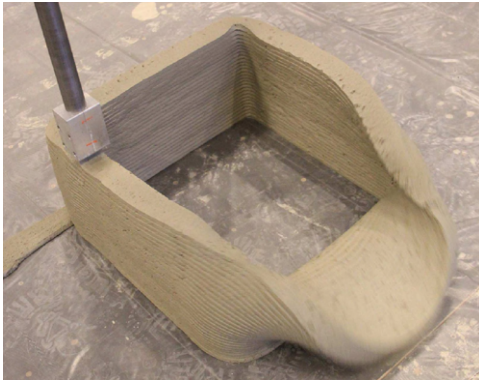


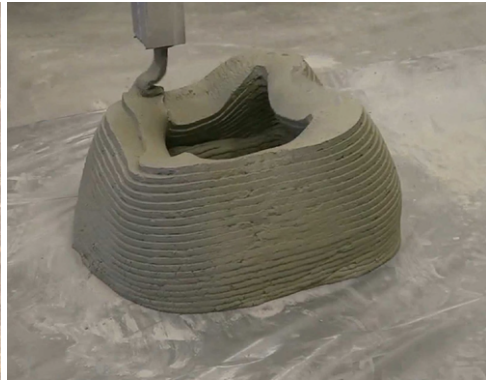
Figure 2.9: An example of the buildability test, adapted from [149].



(a)



(b)



(c)

Figure 2.10: (a) Diagram showing two failure modes of a wall; (b) Elastic buckling of a large square wall (wall width: 500 mm); (c) Plastic collapse of a small square wall (wall width: 250 mm). Adapted from [152].



### GREEN STRENGTH

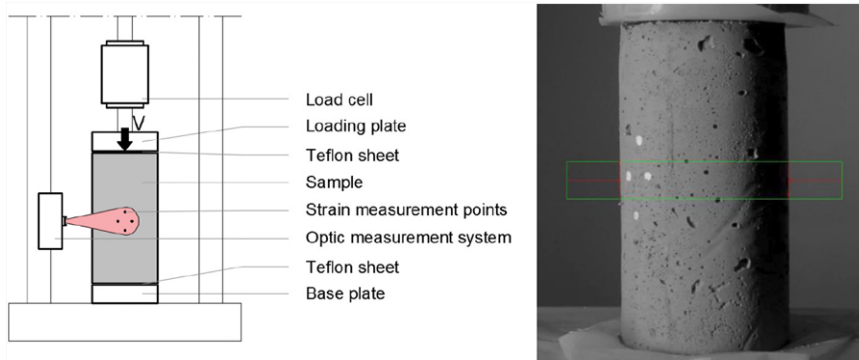
Since the printing period may be up to 3-4 h to finish one building component (about 3 h is required to print a wall with 3 m height at the building rates of 1.1 m/h from [153]), the yield stress evolution of the bottom layers is severely critical during this period. Applying direct load on the fresh cementitious materials is one way to determine the applicable building rate and to assess the shape stability for specific printable materials [15, 153]. Perrot et al. [153] simulated the loading induced by the layer-by-layer construction process on the first deposited layer by using a plate-stacking test. The cylindrical sample with a 60 mm diameter and 30 mm height (aspect ratio: Height/Width=0.5) was employed and placed between two parallel plates. The authors applied a 1.5 kN load increment on the top plate with a time gap ranging from 11 s to 60 s, simulating a building rate of about 1.1-6 m/h. The deformation of the tested sample was recorded using an LVDT-type displacement transducer. Similar approaches were also conducted in studies [10, 34, 58, 126, 154].

Measuring the uniaxial unconfined compressive strength of fresh cementitious materials at different ages (e.g., within the first 4 h) is an approach to monitor the very early-age strength development of studied mixtures (see Figure 2.11). The obtained compressive strength is regarded as the green strength of the tested young age sample [155]. In such a test, the cylindrical samples with an aspect ratio of 2 are commonly used in many studies [39, 151, 155–157]. This aspect ratio could potentially indicate the failure of printed structure [15] and allow the formation of a diagonal shear failure plane [151]. Displacement control at a rate of 0.2-0.5 mm/s [151, 156, 157] is preferred for performing the green strength test. Up to 20-25% of strain could be reached for each sample eventually. Note that, as mentioned by [151, 156], a double-layer of Teflon or other types of sheets should be placed on both sides of the sample to reduce the friction between the sample and steel base plates. Optic measurement methods (see [39, 151, 157]) were employed to record the horizontal displacement of the sample during the test. According to the test results in most studies [39, 151, 156, 157], two typical strain/stress curves and crack patterns were observed (see Figures 2.11(b) and 2.11(c)). For the samples with younger ages (within the first 1 h, however, it largely depends on the mixture), the stress near-linearly increased with the increase of strain until to reach a plateau. The cross-section of the sample expands during the increase of deformation. Finally, instead of forming a distinct crack pattern, the young age sample failed with a barreling effect. In contrast, for the samples with older ages (after 1 or 2 h), a strain-softening behavior is observed after the stress reached the peak value. Meanwhile, more distinct cracks were formed during testing older age samples. Additionally, the obtained experimental results could be used as one of the inputs for optimizing the printing process via numerical studies (see [150, 151]).

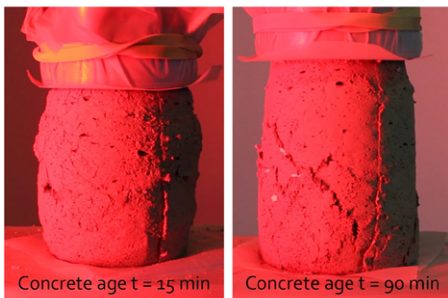
### PENETRATION RESISTANCE

The penetration test is a continuous mechanical measurement to indicate the structuration of fresh cementitious materials at rest [17]. The penetration setup is very commonly used in the field of civil engineering, e.g., Hilti nail gun, Vicat, and Gillmore needles [158], penetration plunger [159], and penetrometer [160]. In the cases of Vicat needle and cone plunger tests, the penetration force was kept identical (induced by the weight of the needle or plunger), and the penetration depth was used to indicate the

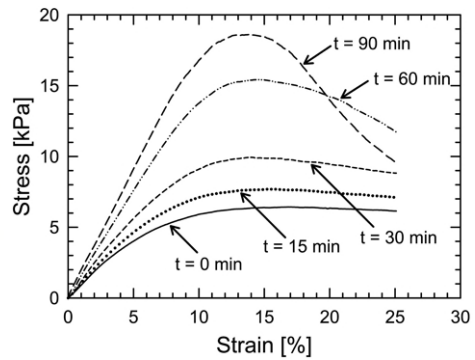




(a)



(b)



(c)

Figure 2.11: (a) Illustration of green strength test setup (Left) and a cylindrical sample (Right); (b) Typical failures observed in green strength tests at different material ages; (c) Typical stress-strain relations in green strength tests. Adapted from [151].

stiffness of fresh cementitious materials [158, 159]. The use of a Vicat needle in the research for investigating the setting behavior of 3D printable cementitious materials could be found in [60, 161–165]. During the Vicat test, two forces induced by the tested materials, i.e., compressive and shear resistances, are exerted on the needle. A balance between the Vicat needle's gravity and such resistances could be reached during the initial and final set of cementitious material [166]. If assuming a plastic failure criterion for the compressive resistance in this context, the compressive strength is of the order of twice the shear strength [166, 167]. The force equilibrium equation can be expressed as:

$$\tau_p = \frac{mg}{2\pi r h + 2\pi r^2} \quad (2.10)$$

where  $\tau_p$  is the shear strength, and  $h$  is the penetration depth.  $m$  and  $r$  denote the mass and radius of the Vicat needle. However, due to its standard dimension of cone mold and penetration needle, the Vicat apparatus could only measure or indicate a limited range of static yield stress, especially between the initial and final setting times of the studied mixture. This could not satisfy the demands for monitoring the yield stress evolution of printable cementitious material at a very early age (for example, after deposited the first several layers).

Penetrometer uses a different technique in comparison with Vicat. The penetration tip is driven at a constant speed to penetrate the sample, and the required force was measured and recorded at different material ages until the final set [160]. Customized penetrometers were developed and employed by researchers [158, 168, 169]. The penetration resistance measurement based on a penetrometer could be used to determine the stiffness development of fresh printable cementitious materials directly, see [7, 35, 170]. Compared to the Vicat test, the penetration test performed by using a penetrometer could measure a broader range of yield stress from 1 kPa to 200 kPa, which is of interest for indicating the structuration of deposited material in the digital fabrication of concrete [17]. Lootens et al. [160] employed many penetration tips with different geometries (conical and hemispherical) and dimensions (see Figure 2.12) in the penetration test under a slow speed (1  $\mu\text{m/s}$ ). The relations between the yield stress of the cement paste and penetration force in different conditions were determined in their work. The penetration forces scale with the yield stress, which is related to the contact surface between the penetration tip and tested materials. It should be noted that the yield stress in their study was obtained from ultrasonic measurements. Different contact surfaces could be attributed to the different shapes and sizes of penetration tips. The correlation between penetration forces and yield stress in [160] was validated and strengthened by [171]. The authors studied the very early-age strength development of self-compacting mortar that was employed in slip-forming by employing a set of mechanical experiments, including compression (green strength measurement), tensile, shear, and bending tests. Similar validation can also be found in [17, 20]. Based on these studies [17, 20, 160, 171], using penetration measurement could indicate the yield stress evolution of fresh paste and mortar, which showed good agreement with the results obtained by compression, vane rheometry, ultrasound, and other tests (see Figure 2.13(b)).

In comparison with slow penetration measurement in [160], the fast penetration test (see Figure 2.13(a)) was also applied by many studies [17, 171, 172] (penetrating

rate: 1 mm/s). As shown in Figure 2.13(b), a similar result can be obtained by using fast and slow rates once the penetration tip was kept identical [17]. However, in the fast penetration test, multiple samples were required for determining the yield stress at different rest times. Compared to the fast one, the slow penetration test could provide a continuous measurement of yield stress for the tested materials using a single sample. This advantage becomes quite significant if an extended period test is of interest [17, 20]. The measured real-time penetration forces were already used for monitoring the evolution of yield stress of cementitious materials in the digital fabrication of concrete, such as slip forming, smart casting, and 3DCP [15, 20, 172]. Nevertheless, the limitations of the penetration test should be noted. Reiter et al. [20] stated that the yield stress in mortar and concrete is dominated by friction between aggregates, which is also variable with time induced by water consumption of cement hydration process. The internal friction angle could not be determined via penetration measurement directly. The slow penetration test currently is only applied to examine the yield stress of mortar that contained a small volume fraction of sand.

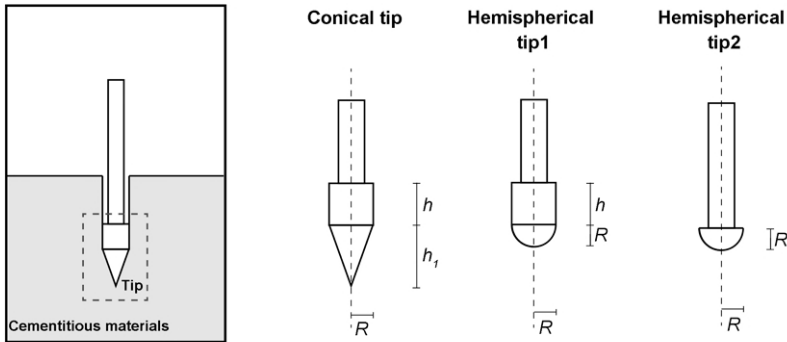


Figure 2.12: Schematic illustration of different penetrometer tips, modified from [160].

## RHEOMETRY

The coaxial rheometer was successfully used to characterize the rheological behaviors of 3D printable cementitious materials in many earlier studies [28, 30, 31, 35, 38, 39, 72, 173]. The vane-in-cup geometry is very suitable and commonly used to study the rheology of concentrated suspensions [174, 175]. Some 3D printable cementitious materials containing fine aggregate (maximum size: 1 mm) can be tested by using this geometry [11]. The employment of rheometry with different specific test protocols could characterize the minimum shear stress, critical strain for flow, suitable printing rate (material flow rate) for extrusion, and the structural build-up of cementitious materials after deposition [173, 176].

## Flow onset

Due to the thixotropy, the rheological behavior of fresh cementitious materials largely

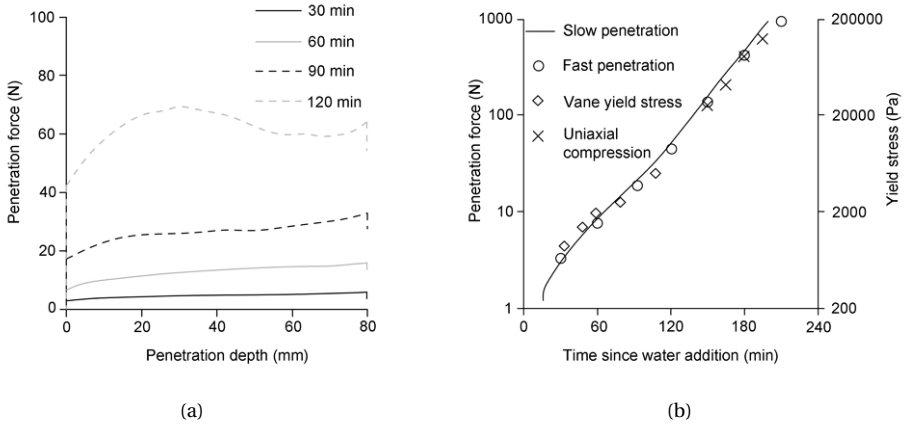


Figure 2.13: (a) Fast penetration test at different times (using conical tip); (b) The evolution of penetration force and yield stress obtained by using different approaches. Both (a) and (b) adapted from [17].

depends on their flow history. Therefore, care should be taken before starting the measurement of the shear stress peak and critical strain for ensuring the test reproducibility. It is essential to perform a pre-shearing process to keep the same destructed status [176, 177]. A specific protocol of the constant shear rate (CSR) test proposed by Roussel et al. [178] was recommended and summarized. First, during the pre-shearing session, the sample is sheared at a relatively high shear rate (e.g.,  $150 \text{ s}^{-1}$ ) for about 200 s. Second, the sample is kept at rest of 5 min and afterwards tested under a constant and low shear rate (e.g.,  $0.005 \text{ s}^{-1}$ ). Consequently, a typical shear stress vs. shear rate curve can be obtained in Figure 2.14(a). It could be found that the shear stress showed a linear increase before reached the yield stress. This demonstrates the elastic behavior of tested material in its solid regime. The material starts to flow after the shear stress and strain exceeds the static yield stress and critical strain. The peak stress is related to the breakage of attractive colloidal interactions between particles. Besides, as shown in Figure 2.14(b), another peak stress can be identified before the critical strain because of the breakage of hydrates formed between particle grains [176].

### Hysteresis loop test

Fresh concrete can be described as a Bingham fluid within a specific range of shear rates. For a typical Bingham material, the shear stress, above the threshold value for flow called yield stress, was increased linearly with the increase of shear rate [179]. The Bingham model is expressed as Eq 2.11.

$$\tau = \tau_d + \mu_p \dot{\gamma} \quad (2.11)$$

where  $\tau$  and  $\dot{\gamma}$  are the shear stress and shear rate.  $\tau_d$  and  $\mu_p$  denote the yield stress and plastic viscosity of the tested material. In many studies [31, 32, 38, 58, 122, 126, 180, 181], 3D printable cementitious materials are assumed to show the Bingham fluid behaviors within a range of shear rate. A hysteresis loop test protocol can be employed by using the rheometer in this context. As shown in Figure

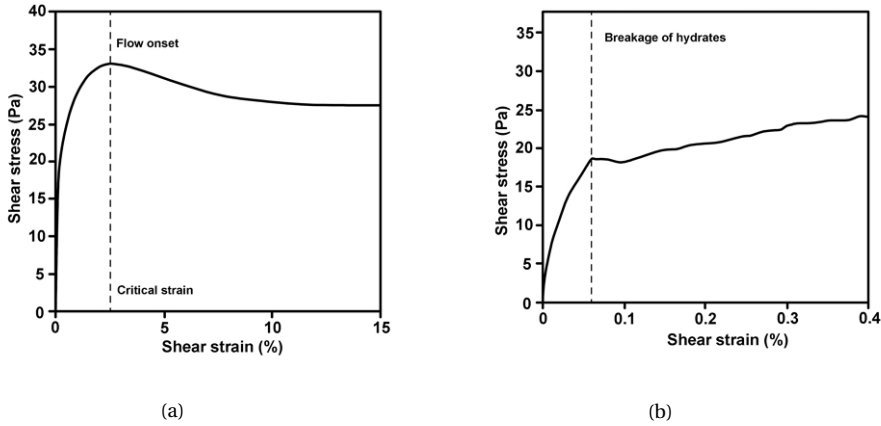


Figure 2.14: CSR test of cement paste (W/C=0.4)-the relationship between shear strain and shear stress. (a) Shear strain from 0% to 15%; (b) Shear strain from 0% to 0.4%. Adapted from [178].

2.15(a), the shear rate was increased from  $0 \text{ s}^{-1}$  to the maximum value (e.g.,  $60 \text{ s}^{-1}$ ,  $100 \text{ s}^{-1}$ , or  $200 \text{ s}^{-1}$ ) within a short time. The shear rate was directly decreased to  $0 \text{ s}^{-1}$  at the same time as it increased (see [31, 32, 122, 180, 181]), or it was kept at the maximum value for about several minutes and then decreased to  $0 \text{ s}^{-1}$  (see [38, 58, 126, 173]). The relation between the measured torque/shear stress and shear rate showed a thixotropic loop containing the up and down curves (see Figure 2.15(b)). The larger the enclosed area between the up and down curves, the higher thixotropy of the tested material [180]. The down curve could be used to fit Bingham model (Eq 2.8) for obtaining the flow parameters, including dynamic yield stress and apparent viscosity [31, 38, 180]. These material parameters can be further used to compare different mixtures and achieve the optimal mix design of 3D printing. According to [144], the fresh mixtures should exhibit moderate dynamic yield stress and relatively low apparent viscosity for displaying favorable pumpability and extrudability. Additionally, based on the test results of hysteresis loop measurement, Herschel-Bulkey model was found to be more suitable for characterizing the dynamic rheological behaviors of some 3D printable cementitious materials, and more details could refer to [122].

Nonetheless, it must be noted that the wall slip phenomena cannot be avoided in rheometry, no matter the applied rotor geometry [11, 175], mainly when we tested the printable mixture with high stiffness and less fluidity. Once the material contains aggregate, even the fine sand (less than 1 mm of diameter), the particle migration could occur during the measurement, leading to the measured viscosity lower than the expected one [11]. Besides, for the same material (at the same material age), the results of Bingham fluid parameters obtained by using different rheometers and/or test protocols seem to be less comparable, probably due to the variables in flow history.

## Structural build-up

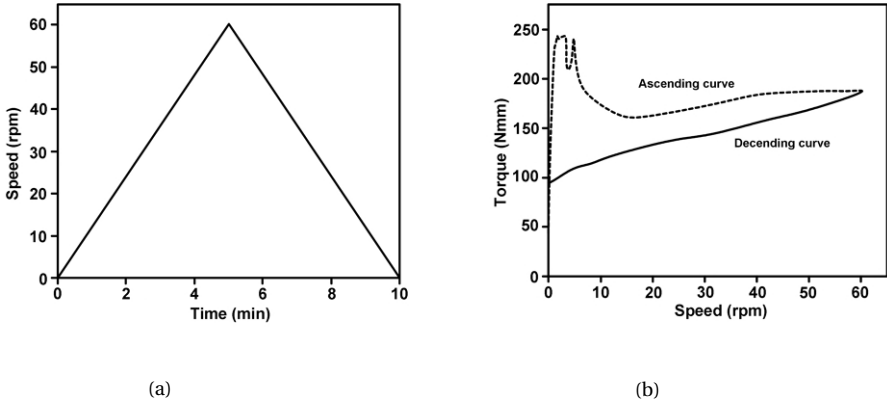


Figure 2.15: (a) A hysteresis loop test protocol; (b) A typical result of the hysteresis loop test. Adapted from [37].

For quantifying the structuration rate of fresh cementitious materials at rest, two methods were commonly employed, including the CSR test and small amplitude oscillatory shear (SAOS) test [182]. Both methods have been applied in the context of 3D printable cementitious materials. In this case, the CSR test was performed at different material ages for determining the evolution of material static yield stress. The obtained static yield stresses at different ages could be furtherly used to predict the structuration rate of the studied material [153, 182–185]. Due to the low yield stress of self-compacting concrete, a very low shear rate, such as in the range of  $0.001\text{--}0.01\text{ s}^{-1}$  [178, 185–187], is feasible to reach flow onset within a short test duration (e.g., 100–200 s) [173]. In contrast, the printable cementitious materials show relatively high stiffness. Also, this test is conducted at different material ages. With time passing, the rigidity and stiffness of studied fresh cementitious material are increased. According to Yuan et al. [187], a relatively long test duration is required for achieving flow onset by using the slow shear rate ( $0.001\text{--}0.01\text{ s}^{-1}$ ), which may not be suitable in this situation. Nerella et al. [173] introduced a strain-based test method for quantifying structural build-up of printable cementitious materials. They employed different shear rates from  $0.08\text{ s}^{-1}$  to  $0.24\text{ s}^{-1}$  at different resting times. A similar approach was used in [119]. Their results confirmed that the structuration of less/non-flowable cementitious materials could be characterized via this strain-based approach.

The measured static yield stresses at the different material ages could be analyzed by using either the linear model (Eq 2.12) proposed by Roussel [70] or the exponential model (Eq 2.13) from Perrot et al. [153].

$$\tau(t) = \tau_{0,0} + A_{thix}t \quad (2.12)$$

where  $\tau_{0,0}$  and  $A_{thix}$  mean the initial static yield stress and structuration rate constant that is the increased rate of static yield stress over time. The exponential model is the extension of the linear one since the structural build-up of cement paste showed an

exponential increase after a critical time point ( $t_c$ ), as reported by Perrot et al. [153].

$$\tau(t_{rest}) = \tau_{0,0} + A_{thix}(e^{t_{rest}/t_c} - 1)t_c \quad (2.13)$$

The value of  $t_c$  is used to adjust the curve to achieve the best fit with test results. When  $t_c$  tends to 0, Perrot et al. model asymptotically tends to Roussel model. According to [13, 153], the value of  $t_c$  is related to the setting of the studied material.

SAOS test is a proper way to investigate the viscoelastic properties of fresh cementitious materials for studying the structuration behavior [173, 176, 188]. Both static yield stress (CSR test) and elasticity (SAOS test) are essential for evaluating the structural build-up of printable cementitious materials since both colloidal and hydration effects strongly influenced the control of printing process, e.g., shape retention for each layer, building rate, and stability of printed structure [176]. The SAOS test procedures can be described as: applied a continuous sinusoidal excitation with a controlled shear strain (deformation) on a single sample and recorded the stress response [173, 176, 182, 188]. The complex modulus ( $G^*$ ) can be given as Eq 2.14.

$$G^* = G' + G''i \quad (2.14)$$

$G'$  is the storage modulus that belongs to the in-phase and elastic component of the response. In contrast,  $G''$  means the loss modulus, and is the out-of-phase and viscous component of the response [176]. The SAOS test can be regarded as a nondestructive approach, when a very low excitation is applied, which could ensure the tested material remains in the elastic regime [188]. For cementitious pastes, the applied strain is  $10^{-4}$  to  $10^{-5}$  (with or without superplasticizer), which is also the critical strain range of such materials [182, 188]. The evolution of  $G'$  with time showed a similar pattern with static yield stress obtained using a CSR test [173, 187]. As mentioned earlier, the critical strain of cementitious materials in the SAOS test is related to the breakage of C-S-H bridges between cement particles [173, 176, 178]. A few examples employed the SAOS test for quantifying the viscoelastic properties of 3D printable cementitious materials. Tay et al. [29] measured storage modulus  $G'$  development of studied material over time. They found that the storage modulus at the bottom layer strongly influenced not only the layer stability but also the interlayer bond strength. Moeini et al. [189] studied the effects of superplasticizer and nano-clay on the critical shear strain and storage modulus of their pastes at different resting times. However, as mentioned by [13, 182], the SAOS test is only valid for pastes and fine mortars. Sensitive and expensive devices are highly demanded.

On the other hand, a large amplitude oscillatory shear (LAOS) test is a promising method to characterize the thixotropy of cementitious materials [11, 176, 190]. As stated by Conte and Chaouche [190], the yield stress and flow curves measured by using the SAOS test cannot be defined rigorously in cementitious materials, since the test duration and flow history dominate such properties. The steady-state cannot be reached under a stress or strain rate in the SAOS test of cement pastes. Theoretically, the flow curve cannot be obtained in this case. Compared to the SAOS test, the LAOS test showed many advantages for dealing with non-linear properties, such as thixotropy, shear-thinning, or -thickening. Generally, the rheometer equipped with a cross-hatched parallel plate geometry was employed for performing the LAOS test

[11, 118, 190]. An example of using the LAOS test to study the flow behaviors and predict the open time of 3D printable cementitious materials was reported by [11]. Further study is still required to provide more data and details of such tests.

#### 2.4.2. INTERLAYER BEHAVIORS AND TEST METHODS

Compared to mold-cast cementitious materials, interlayer behaviors may be the most critical research direction for 3D printed cementitious materials. Thus, hardened properties and test methods related to the interlayer behaviors of 3D printed cementitious materials were discussed in detail.

##### INTERLAYER BONDING

Due to the layer-by-layer printing process in 3DCP, the interlayer bonding, also known as interface, and layer adhesion, is a potential and unavoidable weak point in the 3D printed structure [153, 191]. The weak interlayer bonding that is also referred to 'cold-joint' could result in anisotropy and affect both mechanical performance and durability of the printed element/structure [191, 192]. As mentioned earlier, the high thixotropy/structural build-up of printable material is desired. However, a weak interface may be formed because of the high thixotropy [12, 193–195]. Except for the thixotropy, many printing parameters may also influence the interlayer bond strength.

##### Printing parameters

According to [196, 197], different printing parameters might affect the interlayer bonding of the printed cementitious material. In this study, the following parameters that have been reported in earlier works are selected and discussed.

- Time intervals

The time interval between two subsequent layers may be one of the most critical printing parameters influencing both buildability and interlayer bond strength. By extending the time gap between layers, the shape stability of deposited layers could be enhanced [153], whereas the interlayer bond strength may be significantly reduced [29, 196, 197]. In literature, the time interval ranges from several seconds/minutes to more than a few hours. For the short time intervals (within 1 h), the structural build-up behavior of deposited materials has a severe impact on the layer adhesion. Tay et al. [29] reported a good correlation between the interlayer bond strength and the storage modulus evolution of material over a series of short time intervals (1-20 min). Wangler et al. [147] pointed out that the maximum operation time (time gap)  $t_{h,max}$  for avoiding the cold-joint is primarily dependent on the structuration rate  $A_{thix}$  and plastic viscosity  $\mu_p$  of printable cementitious materials (see Eq 2.15), for the fixed printing parameters, such as speed, nozzle standoff distance and others.

$$t_{h,max} = \frac{\sqrt{\left(\frac{2\mu_p V}{h}\right)^2 + \frac{(\rho g h)^2}{12}}}{A_{thix}} \quad (2.15)$$

where  $\rho$ ,  $g$  and  $h$  denote the density of the material, gravity constant, and layer thickness.  $V$  is the printing rate in the horizontal direction.



For some printable cementitious materials, increasing the time interval between layers could increase the chance of air void formation at the interface region [29, 40], which can be regarded as the main reason for the reduction of interlayer bond strength. The formation of the air void seems to be mostly dependent on the stiffness of the bottom layer. However, after long-time intervals, such as a few hours, or even tens of hours, the printing environment may dominate the interlayer bond strength instead of the thixotropy of material since the deposited material may be set already.

- Printing environment and curing conditions

In practice, it may require several printing sessions to finish a large-scale building element. The time gap between two sessions can range from several hours to one day that is regarded as the long-time interval. The impacts of the printing environment on interlayer bonding may become significant. Many studies [9, 196, 197] attempted to investigate the effect of long time-intervals on the bond strength of printed samples. For example, Panda et al. [197] measured the bond strength of printed samples with up to 6 h of time gap. Wolfs et al. [196] extended the maximum time interval to 24 h. If keeping the time gap identical, the curing conditions of the first/deposited layer(s), including the ambient temperature, and humidity, may dominate the interlayer bonding of printed samples. Both the ambient temperature and humidity could influence the drying rate of deposited materials. As reported by [12, 193], exposing the substrate under the drying environment can induce a severe reduction of bond strength. Keita et al. [193] pointed out that the superficial, extremely localized drying is attributed to the origin of this decrease in interlayer bond strength. In contrast, protecting the layer from drying during the time interval, such as increasing the moisture of the deposited layer, is a proper way to improve the layer adhesion. A good correlation between the moisture content and interlayer bond strength was observed by [165, 198].

- Nozzle standoff distances

The deformation of deposited layers is unavoidable, and it is hard to keep the default setting of nozzle standoff distance continuously during the printing process. The nozzle standoff distance is increased with the growth of substrate deformation. The increase of nozzle standoff distance could increase the possibility of inaccurate layer deposition, which changes the contact areas and pressures between layers. Therefore, the interlayer bonding may be influenced. The effects of different nozzle standoff distances on the interlayer bonding have been studied by [196, 197]. With increasing the nozzle standoff distance, a severe reduction in more than 30% of bond strength was reported by Panda et al. [197]. In contrast, Wolfs et al. [196] found less significant effects of this parameter on the average interlayer bond strength. Only the standard deviations of results were increased by increasing the nozzle height from the default value in their studies. The various effects between different studies may be attributed to the variables of materials and printing setup, especially the nozzle types.

- Nozzle types

The nozzle variables include the flow direction (e.g., the down-flow, back-flow, or hybrid of back- and down-flow), the size and geometry of the nozzle opening (e.g., round or rectangle). The down-flow nozzle (for both round and rectangle openings) may enhance the interlayer bond strength of the printed sample, mostly when the nozzle standoff distance is smaller than the width or diameter of the nozzle opening. This is due to the fact that the nozzle may add extra force on the deposited substrate. The pressing layer process may provide good compaction and increase the contacted areas between two layers. This pressing force should be diminished with the increase of nozzle standoff distance induced by the layer deformation. Once the nozzle standoff distance is equal to the width or diameter of the nozzle opening, the effect of the down-flow nozzle on interlayer bond strength is minimized, which is the same as the back-flow nozzle. In this situation, the substrate only sustains the gravity-induced dead weight of the top layer. The hybrid of back- and down-flow nozzle (generally with a rectangle opening) may be a better choice to compare with totally down-flow or back-flow nozzles [10]. The material flow angle in the hybrid-flow nozzle can be adjusted/designed by the researchers for providing suitable pressing force, which is less than that of the down-flow nozzle but is still sufficient for increasing the contact areas between layers. However, to date, the optimal nozzle for 3DCP is still an opened research question. It requires a series of tests to validate how these variables influence bond strength and printability quantitatively.

### Measurement of interlayer bond strength

Experimental approaches, i.e., uniaxial tensile, splitting, and flexural tests, were generally conducted by researchers to quantify the interlayer bond strength of the printed sample. As a direct way to obtain the bond strength, uniaxial tensile test was utilized by many studies [29, 87, 165, 197–200]. For tensile splitting and flexural tests, the readers could refer to [191, 195, 196, 199, 201]. However, due to a lack of standard, the variable test parameters, including sample sizes, boundary conditions, loading rates, and setups, were adopted in different papers and yielded many difficulties in comparison. The same issues can also be observed in tensile splitting and flexural tests. In most cases, the test results obtained from different studies are incomparable. For example, two types of boundary conditions for the uniaxial tensile test were implemented in literature: rotating and non-rotating loading platens (see Figure 2.16). Wolfs [10] performed uniaxial tensile tests of printed samples under both boundary conditions for comparing the differences. In his results, both pre- and post-peak can be achieved by using the non-rotating loading platen, whereas only the pre-peak was rational and can represent the tensile behavior of specimen by using the rotating loading platen. Besides, the measured tensile strength (peak load/cross-section of the sample) via uniaxial tensile test with rotating loading platen is slightly lower than the obtained value in non-rotating condition. Due to the rotating supports, uneven deformation occurred during the whole test, which was less evident in the case of non-rotating platen. This uneven deformation appears to be enhanced by increasing the degree of rotation. Compressions showed negative values in the load/displacement curve were expected at a very early test point and became pronounced since the cracking initiates. Consequently, the rotating condition may induce a bending moment,

which leads to the extra stress concentration at the beginning of the test [10]. Even using the non-rotating loading platen can show the required material behaviors regarding fracture mechanics, the current set-up of uniaxial tensile test in [10] is still not the ideal one. Limited by the small sample size, the deformation was measured in between the two steel plates (see Figure 2.16) instead on the sample locally. Increasing the sample size by increasing layer thickness or casting excess materials on both sides [133] may properly address this issue.

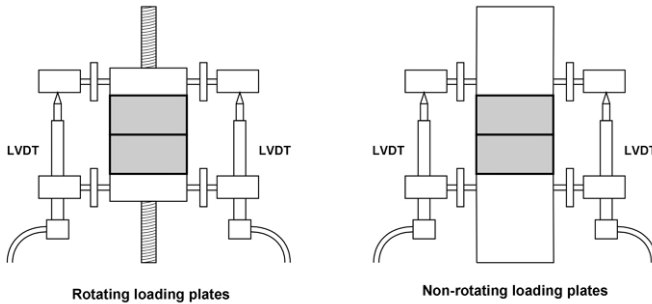


Figure 2.16: Uniaxial tensile test setup with rotating loading plates (Left) and non-rotating loading plates (Right).

### Methods for enhancing the interlayer bonding

Other than applying the suitable printing parameters during the printing process, two main techniques are employed in the literature for improving interlayer bond strength between layers of the printed cementitious materials.

A lack of effective contact areas between layers is a critical issue resulting in the high void content at the interface. For increasing the effective contact areas, Zareiyan and Khoshnevis [195] made interlocking between two subsequent layers, which indicated clearly enhancement of interlayer bond strength. Similarly, Van der Putten et al. [198] used a comb to increase the surface roughness of the deposited layer and create the interlayer interlocking manually. Positive results were also determined in their case.

Applying a thin layer of cementitious 'glue' paste between two subsequent layers is also an effective way to improve the interlayer bond strength. This method is particularly suitable for the material exhibited in the high stiffness and weak intermixing property after deposition. A twin-nozzle printhead that can fully employ this concept (one nozzle for general material layer and another for cementitious 'glue' paste) was proposed by Marchment et al. [200]. The authors also found that the high and sustained flowable OPC paste could significantly enhance the bond strength. This is attributed to the presence of a greater malleable surface area for creating an effective contact area achieved by the mixture with a higher flowability. A similar approach was applied by Ma et al. [202], whereas the 'glue' material in their case was a blend of OPC and high-belite CSA cement-based mortar. In their additive mortar, cellulose fiber was added as an internal curing agent, and fine limestone filler was used for adjusting the workability and hydration.

## 2.5. SUMMARY AND PERSPECTIVES

BASED on the information discussed in this study, the conclusions and perspectives could be made as follows.

2

- Extrusion of very high/sufficiently stiff materials is still the most common printing strategy in the field of 3DCP. However, the pumping distance for extrusion of stiff materials is limited due to the high pumping pressure induced by the high yield stress and plastic viscosity.
- Compared to the very high/sufficiently stiff material, the material for set-on-demand printing exhibits exceptionally high fluidity during mixing, pumping, and extrusion processes, which may be more suitable for large-scale construction projects. However, the study of set-on-demand printing is still limited and requires further investigations.
- Physical and chemical characteristics of SCMs were generally believed as the main reason for influencing the rheology of fresh mixtures.
- Compared with fly ash, slag, and silica fume, calcined clay and limestone appear to be suitable alternatives to common SCMs for developing sustainable cementitious materials in the longer term. Feasibility of using high volumes of limestone and calcined clay as cement substitutions in 3DCP needs further research. The variables of calcined clay, including the metakaolin content, secondary phase, fineness, SSA, morphology, and the presence of uncalcined kaolinitic clay or swelling clays, could strongly influence the fresh and hardened properties of the blended cementitious materials.
- For characterizing the fresh properties of printable cementitious materials during the pumping, and extrusion processes, offline methods<sup>2</sup>, like flowability, ram extrusion, and rheometry (CSR/hysteresis loop) tests can be employed. The inline measurements, including pumpability, extrudability, and open time tests, are also necessary to be applied for validating the printability of developed mixtures.
- After material deposition, the quantification of buildability and structural build-up becomes critical. Development of yield stress/stiffness with time can be quantitatively determined using the green strength test, penetration test, and rheometry (static yield stress measurement with time, SAOS, and LAOS tests). The inline buildability test incorporating experiment monitoring systems can be implemented to evaluate the developed mixtures directly.
- Except for material compositions, printing parameters, i.e., time intervals, nozzle standoff distances, printing environmental conditions, and nozzle types, can also affect the interlayer bond strength of printed cementitious materials. Additionally, the current strategies for enhancing interlayer bonding can be summarized as increasing the contact area (interlocking), and the adhesion between layers.

<sup>2</sup>Offline test/method/measurement is defined as the experiment used to quantify the fresh properties of studied materials without using a 3DCP setup in this thesis.

## REFERENCES

- [1] B. Panda, S. Ruan, C. Unluer, and M. J. Tan, *Improving the 3D printability of high volume fly ash mixtures via the use of nano attapulgite clay*, *Composites Part B: Engineering* **165**, 75 (2019).
- [2] V. Nerella, M. Näther, A. Iqbal, M. Butler, and V. Mechtcherine, *Inline quantification of extrudability of cementitious materials for digital construction*, *Cement and Concrete Composites* **95**, 260 (2019).
- [3] T. Ding, J. Xiao, S. Zou, and Y. Wang, *Hardened properties of layered 3D printed concrete with recycled sand*, *Cement and Concrete Composites* **113**, 103724 (2020).
- [4] T. Ding, J. Xiao, F. Qin, and Z. Duan, *Mechanical behavior of 3D printed mortar with recycled sand at early ages*, *Construction and Building Materials* **248**, 118654 (2020).
- [5] J. Xiao, S. Zou, Y. Yu, Y. Wang, T. Ding, Y. Zhu, J. Yu, S. Li, Z. Duan, Y. Wu, and L. Li, *3D recycled mortar printing: System development, process design, material properties and on-site printing*, *Journal of Building Engineering* **32**, 101779 (2020).
- [6] X. Li, N. Zhang, J. Yuan, X. Wang, Y. Zhang, F. Chen, and Y. Zhang, *Preparation and microstructural characterization of a novel 3D printable building material composed of copper tailings and iron tailings*, *Construction and Building Materials* **249**, 118779 (2020).
- [7] G. Ma, Z. Li, and L. Wang, *Printable properties of cementitious material containing copper tailings for extrusion based 3D printing*, *Construction and Building Materials* **162**, 613 (2018).
- [8] S. Lim, R. A. Buswell, T. T. Le, S. A. Austin, A. G. Gibb, and T. Thorpe, *Developments in construction-scale additive manufacturing processes*, *Automation in Construction* **21**, 262 (2012).
- [9] T. T. Le, S. A. Austin, S. Lim, R. A. Buswell, A. G. Gibb, and T. Thorpe, *Mix design and fresh properties for high-performance printing concrete*, *Materials and Structures/Materiaux et Constructions* **45**, 1221 (2012).
- [10] R. Wolfs, *Experimental characterization and numerical modelling of 3D printed concrete*, Ph.D. thesis, Eindhoven University of Technology (2019).
- [11] R. A. Buswell, W. R. Leal de Silva, S. Z. Jones, and J. Dirrenberger, *3D printing using concrete extrusion: A roadmap for research*, *Cement and Concrete Research* **112**, 37 (2018).
- [12] N. Roussel, *Rheological requirements for printable concretes*, *Cement and Concrete Research* **112**, 76 (2018).

- [13] V. Mechtcherine, F. Bos, A. Perrot, W. L. da Silva, V. Nerella, S. Fataei, R. Wolfs, M. Sonebi, and N. Roussel, *Extrusion-based additive manufacturing with cement-based materials – Production steps, processes, and their underlying physics: A review*, *Cement and Concrete Research* **132**, 106037 (2020).
- [14] Y. W. D. Tay, Y. Qian, and M. J. Tan, *Printability region for 3D concrete printing using slump and slump flow test*, *Composites Part B: Engineering* **174**, 106968 (2019).
- [15] L. Reiter, T. Wangler, N. Roussel, and R. J. Flatt, *The role of early age structural build-up in digital fabrication with concrete*, *Cement and Concrete Research* **112**, 86 (2018).
- [16] A. Anton, L. Reiter, T. Wangler, V. Frangez, R. J. Flatt, and B. Dillenburger, *A 3D concrete printing prefabrication platform for bespoke columns*, *Automation in Construction* **122**, 103467 (2021).
- [17] L. Reiter, *Structural build-up for digital fabrication with concrete - materials, methods and processes*, Ph.D. thesis, ETH Zurich (2019).
- [18] V. Mechtcherine, V. N. Nerella, F. Will, M. Näther, J. Otto, and M. Krause, *Large-scale digital concrete construction – CONPrint3D concept for on-site, monolithic 3D-printing*, *Automation in Construction* **107**, 102933 (2019).
- [19] G. De Schutter, K. Lesage, V. Mechtcherine, V. N. Nerella, G. Habert, and I. Agusti-Juan, *Vision of 3D printing with concrete — Technical, economic and environmental potentials*, *Cement and Concrete Research* **112**, 25 (2018).
- [20] L. Reiter, T. Wangler, A. Anton, and R. J. Flatt, *Setting on demand for digital concrete – Principles, measurements, chemistry, validation*, *Cement and Concrete Research* **132**, 106047 (2020).
- [21] D. Marchon, S. Kawashima, H. Bessaies-Bey, S. Mantellato, and S. Ng, *Hydration and rheology control of concrete for digital fabrication: Potential admixtures and cement chemistry*, *Cement and Concrete Research* **112**, 96 (2018).
- [22] W. R. Leal da Silva, H. Fryda, J.-N. Bousseau, P.-A. Andreani, and T. J. Andersen, *Evaluation of early-age concrete structural build-up for 3D concrete printing by oscillatory rheometry*, in *Advances in Intelligent Systems and Computing*, Vol. 975 (2020) pp. 35–47.
- [23] C. Gosselin, R. Duballet, P. Roux, N. Gaudillière, J. Dirrenberger, and P. Morel, *Large-scale 3D printing of ultra-high performance concrete - a new processing route for architects and builders*, *Materials and Design* **100**, 102 (2016).
- [24] V. Esnault, A. Labyad, M. Chantin, and F. Toussaint, *Experience in online modification of rheology and strength acquisition of 3D printable mortars*, in *First RILEM International Conference on Concrete and Digital Fabrication – Digital Concrete*, edited by T. Wangler and R. Flatt (2018) pp. 24–38.
- [25] T. Wangler, in *Proceedings of the 10th International Concrete Congress*, pp. 2–12.

- [26] K. Mehta and P. J. M. Monteiro, *Concrete: Microstructure, Properties, and Materials*, (McGraw-Hill, New York, 2006) 3rd ed.
- [27] M. K. Mohan, A. Rahul, K. Van Tittelboom, and G. De Schutter, *Rheological and pumping behaviour of 3D printable cementitious materials with varying aggregate content*, *Cement and Concrete Research* **139**, 106258 (2021).
- [28] C. Zhang, Z. Hou, C. Chen, Y. Zhang, V. Mechtcherine, and Z. Sun, *Design of 3D printable concrete based on the relationship between flowability of cement paste and optimum aggregate content*, *Cement and Concrete Composites* **104**, 103406 (2019).
- [29] Y. W. D. Tay, G. H. A. Ting, Y. Qian, B. Panda, L. He, and M. J. Tan, *Time gap effect on bond strength of 3D-printed concrete*, *Virtual and Physical Prototyping* **14**, 104 (2019).
- [30] Y. W. D. Tay, M. Y. Li, and M. J. Tan, *Effect of printing parameters in 3D concrete printing: Printing region and support structures*, *Journal of Materials Processing Technology* **271**, 261 (2019).
- [31] A. Rahul, A. Sharma, and M. Santhanam, *A desorptivity-based approach for the assessment of phase separation during extrusion of cementitious materials*, *Cement and Concrete Composites* **108**, 103546 (2020).
- [32] S. C. Paul, Y. W. D. Tay, B. Panda, and M. J. Tan, *Fresh and hardened properties of 3D printable cementitious materials for building and construction*, *Archives of Civil and Mechanical Engineering* **18**, 311 (2018).
- [33] B. Panda and M. J. Tan, *Rheological behavior of high volume fly ash mixtures containing micro silica for digital construction application*, *Materials Letters* **237**, 348 (2019).
- [34] B. Panda and M. J. Tan, *Material properties of 3D printable high-volume slag cement*, in *First International Conference on 3D Construction Printing (3DcP) in conjunction with the 6th International Conference on Innovative Production and Construction (IPC 2018)*, November (2018).
- [35] A. Kazemian, X. Yuan, E. Cochran, and B. Khoshnevis, *Cementitious materials for construction-scale 3D printing: Laboratory testing of fresh printing mixture*, *Construction and Building Materials* **145**, 639 (2017).
- [36] A. V. Rahul, M. Santhanam, H. Meena, and Z. Ghani, *3D printable concrete: Mixture design and test methods*, *Cement and Concrete Composites* **97**, 13 (2019).
- [37] Y. Weng, M. Li, M. J. Tan, and S. Qian, *Design 3D printing cementitious materials via Fuller Thompson theory and Marson-Percy model*, *Construction and Building Materials* **163**, 600 (2018).
- [38] Y. Zhang, Y. Zhang, G. Liu, Y. Yang, M. Wu, and B. Pang, *Fresh properties of a novel 3D printing concrete ink*, *Construction and Building Materials* **174**, 263 (2018).



- [39] B. Panda, J. H. Lim, and M. J. Tan, *Mechanical properties and deformation behaviour of early age concrete in the context of digital construction*, Composites Part B: Engineering **165**, 563 (2019).
- [40] B. Panda, N. A. N. Mohamed, S. C. Paul, G. V. Singh, M. J. Tan, and B. Šavija, *The effect of material fresh properties and process parameters on buildability and interlayer adhesion of 3D printed concrete*, Materials **12**, 2149 (2019).
- [41] Y. Chen, Z. Li, S. Chaves Figueiredo, O. Çopuroğlu, F. Veer, and E. Schlangen, *Limestone and calcined clay-based sustainable cementitious materials for 3D concrete printing: A fundamental study of extrudability and early-age strength development*, Applied Sciences **9**, 1809 (2019).
- [42] Y. Chen, F. Veer, and O. Çopuroğlu, *A critical review of 3D concrete printing as a low CO<sub>2</sub> concrete approach*, Heron **62**, 167 (2017).
- [43] Y. Chen, F. Veer, O. Copuroglu, and E. Schlangen, *Feasibility of using low CO<sub>2</sub> concrete alternatives in extrusion-based 3D concrete printing*, in *First RILEM International Conference on Concrete and Digital Fabrication – Digital Concrete*, Vol. 19, edited by R. Flatt and T. Wangler (2018) pp. 269–276.
- [44] Z. Giergiczny, *Fly ash and slag*, Cement and Concrete Research **124**, 105826 (2019).
- [45] K. Sideris, H. Justnes, M. Soutsos, and T. Sui, *Fly ash*, in *Properties of Fresh and Hardened Concrete Containing Supplementary Cementitious Materials*, Vol. 04, edited by N. De Belie, M. Soutsos, and E. Gruyaert (2018) pp. 55–98.
- [46] I. Domanskaya and V. Oleinik, *Peculiarities of formation of phase structure and the hydraulic activity of high-calcium fly ash*, in *Progress in Materials Science and Engineering. Innovation and Discovery in Russian Science and Engineering*, 1, edited by C. Brebbia and J. Connor (2018) pp. 149–154.
- [47] D. Jiao, C. Shi, Q. Yuan, X. An, Y. Liu, and H. Li, *Effect of constituents on rheological properties of fresh concrete-A review*, Cement and Concrete Composites **83**, 146 (2017).
- [48] A. Beyciolu and H. Yilmaz Aruntaş, *Workability and mechanical properties of self-compacting concretes containing LLFA, GBFS and MC*, Construction and Building Materials **73**, 626 (2014).
- [49] M. Jalal, M. Fathi, and M. Farzad, *Effects of fly ash and TiO<sub>2</sub> nanoparticles on rheological, mechanical, microstructural and thermal properties of high strength self compacting concrete*, Mechanics of Materials **61**, 11 (2013).
- [50] Y. Zhang, Y. Zhang, W. She, L. Yang, G. Liu, and Y. Yang, *Rheological and harden properties of the high-thixotropy 3D printing concrete*, Construction and Building Materials **201**, 278 (2019).



- [51] X. Zhang, M. Li, J. H. Lim, Y. Weng, Y. W. D. Tay, H. Pham, and Q. C. Pham, *Large-scale 3D printing by a team of mobile robots*, *Automation in Construction* **95**, 98 (2018).
- [52] S. Chaves Figueiredo, C. Romero Rodríguez, Z. Y. Ahmed, D. H. Bos, Y. Xu, T. M. Salet, O. Çopuroğlu, E. Schlangen, and F. P. Bos, *An approach to develop printable strain hardening cementitious composites*, *Materials and Design* **169**, 107651 (2019).
- [53] M. C. Juenger, R. Snellings, and S. A. Bernal, *Supplementary cementitious materials: New sources, characterization, and performance insights*, *Cement and Concrete Research* **122**, 257 (2019).
- [54] I. Yuksel, *Blast-furnace slag*, in *Waste and Supplementary Cementitious Materials in Concrete: Characterisation, Properties and Applications* (Elsevier Ltd, 2018) pp. 361–415.
- [55] EN 197-1, *Cement - Part 1: Composition, specifications and conformity criteria for common cements*, (2000).
- [56] C. K. Park, M. H. Noh, and T. H. Park, *Rheological properties of cementitious materials containing mineral admixtures*, *Cement and Concrete Research* **35**, 842 (2005).
- [57] R. S. Ahari, T. K. Erdem, and K. Ramyar, *Thixotropy and structural breakdown properties of self consolidating concrete containing various supplementary cementitious materials*, *Cement and Concrete Composites* **59**, 26 (2015).
- [58] B. Panda, S. C. Paul, L. J. Hui, Y. W. D. Tay, and M. J. Tan, *Additive manufacturing of geopolymer for sustainable built environment*, *Journal of Cleaner Production* **167**, 281 (2017).
- [59] B. Panda, S. Ruan, C. Unluer, and M. J. Tan, *Investigation of the properties of alkali-activated slag mixes involving the use of nanoclay and nucleation seeds for 3D printing*, *Composites Part B: Engineering* **186**, 107826 (2020).
- [60] H. Alghamdi, S. A. Nair, and N. Neithalath, *Insights into material design, extrusion rheology, and properties of 3D-printable alkali-activated fly ash-based binders*, *Materials and Design* **167**, 107634 (2019).
- [61] B. Panda, C. Unluer, and M. J. Tan, *Investigation of the rheology and strength of geopolymer mixtures for extrusion-based 3D printing*, *Cement and Concrete Composites* **94**, 307 (2018).
- [62] Z. Li, L. Wang, and G. Ma, *Mechanical improvement of continuous steel microcable reinforced geopolymer composites for 3D printing subjected to different loading conditions*, *Composites Part B: Engineering* **187**, 107796 (2020).

- [63] S. Bong, B. Nematollahi, A. Nazari, M. Xia, and J. Sanjayan, *Method of optimisation for ambient temperature cured sustainable geopolymers for 3D printing construction applications*, *Materials* **12**, 902 (2019).
- [64] C. Sun, J. Xiang, M. Xu, Y. He, Z. Tong, and X. Cui, *3D extrusion free forming of geopolymer composites: Materials modification and processing optimization*, *Journal of Cleaner Production* **258**, 120986 (2020).
- [65] P. Nanthagopalan, M. Haist, M. Santhanam, and H. S. Müller, *Investigation on the influence of granular packing on the flow properties of cementitious suspensions*, *Cement and Concrete Composites* **30**, 763 (2008).
- [66] M. Benaicha, X. Roguiez, O. Jalbaud, Y. Burtschell, and A. H. Alaoui, *Influence of silica fume and viscosity modifying agent on the mechanical and rheological behavior of self compacting concrete*, *Construction and Building Materials* **84**, 103 (2015).
- [67] M. Nehdi, S. Mindess, and P.-C. Aitcin, *Rheology of high-performance concrete: Effect of ultrafine particles*, *Cement and Concrete Research* **28**, 687 (1998).
- [68] A. I. Laskar and S. Talukdar, *Rheological behavior of high performance concrete with mineral admixtures and their blending*, *Construction and Building Materials* **22**, 2345 (2008).
- [69] N. Roussel, *Rheology of fresh concrete: From measurements to predictions of casting processes*, *Materials and Structures/Materiaux et Constructions* **40**, 1001 (2007).
- [70] N. Roussel, *A thixotropy model for fresh fluid concretes: Theory, validation and applications*, *Cement and Concrete Research* **36**, 1797 (2006).
- [71] M. K. Rahman, M. H. Baluch, and M. A. Malik, *Thixotropic behavior of self compacting concrete with different mineral admixtures*, *Construction and Building Materials* **50**, 710 (2014).
- [72] Z. Liu, M. Li, Y. Weng, T. N. Wong, and M. J. Tan, *Mixture design approach to optimize the rheological properties of the material used in 3D cementitious material printing*, *Construction and Building Materials* **198**, 245 (2019).
- [73] X. Zhang and J. Han, *The effect of ultra-fine admixture on the rheological property of cement paste*, *Cement and Concrete Research* **30**, 827 (2000).
- [74] R. Saleh Ahari, T. Kemal Erdem, and K. Ramyar, *Effect of various supplementary cementitious materials on rheological properties of self-consolidating concrete*, *Construction and Building Materials* **75**, 89 (2015).
- [75] B. Lu, Y. Weng, M. Li, Y. Qian, K. F. Leong, M. J. Tan, and S. Qian, *A systematical review of 3D printable cementitious materials*, *Construction and Building Materials* **207**, 477 (2019).

- [76] Z. Li, L. Wang, and G. Ma, *Method for the enhancement of buildability and bending resistance of 3D printable tailing mortar*, *International Journal of Concrete Structures and Materials* **12**, 37 (2018).
- [77] B. Lothenbach, K. Scrivener, and R. D. Hooton, *Supplementary cementitious materials*, *Cement and Concrete Research* **41**, 1244 (2011).
- [78] K. Scrivener, F. Martirena, S. Bishnoi, and S. Maity, *Calcined clay limestone cements (LC3)*, *Cement and Concrete Research* **114**, 49 (2018).
- [79] R. Snellings, *Assessing, understanding and unlocking supplementary cementitious materials*, *RILEM Technical Letters* **1**, 50 (2016).
- [80] K. Vance, A. Kumar, G. Sant, and N. Neithalath, *The rheological properties of ternary binders containing Portland cement, limestone, and metakaolin or fly ash*, *Cement and Concrete Research* **52**, 196 (2013).
- [81] K. Ma, G. Long, Y. Xie, and R. Zhu, *Rheological properties of compound pastes with cement-fly ash-limestone powder*, *Journal of the Chinese Ceramic Society* **41**, 582 (2013).
- [82] D. P. Bentz, T. Sato, I. De La Varga, and W. J. Weiss, *Fine limestone additions to regulate setting in high volume fly ash mixtures*, *Cement and Concrete Composites* **34**, 11 (2012).
- [83] E. Berodier and K. Scrivener, *Understanding the filler effect on the nucleation and growth of C-S-H*, *Journal of the American Ceramic Society* **97**, 3764 (2014).
- [84] T. Matschei, B. Lothenbach, and F. P. Glasser, *The role of calcium carbonate in cement hydration*, *Cement and Concrete Research* **37**, 551 (2007).
- [85] D. P. Bentz, S. Z. Jones, I. R. Bentz, and M. A. Peltz, *Towards the formulation of robust and sustainable cementitious binders for 3-D additive construction by extrusion*, *Construction and Building Materials* **175**, 215 (2018).
- [86] Y. Tao, K. Lesage, K. Van Tittelboom, Y. Yuan, and G. De Schutter, *Effect of limestone powder substitution on fresh and hardened properties of 3D printable mortar*, in *Second RILEM International Conference on Concrete and Digital Fabrication – Digital Concrete 2020*, Vol. 28, edited by F. Bos, S. Lucas, R. Wolfs, and T. Salet (2020) pp. 135–143.
- [87] S. Chaves Figueiredo, C. Romero Rodríguez, Z. Y. Ahmed, D. H. Bos, Y. Xu, T. M. Salet, O. Çopuroğlu, E. Schlangen, and F. P. Bos, *Mechanical behavior of printed strain hardening cementitious composites*, *Materials* **13**, 2253 (2020).
- [88] S. A. Nair, H. Alghamdi, A. Arora, I. Mehdipour, G. Sant, and N. Neithalath, *Linking fresh paste microstructure, rheology and extrusion characteristics of cementitious binders for 3D printing*, *Journal of the American Ceramic Society* **102**, 3951 (2019).

- [89] K. L. Scrivener, *Options for the future of cement*, The Indian Concrete Journal **88**, 11 (2014).
- [90] M. Antoni, J. Rossen, F. Martirena, and K. Scrivener, *Cement substitution by a combination of metakaolin and limestone*, Cement and Concrete Research **42**, 1579 (2012).
- [91] R. San Nicolas, M. Cyr, and G. Escadeillas, *Characteristics and applications of flash metakaolins*, Applied Clay Science **83-84**, 253 (2013).
- [92] W. Huang, H. Kazemi-Kamyab, W. Sun, and K. Scrivener, *Effect of replacement of silica fume with calcined clay on the hydration and microstructural development of eco-UHPFRC*, Materials and Design **121**, 36 (2017).
- [93] F. Avet and K. Scrivener, *Investigation of the calcined kaolinite content on the hydration of Limestone Calcined Clay Cement (LC3)*, Cement and Concrete Research **107**, 124 (2018).
- [94] Y. Dhandapani, T. Sakthivel, M. Santhanam, R. Gettu, and R. G. Pillai, *Mechanical properties and durability performance of concretes with Limestone Calcined Clay Cement (LC 3)*, Cement and Concrete Research **107**, 136 (2018).
- [95] F. Zunino and K. Scrivener, *The reaction between metakaolin and limestone and its effect in porosity refinement and mechanical properties*, Cement and Concrete Research **140**, 106307 (2021).
- [96] F. Avet, R. Snellings, A. Alujas Diaz, M. Ben Haha, and K. Scrivener, *Development of a new rapid, relevant and reliable (R3) test method to evaluate the pozzolanic reactivity of calcined kaolinitic clays*, Cement and Concrete Research **85**, 1 (2016).
- [97] A. Alujas, R. Fernández, R. Quintana, K. L. Scrivener, and F. Martirena, *Pozzolanic reactivity of low grade kaolinitic clays: Influence of calcination temperature and impact of calcination products on OPC hydration*, Applied Clay Science **108**, 94 (2015).
- [98] J. Skibsted and R. Snellings, *Reactivity of supplementary cementitious materials (SCMs) in cement blends*, Cement and Concrete Research **124**, 105799 (2019).
- [99] M. Antoni, *Investigation of cement substitution by blends of calcined clays and limestone*, Ph.D. thesis, EPFL (2013).
- [100] H. Maraghechi, F. Avet, H. Wong, H. Kamyab, and K. Scrivener, *Performance of Limestone Calcined Clay Cement (LC3) with various kaolinite contents with respect to chloride transport*, Materials and Structures/Materiaux et Constructions **51**, 1 (2018).
- [101] Z. Shi, M. R. Geiker, K. De Weerd, T. A. Østnor, B. Lothenbach, F. Winnefeld, and J. Skibsted, *Role of calcium on chloride binding in hydrated Portland cement–metakaolin–limestone blends*, Cement and Concrete Research **95**, 205 (2017).

- [102] Y. Dhandapani and M. Santhanam, *Investigation on the microstructure-related characteristics to elucidate performance of composite cement with limestone-calcined clay combination*, *Cement and Concrete Research* **129**, 105959 (2020).
- [103] F. Avet, *Investigation of the grade of calcined clays used as clinker substitute in Limestone Calcined Clay Cement (LC3)*, Ph.D. thesis, EPFL (2017).
- [104] R. Siddique and J. Klaus, *Influence of metakaolin on the properties of mortar and concrete: A review*, *Applied Clay Science* **43**, 392 (2009).
- [105] Z. Shi, S. Ferreiro, B. Lothenbach, M. R. Geiker, W. Kunther, J. Kaufmann, D. Herfort, and J. Skibsted, *Sulfate resistance of calcined clay – Limestone – Portland cements*, *Cement and Concrete Research* **116**, 238 (2019).
- [106] Q. D. Nguyen, T. Kim, and A. Castel, *Mitigation of alkali-silica reaction by limestone calcined clay cement (LC3)*, *Cement and Concrete Research* **137**, 106176 (2020).
- [107] M. F. Brigatti, E. Galán, and B. K. Theng, *Structure and Mineralogy of Clay Minerals*, in *Developments in Clay Science*, Vol. 5 (2013) pp. 21–81.
- [108] L. Lei and J. Plank, *A study on the impact of different clay minerals on the dispersing force of conventional and modified vinyl ether based polycarboxylate superplasticizers*, *Cement and Concrete Research* **60**, 1 (2014).
- [109] D. Marchon, S. Mantellato, A. B. Eberhardt, and R. J. Flatt, *Adsorption of chemical admixtures*, in *Science and Technology of Concrete Admixtures* (Elsevier Ltd, 2015) pp. 219–256.
- [110] R. Sposito, N. Beuntner, and K.-C. Thienel, *Characteristics of calcined clay particles and their influence on the efficiency of superplasticizers*, *Cement and Concrete Composites* **110**, 103594 (2020).
- [111] H. Paiva, A. Velosa, P. Cachim, and V. M. Ferreira, *Effect of metakaolin dispersion on the fresh and hardened state properties of concrete*, *Cement and Concrete Research* **42**, 607 (2012).
- [112] C. Perlot, P. Rougeau, and S. Dehaut, *Slurry of metakaolin combined with limestone addition for self-compacted concrete. Application for precast industry*, *Cement and Concrete Composites* **44**, 50 (2013).
- [113] N. Nair, K. Mohammed Haneefa, M. Santhanam, and R. Gettu, *A study on fresh properties of limestone calcined clay blended cementitious systems*, *Construction and Building Materials* **254**, 119326 (2020).
- [114] S. Ferreiro, D. Herfort, and J. S. Damtoft, *Effect of raw clay type, fineness, water-to-cement ratio and fly ash addition on workability and strength performance of calcined clay – Limestone Portland cements*, *Cement and Concrete Research* **101**, 1 (2017).

- [115] F. Cassagnabère, P. Diederich, M. Mouret, G. Escadeillas, and M. Lachemi, *Impact of metakaolin characteristics on the rheological properties of mortar in the fresh state*, *Cement and Concrete Composites* **37**, 95 (2013).
- [116] M. Claverie, F. Martin, J. P. Tardy, M. Cyr, P. De Parseval, O. Grauby, and C. Le Roux, *Structural and chemical changes in kaolinite caused by flash calcination: Formation of spherical particles*, *Applied Clay Science* **114**, 247 (2015).
- [117] O. Akhlaghi, T. Aytas, B. Tatli, D. Sezer, A. Hodaei, A. Favier, K. Scrivener, Y. Z. Menciloglu, and O. Akbulut, *Modified poly(carboxylate ether)-based superplasticizer for enhanced flowability of calcined clay-limestone-gypsum blended Portland cement*, *Cement and Concrete Research* **101**, 114 (2017).
- [118] T. R. Muzenda, P. Hou, S. Kawashima, T. Sui, and X. Cheng, *The role of limestone and calcined clay on the rheological properties of LC3*, *Cement and Concrete Composites* **107**, 103516 (2020).
- [119] M. A. B. Beigh, V. N. Nerella, E. Secrieru, and V. Mechtcherine, *Structural build-up behavior of limestone calcined clay cement ( LC<sup>3</sup> ) pastes in the context of digital concrete construction . in Rheology and Processing of Construction Materials (RheoCon2)*, November (2019) pp. 1–8.
- [120] C. Aramburo, C. Pedrajas, V. Rahhal, M. González, and R. Talero, *Calcined clays for low carbon cement: Rheological behaviour in fresh Portland cement pastes*, *Materials Letters* **239**, 24 (2019).
- [121] M. A. B. Beigh, V. N. Nerella, C. Schröfl, and V. Mechtcherine, *Studying the rheological behavior of limestone calcined clay cement (LC3) mixtures in the context of extrusion-based 3D-printing*, in *Calcined Clays for Sustainable Concrete*, Vol. 26, edited by S. Bishnoi (2020) pp. 229–236.
- [122] M. Chen, L. Yang, Y. Zheng, Y. Huang, L. Li, P. Zhao, S. Wang, L. Lu, and X. Cheng, *Yield stress and thixotropy control of 3D-printed calcium sulfoaluminate cement composites with metakaolin related to structural build-up*, *Construction and Building Materials* **252**, 119090 (2020).
- [123] M. Bohuchval, M. Sonebi, S. Amziane, and A. Perrot, *Effect of metakaolin, and natural fibres on rheological properties of 3D printing concrete*, *Proceedings of the Institution of Civil Engineers - Construction Materials* **19(6)**, 1 (2020).
- [124] G. Ma and L. Wang, *A critical review of preparation design and workability measurement of concrete material for largescale 3D printing*, *Frontiers of Structural and Civil Engineering* **12**, 382 (2018).
- [125] H. Alghamdi and N. Neithalath, *Synthesis and characterization of 3D-printable geopolymeric foams for thermally efficient building envelope materials*, *Cement and Concrete Composites* **104**, 103377 (2019).

- [126] B. Panda and M. J. Tan, *Experimental study on mix proportion and fresh properties of fly ash based geopolymer for 3D concrete printing*, *Ceramics International* **44**, 10258 (2018).
- [127] R. J. Flatt, D. Larosa, and N. Roussel, *Linking yield stress measurements: Spread test versus Viskomat*, *Cement and Concrete Research* **36**, 99 (2006).
- [128] ASTM C1437-15, *Standard Test Method for Flow of Hydraulic Cement Mortar*, (2015).
- [129] A. Perrot, D. Rangeard, V. Nerella, and V. Mechtcherine, *Extrusion of cement-based materials - An overview*, *RILEM Technical Letters* **3**, 91 (2019).
- [130] R. Alfani and G. L. Guerrini, *Rheological test methods for the characterization of extrudable cement-based materials - A review*, *Materials and Structures/Materiaux et Constructions* **38**, 239 (2005).
- [131] X. Zhou and Z. Li, *Characterization of rheology of fresh fiber reinforced cementitious composites through ram extrusion*, *Materials and Structures/Materiaux et Constructions* **38**, 17 (2005).
- [132] A. Perrot, Y. Mélinge, D. Rangeard, F. Micaelli, P. Estellé, and C. Lanos, *Use of ram extruder as a combined rheo-tribometer to study the behaviour of high yield stress fluids at low strain rate*, *Rheologica Acta* **51**, 743 (2012).
- [133] H. Ogura, V. N. Nerella, and V. Mechtcherine, *Developing and testing of Strain-Hardening Cement-Based Composites (SHCC) in the context of 3D-printing*, *Materials* **11**, 1375 (2018).
- [134] A. Pierre, A. Perrot, A. Histace, S. Gharsalli, and E. H. Kadri, *A study on the limitations of a vane rheometer for mineral suspensions using image processing*, *Rheologica Acta* **56**, 351 (2017).
- [135] X. Zhou, Z. Li, M. Fan, and H. Chen, *Rheology of semi-solid fresh cement pastes and mortars in orifice extrusion*, *Cement and Concrete Composites* **37**, 304 (2013).
- [136] J. Benbow and J. Bridgwater, *The influence of formulation on extrudate structure and strength*, *Chemical Engineering Science* **42**, 753 (1987).
- [137] S. Chaves Figueiredo, O. Çopuroğlu, and E. Schlangen, *Effect of viscosity modifier admixture on Portland cement paste hydration and microstructure*, *Construction and Building Materials* **212**, 818 (2019).
- [138] R. Basterfield, C. Lawrence, and M. Adams, *On the interpretation of orifice extrusion data for viscoplastic materials*, *Chemical Engineering Science* **60**, 2599 (2005).
- [139] Y. Chen, S. Chaves Figueiredo, Yalçinkaya, O. Çopuroğlu, F. Veer, and E. Schlangen, *The effect of viscosity-modifying admixture on the extrudability of limestone and calcined clay-based cementitious material for extrusion-based 3D concrete printing*, *Materials* **12**, 1374 (2019).



- [140] P. R. Chhabra and J. F. Richardson, *Non-Newtonian Flow and Applied Rheology: Engineering Applications* (Butterworth-Heinemann, 2008).
- [141] V. Mechtcherine, V. N. Nerella, and K. Kasten, *Testing pumpability of concrete using Sliding Pipe Rheometer*, *Construction and Building Materials* **53**, 312 (2014).
- [142] V. N. Nerella and V. Mechtcherine, *Virtual Sliding Pipe Rheometer for estimating pumpability of concrete*, *Construction and Building Materials* **170**, 366 (2018).
- [143] E. Secrieru, S. Fataei, C. Schröfl, and V. Mechtcherine, *Study on concrete pumpability combining different laboratory tools and linkage to rheology*, *Construction and Building Materials* **144**, 451 (2017).
- [144] V. N. Nerella and V. Mechtcherine, *Studying the printability of fresh concrete for formwork-free concrete onsite 3D printing technology (CONPrint3D)*, in *3D Concrete Printing Technology* (Elsevier Inc., 2019) pp. 333–347.
- [145] T. Wangler, N. Roussel, F. P. Bos, T. A. Salet, and R. J. Flatt, *Digital concrete: A review*, *Cement and Concrete Research* **123**, 105780 (2019).
- [146] B. Panda, G. B. Singh, C. Unluer, and M. J. Tan, *Synthesis and characterization of one-part geopolymers for extrusion based 3D concrete printing*, *Journal of Cleaner Production* **220**, 610 (2019).
- [147] T. Wangler, E. Lloret, L. Reiter, N. Hack, F. Gramazio, M. Kohler, M. Bernhard, B. Dillenburger, J. Buchli, N. Roussel, and R. Flatt, *Digital concrete: opportunities and challenges*, *RILEM Technical Letters* **1**, 67 (2016).
- [148] Y. Chen, C. R. Rodriguez, Z. Li, B. Chen, O. Çopuroğlu, and E. Schlangen, *Effect of different grade levels of calcined clays on fresh and hardened properties of ternary-blended cementitious materials for 3D printing*, *Cement and Concrete Composites* **114**, 103708 (2020).
- [149] V. N. Nerella, M. Krause, and V. Mechtcherine, *Direct printing test for buildability of 3D-printable concrete considering economic viability*, *Automation in Construction* **109**, 102986 (2020).
- [150] R. Wolfs, F. Bos, and T. Salet, *Triaxial compression testing on early age concrete for numerical analysis of 3D concrete printing*, *Cement and Concrete Composites* **104**, 103344 (2019).
- [151] R. J. Wolfs, F. P. Bos, and T. A. Salet, *Early age mechanical behaviour of 3D printed concrete: Numerical modelling and experimental testing*, *Cement and Concrete Research* **106**, 103 (2018).
- [152] A. Suiker, R. Wolfs, S. Lucas, and T. Salet, *Elastic buckling and plastic collapse during 3D concrete printing*, *Cement and Concrete Research* **135**, 106016 (2020).
- [153] A. Perrot, D. Rangeard, and A. Pierre, *Structural built-up of cement-based materials used for 3D-printing extrusion techniques*, *Materials and Structures/Materiaux et Constructions* **49**, 1213 (2016).



- [154] A. R. Arunothayan, B. Nematollahi, R. Ranade, S. H. Bong, and J. Sanjayan, *Development of 3D-printable ultra-high performance fiber-reinforced concrete for digital construction*, *Construction and Building Materials* **257**, 119546 (2020).
- [155] T. Voigt, T. Malonn, and S. P. Shah, *Green and early age compressive strength of extruded cement mortar monitored with compression tests and ultrasonic techniques*, *Cement and Concrete Research* **36**, 858 (2006).
- [156] R. J. Wolfs, F. P. Bos, and T. A. Salet, *Correlation between destructive compression tests and non-destructive ultrasonic measurements on early age 3D printed concrete*, *Construction and Building Materials* **181**, 447 (2018).
- [157] A. V. Rahul and M. Santhanam, *Evaluating the printability of concretes containing lightweight coarse aggregates*, *Cement and Concrete Composites* **109**, 103570 (2020).
- [158] U. Pott, C. Ehm, C. Jakob, and D. Stephan, *Investigation of the early cement hydration with a new penetration test, rheometry and in-situ XRD*, in *Rheology and Processing of Construction Materials. RheoCon 2019, SCC 2019*, Vol. 23, edited by V. Mechtcherine, K. Khayat, and E. Secrieru (2020) pp. 246–255.
- [159] M. Rubio, M. Sonebi, and S. Amziane, *3D printing of fibre cement-based materials: fresh and rheological performances*, in *Proceedings of 2nd ICBBM (PRO 119)* (2017) pp. 284—291.
- [160] D. Lootens, P. Jousset, L. Martinie, N. Roussel, and R. J. Flatt, *Yield stress during setting of cement pastes from penetration tests*, *Cement and Concrete Research* **39**, 401 (2009).
- [161] Y. Weng, S. Ruan, M. Li, L. Mo, C. Unluer, M. J. Tan, and S. Qian, *Feasibility study on sustainable magnesium potassium phosphate cement paste for 3D printing*, *Construction and Building Materials* **221**, 595 (2019).
- [162] P. Shakor, S. Nejadi, and G. Paul, *A study into the effect of different nozzles shapes and fibre-reinforcement in 3D printed mortar*, *Materials* **12**, 1708 (2019).
- [163] M. Chen, L. Li, J. Wang, Y. Huang, S. Wang, P. Zhao, L. Lu, and X. Cheng, *Rheological parameters and building time of 3D printing sulphoaluminate cement paste modified by retarder and diatomite*, *Construction and Building Materials* **234**, 117391 (2020).
- [164] B. Panda, C. Unluer, and M. J. Tan, *Extrusion and rheology characterization of geopolymer nanocomposites used in 3D printing*, *Composites Part B: Engineering* **176**, 107290 (2019).
- [165] J. G. Sanjayan, B. Nematollahi, M. Xia, and T. Marchment, *Effect of surface moisture on inter-layer strength of 3D printed concrete*, *Construction and Building Materials* **172**, 468 (2018).

- [166] Y. Liao and X. Wei, *Penetration resistance and electrical resistivity of cement paste with superplasticizer*, *Materials and Structures/Materiaux et Constructions* **47**, 563 (2014).
- [167] G. Sant, C. F. Ferraris, and J. Weiss, *Rheological properties of cement pastes: A discussion of structure formation and mechanical property development*, *Cement and Concrete Research* **38**, 1286 (2008).
- [168] U. Pott, C. Jakob, D. Jansen, J. Neubauer, and D. Stephan, *Investigation of the incompatibilities of cement and superplasticizers and their influence on the rheological behavior*, *Materials* **13**, 977 (2020).
- [169] H. Sleiman, A. Perrot, and S. Amziane, *A new look at the measurement of cementitious paste setting by Vicat test*, *Cement and Concrete Research* **40**, 681 (2010).
- [170] G. Ma, Y. Li, L. Wang, J. Zhang, and Z. Li, *Real-time quantification of fresh and hardened mechanical property for 3D printing material by intellectualization with piezoelectric transducers*, *Construction and Building Materials* **241**, 117982 (2020).
- [171] L. K. Mettler, F. K. Wittel, R. J. Flatt, and H. J. Herrmann, *Evolution of strength and failure of SCC during early hydration*, *Cement and Concrete Research* **89**, 288 (2016).
- [172] A. Szabo, L. Reiter, E. Lloret-fritschi, F. Gramazio, and M. Kohler, *Mastering yield stress evolution and formwork friction for smart dynamic casting*, *Materials* **13**, 2084 (2020).
- [173] V. N. Nerella, M. A. Beigh, S. Fataei, and V. Mechtcherine, *Strain-based approach for measuring structural build-up of cement pastes in the context of digital construction*, *Cement and Concrete Research* **115**, 530 (2019).
- [174] H. A. Barnes and J. O. Carnali, *The vane-in-cup as a novel rheometer geometry for shear thinning and thixotropic materials*, *Journal of Rheology* **34**, 841 (1990).
- [175] G. Ovarlez, *Introduction to the rheometry of complex suspensions*, in *Understanding the Rheology of Concrete* (Woodhead Publishing Limited, 2011) pp. 23–62.
- [176] N. Roussel, H. Bessaies-Bey, S. Kawashima, D. Marchon, K. Vasilic, and R. Wolfs, *Recent advances on yield stress and elasticity of fresh cement-based materials*, *Cement and Concrete Research* **124**, 105798 (2019).
- [177] D. Feys, R. Cepuritis, S. Jacobsen, K. Lesage, E. Secrieru, and A. Yahia, *Measuring rheological properties of cement pastes: Most common techniques, procedures and challenges*, *RILEM Technical Letters* **2**, 129 (2017).
- [178] N. Roussel, G. Ovarlez, S. Garrault, and C. Brumaud, *The origins of thixotropy of fresh cement pastes*, *Cement and Concrete Research* **42**, 148 (2012).

- [179] A. Yahia, S. Mantellato, and R. Flatt, *Concrete rheology*, in *Science and Technology of Concrete Admixtures* (Elsevier, 2016) pp. 97–127.
- [180] Y. Weng, *Development and optimization of 3D printable cementitious composites for printing applications*, Ph.D. thesis, Nanyang Technological University (2019).
- [181] M. Chen, B. Liu, L. Li, L. Cao, Y. Huang, S. Wang, P. Zhao, L. Lu, and X. Cheng, *Rheological parameters, thixotropy and creep of 3D-printed calcium sulfoaluminate cement composites modified by bentonite*, *Composites Part B: Engineering* **186**, 107821 (2020).
- [182] I. Ivanova and V. Mechtcherine, *Possibilities and challenges of constant shear rate test for evaluation of structural build-up rate of cementitious materials*, *Cement and Concrete Research* **130**, 105974 (2020).
- [183] D. Lowke, *Thixotropy of SCC—A model describing the effect of particle packing and superplasticizer adsorption on thixotropic structural build-up of the mortar phase based on interparticle interactions*, *Cement and Concrete Research* **104**, 94 (2018).
- [184] Q. Yuan, D. Zhou, B. Li, H. Huang, and C. Shi, *Effect of mineral admixtures on the structural build-up of cement paste*, *Construction and Building Materials* **160**, 117 (2018).
- [185] F. Mahaut, S. Mokéddem, X. Chateau, N. Roussel, and G. Ovarlez, *Effect of coarse particle volume fraction on the yield stress and thixotropy of cementitious materials*, *Cement and Concrete Research* **38**, 1276 (2008).
- [186] A. Perrot, T. Lecompte, H. Khelifi, C. Brumaud, J. Hot, and N. Roussel, *Yield stress and bleeding of fresh cement pastes*, *Cement and Concrete Research* **42**, 937 (2012).
- [187] Q. Yuan, D. Zhou, K. H. Khayat, D. Feys, and C. Shi, *On the measurement of evolution of structural build-up of cement paste with time by static yield stress test vs. small amplitude oscillatory shear test*, *Cement and Concrete Research* **99**, 183 (2017).
- [188] Q. Yuan, X. Lu, K. H. Khayat, D. Feys, and C. Shi, *Small amplitude oscillatory shear technique to evaluate structural build-up of cement paste*, *Materials and Structures/Materiaux et Constructions* **50**, 1 (2017).
- [189] M. A. Moeini, M. Hosseinpour, and A. Yahia, *Effectiveness of the rheometric methods to evaluate the build-up of cementitious mortars used for 3D printing*, *Construction and Building Materials* **257**, 119551 (2020).
- [190] T. Conte and M. Chaouche, *Rheological behavior of cement pastes under Large Amplitude Oscillatory Shear*, *Cement and Concrete Research* **89**, 332 (2016).
- [191] V. N. Nerella, S. Hempel, and V. Mechtcherine, *Effects of layer-interface properties on mechanical performance of concrete elements produced by extrusion-based 3D-printing*, *Construction and Building Materials* **205**, 586 (2019).

- [192] J. Van Der Putten, M. Deprez, V. Cnudde, G. De Schutter, and K. Van Tittelboom, *Microstructural characterization of 3D printed cementitious materials*, *Materials* **12**, 2993 (2019).
- [193] E. Keita, H. Bessaies-Bey, W. Zuo, P. Belin, and N. Roussel, *Weak bond strength between successive layers in extrusion-based additive manufacturing: measurement and physical origin*, *Cement and Concrete Research* **123**, 105787 (2019).
- [194] N. Roussel and F. Cussigh, *Distinct-layer casting of SCC: The mechanical consequences of thixotropy*, *Cement and Concrete Research* **38**, 624 (2008).
- [195] B. Zareiyan and B. Khoshnevis, *Effects of interlocking on interlayer adhesion and strength of structures in 3D printing of concrete*, *Automation in Construction* **83**, 212 (2017).
- [196] R. J. Wolfs, F. P. Bos, and T. A. Salet, *Hardened properties of 3D printed concrete: The influence of process parameters on interlayer adhesion*, *Cement and Concrete Research* **119**, 132 (2019).
- [197] B. Panda, S. C. Paul, N. A. N. Mohamed, Y. W. D. Tay, and M. J. Tan, *Measurement of tensile bond strength of 3D printed geopolymers mortar*, *Measurement: Journal of the International Measurement Confederation* **113**, 108 (2018).
- [198] J. Van Der Putten, G. De Schutter, and K. Van Tittelboom, *Surface modification as a technique to improve inter-layer bonding strength in 3D printed cementitious materials*, *RILEM Technical Letters* **4**, 33 (2019).
- [199] T. Le, S. Austin, S. Lim, R. Buswell, R. Law, A. Gibb, and T. Thorpe, *Hardened properties of high-performance printing concrete*, *Cement and Concrete Research* **42**, 558 (2012).
- [200] T. Marchment, J. Sanjayan, and M. Xia, *Method of enhancing interlayer bond strength in construction scale 3D printing with mortar by effective bond area amplification*, *Materials & Design* **169**, 107684 (2019).
- [201] Z. Y. Ahmed, F. P. Bos, M. C. A. J. V. Brunschot, T. A. M. Salet, F. P. Bos, M. C. A. J. V. Brunschot, and T. A. M. S. On, *On-demand additive manufacturing of functionally graded concrete*, *Virtual and Physical Prototyping* **15**, 194 (2020).
- [202] G. Ma, N. Muhammad, L. Wang, and F. Wang, *A novel additive mortar leveraging internal curing for enhancing interlayer bonding of cementitious composite for 3D printing*, *Construction and Building Materials* **244**, 118305 (2020).

# II

## EXPERIMENTAL INVESTIGATION



# 3

## EFFECT OF PORTLAND CEMENT SUBSTITUTIONS BY CALCINED CLAY AND LIMESTONE ON 3D PRINTABILITY, STIFFNESS EVOLUTION AND EARLY-AGE HYDRATION

*This chapter aims to investigate the influences of different replacement levels of Portland cement by using low-grade calcined clay (LGCC) and limestone (LP) on 3D concrete printability, stiffness evolution and early-age hydration. Results show that, with the same dosage of admixtures (superplasticizer and viscosity modifier), increasing LP and LGCC content reduced the slump, flowability and initial material flow rate, and significantly improved the buildability of fresh mixtures, which can be attributed to the reduced water film thickness (WFT). Furthermore, the initial set and  $SSA_{total}$  development up to the first 3 h were accelerated by increasing LGCC content, which can also be linked to the change of WFT, and consumption of superplasticizer for the dispersion induced by hydration products. Additionally, the dilution effect on compressive strength and hydration caused by the high cement replacement was observed. The impact of LGCC content on the time and intensity of the main hydration peak was also discussed.*

### 3.1. INTRODUCTION

As reported in Section 2.3.2, Chapter 2, there have been no attempts to formulate a printable mixture with a higher content (>45% of the binder mass) calcined clay and limestone for extrusion-based 3D concrete printing (3DCP). The impacts caused by increasing the proportion of limestone and calcined clay in the binder on 3D printability, fresh and hardened properties are not clear yet.

The goal of this study is to investigate the effect of high Portland cement substitutions (>45 wt.%) by blends of low-grade calcined clay and limestone on 3D printability, stiffness evolution and early-age hydration. Slump, slump-flow, and water retention tests were performed at the beginning for developing the printable mixtures. Afterwards, the developed mixtures were assessed by using inline printing methods (definition: see footnote in Section 2.4.1), i.e., extrudability and operation windows, and buildability tests. In addition, the impacts on stiffness development and early-age hydration were determined through measuring the initial setting time, total specific surface areas at 1 h and 3 h, released reaction heat within the first 7 days and compressive strength of mold-cast samples at 1, 3, 7 and 28 days. Finally, a discussion of the obtained results, limitations and perspectives is given.

### 3.2. MATERIALS AND METHODS

#### 3.2.1. RAW MATERIALS AND MIX DESIGNS

CEM I 52.5R type Portland cement (PC), limestone powder (LP), and low-grade calcined clay (LGCC) formed the binder of printable mixtures. LGCC that contained about 50 wt.% of metakaolin was supplied by Argeco, France. The particle size distribution of all these materials is illustrated in Figure 3.1, determined using laser diffractometry. Due to the presence of quartz impurity, LGCC shows the largest average particle size compared to other fines used in this study. The grain size of metakaolin in LGCC is comparable or even finer than LP (see Figure 3.2). The oxide composition obtained by X-ray fluorescence spectrometry (XRF) and physical characteristics of all binding materials are presented in Table 3.1. The Brunauer-Emmett-Telle (BET) method using liquid nitrogen ( $N_2$ ) was employed to measure the specific surface area (SSA) of PC, LP, and LGCC. It was found that LGCC showed a much higher SSA than other binding materials. Under secondary electron (SE) mode of scanning electron microscopy (SEM), the LGCC particles were observed to exhibit subhedral flaky habit and clustered structure (see Figure 3.2), which might be the reason for its extremely high SSA.

Figure 3.3 gives X-ray diffraction (XRD) patterns of PC, LP, and LGCC. XRD was conducted on a PhilipsPW1830 powder X-ray diffractometer, with  $Cu-K\alpha$  radiation operated at 45 kV and 40 mA, for  $2\theta$  values between  $5^\circ$  and  $75^\circ$ . The broad shallow hump appeared at  $15-30^\circ 2\theta$  in LGCC indicated the presence of amorphous phases. Besides, many crystalline phases like mullite ( $3Al_2O_3 \cdot 2SiO_2$ ), kaolinite ( $Al_2O_3 \cdot 2SiO_2 \cdot 2H_2O$ ), and quartz ( $SiO_2$ ) were found in LGCC. PC was mainly composed of alite ( $3CaO \cdot SiO_2$ ), belite ( $2CaO \cdot SiO_2$ ), tricalcium aluminate ( $3CaO \cdot Al_2O_3$ ) and gypsum ( $CaSO_4 \cdot 2H_2O$ ). Calcite ( $CaCO_3$ ) was the primary phase found in the LP. A chemical dissolution method on the basis of NEN-EN 192-2 [1] was utilized for determining the amorphous



phase content in LGCC. A proper amount of LGCC was dissolved in dilute hydrochloric acid solution and afterwards treated with boiling sodium carbonate solution. The insoluble residue (I.R.) was rinsed, heated to around 950 °C, and cooled to the room's temperature (20 °C). Finally, the residue part was weighed by a scale and tested by XRF. The mass loss due to chemical dissolution can be regarded as the amorphous phase content. The total reactive content of LGCC was about 48.8 wt.% (12.3 wt.% reactive silicate, 32.0 wt.% reactive aluminite, and 4.5 wt.% other reactive phases). Due to the size limitation of the pump-hose-nozzle system, quartz sand with a maximum diameter of 2 mm was used as aggregate in this study. The cumulative particle size distribution of all dry components is given in Figure 3.1.

Table 3.2 presents the preliminary mixture compositions of 3D printable cementitious materials. The water-to-binder ratio (W/B) of 0.3 and sand-to-binder ratio (S/B) of 1.5 were kept identical in this thesis. In mixtures B45, B75, and B90, PC was replaced by the blend of LP and LGCC in a mass ratio of 1:2 with different proportions. According to earlier studies [2, 3], a limestone-to-calcined clay ratio of 1:2 may give the best compressive strength development compared to other mass ratios. In addition to these mixtures, the binder of mixture B0 contained only PC as a reference to investigate the influences of LP and LGCC on fresh state behaviors, cement hydration, and compressive strength. Note that the current mix designs in Table 3.2 could not be used for 3D printing directly. According to earlier studies [4–6], the addition of admixtures (i.e., superplasticizer and viscosity modifying admixture) could help to modify the rheology of fresh mixtures for acceptable 3D printability. As the swelling clay was not found in LGCC, a polycarboxylate ether (PCE)-based superplasticizer (SP) (MasterGlenium®51, BASF) was selected in this study. To modify the cohesion, viscosity, and water-retaining properties, a hydroxypropyl methylcellulose (HPMC)-based viscosity-modifying admixture (VMA) in powder form was used. It was supplied by Shanghai Ying Jia Industrial Development Co., Ltd. The viscosity of HPMC was reported by the manufacturer as 201,000 mPa.s. The proper dosages for such admixtures were determined via a series of trial-based tests in Section 3.2.3. All fresh mixtures (paste and mortar) were prepared in accordance with the mixing procedures as described in Table 3.3. Note that the time of mixing liquid components (water and SP) with dry materials was defined as time zero ( $t=0$  min) in this thesis.

### 3.2.2. LAB-SCALE 3D CONCRETE PRINTING SETUP

A lab-scale 3DCP setup was designed and assembled at the Delft University of Technology. As shown in Figure 3.4, this system comprises three main parts: a 3-degree of freedom Computer Numerical Control (CNC) system, a PFT Swing-M type material conveying pump, and a nozzle. The CNC machine can operate within an area of 1100 mm length, 720 mm width, and 290 mm height. The moving speed could be adjusted between 0 mm/min and 7200 mm/min. The material conveying pump (also known as progressive cavity pump) that provided primary forces for pumping and extrusion of fresh mixtures was based on a rotor and stator configuration. More details about the pump were given in Section 3.2.4. A 5 m material hose with an inner diameter of 25 mm was used to connect the pump and the nozzle. In this study, a down-flow nozzle with a round opening (diameter: 15 mm) was selected for performing the 3D printing test.

Table 3.1: Physical properties and XRF composition of PC, LP and LGCC.

	PC	LP	LGCC
Density [g/cm <sup>3</sup> ]	3.120	2.646	2.512
SSA [m <sup>2</sup> /g]	1.16	1.22	10.06
$D_{v50}$ [ $\mu\text{m}$ ]	14.86	24.19	69.35
XRF [wt.%]			
CaO	68.7	39.6	0.6
SiO <sub>2</sub>	17.4	0.2	55.1
Al <sub>2</sub> O <sub>3</sub>	4.1	0	38.4
Fe <sub>2</sub> O <sub>3</sub>	2.8	0.1	2.6
K <sub>2</sub> O	0.6	0	0.2
TiO <sub>2</sub>	0.3	0	1.1
ZrO <sub>2</sub>	0	0	0.1
Other	6.1	60.1	1.9
Total	100.0	100.0	100.0

Table 3.2: Preliminary mix composition of cementitious materials excluding admixtures (% of the binder mass).

Type	PC	LGCC	LP	Sand	Water
B0	100	0	0	150	30
B45	55	30	15	150	30
B75	25	50	25	150	30
B90	10	60	30	150	30

### 3.2.3. FORMULATION OF PRINTABLE MIX DESIGNS

#### SLUMP AND SLUMP-FLOW TESTS

In this study, Hägermann cone (70 mm upper internal diameter, 100 mm bottom internal diameter, and 60 mm height) was employed to perform both slump and slump-flow tests. The slump-flow test is also known as Hägermann flow table test. The test procedures could refer to studies [7]. Before the test, the interior surface of the mold was lubricated by mold oil. One half of the mold was filled by the fresh mixture, and then the fresh mixture was agitated using a timber stick about 20 times. The same procedure was repeated for the second half of the mold. The excess material was slowly scraped off by a trowel. For the slump test, the height of the sample was measured after removal of the cone mold. However, if the sample could not retain its shape and the measured height was lower than 20 mm, the sample's height was recorded as 0 mm. After that, 25 times of table drops were conducted on the demolded sample within 25 s. By using a vernier caliper, the spread diameter was measured in four perpendicular directions. The average value of spread diameters was recorded as the result of slump-flow test. For each mixture, three repetitions were executed.

#### WATER RETENTION TEST

Under a specific pumping or extrusion pressure, the material must remain stable and homogenous to avoid pressurized bleeding and segregation, which may cause clogging of printing setup or adversely affect the material performances after extrusion [8]. Therefore, a proper water retention capacity of printable mixture is required. In this study, the water retention test was performed in accordance with ASTM C1506-09 [9]. The freshly mixed cementitious paste (about 15 min of material age) was weighed and

Table 3.3: Mixing protocol for the fresh paste/mortar preparation.

Time [min:s]	Mixing procedures
-4:00	Mix dry blends at low speed by using a HOBART mixing machine.
0:00	Add water and SP during mixing.
2:00	Pause, scrape the bottom of bowl. Mix at high speed.
3:30	Pause, add VMA, and mix at low speed (for the mixture without VMA: stop, start to test/cast).
7:30	Pause, scrape the bottom of bowl. Mix at high speed.
10:00	Stop, start to test/cast.

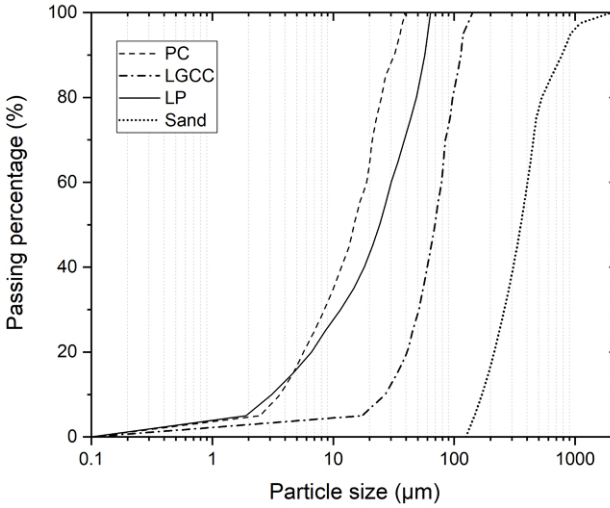


Figure 3.1: Particle size distribution of PC, LGCC, LP and sand used in this chapter.

filled in a Büchner funnel attached to a vacuum assembly. An ashless filter paper (20  $\mu\text{m}$  sieve size, 110 mm diameter, Whatman<sup>TM</sup>) was fixed between the paste and funnel. After exposing the apparatus to a vacuum condition for about 15 min, the loss of mixing water  $W_l$  was determined. The water retention capacity  $W_r$  of fresh paste can be calculated via Eq 3.1.

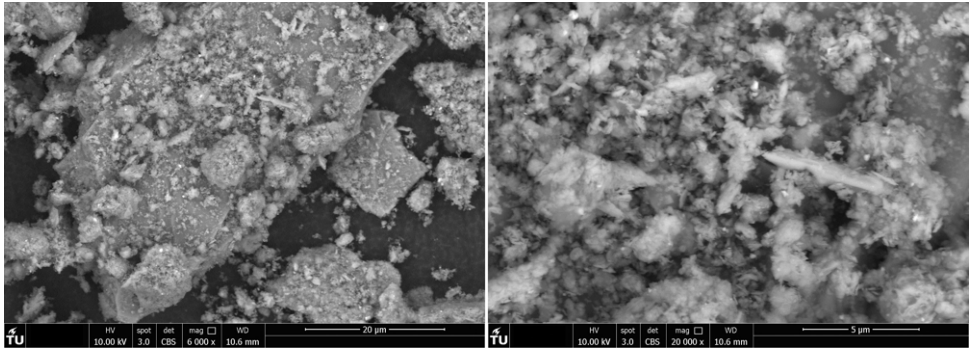
$$W_r = \left(1 - \frac{W_l}{W_o}\right) \times 100\% \quad (3.1)$$

where  $W_o$  denotes the mass of mixing water in the fresh paste.

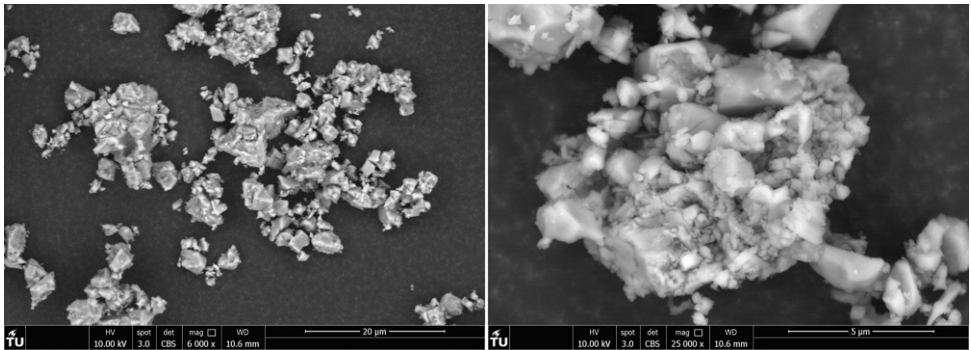
### 3.2.4. EVALUATION OF 3D PRINTABILITY

#### EXTRUDABILITY AND OPERATION WINDOWS

The section of the material conveying pump is illustrated in Figure 3.5(a). Up to 38 L fresh mixtures can be filled in the hopper of the pump. Driving by the motor and rotor-stator system, the fresh mixture can be extruded at a specific flow rate ( $Q$ ) constrained by both the motor speed and the rheology of fresh mixture. According to studies [7, 10], the



(a)



(b)

Figure 3.2: Electron micrograph of (a) LGCC and (b) LP under secondary electron mode (Left: magnification of  $\times 6,000$ ; Right: magnification of  $\times 20,000$ ).

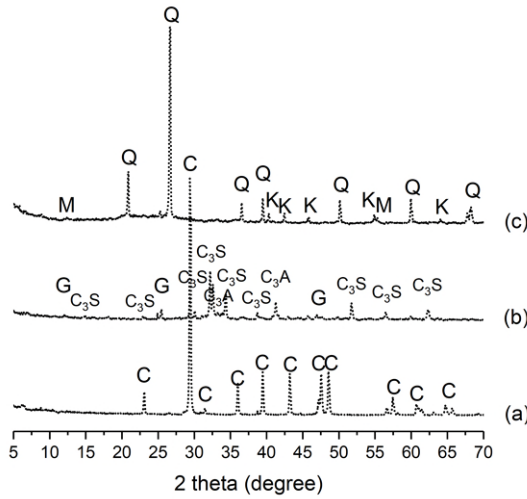


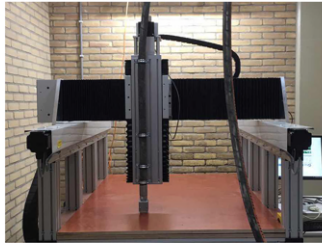
Figure 3.3: XRD analysis results: (a) LP; (b) PC; (c) LGCC. M-mullite, Q-quartz, K-kaolinite, G-gypsum,  $C_3S$ -alite,  $C_3A$ -tricalcium aluminate, C-calcite.

linear material flow rate ( $V_{linear}$ ) of fresh mixture should be near to the nozzle/printhead moving speed ( $V_n$ ) for archiving an acceptable printing quality.

$$V_n = V_{linear} = \frac{Q}{A} \quad (3.2)$$

where  $A$  is the area of nozzle opening ( $\text{mm}^2$ ). The workability of fresh mixture should change with time due to the stiffness evolution and hydration of cementitious materials. Besides, the fresh mixture may suffer high friction when it passes through the rotor-stator component, which appears to increase the material temperature. Such effects could also accelerate the workability loss of fresh cementitious material. The change of material rheology (in terms of workability loss) can lead to a decrease in material flow rate during printing, which severely affects the printing quality. For example, when  $V_n > V_{linear}$ , the extruded filaments become thinner or even discontinuous (see [7, 10]). Thus, in this study, I proposed an extrudability window test, which was based on the pumpability test by [7] and open time test by [11, 12], to characterize the change of material flow rate with time. The test procedures were summarized as follows:

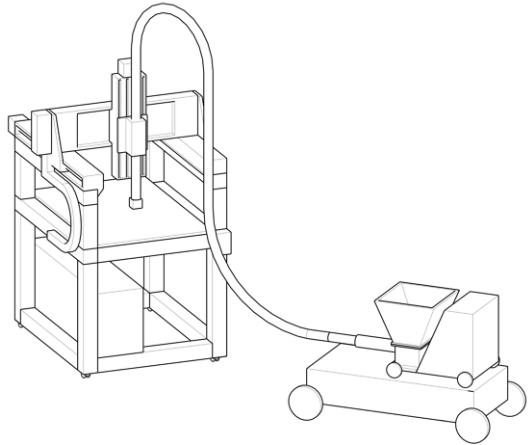
- First, about 8 L of the fresh mixture was prepared in accordance with the mixing protocol in Table 3.3. The freshly mixed material was poured in the hopper of the material conveying pump and the surface temperature of fresh mixture  $T_1$  was measured by using a non-contact thermometer (TENMA) (see Figure 3.5(b)).
- Second, the extrusion test was started at the material age of 15 min (the time since water addition). Note that the material hose was not used since the tested



3D CNC machine

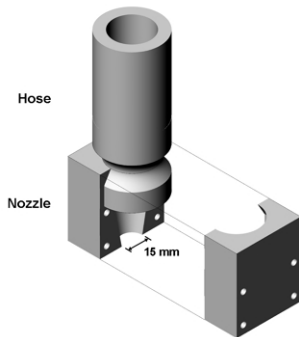


Material conveying pump



Schematic illustration of the 3DCP setup

(a)



Hose

Nozzle

15 mm



(b)

Figure 3.4: A lab-scale 3DCP configuration at TU Delft: (a) 3D CNC table and material conveying pump; (b) Down-flow nozzle with a round opening ( $\varnothing$  15 mm).

material may lead to blockage during testing. Under a constant pumping rate of 58-60 rpm, the fresh mixture was delivered through the pump and the surface temperature of the extruded material  $T_2$  was measured as well (see Figure 3.5(b)). The extruded material was collected for about 10 s. The mass of collected material and the unit of weight of the mixture were employed to compute the real-time material flow rate. This process was repeated twice for each mixture. Besides, the extruded material was also used to conduct the setting time test (see Section 3.2.5).

- Afterwards, the extrusion trial was repeated at the material age from 30 min to 2 h with a time gap of 10 min. For some mixtures, this test may be terminated earlier if the loss of material flow rate is more than 30%. Concerned about the thixotropy of fresh cementitious materials, a pre-extrusion session was designed at the last two minutes of the time gap. The pump was initiated at a 58-60 rpm pumping rate to extrude fresh cementitious material during the pre-extrusion session. The measurement was not started until the continuous filament was obtained (see Figure 3.5(b)).

I proposed two indicators in this test, i.e., extrudability window and operation window. The former one was defined as the time window for ensuring a good printing quality (the loss of material flow rate is less than 5%). The operation window was the maximum time to perform the printing work using one-batch material (the loss of material flow rate is less than 30%). If exceeding the operation window, the material with high stiffness may block the hose.

#### BUILDABILITY TEST

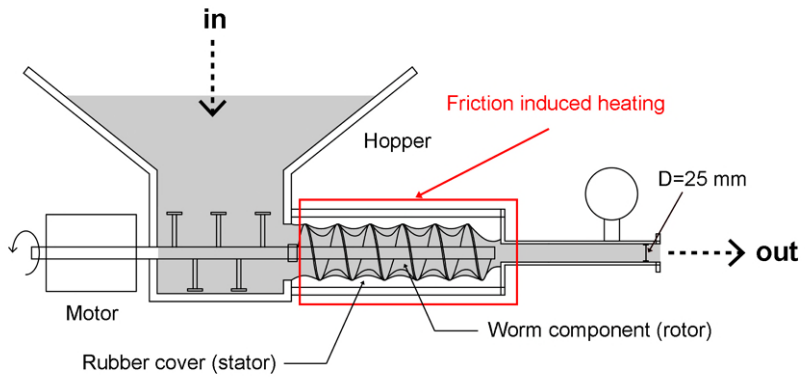
The test process is illustrated in Figure 3.6. A hollow cylinder with a 200 mm diameter was printed by using different mixtures to evaluate their buildability. The nozzle was moved up with a height of 8 mm at the end position of each layer. Thus, the designed layer thickness was about 8 mm, whereas this thickness may be increased with the increase of nozzle standoff distance induced by the deformation of the bottom layers. The pump rate of 58-60 rpm (the same as the speed in the extrudability window test) was kept identical for various mixtures. Within the extrudability window, the material flow rate of one fresh mixture could be a relatively constant value, which was used to compute the nozzle moving speed. Therefore, the test time should not exceed the extrudability window of the fresh mixture. According to studies [7, 12], the maximum number and height of deposited layers before collapsing were recorded as indicators for this test.

### 3.2.5. CHARACTERIZATION OF EARLY-AGE HYDRATION

#### INITIAL SETTING TIME AND $SSA_{total}$ MEASUREMENTS

The initial setting time of studied mixtures (mortar) was measured via an automatic Vicat test apparatus. The test was performed under NEN-EN 196-3 [13]. At the beginning (before the initial setting: penetration depth > 36.5 mm), the Vicat needle dropped automatically after each 10 min. Until the penetration depth equal to or smaller than 36.5 mm, which stands for the initial set of the tested material, the time





(a)



(b)

Figure 3.5: (a) Illustration of the section of material conveying pump; (b) Measurements of material flow rate and increased temperature ( $T=T_2-T_1$ ).



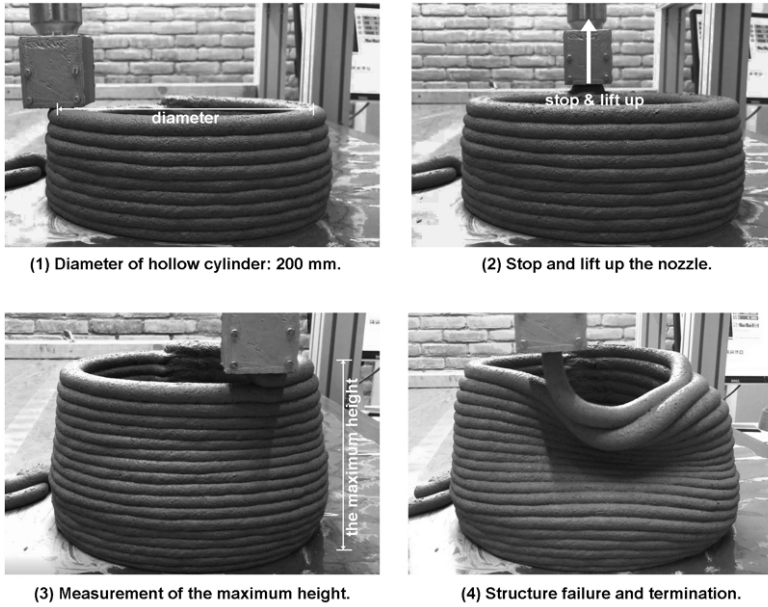


Figure 3.6: Example of the buildability test process.

between two drops was reduced to 5 min. For each test, 44 times drops were conducted in total. Both regular cast (directly use the material after mixing) and “pump” cast (extruded material from Section 3.2.4) mortars were tested in this study.

As mentioned earlier, the early-age behaviors, including the loss of workability/flowability, evolution of material stiffness, development of green strength and microstructure, within the first 3-4 h, are of great interest for material researchers in the field of 3DCP. From a microstructural point of view, the evolution of material stiffness seems to be dominated by the nucleation and growth of hydrates between particles [14], resulting in a considerable increase of  $SSA_{total}$  [15]. Therefore,  $SSA_{total}$  of each studied mixture (paste) was measured at the material ages of 1 h and 3 h in this study. Solvent exchange with isopropanol was employed to stop the hydration of paste samples. According to Ref [15, 16], about 3-5 g of paste extracted from a sealed sample was mixed with a proper amount of isopropanol solvent (paste/solvent=1:10) for 10-15 min. Subsequently, the suspension was filtered to remove the solvent by using a filter paper (2.5  $\mu\text{m}$  sieve size, 55 mm diameter, Whatman<sup>TM</sup>), a Büchner funnel and an aspirator pump. The moist powder was collected and dried in a 40 °C aerated oven for 30-40 min. Finally, the sample was stored in a light vacuum desiccator until constant mass. For determining the total SSA ( $SSA_{total}$ ) of hydrated cementitious materials, dry powders (after the hydration process was stopped) were gently homogenized in an agate mortar. By using a BET multi-point nitrogen ( $\text{N}_2$ ) physisorption apparatus (Gemini VII 2390), the  $SSA_{total}$  of dry powders was measured.

### ISOTHERMAL CALORIMETRY AND COMPRESSIVE STRENGTH TESTS

An eight-channel TAM Air isothermal calorimeter was used to measure the heat flow from all of the mixtures in this study. Each channel contains two parallel cells, one for a testing vessel and the other for a reference vessel. 20 ml glass vessels were employed for the tested and reference samples. The reference vessel was filled with fine sand, which has a similar specific heat capacity as the tested sample. Each channel was an independent unit and was calibrated before starting the tests. The aggregate portion of each mix was excluded. Before placing the samples, a baseline was recorded for about 30 min. The samples with the same mass (6 g) were filled in the glass vessel and immediately moved into the calorimeter, which had been kept constantly at 20 °C. Heat values from the reactions of each mixture were recorded every 20 s for a period of 168 h (7 days).

Mold-cast mortar specimens (40 mm cube) were prepared and tested at the material ages of 1, 3, 7, and 28 days to monitor the evolution of compressive strength with time. All specimens were cured and stored in a fog room (20 ± 2 °C, and above 95% RH) until conducting the test. According to NEN-EN 196-1 [17], a loading rate of 2.4 kN/s was employed to perform the compressive strength test. For each mixture at each material age, the average value of compressive strength was obtained through 3 repeated tests.

## 3.3. RESULTS

### 3.3.1. MIX DESIGNS AND FRESH PROPERTIES

#### SLUMP AND SLUMP-FLOW

ACCORDING to the preliminary test, W/B of 0.3 could not maintain mixtures in Table 3.2 saturated without adding SP. Thus, 0.5-2% (of the binder mass) of SP with a 0.5% increment was added into mixtures. The slump and slump-flow test results of these mixtures containing a certain amount of SP are illustrated in Figure 3.7. Mixtures with relatively weak flowability exhibited a considerable height after demolding (Figure 3.7(a)), and a small spread diameter after the table dropped 25 times (Figure 3.7(b)). It could be found that 0.5% SP only satisfied the demand of mixture B0. For mixtures B45, B75 and B90, the required minimum dosage of SP was increased with the increase of LGCC and LP content. The high PCE-based SP demand for calcined clay/MK-based cementitious materials has been reported by [18–21]. This may be mainly induced by the high SSA and layered particle structure of calcined clay if the swelling clay, e.g., montmorillonite, was not available. Overall, at least 1.5% SP was required to keep all mixtures saturated, and the addition of 2% SP resulted in the similar flowability of all fresh mixtures.

For modifying rheology and enhancing water retention property of studied mixtures, 0.12-0.36% (of the binder mass) of VMA was mixed in the fresh mixtures with 1.5% of SP. As shown in Figure 3.8, increasing the dosage of VMA can reduce the slump of demolded sample and the spread diameter. Also, the increase of LGCC and LP content can improve the shape retention capacity and reduce the flowability of tested samples. Almost zero-slump can be found in Figure 3.8(a) for mixtures B75 and B90 with the addition of 1.5% SP and 0.36% VMA. However, the high dosage of VMA could lead to excessively high pumping pressure (which limits the material flow rate), high

porosity of the printed filament and adverse effects on hydration (see Chapter 4). Thus, 0.36% of VMA was not considered for further tests in this study. The mixtures with 0.24% VMA showed a much smaller slump value and moderate spread diameter compared to that of mixtures containing 0.12% VMA. If the addition of 0.24% VMA was kept identical, increasing SP dosage from 1.5% to 2% in mixtures B75 and B90 can enhance the flowability and only slightly affect the slump of demolded sample, as shown in Figure 3.8.

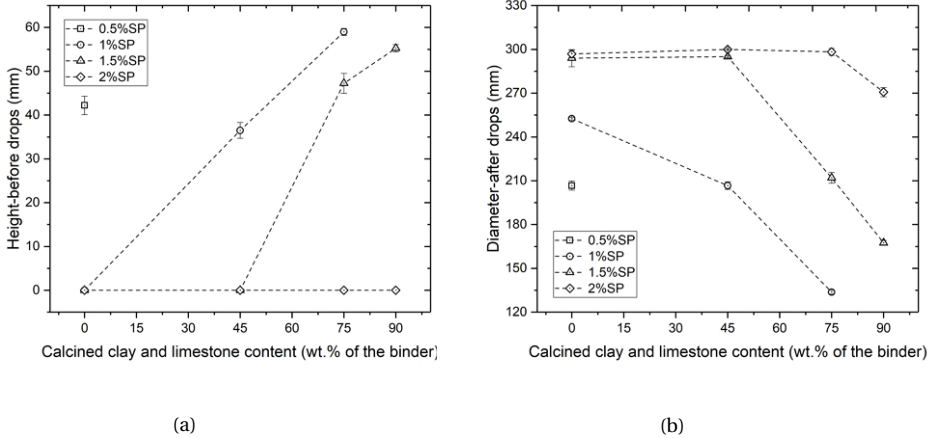


Figure 3.7: Slump and slump-flow test results of mixtures with different SP dosages: (a) Height (before table drops), the height smaller than 20 mm is recorded as 0 mm; (b) Spread diameter (after 25 times of table drops).

### WATER RETENTION CAPACITY

Based on the results of slump and slump-flow tests, three admixture options, i.e., 1.5% SP+0.12% VMA, 1.5% SP+0.24% VMA, and 2% SP+0.24% VMA (only for mixtures B75 and B90) were employed for assessing the water retention property of fresh mixtures. Also, 1.5% SP was designed as a reference. Figure 3.9 shows the water retention capacity of different mixtures containing different dosages of SP and VMA. For these mixtures with 1.5% SP, the increase of VMA addition could significantly improve the water retention property. These results confirmed that the water retention of cellulose ether-derived polymer (HPMC in this study) primarily depends on the concentration used in the mixture [22]. Besides, as shown in Figure 3.9, more quantities of water were retained in mixtures containing LP and LGCC (B45, B75 and B90) in comparison with mixture B0 for the same admixture addition. This might be attributed to the water adsorption on (calcined) clay minerals. Such water adsorption behaviors of kaolinite, illite and montmorillonite clays have been comprehensively studied by Hatch et al. [23]. Additionally, mixtures with 2% SP+0.24% VMA showed very close water retention value compared to mixtures with 1.5% SP+0.24% VMA. The possible reasons why the higher SP content did not result in more amount of bleed water have been explained by Rahul et al. [8]. The high content of SP may lead to many non-adsorbing PCE polymers

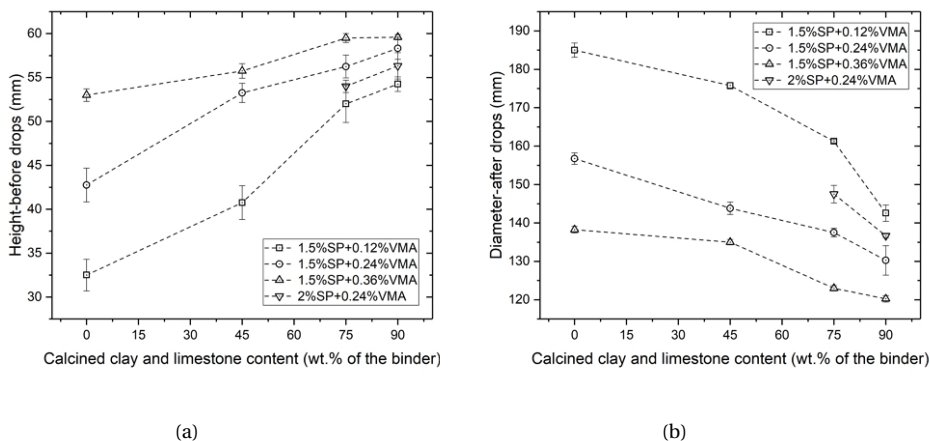


Figure 3.8: Slump and slump-flow test results of mixtures with different dosages of SP and VMA: (a) Height (before table drops); (b) Spread diameter (after 25 times of table drops).

remained in the suspension, which could increase the viscosity of pore solution [8] and generate a kind of depletion force resulting in particle flocculation [24, 25]. Such effects may raise difficulties of bleeding and enhance the water retention capacity of fresh mixtures.

According to results of water retention, slump and slump-flow tests, mixtures including 1.5% SP+0.24% VMA exhibited good shape retention (small slump after demolding), moderate flowability, and optimal water retention capacity. Thus, 1.5% SP+0.24% VMA was selected for all mixtures. Acceptable fresh properties could be observed in mixtures B75 and B90 with 2% SP+0.24% VMA, which were also employed for further characterization. Table 3.4 presents all mix designs prepared for the following assessments. Note that B0-1 was not used for 3D printing and designed as a reference for determining the effect of increasing LGCC and LP fractions on the early age hydration.

Table 3.4: Amounts of admixtures for acceptable printing performance of the binders formulating the printable cementitious materials.

Binder + Water + Aggregate		Admixture	
Based on Table 3.2		SP (wt.% of the binder mass)	VMA (wt.% of the binder mass)
B0-1	B0	1.5	0.24
B45-1	B45	1.5	0.24
B75-1	B75	1.5	0.24
B75-2	B75	2.0	0.24
B90-1	B90	1.5	0.24
B90-2	B90	2.0	0.24

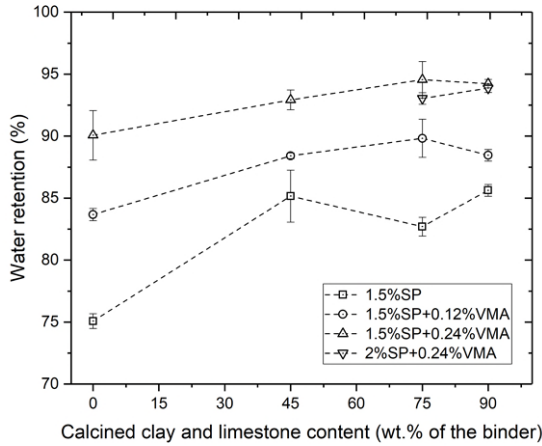


Figure 3.9: Water retention of fresh mixtures with different dosages of SP and VMA.

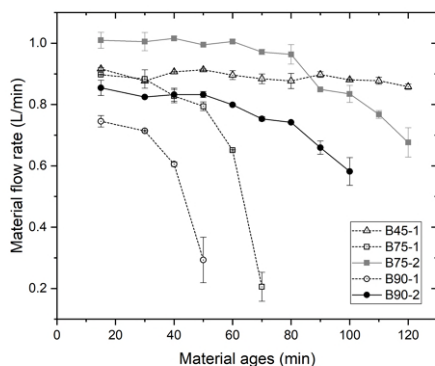
### 3.3.2. 3D PRINTABILITY

#### EXTRUDABILITY AND OPERATION WINDOWS

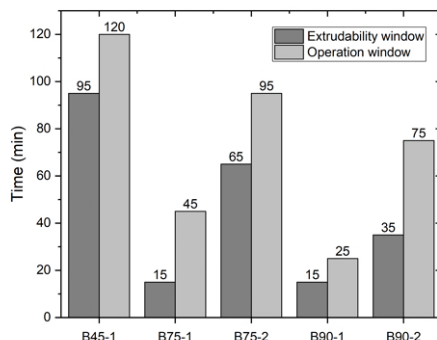
Figure 3.10(a) gives the material flow rates of various mixtures at different material ages. Under the same pumping rate of 58–60 rpm, the material flow rate of different mixtures at the same material age was not similar due to the various rheological properties. Under an identical extrusion shearing, mixtures demonstrating a relatively low flow rate may have the high Bingham rheological parameters (yield stress and/or plastic viscosity). At the materials age of 15 min, mixture B90-1 showed the minimum material flow rate. A similar initial material flow rate can be found in mixtures B45-1 and B75-1. Compared to mixtures B75-1 and B90-1, mixtures B75-2 and B90-2 had a much higher material flow rate induced by the 0.5% SP increment. For mixtures B75-1 and B90-1, the loss of material flow rate was evident after 30 min. The change of material flow rate can be attributed to the loss of material workability with time. However, for mixtures B45-1, B75-2 and B90-2, the relatively constant material flow rate can be maintained for a long time. The material flow rate of mixture B45-1 could be kept at about 0.9 L/min during the first two hours. For the same admixture addition (1.5% SP+0.24% VMA or 2% SP+0.24% VMA), increasing the LGCC and LP content could result in a fast change of material flow rate. Based on the definition of extrudability and operation windows in Section 3.2.4, Figure 3.10(b) presents the results of both windows for different mixtures. Mixtures B75-1 and B90-1 exhibited relatively short times for extrusion and operation. In contrast, the increase of 0.5% SP (mixtures B75-2 and B90-2) can extend both extrudability and operation windows about 20–50 min.

The increased material temperatures between before and after extrusion for each mixture at different material ages are plotted in Figure 3.10(c). The mixture with a low material flow rate shows a relatively high temperature increase, as seen from Figure 3.10(d). This is probably induced by the high friction between the mixture and the

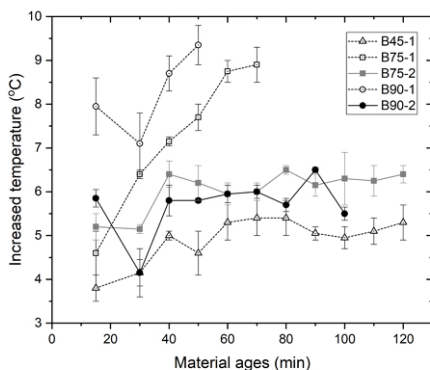
rotor-stator setup during extrusion. For a constant rotation speed (the shear stress is kept identical), such friction was primarily dominated by the rheological behavior of mixtures at the tested time. Besides, the generated heat could influence the stiffness evolution (initial setting) of deposited materials, which was studied in Section 3.3.3.



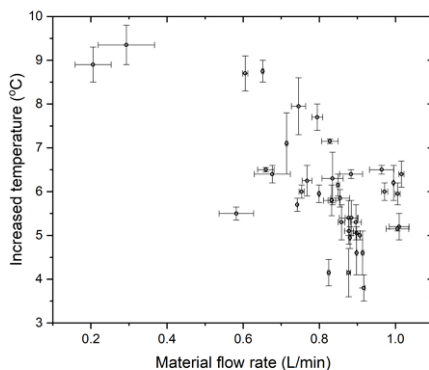
(a)



(b)



(c)



(d)

Figure 3.10: (a) Material flow rates of different mixtures at various material ages; (b) Test results of extrudability and operation windows; (c) Increased temperatures (after extrusion) of different mixtures at various material ages; (d) Correlation between material flow rates and increased temperatures after extrusion.

### BUILDABILITY

The printing parameters for performing buildability tests are summarized in Table 3.5. The pump rate was kept at 58-60 rpm that was the same as the one used in the measurement of extrudability and operation windows. According to the test result of

extrudability window, all studied mixtures can maintain a relatively stable material flow rate at the material age of 15-30 min. Thus, the buildability test was conducted within this period. As mentioned earlier, to ensure continuous printing, the nozzle moving speed  $V_n$  was kept almost equal to the linear extrusion speed of the material  $V_{linear}$ . Due to the different rheological behaviors, the printing speed (nozzle moving speed and material flow rate) of different mixtures was not the same in buildability test. This inequality led to the variation of the time gap between layers. However, owing to the short length of the printing path for each layer used in this test, the time interval deviation between different mixtures was tiny. As seen from Table 3.5, the maximum difference of time gap is only about 2.3 s. Therefore, the influence caused by the different time gaps on the buildability test was not considered.

The buildability test process and results are presented in Figures 3.11 and 3.12. It could be found that mixture B90-1 exhibited the optimal buildability and can be used to stack more than 20 layers vertically without collapse. The buildability test of mixture B90-1 was terminated at the 21<sup>st</sup> layer due to the insufficient amount of material in the hopper. As shown in Figure 3.12, mixtures B75-1 and B90-2 displayed similar buildability, and the printed structure could reach at most 18 layers. By using mixtures B45-1 and B75-2, only 12 layers were stably deposited. Therefore, with the same addition of admixture (SP+VMA), the mixture containing a higher content of LGCC and LP can stack more layers and demonstrated a better buildability. Besides, increasing SP dosage from 1.5% to 2% clearly weakened the buildability of fresh mixtures.

As illustrated in Figure 3.11, the final buckling collapse (except mixture B90-1) can be attributed to the local or global instability of the printed structure, initiated by large plastic deformations occurring in the bottom layers. The unstable layer deposition was induced by the increase of nozzle standoff distance  $h_1$  that decreased the contact area between layers (see Figure 3.13). Due to the employment of a down-flow nozzle with a round opening, the new layer was built on the top of the substrate via a squeezed forming process at the beginning of the printing session. This means that the bottom layers should sustain the load not only from the weight of freshly deposited layers but also from the nozzle (when  $8 \text{ mm} \leq h_1 < 15 \text{ mm}$ ). These forces can lead to the increase of plastic material deformation of the substrate, contributing to the increase of nozzle standoff distance. With increasing the nozzle standoff distance, the squeezing force from nozzle was decreased gradually (when  $8 \text{ mm} < h_1 < 15 \text{ mm}$ ), and then disappeared when the nozzle standoff distance was equal to or larger than the diameter of nozzle opening (when  $h_1 \geq 15 \text{ mm}$ ). Overall, structure collapse in the buildability test is dominated by the large cumulative plastic deformation of bottom layers. For the mixture with a good buildability, the material deformation during the layer-stacking was not significant. For example, the printed structure manufactured using mixture B90-1 showed relatively even layer thickness from the bottom to the top.

#### CORRELATION BETWEEN INLINE AND OFFLINE TEST RESULTS

The test results in this study confirmed that slump and slump-flow tests could indicate the buildability and extrudability/pumpability of 3D printable cementitious materials. A linear relationship between the sample height after demolding in slump test and the maximum height of printed structure before collapsing is illustrated in Figure 3.14(a). Similar findings have been reported elsewhere [7]. The height of demolded sample in



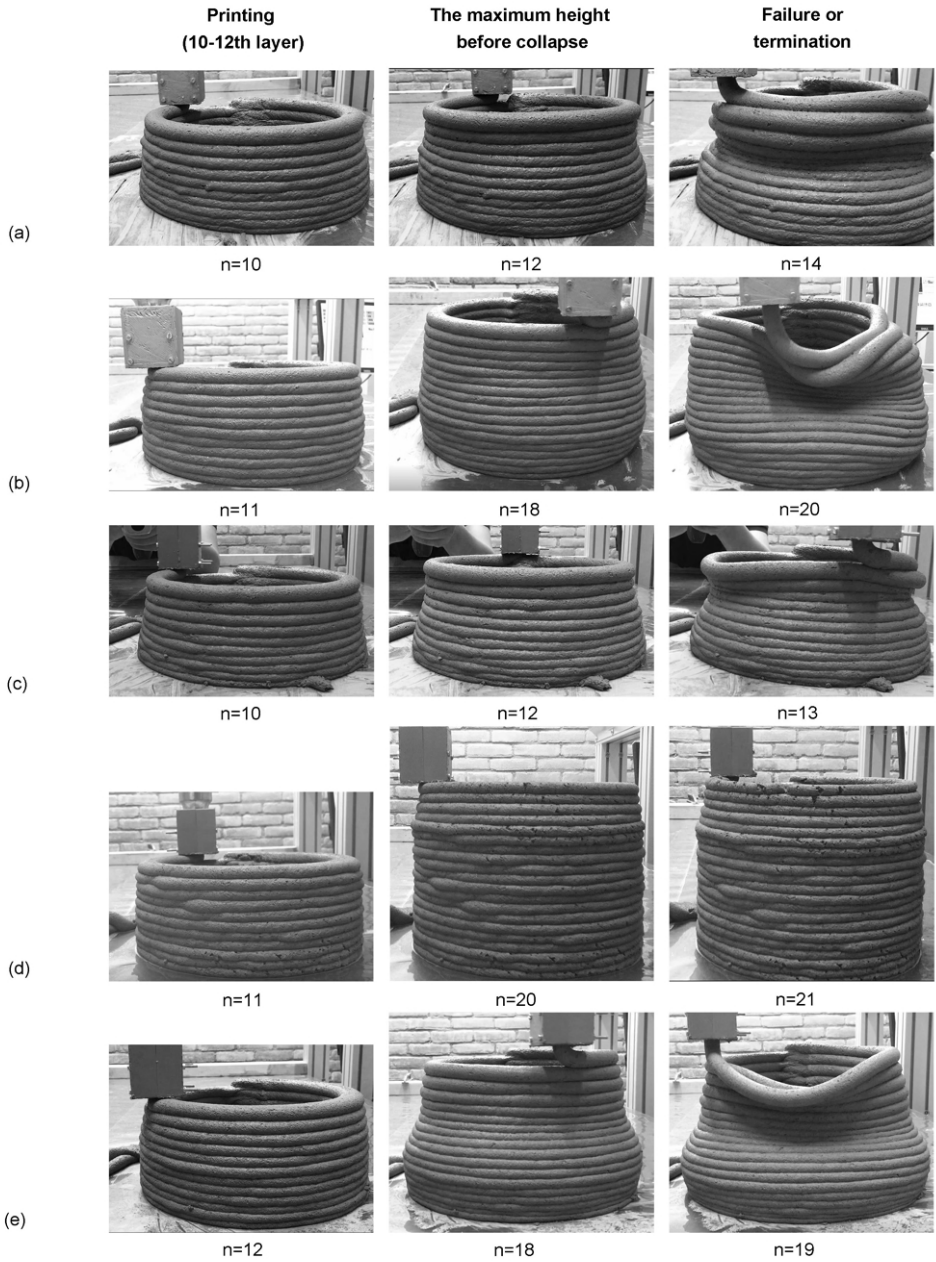


Figure 3.11: Buildability tests of mixtures (a) B45-1; (b) B75-1; (c) B75-2; (d) B90-1; (e) B90-2.



Table 3.5: Printing parameters for performing buildability test.

	Test time (material age) [min]	Predefined nozzle standoff distance [mm]	Pump rate [rpm]	Material flow rate [L/min]	Nozzle opening (diameter) [mm]	Nozzle moving speed [mm/min]	Time gap between layers [s]
B45-1	15-30	8	58-60	0.90	15	5100	7.4
B75-1	15-30	8	58-60	0.89	15	5040	7.6
B75-2	15-30	8	58-60	1.01	15	5700	6.7
B90-1	15-30	8	58-60	0.73	15	4140	9.0
B90-2	15-30	8	58-60	0.85	15	4800	8.1

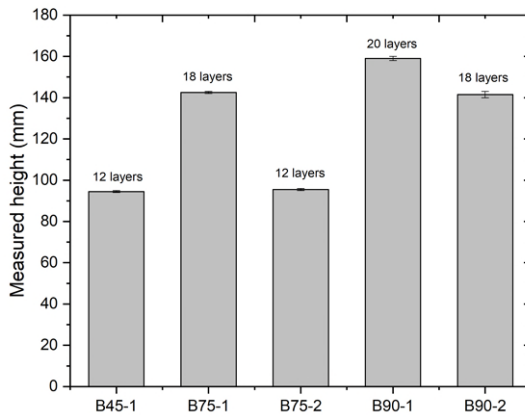


Figure 3.12: Buildability test results of different mixtures. The measured maximum height of printed structure before collapse.

the slump test depends on the static yield stress of the tested cementitious material [15, 26, 27]. As previously described, the buildability of fresh mixtures is dominated by their static yield stress at rest [28–30] when all printing parameters (e.g., printing speed, nozzle standoff distance, and time interval between layers.) are kept identical. The high static yield stress indicates a good buildability in general. Moreover, as seen from Figure 3.14(b), the spread diameter of different samples after 25 times of table drops in slump-flow test seems linearly correlate with the material flow rate under 58-60 rpm at the similar material age. The mixture with a high spread diameter showed a high flow rate, indicating a high flowability and low dynamic yield stress. Overall, employing slump and slump-flow tests can be employed as a simple and efficient way to formulate printable cementitious materials at an early stage. However, using Hägermann cone is not the conventional way to perform the slump test for mortar. The mold height of Hägermann cone is only 60 mm, which may be insufficient for comparing some mixtures with very high static yield stress (zero-slump after demolding). Generally, it is suggested to use a mini-slump cone with 50 mm top diameter, 100 mm base diameter,

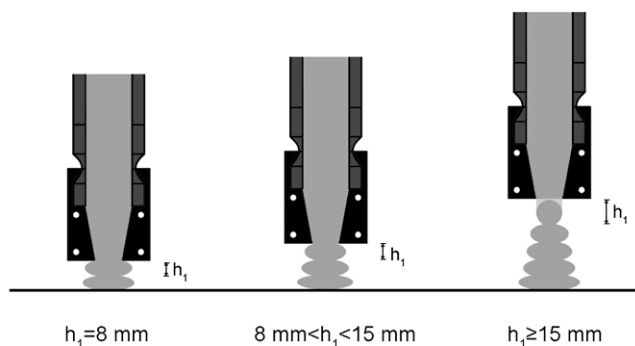


Figure 3.13: Illustration of the increased nozzle standoff distances and the expected cross-section of printed structure during printing.

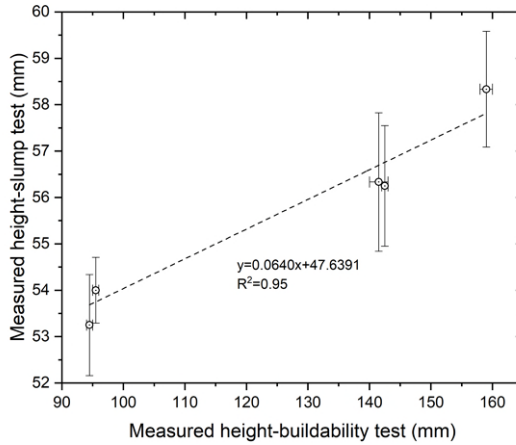
and 150 mm height for conducting the slump test of mortar (see [11]). Also, cylindrical molds with an aspect ratio of 1 can be considered (see [15, 31]).

### 3.3.3. STIFFNESS DEVELOPMENT AND EARLY-AGE HYDRATION

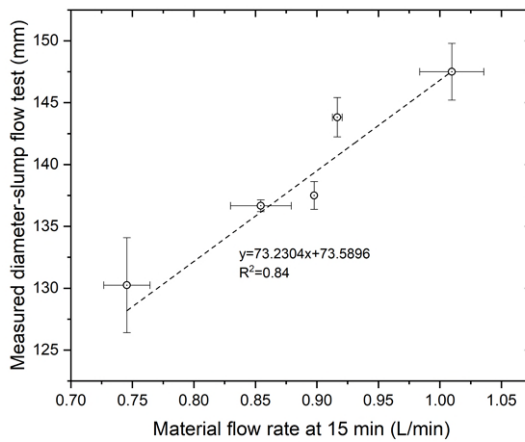
#### INITIAL SETTING TIME AND SSA EVOLUTION

Figure 3.15 compares the initial setting time of different mixtures prepared by a regular casting process or by a pump-casting (after extrusion) process. The pump-casting process can accelerate the initial set of the studied mixtures. The reduction of initial setting time for different mixtures was various and ranged between 23 min and 50 min. As reported in Section 3.3.2, the temperature of mixture was increased during extrusion, which accelerated the water loss of fresh mixture. This may explain the acceleration of initial set induced by the pumping process. Besides, increasing the temperature of cementitious materials may enhance the structuration rate at rest, hydration rate of cement, and formation rate of hydration products [32]. Such effects were not studied in this chapter and will be investigated in the future. In addition, as shown in Figure 3.15, a slight increase of SP in mixtures (see B90-2 and B75-2) can significantly delay the initial setting by about 1 h. For the same admixture addition, the mixture with a high dosage of LGCC and LP displayed a short initial setting time. These phenomena will be discussed in Section 3.4.2.

The test results of  $SSA_{total}$  at 1 h and 3 h are plotted in Figure 3.16(a). For the same admixture addition, mixtures containing a high dosage of LP and LGCC showed a great high  $SSA_{total}$  at both tested material ages. This was due to the relatively high SSA of LGCC and the fast growth of  $SSA_{total}$  during 1-3 h (see Figure 3.16(b)). By increasing the SP dosage (for mixtures B75 and B90), the evolution of  $SSA_{total}$  between 1 h and 3 h was severely decelerated, whereas this influence on  $SSA_{total}$  at the first hour was very limited. The increase of  $SSA_{total}$  within the first hour was probably attributed to the precipitation of some earlier hydration products (likely ettringite [33], and/or other



(a)



(b)

Figure 3.14: The linear correlation between: (a) Measured sample height in slump test and measured printed structure height in buildability test; (b) Measured spread sample diameter in slump-flow test (after 25 times of table drops) and material flow rate (under 58-60 rpm) at 15 min in extrudability window test.

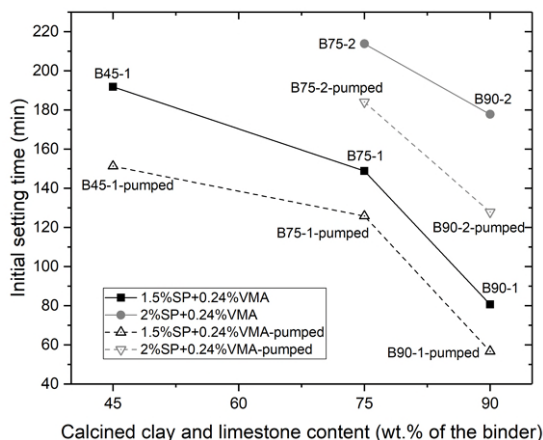


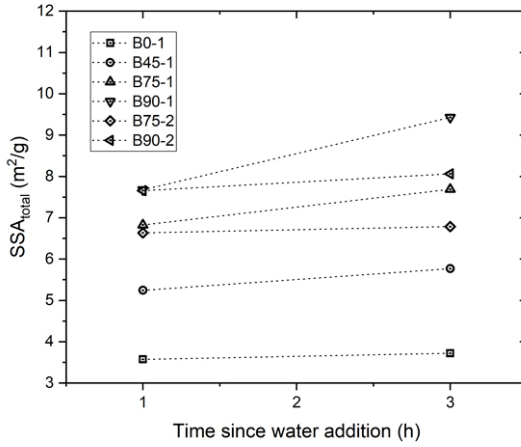
Figure 3.15: Results of the initial setting time.

hydrated aluminate phases) during the initial mixing stage [15]. More discussions about the development of  $SSA_{total}$  will be given in Section 3.4.2.

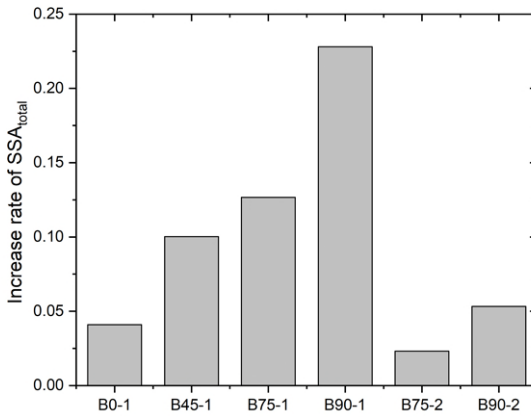
#### ISOTHERMAL CALORIMETRY AND COMPRESSIVE STRENGTH

Figure 3.17 compares isothermal calorimetry test results of different studied paste mixtures. The normalized heat flow and cumulative heat by mass of paste with 7 days are plotted in Figures 3.17(a) and 3.17(b), respectively. With the increase of PC substitution by LP and LGCC, both the intensity of the main hydration peak in Figure 3.17(a) and the cumulative heat value at 7 days in Figure 3.17(b) were significantly decreased, which indicated the dilution effect on hydration. Moreover, the retardation of hydration caused by the higher dosage of SP can also be observed in Figures 3.17(a), 3.17(b) and 3.17(c). Compared to mixtures B75-1 and B90-1, the main hydration peak of mixtures B75-2 and B90-2 were delayed about 6-8 h. However, such effects only retard the early-age hydration and do not heavily modify the cumulative heat value at 7 days (see Figure 3.17(b)).

To better observe the influence of high-content LP and LGCC replacements on early-age hydration, the normalized heat flows of different mixtures containing the same dosages of admixtures (1.5% SP+0.24% VMA) by mass of Portland cement within the first 4 days are extracted from Figure 3.17(c) and demonstrated in Figure 3.17(d). It can be found that there were three curve patterns. First, for mixture B0-1, only one peak primarily induced by alite hydration was observed after the induction period. Second, except the dissolution peak at the very beginning, three peaks, possibly indicating the main hydration, aluminate reaction (sulfate depletion) [34–36], and the formation of AFm and/or other phases [36, 37], were recognized in mixtures B45-1 and B75-1. Compared to mixture B0-1, the main hydration peak of mixtures B45-1 and B75-1 appeared about 3 h and 12 h earlier, owing to the shorter induction period. The possible



(a)



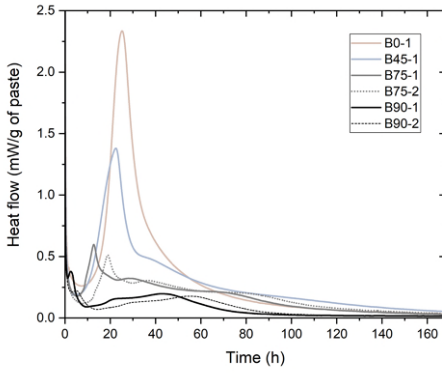
(b)

Figure 3.16: (a)  $SSA_{total}$  of different paste mixtures at the material ages of 1 h and 3 h; (b) Growth rate of  $SSA_{total}$  of different paste mixtures between 1 h and 3 h.

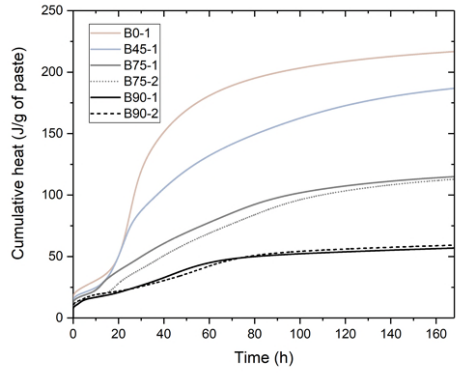
reasons were discussed in Section 3.4.3. Third, the curve shape of mixture B90-1 was dissimilar to that of other mixtures in Figure 3.17(d). Peak 1 may be referred to the aluminate reaction. The additional reactive aluminate was provided by LGCC. According to [36, 38–40], the sulfate depletion may occur in the initial period (a left shift of aluminate peak) if the sulfate amount is insufficient in the binder system. After that, a shoulder, denoted as Peak 2, was observed at 24 h, close to the occurrence of the main hydration peak for mixtures B45-1 and B0-1. About 20 h later, a broad peak (Peak 3) with a higher intensity than Peak 2 was determined. However, it was difficult to recognize which one (Peak 2 or 3) was dominated by alite hydration only based on the current results. As reported by [38, 39], aluminum in the solution can inhibit alite hydration during the C-S-H growth period. In their cases, the alite peak in the under-sulfated system not only appears late but also is much lower and broader compared to that of the single alite phase system. In Figure 3.17(d), both Peak 2 and 3 in mixture B90-1 showed smaller and broader intensity than the main hydration peak of other mixtures. Nevertheless, the time of Peak 2 was very close to the main hydration peak in mixtures B45-1 and B0-1. Thus, in this study, Peak 3 might be caused by alite hydration, and Peak 2 may indicate the formation of AFm and/or other phases. To validate this hypothesis, a series of material characterizations using (in-situ) X-ray diffraction and thermogravimetric analysis are required in further study.

The compressive strength test results of different mixtures (mold-cast mortar) at 1, 3, 7 and 28 days are presented in Figure 3.18(a). For the same dosage of SP and VMA, increasing the content of LGCC and LP in the binder decreased the compressive strength at all tested ages. Mixture B0-1 containing 0% of LGCC and LP showed the optimal compressive strength among all mixtures. In comparison with mixture B0-1, mixture B45-1 displayed much lower early-age compressive strength, i.e., 1 and 3 days, and comparable strength at 7 and 28 days, which agreed with the findings of Avet et al. [3]. The moderate compressive strength of about 25 MPa can be obtained at 28 days by replacing 75% of PC with LP and LGCC (mixtures B75-1 and B75-2). Further reducing the PC content resulted in a significant decrease of compressive strength (mixtures B90-1 and B90-2). Moreover, for mixtures B75 and B90, the increase of SP dosage from 1.5% to 2% can reduce nearly 50% of compressive strength at 1 day, whereas such influences were diminished obviously from 3 days onwards.

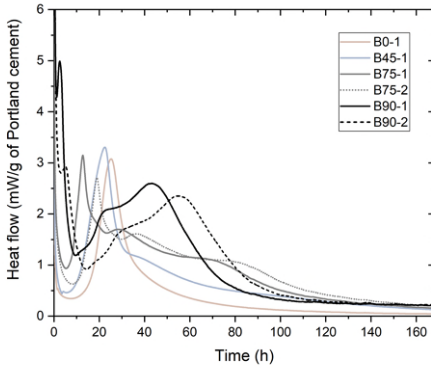
If all cast samples with the similar air void content and distribution, the compressive strength may mainly depend on the hydration of cementitious materials. A linear correlation between the compressive strength of mortar and the normalized cumulative heat value of paste at 1, 3 and 7 days is illustrated in Figure 3.18(b). The R-squared value of the fitted curve was higher than 0.9, which appeared to confirm the critical role of cement hydration on the compressive strength of cast samples in this context.



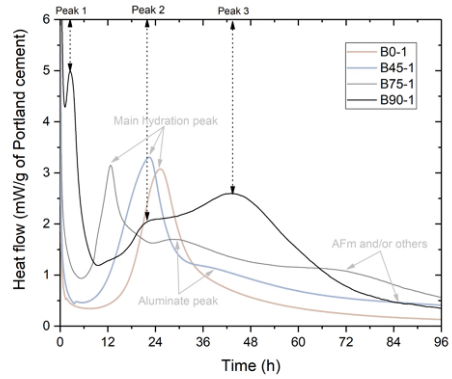
(a)



(b)

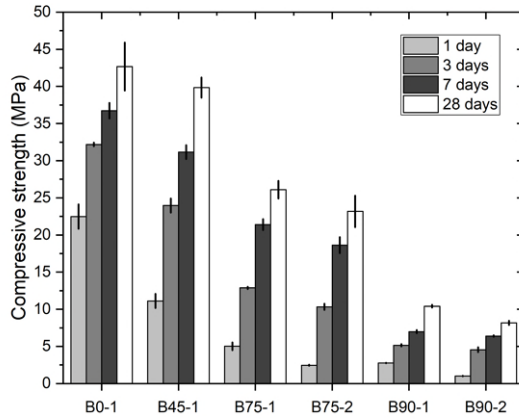


(c)

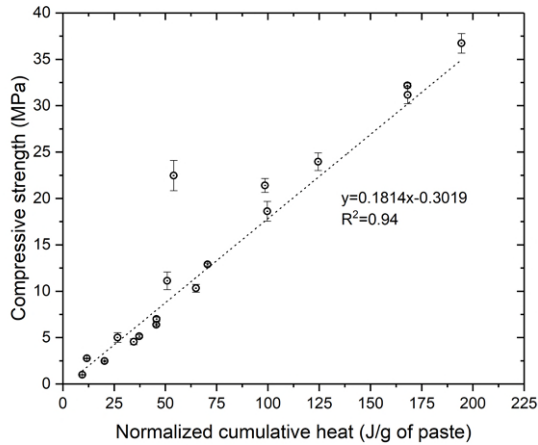


(d)

Figure 3.17: Test results of isothermal calorimetry: (a) Normalized heat flow by mass of paste with time (7 days); (b) Normalized cumulative heat by mass of paste with time (7 days); (c) Normalized heat flow by mass of Portland cement with time (7 days); (d) Normalized heat flow by mass of Portland cement with time (4 days).



(a)



(b)

Figure 3.18: (a) Compressive strength of different mixtures at 1, 3, 7, and 28 days. (b) The linear relationship between compressive strength and normalized cumulative heat by mass of paste at 1, 3, and 7 days (excluding any heat within the first 2 h after mixing).



### 3.4. DISCUSSION

#### 3.4.1. EFFECT OF INCREASING LGCC AND LP CONTENT ON FLOWABILITY AND 3D PRINTABILITY

If the dosage of admixtures remains unchanged, the main difference between mixtures in this study is the binder composition. Thus, for mixtures B0-1, B45-1, B75-1, and B90-1, the various material behaviors in aspects of flowability and 3D printability appear to be dominated by the LGCC and LP content. The physical characteristics, including the total SSA, solid fraction, and packing density, may be modified by increasing the proportion of LGCC and LP in the binder. In cementitious pastes, the initial role of water is to occupy the voids between particles. In most cases, the water content is higher than the required minimum amount for filling all voids. The excess water may form water films on surfaces of particles to ease the friction between solid particles [41]. Earlier studies [41–45] showed that the flowability, rheology and strength of fresh cementitious materials are strongly related to the corresponding water film thickness (WFT). According to [42, 45], the WFT of paste can be calculated via the following equations:

$$WFT = \frac{\mu_{excess}}{SSA_0} \quad (3.3)$$

$$SSA_0 = \frac{V_{PC}SSA_{PC}}{\rho_{PC}} + \frac{V_{LP}SSA_{LP}}{\rho_{LP}} + \frac{V_{LGCC}SSA_{LGCC}}{\rho_{LGCC}} \quad (3.4)$$

where  $SSA_0$  is the total SSA of dry binder ( $\text{m}^2/\text{cm}^3$ );  $V_{PC}$ ,  $V_{LP}$  and  $V_{LGCC}$  denote the volumetric ratio of PC, LP and LGCC in the binder;  $SSA_{PC}$ ,  $SSA_{LP}$  and  $SSA_{LGCC}$  stand for the measured SSA ( $\text{m}^2/\text{g}$ ) of PC, LP and LGCC.  $\rho_{PC}$ ,  $\rho_{LP}$  and  $\rho_{LGCC}$  denote the density of PC, LP and LGCC (see Table 3.1).  $\mu_{excess}$  is the excess water volume fraction (the excess water volume/the solid volume), which is obtained by:

$$\mu_{excess} = \mu_{total} - \mu_{void} \quad (3.5)$$

where  $\mu_{total}$  and  $\mu_{void}$  denote the water ratio of the paste (total water volume/the solid volume) and void ratio (total void volume/the solid volume), respectively.  $\mu_{void}$  is quantified by:

$$\mu_{void} = \frac{1 - \tau}{\tau} \quad (3.6)$$

where  $\tau$  is the packing density of the binder. In this study, the packing density of each binder was measured by using the Puntke test. The test was conducted under the description given by [8, 46]. The mixing liquid in the Puntke test comprised water and 5% SP (1.5% of the binder mass). Note that the packing density used in Eq 3.6 can also be acquired via the wet packing method [47] or a packing algorithm [45]. Besides, sand and VMA of each mixture (see Tables 3.2 and 3.4) were excluded from the calculation of WFT. The packing density,  $SSA_0$  and WFT of studied cementitious systems are illustrated in Figure 3.19. The impact of LGCC and LP addition on packing density is very limited. Only mixture B90 shows a slight decrease in packing density compared to others. In contrast, increasing the content of LP and LGCC in the binder leads to a vast increase of  $SSA_0$ , which is probably due to the extremely high SSA of LGCC. Consequently, a steep reduction of WFT was expected as the increase of  $SSA_0$ . For the

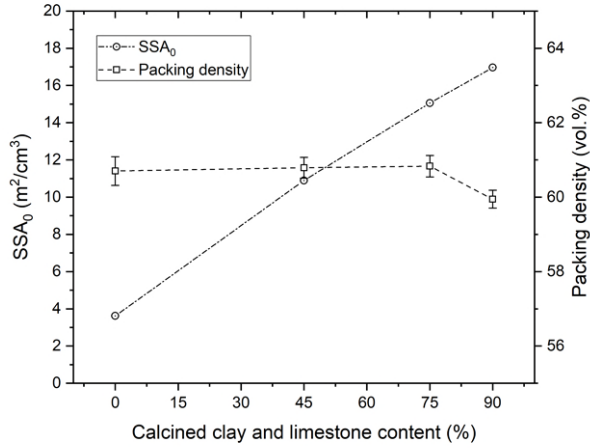
tests performed within 30 min after water addition, i.e., slump and slump-flow, buildability, and extrudability window tests (first two trials), the nucleation and structuration between particles should not start yet. Mixtures with a small WFT of paste (high content of LGCC and LP) displayed a strong shape retention and buildability, as well as a weak flowability and extrudability (see Figures 3.7, 3.8, 3.10, 3.12 and 3.20). Without considering about structural build-up, the rheological performance of fresh mortar is primarily dependent on the WFT of paste and cement (binder in this context) to aggregate ratio [48]. In this chapter, the binder to aggregate ratio and aggregate gradation were kept constant for all tested mixtures. Thus, the WFT of pastes as an intrinsic indicator combining many physical features of mixture, i.e., water content, packing density and SSA, plays the most critical role in influencing fresh-state behaviors at this stage.

### 3.4.2. EFFECT OF INCREASING LGCC AND LF CONTENT ON STIFFNESS EVOLUTION WITH TIME

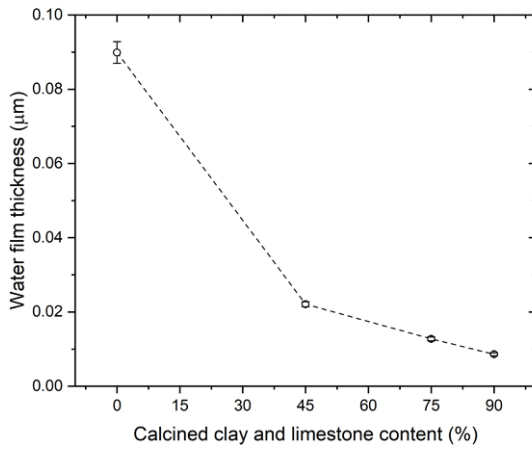
The structural build-up at rest within the material age of 3-4 h is of great importance for 3D printable cementitious materials considering the printing process. The mixture exhibited a fast stiffness evolution or structuration rate at rest (after deposition) can be regarded as merit in applying 3D printing. For the same addition of admixtures, the results of extrudability test (see Figure 3.10) showed that the mixture containing a higher dosage of LGCC and LP experienced a faster material flowability and extrudability loss (material flow rate). Due to the short gap between two test trials (8 min), the tested materials were not at a constantly dynamic status. The material stiffness appeared to be developed during the short resting time, leading to a gradual workability reduction. Consequently, a significant decrease in material flow rate with time was observed for these mixtures, i.e., mixtures B75-1 and B90-1, which displayed a fast stiffness evolution. Similarly, increasing the LP and LGCC substitution of the binder accelerates the initial set of fresh mixtures, as shown in Figure 3.15.

The LP with the similar fineness and SSA compared to that of PC was used as an ideal inert filler in studied mixtures. In contrast to LP, LGCC containing a relatively high dosage of reactive aluminate phases (32 wt.%) seems to play a dominant role in accelerating the stiffness development of fresh cementitious materials within the first several hours. For the cementitious systems consisted of high content of LGCC and LP (mixtures B75 and B90), the amount of calcium sulfate (gypsum) was very low due to the limited addition of PC. At the very early age of hydration (3-4 h since water addition), lack of gypsum in the binder system can lead to a sulfate depletion caused by aluminate reaction at the initial stage (see Peak 1 of mixture B90-1 in Figure 3.17(d)), whereas this phenomenon was not observed in mixtures B45-1 and B75-1. Additionally, the formation of massive hydration products, especially hydrated aluminate phases, relating to the increase of SSA seems the main reason governing the workability loss and stiffness evolution of fresh mixtures. As shown in Figure 3.16, increasing the content of LGCC and LP in the binder accelerated the development of  $SSA_{total}$  during 1-3 h. From the perspective of water film theory in Section 3.4.1, the increment of  $SSA_{total}$  can further reduce WFT affecting the fresh-state behaviors of mixtures (without considering the difference in water consumption rate).

The stiffness evolution of studied mixtures was also influenced by the presence of



(a)



(b)

Figure 3.19: (a) Packing density and  $SSA_0$ ; (b) Water film thickness of cementitious systems containing different contents of limestone and calcined clay.

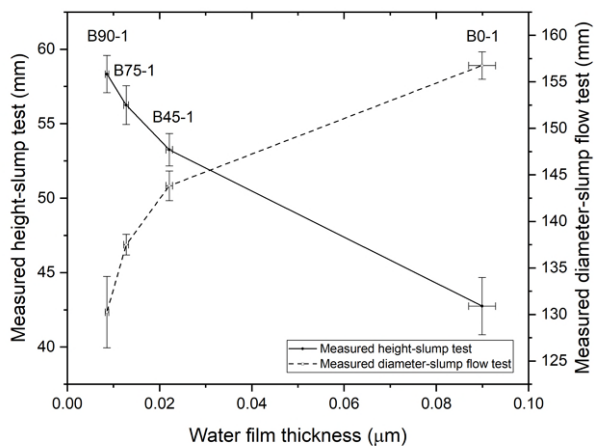


Figure 3.20: Correlation between: Water film thickness and measured sample height in slump test; Water film thickness and measured sample diameter in slump flow test.

PCE-based SP. At the very beginning, PCEs adsorbed on the surface of cementitious particles for dispersing them and controlling their flocculation [15, 49]. However, as mentioned by [15], compared to adsorbing on cement particles, PCEs may tend to be consumed by hydrated aluminate phases owing to the preferential sequestration [50, 51] or adsorb on ettringite [33, 52] at the early-age hydration. The precipitation of such crystal phases can provide more specific surface areas [33], which vastly reduces the available PCEs for the dispersion [15, 50, 53]. Also, this process could improve the delay of anhydrous phase dissolution caused by PCEs and accelerate the nucleation and hydration of cement [35, 54]. For mixtures B75 and B90, the slight increment of SP dosage from 1.5% to 2% can increase the available PCEs in the solid suspension for extending its dispersion effect. The extrudability window of fresh mixture was prolonged due to this effect (see Figure 3.10). Nonetheless, the development of material stiffness, as indicated by the initial setting time and the growth rate of  $SSA_{total}$  (see Figures 3.15 and 3.16), were severely declined.

### 3.4.3. EFFECT OF INCREASING LGCC AND LF CONTENT ON THE MAIN HYDRATION PEAK

For the same addition of admixture (1.5% SP and 0.24% VMA), the hydration of various mixtures in Figure 3.17 was only influenced by the content of LP and LGCC. According to Section 5.3.5, Chapter 5, the addition of LGCC appears to play a significant role in accelerating the alite hydration instead of LP. As mentioned in Section 3.4.2, increasing LGCC dosages in the binder can increase the amount of reactive aluminate phases, which may govern most of the phenomena observed in Figure 3.17. The time of the main hydration peak was reduced by increasing the reactive aluminate content from 0% to 16% (0-75% of LP and LGCC), as seen from Figure 3.21. The acceleration of alite

hydration may be attributed to the consumption of PCEs induced by the hydrated aluminate products, as explained in Section 3.4.2. However, the further increment of reactive aluminate (19.2% in mixture B90-1) resulted in huge retardation of the main hydration peak. Note that I assumed Peak 3 as the main hydration peak of mixture B90-1. Even using Peak 2 in this context, an apparent delay of the time of the main hydration peak compared to that of mixture B75-1 can also be found in Figure 3.17. According to [55, 56], the dissolution of  $C_3S$  and growth of C-S-H nuclei may be inhabited and poisoned by the high concentration of aluminate ions from the dissolved metakaolin. Due to the low dissolution rate of metakaolin compared to  $C_3S$ , such inhibitions are only significant once a high metakaolin content was employed. This hypothesis seems to fit very well to the obtained results in this study. For mixture B90-1, the reactive aluminate content is only slightly higher than mixture B75-1 (about 3.2%), whereas the reactive aluminate to Portland cement mass ratio is near four times of mixture B75-1. Thus, the concentration of aluminate ions in mixture B90-1 might be too high to affect  $C_3S$  hydration. Such effects could not only delay the time but also reduce and broaden the intensity of the main hydration peak, as discussed in Section 3.3.3.

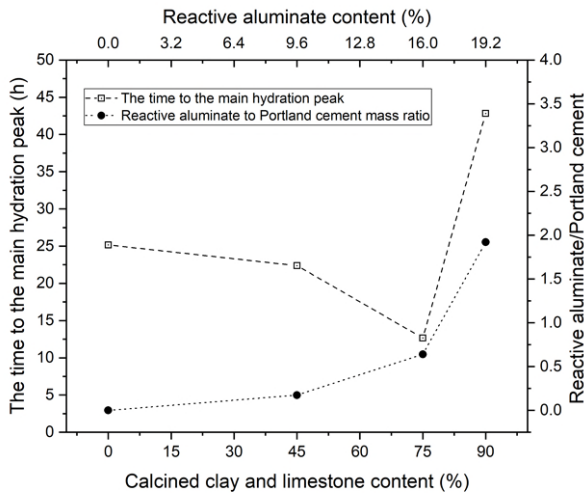


Figure 3.21: The time to the main hydration peak (mixtures B0-1, B45-1, B75-1 and B90-1) and reactive aluminate to Portland cement mass ratio varying with different calcined clay and limestone contents and reactive aluminate dosages (sourced from calcined clay).

### 3.5. CONCLUSION

**B**ASED on the present study, the following conclusions were drawn:

- Increasing the content of LP and LGCC can decrease both slump and flowability. The obtained results of slump and slump-flow tests were feasible for obtaining the extrudability and buildability of studied mixtures. Increasing VMA% can enhance

the shape retention property and water retention capacity of fresh mixtures but affect the corresponding flowability.

- By adding the same admixtures (1.5% SP+0.24% VMA), the mixtures containing a high content of LGCC and LP displayed a low material flow rate at the same tested time, short extrudability and operation windows, and a strong buildability. Such effects can be attributed to the reduced WFT of pastes owing to the high SSA of LGCC.
- The mixture with a low material flow rate displayed a relatively high temperature increase after extrusion. The increase of material temperature induced by the extrusion process can accelerate the water loss of fresh mixture, consequently reducing the initial setting time.
- By increasing the amount of LGCC and LP in the binder with the same admixture addition, the initial setting time was decreased, whereas the  $SSA_{total}$  at 1 h and 3 h was increased. The  $SSA_{total}$  evolution may lead to the reduction of WFT and available PCEs for the dispersion, which appears to govern the stiffness development.
- The dilution effect on hydration and compressive strength was enhanced by the increase of LP and LGCC content. Due to the weak compressive strength, mixtures containing more than 75% of LF and LGCC in the binder may not be suitable to be employed as building materials. With the same addition of admixtures (1.5% SP+0.24% VMA), increasing the blend amount of LGCC and LP from 0% to 75% seemed to accelerate the alite hydration, possibly attributed to the consumption of PCEs induced by the hydrated aluminate products. However, mixture B90-1 showed an earlier sulfate depletion (before the dormant period) and a delayed and broad main hydration peak with much lower intensity compared to others, probably due to the high concentration of aluminate ions.
- The 0.5% SP increment (see Mixtures B75-2 and B90-2) led to the increase of material flow rate, extrudability and operation windows, initial setting time, the time to the main hydration peak, as well as the reduction of buildability and  $SSA_{total}$  at 3 h.

## REFERENCES

- [1] NEN-EN 196-2, *Method of testing cement - Part 2: Chemical analysis of cement*, (2013).
- [2] M. Antoni, J. Rossen, F. Martirena, and K. Scrivener, *Cement substitution by a combination of metakaolin and limestone*, *Cement and Concrete Research* **42**, 1579 (2012).
- [3] F. Avet, R. Snellings, A. Alujas Diaz, M. Ben Haha, and K. Scrivener, *Development of a new rapid, relevant and reliable (R3) test method to evaluate the pozzolanic reactivity of calcined kaolinitic clays*, *Cement and Concrete Research* **85**, 1 (2016).

- [4] S. Chaves Figueiredo, C. Romero Rodríguez, Z. Y. Ahmed, D. H. Bos, Y. Xu, T. M. Salet, O. Çopuroğlu, E. Schlangen, and F. P. Bos, *An approach to develop printable strain hardening cementitious composites*, *Materials and Design* **169**, 107651 (2019).
- [5] A. V. Rahul, M. Santhanam, H. Meena, and Z. Ghani, *3D printable concrete: Mixture design and test methods*, *Cement and Concrete Composites* **97**, 13 (2019).
- [6] D. Marchon, S. Kawashima, H. Bessaies-Bey, S. Mantellato, and S. Ng, *Hydration and rheology control of concrete for digital fabrication: Potential admixtures and cement chemistry*, *Cement and Concrete Research* **112**, 96 (2018).
- [7] Y. W. D. Tay, Y. Qian, and M. J. Tan, *Printability region for 3D concrete printing using slump and slump flow test*, *Composites Part B: Engineering* **174**, 106968 (2019).
- [8] A. Rahul, A. Sharma, and M. Santhanam, *A descriptivity-based approach for the assessment of phase separation during extrusion of cementitious materials*, *Cement and Concrete Composites* **108**, 103546 (2020).
- [9] ASTM C1506-09, *Standard Test Method for Water Retention of Hydraulic Cement-Based Mortars and Plasters*, (2009).
- [10] V. Nerella, M. Näther, A. Iqbal, M. Butler, and V. Mechtcherine, *Inline quantification of extrudability of cementitious materials for digital construction*, *Cement and Concrete Composites* **95**, 260 (2019).
- [11] G. Ma, Z. Li, and L. Wang, *Printable properties of cementitious material containing copper tailings for extrusion based 3D printing*, *Construction and Building Materials* **162**, 613 (2018).
- [12] T. T. Le, S. A. Austin, S. Lim, R. A. Buswell, A. G. Gibb, and T. Thorpe, *Mix design and fresh properties for high-performance printing concrete*, *Materials and Structures/Materiaux et Constructions* **45**, 1221 (2012).
- [13] NEN-EN 196-3, *Methods of testing cement. Part 3: Determination of setting times and soundness*, (2016).
- [14] N. Roussel, *Rheological requirements for printable concretes*, *Cement and Concrete Research* **112**, 76 (2018).
- [15] S. Mantellato, M. Palacios, and R. J. Flatt, *Relating early hydration, specific surface and flow loss of cement pastes*, *Materials and Structures/Materiaux et Constructions* **52**, 1 (2019).
- [16] E. Berodier and K. Scrivener, *Understanding the filler effect on the nucleation and growth of C-S-H*, *Journal of the American Ceramic Society* **97**, 3764 (2014).
- [17] NEN-EN 196-1, *Methods of testing cement - Part 1: Determination of strength*, (2016).
- [18] J. M. Justice and K. E. Kurtis, *Influence of metakaolin surface area on properties of cement-based materials*, *Journal of Materials in Civil Engineering* **19**, 762 (2007).

- [19] N. Nair, K. Mohammed Haneefa, M. Santhanam, and R. Gettu, *A study on fresh properties of limestone calcined clay blended cementitious systems*, *Construction and Building Materials* **254**, 119326 (2020).
- [20] R. Sposito, N. Beuntner, and K.-C. Thienel, *Characteristics of calcined clay particles and their influence on the efficiency of superplasticizers*, *Cement and Concrete Composites* **110**, 103594 (2020).
- [21] B. H. Zaribaf and K. E. Kurtis, *Admixture compatibility in metakaolin–portland-limestone cement blends*, *Materials and Structures/Materiaux et Constructions* **51**, 1 (2018).
- [22] M. Palacios and R. J. Flatt, *Working mechanism of viscosity-modifying admixtures*, in *Science and Technology of Concrete Admixtures*, Vol. i (Elsevier Ltd, 2015) pp. 415–432.
- [23] C. D. Hatch, J. S. Wiese, C. C. Crane, K. J. Harris, H. G. Kloss, and J. Baltrusaitis, *Water adsorption on clay minerals as a function of relative humidity: Application of BET and Freundlich adsorption models*, *Langmuir* **28**, 1790 (2012).
- [24] H. Bessaies-Bey, M. Palacios, E. Pustovgar, M. Hanafi, R. Baumann, R. J. Flatt, and N. Roussel, *Non-adsorbing polymers and yield stress of cement paste: Effect of depletion forces*, *Cement and Concrete Research* **111**, 209 (2018).
- [25] N. Roussel, H. Bessaies-Bey, S. Kawashima, D. Marchon, K. Vasilic, and R. Wolfs, *Recent advances on yield stress and elasticity of fresh cement-based materials*, *Cement and Concrete Research* **124**, 105798 (2019).
- [26] R. J. Flatt, D. Larosa, and N. Roussel, *Linking yield stress measurements: Spread test versus Viskomat*, *Cement and Concrete Research* **36**, 99 (2006).
- [27] A. W. Saak, H. M. Jennings, and S. P. Shah, *A generalized approach for the determination of yield stress by slump and slump flow*, *Cement and Concrete Research* **34**, 363 (2004).
- [28] M. Chen, L. Yang, Y. Zheng, Y. Huang, L. Li, P. Zhao, S. Wang, L. Lu, and X. Cheng, *Yield stress and thixotropy control of 3D-printed calcium sulfoaluminate cement composites with metakaolin related to structural build-up*, *Construction and Building Materials* **252**, 119090 (2020).
- [29] B. Panda, S. Ruan, C. Unluer, and M. J. Tan, *Improving the 3D printability of high volume fly ash mixtures via the use of nano attapulgite clay*, *Composites Part B: Engineering* **165**, 75 (2019).
- [30] Y. Weng, M. Li, M. J. Tan, and S. Qian, *Design 3D printing cementitious materials via Fuller Thompson theory and Marson-Percy model*, *Construction and Building Materials* **163**, 600 (2018).



- [31] C. Zhang, Z. Hou, C. Chen, Y. Zhang, V. Mechtcherine, and Z. Sun, *Design of 3D printable concrete based on the relationship between flowability of cement paste and optimum aggregate content*, *Cement and Concrete Composites* **104**, 103406 (2019).
- [32] H. Huang, T. Huang, Q. Yuan, D. Zhou, D. Deng, and L. Zhang, *Temperature dependence of structural build-up and its relation with hydration kinetics of cement paste*, *Construction and Building Materials* **201**, 553 (2019).
- [33] F. Dalas, S. Pourchet, D. Rinaldi, A. Nonat, S. Sabio, and M. Mosquet, *Modification of the rate of formation and surface area of ettringite by polycarboxylate ether superplasticizers during early C3A-CaSO<sub>4</sub> hydration*, *Cement and Concrete Research* **69**, 105 (2015).
- [34] J. W. Bullard, H. M. Jennings, R. A. Livingston, A. Nonat, G. W. Scherer, J. S. Schweitzer, K. L. Scrivener, and J. J. Thomas, *Mechanisms of cement hydration*, *Cement and Concrete Research* **41**, 1208 (2011).
- [35] A. Zingg, F. Winnefeld, L. Holzer, J. Pakusch, S. Becker, R. Figi, and L. Gauckler, *Interaction of polycarboxylate-based superplasticizers with cements containing different C3A amounts*, *Cement and Concrete Composites* **31**, 153 (2009).
- [36] F. Zunino and K. Scrivener, *The influence of the filler effect on the sulfate requirement of blended cements*, *Cement and Concrete Research* **126**, 105918 (2019).
- [37] F. Zunino and K. Scrivener, *The reaction between metakaolin and limestone and its effect in porosity refinement and mechanical properties*, *Cement and Concrete Research* **140**, 106307 (2021).
- [38] S. T. Bergold, F. Goetz-Neunhoeffer, and J. Neubauer, *Interaction of silicate and aluminate reaction in a synthetic cement system: Implications for the process of alite hydration*, *Cement and Concrete Research* **93**, 32 (2017).
- [39] A. Quennoz and K. L. Scrivener, *Interactions between alite and C3A-gypsum hydrations in model cements*, *Cement and Concrete Research* **44**, 46 (2013).
- [40] F. Zunino and K. Scrivener, *Factors influencing the sulfate balance in pure phase C3S/C3A systems*, *Cement and Concrete Research* **133**, 106085 (2020).
- [41] J. J. Chen and A. K. Kwan, *Superfine cement for improving packing density, rheology and strength of cement paste*, *Cement and Concrete Composites* **34**, 1 (2012).
- [42] W. W. Fung and A. K. Kwan, *Role of water film thickness in rheology of CSF mortar*, *Cement and Concrete Composites* **32**, 255 (2010).
- [43] L. G. Li and A. K. Kwan, *Concrete mix design based on water film thickness and paste film thickness*, *Cement and Concrete Composites* **39**, 33 (2013).
- [44] H. Liu, X. Sun, H. Du, H. Lu, Y. Ma, W. Shen, and Z. Tian, *Effects and threshold of water film thickness on multi-mineral cement paste*, *Cement and Concrete Composites* **112**, 103677 (2020).

- [45] K. Vance, M. Aguayo, T. Oey, G. Sant, and N. Neithalath, *Hydration and strength development in ternary portland cement blends containing limestone and fly ash or metakaolin*, *Cement and Concrete Composites* **39**, 93 (2013).
- [46] P. Nanthagopalan, M. Haist, M. Santhanam, and H. S. Müller, *Investigation on the influence of granular packing on the flow properties of cementitious suspensions*, *Cement and Concrete Composites* **30**, 763 (2008).
- [47] H. H. Wong and A. K. Kwan, *Packing density of cementitious materials: Part 1-measurement using a wet packing method*, *Materials and Structures/Materiaux et Constructions* **41**, 689 (2008).
- [48] L. G. Li and A. K. Kwan, *Mortar design based on water film thickness*, *Construction and Building Materials* **25**, 2381 (2011).
- [49] G. Gelardi and R. J. Flatt, *Working mechanisms of water reducers and superplasticizers*, in *Science and Technology of Concrete Admixtures*, Vol. 2 (Elsevier Ltd, 2015) pp. 257–278.
- [50] R. J. Flatt and Y. F. Houst, *A simplified view on chemical effects perturbing the action of superplasticizers*, *Cement and Concrete Research* **31**, 1169 (2001).
- [51] J. Plank, Z. Dai, and P. R. Andres, *Preparation and characterization of new Ca-Al-polycarboxylate layered double hydroxides*, *Materials Letters* **60**, 3614 (2006).
- [52] D. Marchon, P. Juilland, E. Gallucci, L. Frunz, and R. J. Flatt, *Molecular and submolecular scale effects of comb-copolymers on tri-calcium silicate reactivity: Toward molecular design*, *Journal of the American Ceramic Society* **100**, 817 (2017).
- [53] R. J. Flatt, *Towards a prediction of superplasticized concrete rheology*, *Materials and Structures/Materiaux et Constructions* **37**, 289 (2004).
- [54] D. Marchon and R. J. Flatt, *Impact of chemical admixtures on cement hydration*, in *Science and Technology of Concrete Admixtures* (Elsevier Ltd, 2015) pp. 279–304.
- [55] J. Lapeyre and A. Kumar, *Influence of pozzolanic additives on hydration mechanisms of tricalcium silicate*, *Journal of the American Ceramic Society* **101**, 3557 (2018).
- [56] J. Skibsted and R. Snellings, *Reactivity of supplementary cementitious materials (SCMs) in cement blends*, *Cement and Concrete Research* **124**, 105799 (2019).

# 4

## EFFECT OF VISCOSITY MODIFYING ADMIXTURE ON FRESH-STATE BEHAVIORS AND HARDENED PROPERTIES

*In 3D concrete printing (3DCP), it is necessary to meet contradicting rheological requirements: proper fluidity during pumping and extrusion, and high stability and viscosity at rest to build the layered structure. A combination of viscosity-modifying admixture (VMA) and superplasticizer was used for that purpose. In this case, controlling the competitive effects between VMA and superplasticizer becomes critical. The main strategy for 3D printing in this study was to add an optimal dosage of VMA in the solid suspension that was already mixed with water and superplasticizer. A series of tests was performed to characterize the effects of VMA on fresh-state behaviors, 3D printability, and hardened properties. Experiments performed in this chapter showed that the mixture containing 0.24% (of the binder mass) of VMA exhibited satisfactory 3D printability and optimal mechanical performance.*

## 4.1. INTRODUCTION

MANY printable mixtures developed earlier [2–6] contained both superplasticizer and viscosity-modifying admixture (VMA). Superplasticizer in cementitious materials could contribute to increasing flowability at a constant solids content for facilitating the casting, pumping, and extrusion in 3DCP [7]. A small dosage of VMA has been used to replace the fine content (fly ash, silica fume, or limestone) in self-compacting concrete [8] in order to enhance cohesion, stability, and viscosity [9]. Previous studies [2, 4, 6] have demonstrated that addition of VMA could significantly improve the printability of solid suspensions through adjusting the yield stress and plastic viscosity. As explained by Reiter et al. [10], VMA could enhance flocculation of cement grains through providing more contacts and bridges between cement particles, which will promote the evolution of green strength for the deposited layers. VMA can also ensure extrudability since it reduces water drainage of the cementitious materials [6, 11].

Hydroxypropyl methylcellulose (HPMC) is one of the most widespread cellulose-derivative VMAs applied in practice [12]. Many studies have attempted to utilize a combination of HPMC and superplasticizer to develop printable cementitious materials [2, 5, 6, 13, 14]. However, most of them overlook the fact that the HPMC could compete with superplasticizer to adsorb onto cement or other fine particles, thereby affecting the dispersion of superplasticizer. Besides, the competitive effects between HPMC and superplasticizer in a suspension may increase the yield stress and apparent viscosity, which will result in a significant increase in extrusion pressure. This impact may be suitable for buildability, whereas it adversely affects extrudability. The dosage of VMA becomes very critical in this context.

This chapter proposes a strategy to utilize the HPMC-based VMA for developing limestone and calcined clay-based printable cementitious materials, specifically, by adding an optimal dosage of VMA in the fresh mixture. For developing printable cementitious materials in the laboratory, a series of tests were conducted to investigate the effects of VMA dosages on the fresh state behavior of 3DCP, including flowability, extrudability, open time, buildability, and green strength. Furthermore, the impacts on the hydration, mechanical performance, and air void content were determined via isothermal calorimetry, compressive strength (7 days) testing, and X-ray computed tomography scanning.

## 4.2. MATERIALS AND METHODS

### 4.2.1. RAW MATERIALS AND MIX DESIGNS

ALL raw materials are the same as presented in Section 3.2.1, Chapter 3. The mix designs are given in Table 4.1. In the current study, all mixture compositions were kept identical except the VMA dosage, which varied from 0 to 0.48% by mass of binder. The binder, which amounted to about 35.5 wt.% of the total mass in all mixtures, contained 40 wt.% of Portland cement (PC), 40 wt.% of low-grade calcined clay (LGCC) and 20 wt.% of limestone (LP). The fresh mixtures were prepared using a planetary mixer (HOBART) by following the procedures given in Table 3.3.

Table 4.1: Mix designs of cementitious materials (% of the binder mass).

Type	PC	LGCC	LP	Sand	Water	SP	VMA
Ref	40	40	20	150	30	2	0
1.2VMA	40	40	20	150	30	2	0.14
2VMA	40	40	20	150	30	2	0.24
4VMA	40	40	20	150	30	2	0.48

#### 4.2.2. FLOWABILITY TEST

The test procedure was the same as in Section 3.2.3, Chapter 3. For each mixture, this test was performed for each material age from 10 min to 120 min, with intervals of 10 min. The fresh materials were sealed in a plastic bag to prevent evaporation of water. Three repetitions were conducted for each test.

#### 4.2.3. EVALUATION OF 3D PRINTABILITY

3D printability tests were conducted by the 3DCP setup, which has been introduced by Section 3.2.2, Chapter 3. A hybrid down- and back-flow nozzle with a rectangle-opening of  $40 \times 13.5 \text{ mm}^2$  was utilized in this study (see Figure 4.1).

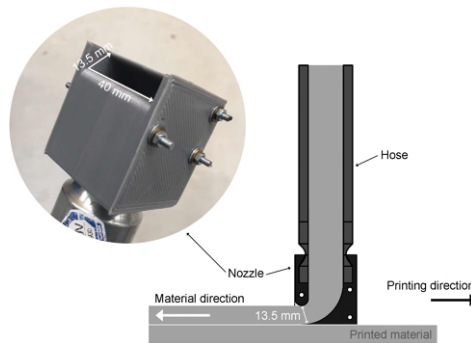


Figure 4.1: Schematic section of the hybrid back- and down-flow nozzle.

#### EXTRUDABILITY TEST

12 L of the fresh mixture were prepared according to Table 3.3 and then poured into the hopper of the pump. Different material flow rates were applied through the controller of the pump. The pressures were recorded under different material flow rates. The test was performed at the material age of 10 min. In this study, the nozzle moving speed was kept equal with the linear flow rate of the materials ( $V_{linear}$ ) that could be calculated through Eq 3.2.

#### OPEN TIME TEST

One filament (length: 800 mm and width: 40 mm) was printed at different material ages. The material flow rate and the nozzle moving speed were kept identical to the speeds of

the extrudability test. The test started at the resting time of 30 min with a time gap of 10 min, and it was not terminated until the disruption of filament occurred. To ensure that the fresh mixture remained in the dynamic state, a pre-pumping/shearing session was designed before printing the filament (see Figure 4.2). Shape retention was checked by measuring the width of the printed segments using a vernier caliper. The shape retention ratio ( $S_1$ ) was introduced by Bong et al. [15] as:

$$S_1 = \frac{W_f}{W_n} \tag{4.1}$$

where  $W_f$  is the measured width of the extruded filament, and  $W_n$  is the width of the nozzle opening. The closer the value of  $S_1$  to 1, the better the shape retention.

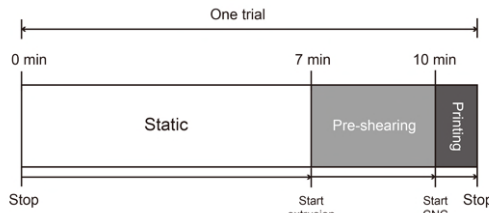


Figure 4.2: Stages of a typical trial for printing a single filament.

#### BUILDABILITY TEST

The assessment of buildability was based on the layer settlement test from Kazemian et al. [5]. One object containing five stacked layers was printed at a fixed time interval of about 40 s. The nozzle standoff distance was kept as 0 mm during printing, which could ensure the same layer thickness of 13.5 mm. The five-layer object was designed to have 900 mm in length, 40 mm in width, and 67.5 mm in height. The test started at the material age of 30 min and finished before the end of open time. The printing speed (material flow rate and nozzle moving speed) was kept the same as the operation speeds used in extrudability and open time tests. The height of deposited layers ( $H$ ) was measured to calculate the shape stability ratio ( $S_2$ ) through:

$$S_2 = \frac{H}{h} \tag{4.2}$$

where  $h$  denotes the designed height of the five-layer object.

#### 4.2.4. GREEN STRENGTH TEST

The green strength test was performed to determine the strength development within the first 4 h for the mixtures incorporating VMA. The test procedure was the same as in studies [16, 17]. The fresh mixtures were prepared and then poured into cylindrical molds with a 33.5 mm internal diameter and 67.5 mm height. A silicon spray was initially

used to coat the molds before filling the fresh mortar. All samples were compacted on a vibration table at a frequency of 30 Hz for 10 s to reduce the amount of air bubbles. The samples were then stored in a sealed plastic bag and demolded right before the green strength testing. The servo-hydraulic Instron 8872 machine was used to perform the green strength tests. Both sides of a sample were covered by a double layer plastic film. In order to reduce the friction between the sample and base plates, Polytetrafluoroethylene was sprayed between two layers of plastic. The tests were performed using displacement control with a rate of 0.2 mm/s until reaching the maximum displacement of 20 mm. The entire test was recorded by a Canon camera model EOS 6D with a Tamron aspherical 28-75 mm lens. Vertical and lateral deformations of each sample were analyzed by a freeware image analysis software ImageJ. A MATLAB-code was employed to measure the change of cross-section of the sample. Each mixture was tested at the ages of 30, 45, 60, 90, 150, and 240 min. Three repetitions were conducted for each age.

#### 4.2.5. ISOTHERMAL CALORIMETRY TEST

The test procedure was the same as in Section 3.2.5, Chapter 3.

#### 4.2.6. COMPRESSIVE STRENGTH TEST

The printed samples were sawn from the printed object that was manufactured in the section of Buildability test. Note that, the fresh mixtures in this study showed low slump during layer deposition. Thus, the printed filament was wider than the nozzle opening (40 mm). 40 mm cube specimens were sawn from the 3D printed prisms before performing the test. Due to the anisotropic mechanical properties of the printed mortar [18–20], the printed samples were tested in X, Y, and Z direction (see Figure 4.3), and the average value was calculated through 5 repeated tests in each direction. Thus, for each mixture, 15 printed samples were prepared and tested in total. The cast samples of mixture Ref were also prepared and tested. All samples had a dimension of  $40 \times 40 \times 40$  mm<sup>3</sup> and were cured in a fog room ( $20 \pm 2$  °C, 99% RH). Compressive strength at 7 days was measured conforming NEN-EN 196-1 [21] at a loading rate of 2.4 kN/s.

#### 4.2.7. X-RAY COMPUTED TOMOGRAPHY SCANNING

X-ray computed tomography (CT) scanning was used to investigate the air void content and distribution within samples printed using different mixtures. Small cylindrical samples with a 25 mm diameter and 24 mm height were drilled and sawn from the printed objects (From top to bottom: the second and third layers were sawn from the cored sample that contained 5 layers) in the section of buildability test. A Phoenix Nanotom Micro CT-Scanner was used for scanning. 1441 images were acquired on a digital GE DXR detector ( $3072 \times 2400$  pixels). The theoretical spatial resolution was  $13.3 \times 13.3 \times 13.3$  μm<sup>3</sup>/voxel. The reconstruction was performed using the Phoenix Datas|x software. A cylindrical region of interest (ROI), which was selected at the area of the two-layer interface, was extracted from the sample for the air void analysis. The obtained image stack with the top view of the cylindrical ROI was analyzed via Trainable Weka Segmentation (TWS) from ImageJ (more information: [22, 23]). The air voids from each image were isolated and measured.

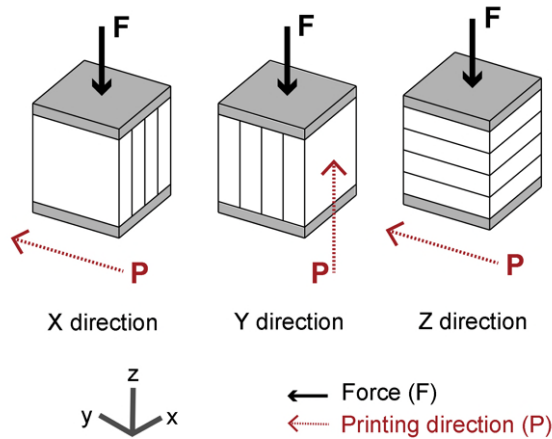


Figure 4.3: Schematic diagram of loading directions for performing the compressive strength test on printed samples.

## 4.3. RESULTS AND DISCUSSION

### 4.3.1. FLOWABILITY

FIGURE 4.4 shows the results of the slump flow test of mixture Ref at different ages within the first 2 h. It could be recognized that the evident workability loss started after the resting time of 40 min. Between 50 min and 90 min, the spread diameter could still reach the value of 300 mm after the table dropped 25 times. However, after 90 min, a notable reduction in flowability was observed, which was likely due to the C-S-H bridges between particles forming a percolated rigid network in the material, as suggested by Roussel et al. [24]. This network of interacting particles is still fragile under a relatively high shear force. However, the table dropping process may not be able to supply sufficient shear energy to break all these inter-particle connections [24, 25].

Figure 4.5 provides the results of the slump and slump flow tests at different ages within the first 2 h. After a specific resting time, increasing the VMA dosage in the mixture could contribute to retaining the shape and height of the demolded sample. Mixture 4VMA showed nearly zero-slump (Figure 4.5(a)). All mixtures demonstrated enhanced shape stability with time. Compared with mixture 1.2VMA, mixture 2VMA presented slightly better shape retention before the age of 90 min. As shown in Figure 4.5(b), the spread diameter of all mixtures decreases with time. Thus, the workability of fresh mixtures decreases with increasing the resting time, which could be attributed to the gradual development of stiffness of the fresh mixture. Mixtures 1.2VMA and 2VMA demonstrated larger spread diameter at any specific age compared with mixture 4VMA. The effects on fluidity were not apparent when increasing the dosage of VMA from 0.14% to 0.24%. However, once the VMA content reached 0.48%, the flowability of fresh mixture was significantly reduced.

### 4.3.2. 3D PRINTABILITY



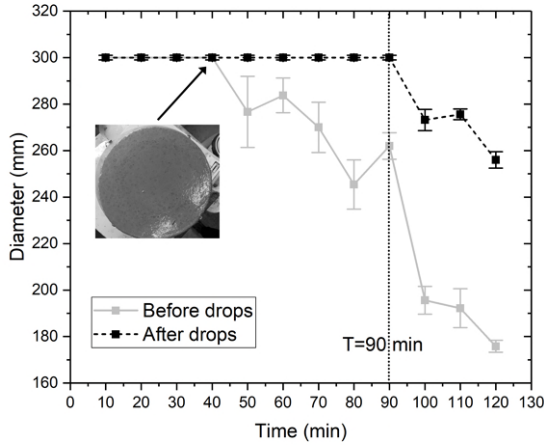
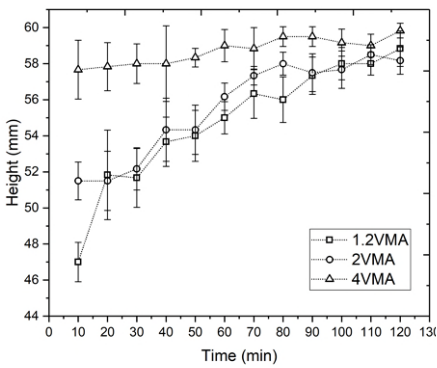
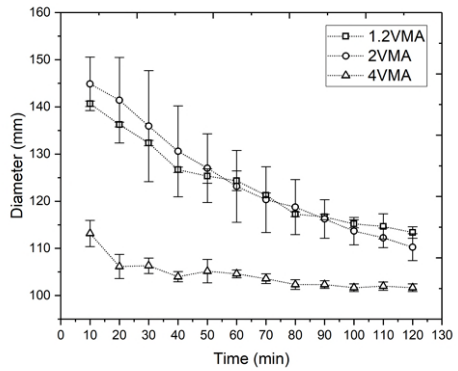


Figure 4.4: The slump flow test results of mixture Ref.



(a)



(b)

Figure 4.5: Flowability test results of mixtures with different VMA contents: (a) Height (before dropping the table) and (b) Spread diameters (after dropping the table for 25 times) of demolded samples varied with different material ages.

## EXTRUDABILITY

Figure 4.6 shows the results of extrudability tests of mixtures 1.2VMA, 2VMA, and 4VMA. With the increase of material flow rate, all mixtures lead to a larger extrusion pressure. A shear-thinning behavior for mixtures 1.2VMA and 2VMA can be recognized. It is evident that the mixture containing a higher dosage of VMA requires higher extrusion pressure to reach a similar material flow rate compared to mixtures containing lower dosages of VMA. A significant difference in extrusion pressure between 4VMA and 2VMA is quite clear. Due to the limitation of extrusion pressure (Maximum: 30 bar), mixture 4VMA could not be conveyed with more than 0.65 L/min of the material flow rate. For mixtures 1.2VMA and 2VMA, a material flow rate of 1.45 L/min was selected to ensure the fresh mixture conveyed stable and consistently without surface ruptures. The nozzle moving speed was calculated according to Eq 3.2 before performing the extrudability test. Finally, the nozzle moving speed was selected as 2700 mm/min for mixtures 1.2VMA and 2VMA and 1200 mm/min for mixture 4VMA.

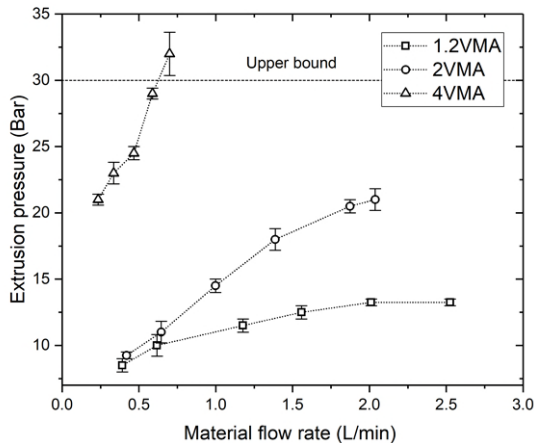


Figure 4.6: The extrudability test results for mixtures 1.2VMA, 2VMA, and 4VMA. 1 bar = 0.1 MPa.

## OPEN TIME

Results of the open time test are presented in Table 4.2 and Figure 4.7. The filaments extruded at different ages were collected to demonstrate the change of printing quality with time. The open time for mixture 4VMA with the printing speed  $V_{p1}$  (material flow rate: 0.65 L/min; nozzle moving speed: 1200 mm/min) was found to be 50 min. The open time of 1.2VMA and 2VMA with the printing speed  $V_{p2}$  (material flow rate: 1.45 L/min; nozzle moving speed: 2700 mm/min) was found to be 90 min and 70 min, respectively. Besides, the width changes of the extruded filament with time are given in Figure 4.8. Shape retention ratios ( $S_1$ ), calculated using Eq 4.1, were employed to describe the accuracy of printing. Values of  $S_1 > 1$  were observed at a relatively early age since the fresh mixture showed low slump at the beginning. The extruded filament was

thus wider than the nozzle opening. When  $S_1$  approached 1, the extruded filament presented a nearly accurate dimension. Values of  $S_1 < 1$  were caused by two factors. First, with the time passing, the material got stuck in the interior walls of the nozzle (see Figure 4.9), which led to thinner filaments. Second, the rheology of fresh mixtures was also changing with time due to the particle flocculation and nucleation process. Once the real material flow rate became much lower than the nozzle moving speed, the width of the filament was reduced, and disruption occurred.

Table 4.2: Open time of different mixtures.

Mixture	Open time (min)
1.2VMA	90
2VMA	70
4VMA	50

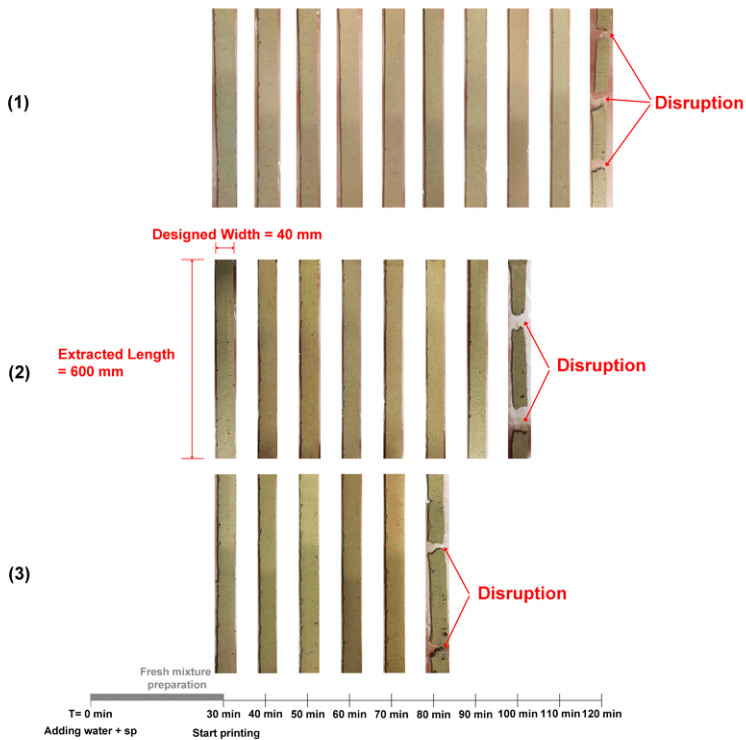


Figure 4.7: Open time test results: (1) Mixture 1.2VMA; (2) Mixture 2VMA; (3) Mixture 4VMA.

## BUILDABILITY

Mixtures 1.2VMA, 2VMA, and 4VMA were used to print a five-layer object (see Figure 4.10) with the time interval of 40 s (between two subsequent layers). The test session

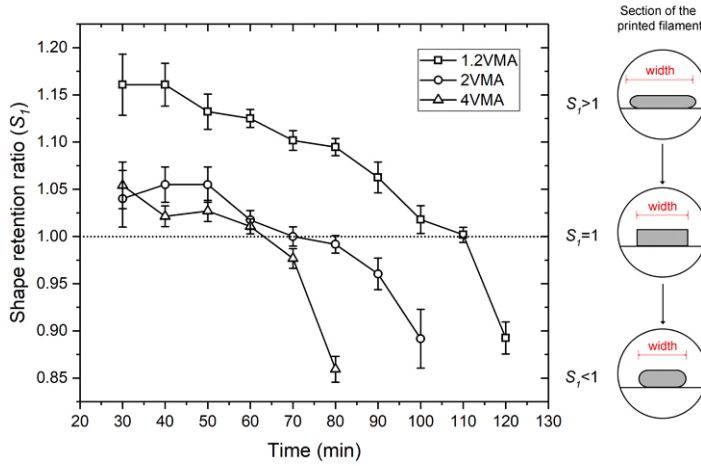


Figure 4.8: Shape retention ratios of mixtures 1.2VMA, 2VMA, and 4VMA at different ages.

started at the material age of 30 min. Figure 4.11 illustrates that shape stability could be enhanced by increasing the percentage of VMA from 0.14% to 0.48%. Mixture 4VMA showed the optimal buildability, and the value of  $S_2$  was close to 0.90. The shape stability of mixture 2VMA was very close to that of mixture 4VMA and much better than mixture 1.2VMA. The deformation of a sample printed using 1.2VMA was evidently larger than that of other mixtures. Figure 4.11 also demonstrates that the cross-section of printed samples of 2VMA and 4VMA had similar bell shapes.



Figure 4.9: The stiff material got stuck in the nozzle during the waiting period of the open time test, which is one of the reasons to restrict the printed amount.

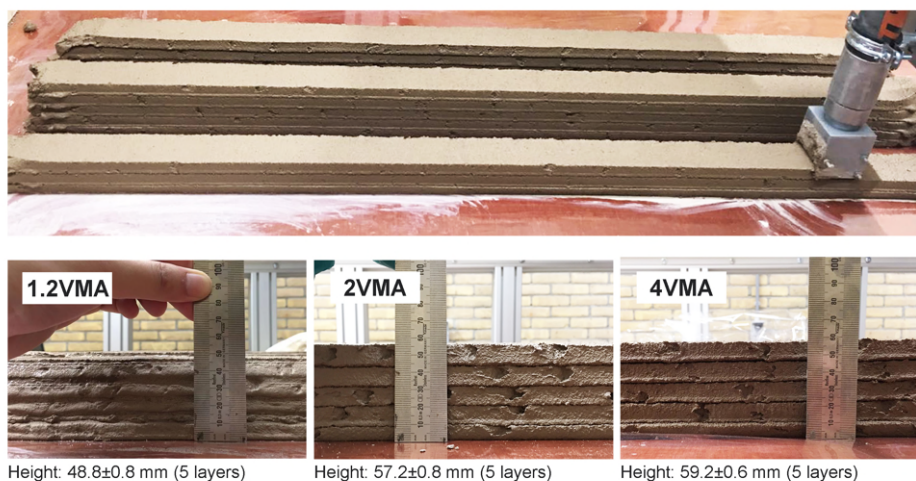


Figure 4.10: Buildability tests of mixtures 1.2VMA, 2VMA, and 4VMA.

#### 4.3.3. GREEN STRENGTH

The green strength development within the first 4 h could be used as an indicator of the proper structural build-up of the mixture. With the help of ImageJ and a MATLAB code, the change of the cross-sectional area was recorded. The average strain/true stress curves of mixtures 1.2VMA, 2VMA, and 4VMA from the age of 30 min to 240 min are given in Figure 4.12. All curves for the 1.2VMA mixture showed a similar pattern. It has been observed that the stress linearly increased with the growth of strain until to reach a certain plateau. For mixtures 2VMA and 4VMA, the samples with younger ages (30 min - 90 min) showed behavior similar to that of the mixture 1.2VMA, whereas older specimens (150 min - 240 min) showed strain softening after the peak value. Figure 4.13 may explain this phenomenon. The samples with a resting time from 30 min to 90 min failed with a barreling effect. Distinct cracks could only be observed during testing of older samples (150 min - 240 min). This is in accordance with the published literature [3, 16, 26]. In Figure 4.12(d), green strength of each test (defined as the peak stress of each curve) is plotted. The green strengths of mixtures 2VMA and 4VMA within the first 4 h were quite close and much higher than mixture 1.2VMA. Mixture 4VMA showed a slightly higher value compared with the mixture 2VMA until the material age of 2.5 h.

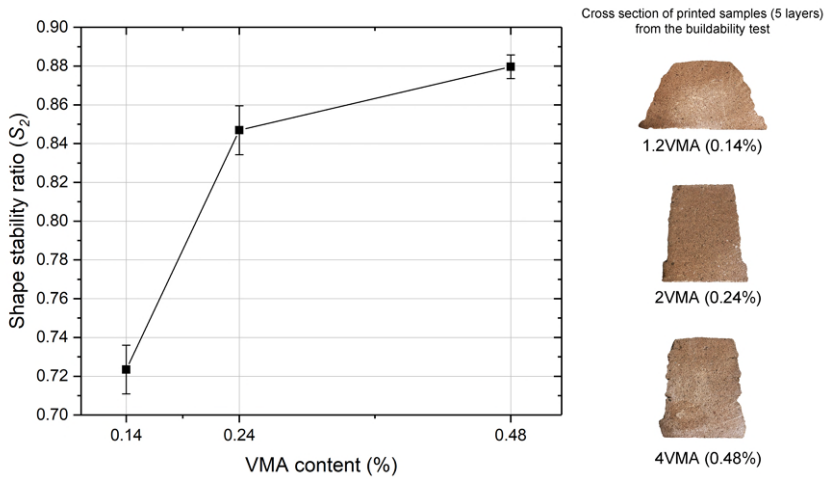


Figure 4.11: Shape stability ratio of mixtures with different VMA contents (measured at 45 min of the resting time).

#### 4.3.4. ISOTHERMAL CALORIMETRY

The normalized heat flow and cumulative heat results are given in Figure 4.14. The results are plotted up to 7 days (168 h). It was found that the normalized heat flow curve pattern of mixtures Ref, 1.2VMA, 2VMA, and 4VMA is almost the same in Figure 4.14(a). All of them showed the main hydration peak after the dormant period, a shoulder (second peak) that may be attributed to the depletion of sulfate, and a small slope (third peak) due to the formation of AFm phases [27]. With the increase of VMA dosage: (1) the reaction speed was slightly reduced in the acceleration stage; (2) the time at which the main hydration peak occurs was delayed; (3) the intensity of the main hydration peak was decreased; (4) the intensity of the second peak was decreased, and less impact was observed on the third peak among mixtures containing VMA. As shown in Figure 4.14(b), the highest cumulative heat was released in mixture Ref, while the addition of VMA led to a decrease in the cumulative heat released in the first 7 days of hydration.

The impact of cellulose-derivative VMAs on cement hydration has been reported by [23, 28–30]. It has been found that the cellulose-derivative VMAs have very limited adsorption capability on anhydrous phases like  $C_3S$ , thus having less influence on the growth rate of C-S-H [28]. Many researchers [28, 29, 31] believe that the main reason for delaying hydration by the cellulose-derivative VMAs is the adsorption onto hydrated phases, including C-S-H and portlandite. Pourchez et al. [29] explained that the cellulose-derivative VMAs acts strongly on the C-S-H precipitation by a three-step process: first, a reduction of the quantity of the initial C-S-H seeds; second, a retardation to form the C-S-H shell around the  $C_3S$ ; and finally, the formation of a thicker and permeable C-S-H layer.

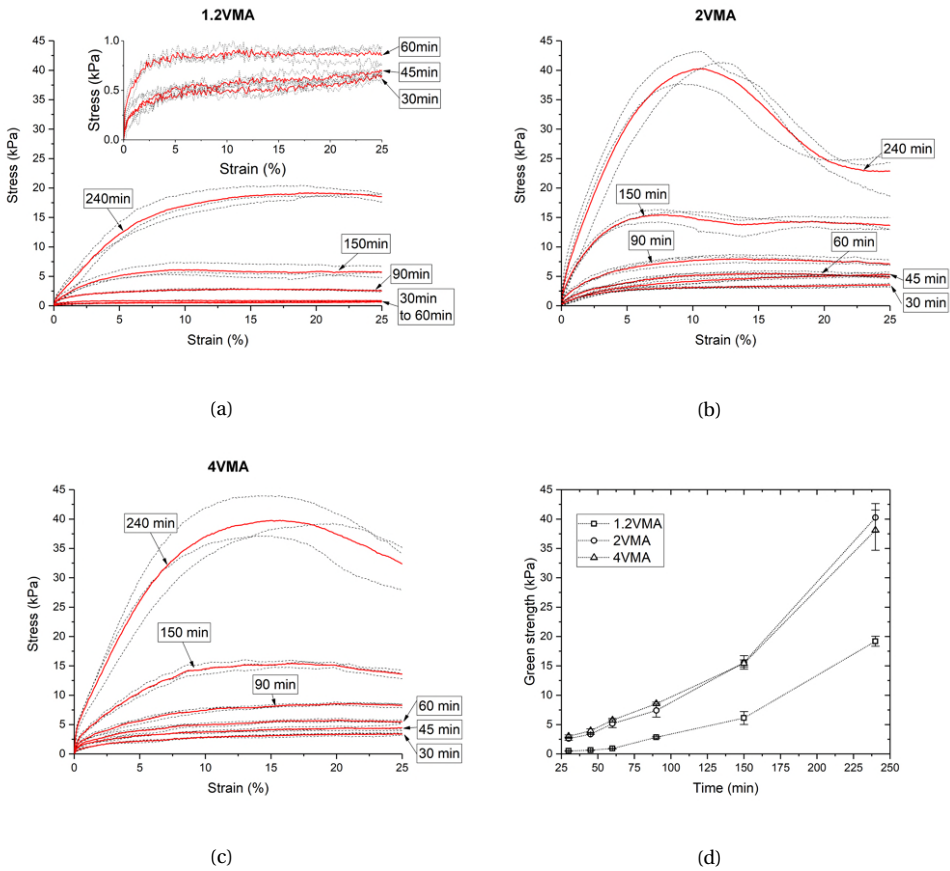


Figure 4.12: (a) The stress/strain curve of mixture 1.2VMA; (b) The stress/strain curve of mixture 2VMA; (c) The stress/strain curve of mixture 4VMA. The black dashed lines indicate the individual test results, and the red curves represent the average stress and strain relation. (d) Comparison of green strength development of mixtures 1.2VMA, 2VMA, and 4VMA.

### 4.3.5. COMPRESSIVE STRENGTH

Figure 4.15(a) shows the extracted areas from the printed objects that were made in the section of buildability test for preparing  $40 \times 40 \times 40 \text{ mm}^3$  samples. According to the test results shown in Figure 4.15(b), printed samples for all mixtures were stronger in the loading direction Y compared to X and Z directions (see Figure 4.3). Similar compressive strength results of printed cementitious materials were reported by [19, 32–34]. The distinct mechanical anisotropy of printed samples might be due to the weak interface and the printing quality. As explained by Panda et al. [34], the motion pattern of material in the printing process might be the main reason for the anisotropic property. The direction Y is the same as the direction of printing. Compared to the other directions (X and Z), the particles in the Y direction might be better placed and compacted. Besides, Nerella et al. [18] identified that the compaction due to the layer weight should also be taken into consideration for the variation of compressive



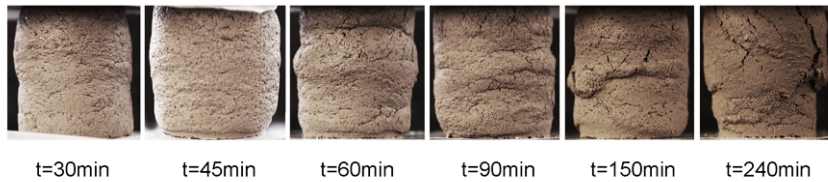


Figure 4.13: Damaged samples of mixture 2VMA at different material ages.

strength. Mixture 2VMA showed the best compressive strength at 7 days in three different directions, compared with mixtures 1.2VMA and 4VMA. However, the mixtures modified by VMA exhibited lower compressive strength than mixture Ref, which agrees well with the result of isothermal calorimetry.

#### 4.3.6. AIR VOID CONTENT AND DISTRIBUTION

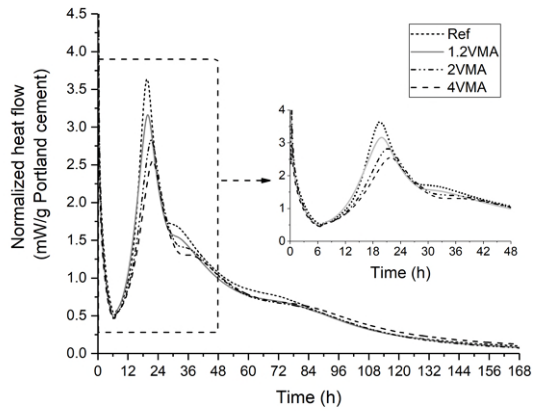
The grayscale images obtained from CT scanning are shown in Figure 4.16(a). In all mixtures, the majority of large air voids can be observed in the interface region. 800 images in ROI from top to the bottom of the cylindrical sample were selected to measure the 2D void content using ImageJ, and the results are given in Figure 4.16(b). Air voids smaller than 5 pixels were neglected to avoid the effect of measurement noise. According to Figure 4.16(a), the interface of the sample 1.2VMA in the cross-section from the front view was of parabolic shape, unlike the relatively straight line in samples 2VMA and 4VMA. This is confirmed by the results presented in Figure 4.16(b). There are two peak values of sample 1.2VMA, which may be attributed to the weak buildability of the 1.2VMA mixture. The severe layer deformation that occurred during the printing process leads to the interface not being on the same horizontal plane. This is also visible in Figure 4.11.

Compared with samples 2VMA and 4VMA, sample 1.2VMA contained a higher amount of relatively large air voids at the interface (see Figure 4.16(c)). However, sample 4VMA showed the highest cumulative void area around the interface. The number of large voids in sample 4VMA was not comparable with sample 1.2VMA based on visual inspection, whereas smaller pores were well-distributed in both the interface and the printed layers. Due to the limits in extrusion pressure, a lower printing speed was used for printing the sample of mixture 4VMA. The extruded filament of mixture 4VMA could therefore be less compacted than the others. Besides, many air voids remained and stabilized in the highly viscous cementitious materials during the mixing process [23, 35]. That could be one of the reasons for the porous structure of the printed sample of mixture 4VMA in Figure 4.16(a).

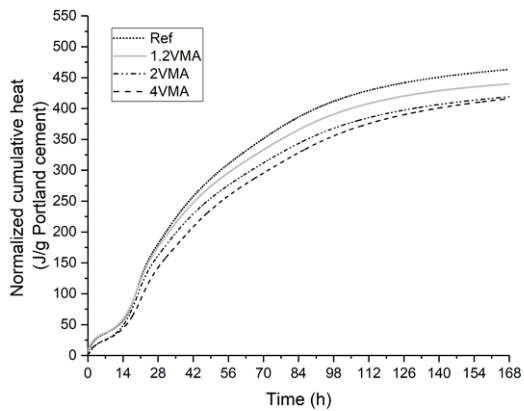
Overall, the sample of mixture 2VMA displayed the densest microstructure and the smallest void content among all studied mixtures, which could explain why mixture 2VMA showed the highest compressive strength at 7 days. However, it should be clarified that findings reported in this section are only based on one sample for each mixture. Further study is needed to ensure the accuracy and reliability of the findings.

Considering the retardation of hydration that occurs when using 0.48% of VMA, it



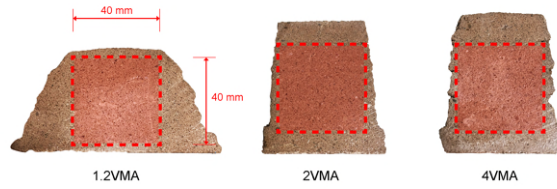


(a)

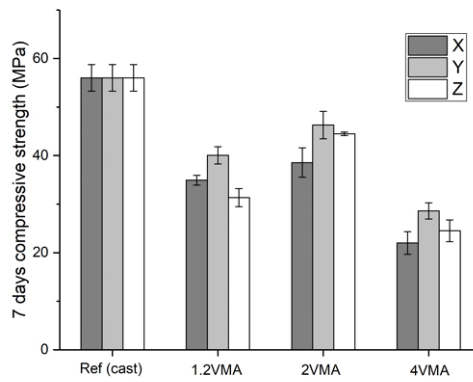


(b)

Figure 4.14: Isothermal calorimetry test results: (a) Normalized heat flow with time, and (b) Normalized cumulative heat with time.

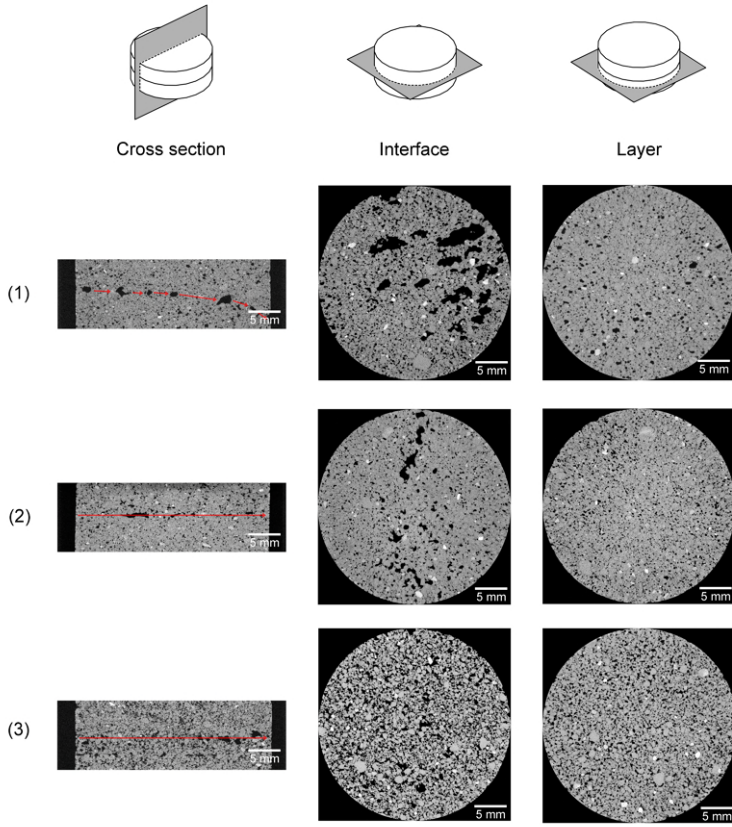


(a)

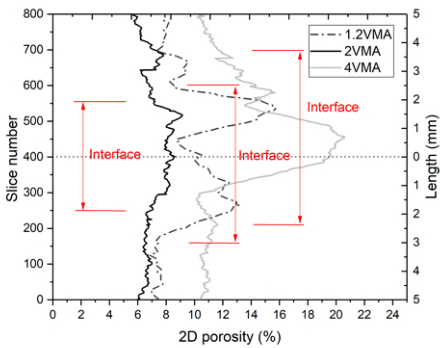


(b)

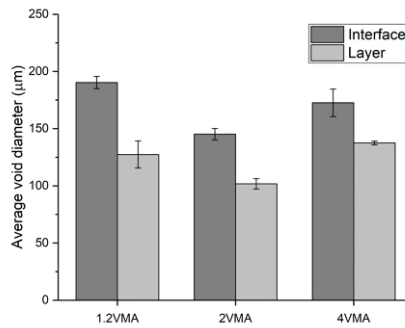
Figure 4.15: (a) Extracted areas from the printed samples for performing compressive strength tests. (b) Compressive strength at the age of 7 days.



(a)



(b)



(c)

Figure 4.16: (a) The grayscale images of the cross-section from the front view, the interface from the top view, and the layer from the top view: (1) Sample 1.2VMA; (2) Sample 2VMA; (3) Sample 4VMA. (b) 2D void content (porosity) from top to bottom of ROI; (c) The average air void diameter of the interface and layer.

might be reasonable to expect that the mixture 4VMA will have the lowest compressive strength. However, the retardation of cement hydration were also quite evident when increasing the dosage of VMA from 0.14% to 0.24% (see Figure 4.14(a)). Mixture 2VMA exhibited higher compressive strength in all directions compared to mixture 1.2VMA. A similar result was reported by Li et al. [6]. The authors explained that a thin water layer might be generated on the surface of the extruded filament by using the cement paste containing 0% or relatively small dosage of VMA. The weak bonding between two adjacent layers was due to that thin water layer.

The thin water layer could be regarded as one part of the lubrication layer. De Schutter and Feys [36] explained the formation of lubrication layer for the pumpable concrete, such as self-compacting concrete. The authors point out that fresh concrete does not remain homogenous during pumping. Under the driving force, the coarse aggregate tends to move to the center of the unsheared region/plug-zone, whereas the cement paste and fine particles with the higher water content migrated to the pipe wall. For the laminar flow-based printing process, Roussel [37] indicated that only the water and the fine particles in the lubrication layer were sheared and play a function during pumping and extruding. The rheology of the unsheared region demonstrated minimal effects on extrusion but contributed more to the structural build-up process.

The higher dosage of VMA results in higher water retention and less water mobility in the matrix, which raises difficulties in forming the lubrication layer. Once the lubrication layer was generated for mixtures containing a higher concentration of VMA, the formed layer showed very high viscosity, which could be proved by the increased extrusion pressure [37] (see Figure 4.6). Finally, the lubrication layer remained on the surface of the extruded filament after deposition (Figure 4.17). Hence, the adhesion between the two extruded layers was dependent on the rheological properties of the lubrication layers in the laminar flow based printing. The viscosity of the lubrication layer could not be too high or too low. The lubrication layer with a low viscosity might contain a higher water content which could increase the porosity in the interface like mixture 1.2VMA (see Figure 4.16). However, the opposite situation, such as mixture 4VMA, would lead to the extremely high extrusion pressure and the porous microstructure in both of the interface and the layer. Overall, the optimal value was found in the mixture 2VMA in this study.

#### 4.4. CONCLUSION

THE following conclusions could be obtained in this study:

- Increasing the VMA dosage from 0.14% to 0.48% of the binder mass could increase the extrusion pressure, buildability, green strength within the first 2.5 h, and reduce the flowability and open time.
- Overall, the optimal VMA dosage for 3D printability is 0.24% of the binder mass (2VMA) in this study. Mixture 2VMA displayed better shape stability, buildability, and green strength than mixture 1.2VMA. Compared with mixture 4VMA, mixture 2VMA exhibited a more appropriate extrusion pressure, longer open time, comparable buildability and green strength.

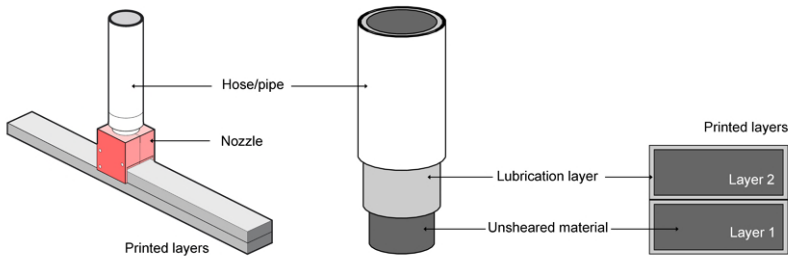


Figure 4.17: Schematic of the laminar flow based printing (Left). Formation of the lubrication layer in the material hose/pipe (Middle). Section of two printed layers (Right).

- The addition and increase of VMA dosage in the mixture can retard the cement hydration. One possible reason is that the VMA might control C-S-H adsorption and massive portlandite precipitation.
- Anisotropy of the printed samples appears to be critical concerning compressive strength tests. For all mixtures, printed samples were stronger in the loading direction Y in comparison with directions X and Z. The mixture with 0.24% of VMA (2VMA) showed the best compressive strength at 7 days in all three directions. The effects induced by VMA addition can be attributed to the following reasons. First, the VMA addition could retard the hydration of the first 7 days. Second, for high viscosity material (4VMA), the air was entrapped and stabilized in the material during the mixing and printing processes. Third, in the laminar flow-based printing process, the composition (free water content) of the lubrication layer influenced the porosity between two layers. Water retention that was modified by VMA might be a critical factor in this aspect.

## REFERENCES

- [1] Y. Chen, S. Chaves Figueiredo, Z. Li, Z. Chang, K. Jansen, O. Çopuroğlu, and E. Schlangen, *Improving printability of limestone-calcined clay-based cementitious materials by using viscosity-modifying admixture*, *Cement and Concrete Research* **132**, 106040 (2020).
- [2] S. Chaves Figueiredo, C. Romero Rodríguez, Z. Y. Ahmed, D. H. Bos, Y. Xu, T. M. Salet, O. Çopuroğlu, E. Schlangen, and F. P. Bos, *An approach to develop printable strain hardening cementitious composites*, *Materials and Design* **169**, 107651 (2019).
- [3] Y. Chen, Z. Li, S. Chaves Figueiredo, O. Çopuroğlu, F. Veer, and E. Schlangen, *Limestone and calcined clay-based sustainable cementitious materials for 3D concrete printing: A fundamental study of extrudability and early-age strength development*, *Applied Sciences* **9**, 1809 (2019).
- [4] Y. Chen, S. Chaves Figueiredo, Yalçinkaya, O. Çopuroğlu, F. Veer, and E. Schlangen,

- The effect of viscosity-modifying admixture on the extrudability of limestone and calcined clay-based cementitious material for extrusion-based 3D concrete printing*, *Materials* **12**, 1374 (2019).
- [5] A. Kazemian, X. Yuan, E. Cochran, and B. Khoshnevis, *Cementitious materials for construction-scale 3D printing: Laboratory testing of fresh printing mixture*, *Construction and Building Materials* **145**, 639 (2017).
- [6] Z. Li, L. Wang, and G. Ma, *Method for the enhancement of buildability and bending resistance of 3D printable tailing mortar*, *International Journal of Concrete Structures and Materials* **12**, 37 (2018).
- [7] D. Marchon, S. Kawashima, H. Bessaies-Bey, S. Mantellato, and S. Ng, *Hydration and rheology control of concrete for digital fabrication: Potential admixtures and cement chemistry*, *Cement and Concrete Research* **112**, 96 (2018).
- [8] M. Palacios, R. J. Flatt, F. Puertas, and A. Sanchez-Herencia, *Compatibility between polycarboxylate and viscosity-modifying admixtures in cement pastes*, *American Concrete Institute, ACI Special Publication* **288**, 29 (2012).
- [9] M. Sonebi and A. Perrot, *Effect of mix proportions on rheology and permeability of cement grouts containing viscosity modifying admixture*, *Construction and Building Materials* **212**, 687 (2019).
- [10] L. Reiter, T. Wangler, N. Roussel, and R. J. Flatt, *The role of early age structural build-up in digital fabrication with concrete*, *Cement and Concrete Research* **112**, 86 (2018).
- [11] A. Perrot, D. Rangeard, and Y. Mélinge, *Prediction of the ram extrusion force of cement-based materials*, *Applied Rheology* **24**, 1 (2015).
- [12] L. Patural, P. Marchal, A. Govin, P. Grosseau, B. Ruot, and O. Devès, *Cellulose ethers influence on water retention and consistency in cement-based mortars*, *Cement and Concrete Research* **41**, 46 (2011).
- [13] M. Chen, L. Li, Y. Zheng, P. Zhao, L. Lu, and X. Cheng, *Rheological and mechanical properties of admixtures modified 3D printing sulphoaluminate cementitious materials*, *Construction and Building Materials* **189**, 601 (2018).
- [14] A. V. Rahul, M. Santhanam, H. Meena, and Z. Ghani, *3D printable concrete: Mixture design and test methods*, *Cement and Concrete Composites* **97**, 13 (2019).
- [15] S. Bong, B. Nematollahi, A. Nazari, M. Xia, and J. Sanjayan, *Method of optimisation for ambient temperature cured sustainable geopolymers for 3D printing construction applications*, *Materials* **12**, 902 (2019).
- [16] R. J. Wolfs, F. P. Bos, and T. A. Salet, *Early age mechanical behaviour of 3D printed concrete: Numerical modelling and experimental testing*, *Cement and Concrete Research* **106**, 103 (2018).

- [17] R. J. Wolfs, F. P. Bos, and T. A. Salet, *Correlation between destructive compression tests and non-destructive ultrasonic measurements on early age 3D printed concrete*, *Construction and Building Materials* **181**, 447 (2018).
- [18] V. N. Nerella, S. Hempel, and V. Mechtcherine, *Effects of layer-interface properties on mechanical performance of concrete elements produced by extrusion-based 3D-printing*, *Construction and Building Materials* **205**, 586 (2019).
- [19] B. Panda, S. Chandra Paul, and M. Jen Tan, *Anisotropic mechanical performance of 3D printed fiber reinforced sustainable construction material*, *Materials Letters* **209**, 146 (2017).
- [20] R. J. Wolfs, F. P. Bos, and T. A. Salet, *Hardened properties of 3D printed concrete: The influence of process parameters on interlayer adhesion*, *Cement and Concrete Research* **119**, 132 (2019).
- [21] NEN-EN 196-1, *Methods of testing cement - Part 1: Determination of strength*, (2016).
- [22] I. Arganda-Carreras, V. Kaynig, C. Rueden, K. W. Eliceiri, J. Schindelin, A. Cardona, and H. S. Seung, *Trainable Weka Segmentation: A machine learning tool for microscopy pixel classification*, *Bioinformatics* **33**, 2424 (2017).
- [23] S. Chaves Figueiredo, O. Çopuroğlu, and E. Schlangen, *Effect of viscosity modifier admixture on Portland cement paste hydration and microstructure*, *Construction and Building Materials* **212**, 818 (2019).
- [24] N. Roussel, G. Ovarlez, S. Garrault, and C. Brumaud, *The origins of thixotropy of fresh cement pastes*, *Cement and Concrete Research* **42**, 148 (2012).
- [25] N. Roussel and F. Cussigh, *Distinct-layer casting of SCC: The mechanical consequences of thixotropy*, *Cement and Concrete Research* **38**, 624 (2008).
- [26] B. Panda, J. H. Lim, and M. J. Tan, *Mechanical properties and deformation behaviour of early age concrete in the context of digital construction*, *Composites Part B: Engineering* **165**, 563 (2019).
- [27] F. Zunino and K. Scrivener, *The influence of the filler effect on the sulfate requirement of blended cements*, *Cement and Concrete Research* **126**, 105918 (2019).
- [28] J. Pourchez, A. Peschard, P. Grosseau, R. Guyonnet, B. Guilhot, and F. Vallée, *HPMC and HEMC influence on cement hydration*, *Cement and Concrete Research* **36**, 288 (2006).
- [29] J. Pourchez, P. Grosseau, and B. Ruot, *Changes in C3S hydration in the presence of cellulose ethers*, *Cement and Concrete Research* **40**, 179 (2010).
- [30] Z. H. Ou, B. G. Ma, and S. W. Jian, *Influence of cellulose ethers molecular parameters on hydration kinetics of Portland cement at early ages*, *Construction and Building Materials* **33**, 78 (2012).

- [31] M. Palacios and R. J. Flatt, *Working mechanism of viscosity-modifying admixtures*, in *Science and Technology of Concrete Admixtures*, Vol. i (Elsevier Ltd, 2015) pp. 415–432.
- [32] T. Le, S. Austin, S. Lim, R. Buswell, R. Law, A. Gibb, and T. Thorpe, *Hardened properties of high-performance printing concrete*, *Cement and Concrete Research* **42**, 558 (2012).
- [33] G. Ma, Z. Li, L. Wang, F. Wang, and J. Sanjayan, *Mechanical anisotropy of aligned fiber reinforced composite for extrusion-based 3D printing*, *Construction and Building Materials* **202**, 770 (2019).
- [34] B. Panda, G. B. Singh, C. Unluer, and M. J. Tan, *Synthesis and characterization of one-part geopolymers for extrusion based 3D concrete printing*, *Journal of Cleaner Production* **220**, 610 (2019).
- [35] A. Jenni, L. Holzer, R. Zurbriggen, and M. Herwegh, *Influence of polymers on microstructure and adhesive strength of cementitious tile adhesive mortars*, *Cement and Concrete Research* **35**, 35 (2005).
- [36] G. De Schutter and D. Feys, *Pumping of Fresh Concrete: Insights and Challenges*, *RILEM Technical Letters* **1**, 76 (2016).
- [37] N. Roussel, *Rheological requirements for printable concretes*, *Cement and Concrete Research* **112**, 76 (2018).



# 5

## EFFECT OF DIFFERENT GRADE LEVELS OF CALCINED CLAYS ON FRESH AND HARDENED PROPERTIES

*This study aims to investigate the influences of different grades of calcined clays on 3D printability, compressive strength (7 days), and hydration of limestone and calcined clay-based cementitious materials. Calcined clays that contained various amounts of metakaolin were achieved by blending low-grade calcined clay (LGCC) and high-grade calcined clay (HGCC) in three different proportions. The results revealed that increasing the HGCC% ranging from 0 wt.% to 50 wt.% in calcined clay could: (1) increase the flow consistency; (2) impressively improve the buildability, and reduce the open time of the fresh mixtures; (3) enhance and accelerate the cement hydration. However, increasing HGCC% led to an increase of air void content in the interface region of the printed sample, which weakened the compressive strength of the printed sample at 7 days. Besides, it confirmed that the cold-joint/weak interface was easily formed by using the fresh mixture with a high structuration rate.*

## 5.1. INTRODUCTION

ACCORDING to the discussion in Section 2.3.2, Chapter 2, research on the development of limestone and calcined clay-based cementitious materials for extrusion-based 3D concrete printing (3DCP) is still at an early stage. Few attempts have been made to explore the 3D printability of such ternary-blended cementitious materials by using different grades of calcined clays. Herein, the objective of this study is to investigate the effects of different grades of calcined clays on the fresh and hardened properties of such materials in the context of 3DCP. This chapter was organized into three distinct aspects, the first of which deals with the characterization of 3D printability. A specific ram extrusion test and Basterfield et al. model [2] were initially utilized to quantify the extrusion rheology of fresh mixtures. After that, based on a lab-scale 3DCP setup, open time and buildability were evaluated. Second, the compressive strength was measured on both mold-cast and printed samples at the material age of 7 days. Additionally, the air void content and distribution of printed samples were quantified by using X-ray computed tomography scanning and image analysis. Third, isothermal calorimetry and thermogravimetric analysis were carried out for assessing phase assemblages of the resulting materials.

5

## 5.2. MATERIALS AND METHODS

### 5.2.1. RAW MATERIALS AND MIX DESIGNS

TWO types of calcined clay were used in this work. A low-grade calcined clay (LGCC), which contained about 50% of metakaolin, was the same as the calcined clay used in Chapters 3 and 4. The other one, with nearly 95% of metakaolin, was regarded as a high-grade calcined clay (HGCC) provided by Burgess, USA. Other raw materials, including Portland cement (PC), limestone powder (LP), viscosity modifying admixture (VMA), superplasticizer (SP), and sand, were the same as presented in Section 3.2.1, Chapter 3. Table 5.1 illustrates physical and XRF characteristics of PC, LP, LGCC, and HGCC.

The XRD (check details in Section 3.2.1, Chapter 3) results for LGCC and HGCC, reported in Figure 5.1, showed higher amorphous content in HGCC from the presence of a broad hump in the  $2\theta$  range of  $15^\circ$  to  $30^\circ$  when compared to LGCC where it ranges from  $20^\circ$  to  $28^\circ$ . Besides, more crystalline phases, such as quartz ( $\text{SiO}_2$ ), mullite ( $3\text{Al}_2\text{O}_3 \cdot 2\text{SiO}_2$ ) and kaolinite ( $\text{Al}_2\text{O}_3 \cdot 2\text{SiO}_2 \cdot 2\text{H}_2\text{O}$ ), were observed in LGCC. For figuring out the contents of the reactive  $\text{SiO}_2$  and  $\text{Al}_2\text{O}_3$  in HGCC, a chemical dissolution method on the basis of NEN-EN 192-2 [3] was utilized (check the test procedure in Section 3.2.1, Chapter 3). The amount of reactive  $\text{SiO}_2$  and  $\text{Al}_2\text{O}_3$  is given in Table 5.2. The molar mass ratios of Si/Al in the reactive part of LGCC and HGCC were 0.33 and 0.74, respectively. The gradings of all dry components were presented in Figure 5.2. HGCC was the finest powder with an average particle size ( $D_{v50}$ ) of  $3.75 \mu\text{m}$ . The morphological properties of LGCC and HGCC were reported in Figure 5.3. For both LGCC and HGCC, the thin layered, irregular flaky morphology was observed.

Table 5.3 shows the specific proportions of the different mixtures studied in this chapter. The binder of mixtures LCC, MCC and HCC was a blend of three primary materials, i.e., 40 wt.% of Portland cement (PC), 20 wt.% of limestone powder (LP), and

Table 5.1: Physical characteristics and oxide composition from XRF of dry components in binders.

	PC	LP	LGCC	HGCC
Density [g/cm <sup>3</sup> ]	3.120	2.646	2.512	2.134
SSA [m <sup>2</sup> /g]	1.16	1.22	10.06	12.60
$D_{v50}$ [ $\mu$ m]	14.86	24.19	69.35	3.75
XRF [wt.%]				
CaO	68.7	39.6	0.6	0
SiO <sub>2</sub>	17.4	0.2	55.1	47.3
Al <sub>2</sub> O <sub>3</sub>	4.1	0	38.4	50.6
Fe <sub>2</sub> O <sub>3</sub>	2.8	0.1	2.6	0.5
K <sub>2</sub> O	0.6	0	0.2	0.2
TiO <sub>2</sub>	0.3	0	1.1	1.3
ZrO <sub>2</sub>	0	0	0.1	0
Other	6.1	60.1	1.9	0.1
Total	100.0	100.0	100.0	100.0

Table 5.2: Reactive content of two different calcined clays (LGCC and HGCC).

Components (wt. %)	I.R.	Reactive Content	Reactive SiO <sub>2</sub>	Reactive Al <sub>2</sub> O <sub>3</sub>	Other Reactive Phases
LGCC	51.2	48.8	12.3	32.0	4.5
HGCC	24.9	75.1	34.6	39.9	0.6

40 wt.% of calcined clay. In addition to mixture LCC, another two mixtures were prepared by replacing 25 wt.% and 50 wt.% of LGCC with HGCC to simulate the calcined clay with about 61.3 wt.% and 72.5 wt.% of metakaolin, respectively. Mixture REF containing 0 wt.% of calcined clay was used as a reference to investigate the effects of calcined clay on cement hydration and compressive strength of mold-cast samples. The fresh mixtures were prepared by following the mixing protocol in Table 3.3, Chapter 3.

The influence of filler additions on the total specific surface area (SSA) of solid ( $SSA_{total}$ ) of the binder system is calculated through:

$$SSA_{total} = \frac{M_{CEM}SSA_{CEM} + M_{other}SSA_{other}}{M_{CEM} + M_{other}} \quad (5.1)$$

where  $M_{CEM}$  and  $M_{other}$  are the mass percentages of PC and other fines (LP, LGCC, HGCC) in the binder.  $SSA_{CEM}$  and  $SSA_{other}$  mean the specific surface areas of PC and other fines (LP, LGCC, HGCC) in the binder. The solid volume fraction ( $\phi$ ) of such binding materials can be computed by using Eq 5.2.

$$\phi = \left(1 + \frac{\rho_b W}{\rho_w B}\right)^{-1} \quad (5.2)$$

where  $\rho_b$  and  $\rho_w$  stand for the density of binder and water, respectively.  $B$  and  $W$  mean the unit of weight of binder and water. Table 5.4 presents  $SSA_{total}$  and  $\phi$  results of different binders in this chapter.

### 5.2.2. RAM EXTRUSION TEST

A ram extruder (see Figure 5.4), which consisted of a barrel, a piston, a stand, and an orifice, was assembled in a servo-hydraulic Instron 8872 machine. The piston was

Table 5.3: Mix designs of cementitious materials prepared in this study (% of the binder mass).

Mixture	PC	LGCC	HGCC	LP	Sand	Water	SP	VMA
REF	40	0	0	60	150	30	2	0.24
LCC	40	40	0	20	150	30	2	0.24
MCC	40	30	10	20	150	30	2	0.24
HCC	40	20	20	20	150	30	2	0.24

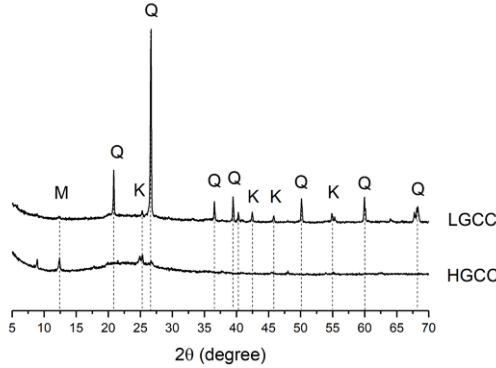


Figure 5.1: XRD patterns (Cu-K $\alpha$  radiation) of LGCC and HGCC. Q-quartz (SiO<sub>2</sub>), M-mullite (3Al<sub>2</sub>O<sub>3</sub> 2SiO<sub>2</sub>), and K-kaolinite (Al<sub>2</sub>O<sub>3</sub> 2SiO<sub>2</sub> 2H<sub>2</sub>O).

connected to a 10 kN load cell that could measure the total extrusion force. Before the test, the barrel was filled with the fresh mixture. Care was taken to ensure a minimum content of entrapped air during the barrel filling process. Afterwards, the piston was operated with different speeds to extrude the fresh mixture through the orifice. All mixtures were tested at a material age of  $15 \pm 2$  min. A typical trial of the ram extrusion test is shown in Figure 5.4(c). The pre-test consists of a piston displacement from 0 to 29.5 mm. Two speeds (1 mm/s and 2 mm/s) were used in the pre-test stage. Within the piston displacement between 29.5 mm and 43 mm, 12 different piston speeds ( $V_0$ ) were employed (for each test, only one speed was used), and the material flow rates ( $V$ ) at the orifice were calculated by:

$$V = \frac{D_0^2}{D^2} V_0 \tag{5.3}$$

where  $D_0$  and  $D$  represent the diameter of the barrel and die, respectively. The computed results were presented in Table 5.5. Based on the collected extrusion forces, the upstream extrusion pressures were determined through:

$$P = \frac{4F}{\pi D_0^2} \tag{5.4}$$

where  $P$  and  $F$  stand for the extrusion pressure and the extrusion force, respectively, under one predefined piston speed.

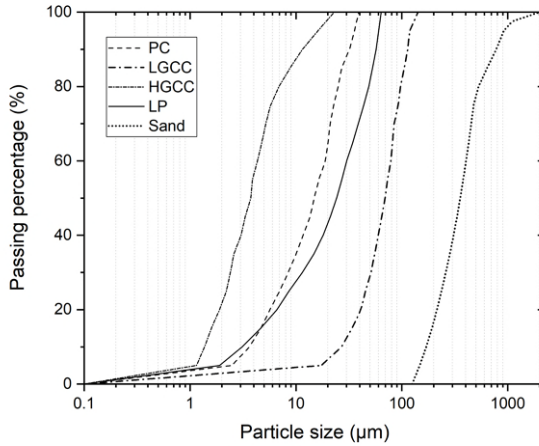


Figure 5.2: The particle size distribution of PC, LGCC, HGCC, LP and sand. The grain size of sand was measured by using a sieving machine. All other dry components were determined by laser diffractometry.

The analytical relationship between the material flow rate and ram extrusion pressure at the orifice was given by Basterfield et al. [2] (see Eq 2.6). As suggested by [2, 4], 45 degree was selected as the value of  $\theta_{max}$ . Since the fresh cementitious materials also followed the Von-Mises criterion [5], the shear yield stress ( $\tau_0$ ) could be obtained by Eq 2.7.

**5.2.3. 3D PRINTING TEST**

**OPEN TIME TEST**

The open time test was almost the same as described in Section 4.2.3, Chapter 4. Two differences were summarized as follows: (1) The test started at the resting time of 20 min; (2) A pre-pumping session of 5 min was arranged before printing the filament.

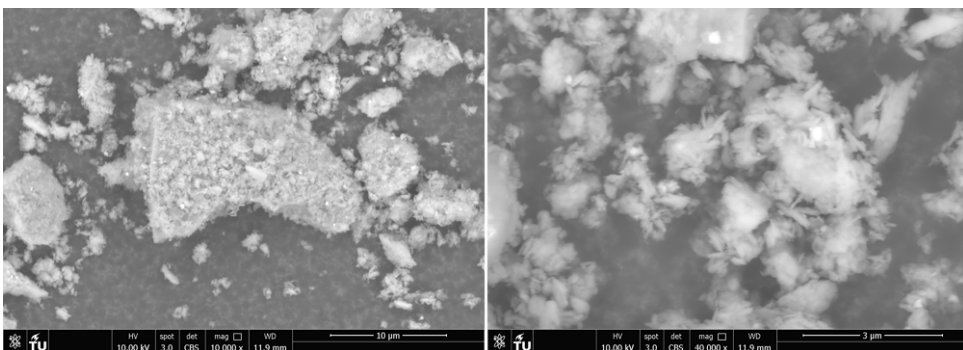


Figure 5.3: Electron micrographs (secondary electron mode) of LGCC (Left) and HGCC (Right).

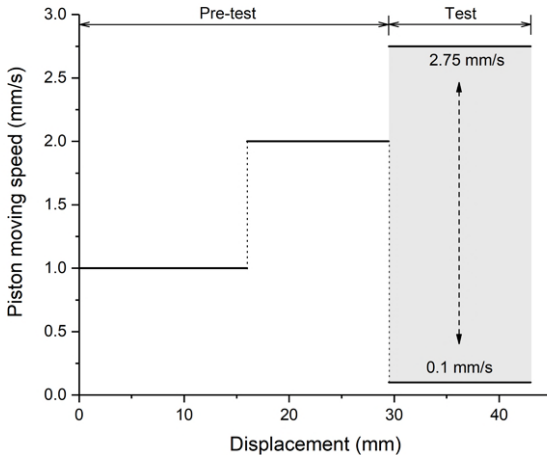
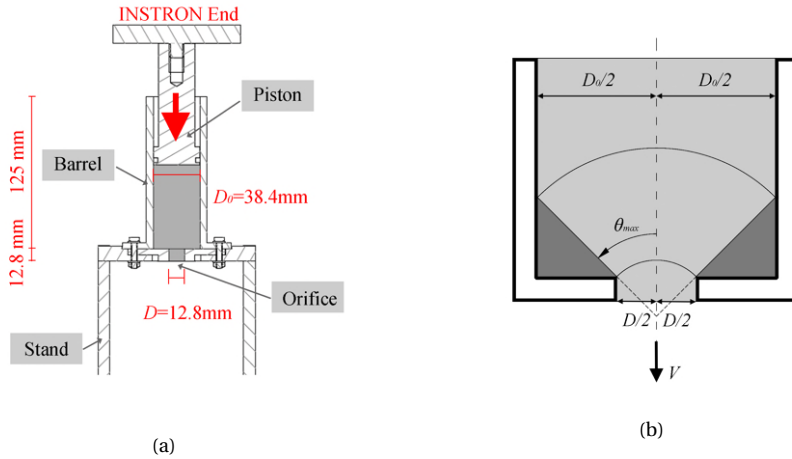


Figure 5.4: (a) Schematic drawing of the ram extruder; (b) Diagram of the orifice entrance flow region in a spherical coordinate system, according to [2, 4]; (c) A typical trial of the ram extrusion test - predefined piston moving speed vs. displacement.

Table 5.4:  $SSA_{total}$  and  $\phi$  of different binders.

	REF	LCC	MCC	HCC
$SSA_{total}$ [m <sup>2</sup> /g]	1.196	4.732	4.986	5.240
$\phi$	0.542	0.548	0.552	0.557

Table 5.5: Piston moving velocity  $V_0$  and material flow velocity  $V$  at the orifice.

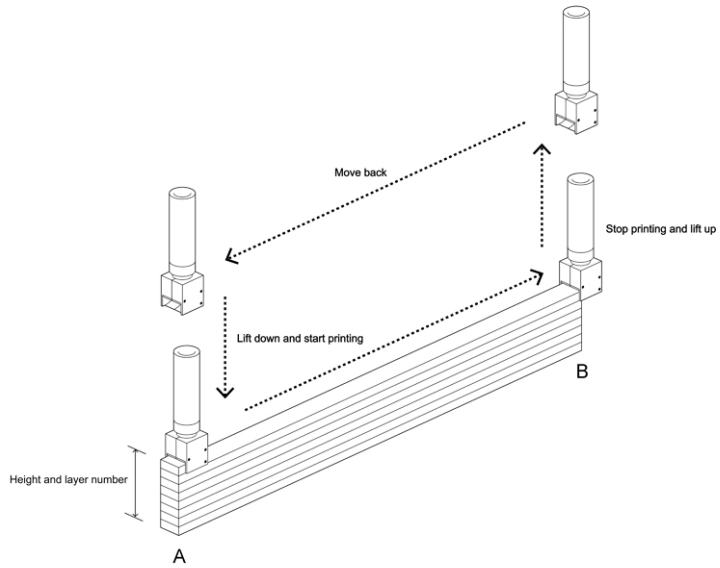
$V_0$ [mm/s]	$V$ [mm/s]
0.10	0.90
0.25	2.25
0.50	4.50
0.75	6.75
1.00	9.00
1.25	11.25
1.50	13.50
1.75	15.75
2.00	18.00
2.25	20.25
2.50	22.50
2.75	24.75

### BUILDABILITY TEST

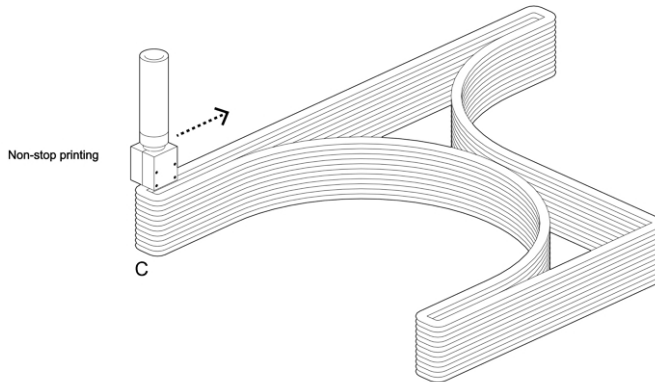
Two methods were employed to evaluate the buildability of the different mixtures. The test parameters of both methods were summarized in Table 5.6. Method 1 is quite similar to the buildability test that was proposed by Nerella et al. [6]. The test started at the material age of 20 min. A wall was designed to stack 21 layers. Nozzle 1 (see Figure 4.1) was employed for Method 1. For each layer, there was only one filament (designed dimension: 900 mm length, 40 mm width, and 13.5 mm height). The process of Method 1 is schematized in Figure 5.5(a). The fresh mixture was deposited from position A to B at a constant printing speed of 2820 mm/min. Once the nozzle reached position B (one filament was finished), the printing work was paused. The nozzle was programmed to be lifted at a maximum height of 285 mm and then to move to Position A. The time gap between two layers was set as 30 s. Method 2 employed nozzle 2 (see Figure 3.4(b)) to print a designed object with a non-stop printing process (Figure 5.5(b)). The path length of each layer was 4200 mm. The height of the nozzle was increased to 8.5 mm each time at the start position C. The time interval between two subsequent layers was 57 s. In comparison to Method 1, a faster printing speed (4500 mm/min) was utilized in Method 2. During the test process (both methods 1 and 2), the height of the printed object was measured and recorded continuously. The test may be terminated earlier (before finishing the printing work) due to collapse by buckling.

#### 5.2.4. COMPRESSIVE STRENGTH TEST

Printed prisms that contained 4 stacked layers (Length: 800 mm; Width: 42-44 mm; Height: 50-54 mm) were manufactured using the 3DCP setup (nozzle 1). The nozzle moving speed and the material flow rate were fixed at 2100 mm/min and 1.2 L/min, respectively. The time interval between two adjacent layers was 2 min. The compressive strength of printed samples was tested along with three loading directions: X, Y, and Z



(a)



(b)

Figure 5.5: Schematic diagram of buildability test: (a) Method 1 (by using nozzle 1); (b) Method 2 (by using nozzle 2).



Table 5.6: Printing parameters for buildability test.

	Method 1	Method 2
Nozzle type	Nozzle 1	Nozzle 2
Nozzle opening [mm]	40 × 13.5	Ø 15
Layer thickness [mm]	13.5	8.5
Nozzle moving speed [mm/min]	2820	4500
Path length for each layer [mm]	900	4200
Material flow rate [L/min]	1.5	0.9
Time interval [s]	30	57
Designed layer number	21	18
Designed structure height [mm]	283.5	153
Test start time [material age: min]	20	20

(see Figure 4.3). For each mixture and each direction, three samples were prepared and tested. Besides, to determine the influence of the printing process on compressive strength,  $40 \times 40 \times 40 \text{ mm}^3$  mold-cast specimens were also prepared. The curing conditions and test procedure were kept the same as described in Section 4.2.6, Chapter 4.

### 5.2.5. AIR VOID ANALYSIS

The air void content and distribution of printed specimens were determined using X-ray computed tomography (CT) scanning and image analysis through the open-source software ImageJ. Cylindrical samples (25 mm diameter and 24 mm height) were drilled and sawn from the upmost two layers of 3D printed beams, manufactured in the section of compressive strength test. The CT scanning, image segmentation, and analysis processes were kept the same as described in Section 4.2.7, Chapter 4. The obtained image resolution was  $13.3 \mu\text{m}$  per pixel.

### 5.2.6. ISOTHERMAL CALORIMETRY TEST AND THERMOGRAVIMETRIC ANALYSIS

The isothermal calorimetry test procedure was the same as described in Section 3.2.5, Chapter 3. The paste mixtures from the isothermal calorimetry test were also used for the thermogravimetric analysis (TGA). The cast cylindrical specimens (33.5 mm diameter and 67.5 mm height) were stored at the fog room with the curing conditions ( $20 \pm 2 \text{ }^\circ\text{C}$ , above 99% RH) up to the time of testing. A three-step procedure, as described by Lothenbach et al. [7], was used for powder sample preparation:

- First, crushing and grinding the sample in isopropanol solvent for about 10-15 min.
- Second, filtrating the suspension by using a Büchner funnel and an aspirator pump (the size of filter paper was  $8 \mu\text{m}$ ), followed by washing the solid with diethylene ether to remove the isopropanol.
- Third, drying the powder for about 8 min in a  $40 \text{ }^\circ\text{C}$  aerated oven. The samples were stored in a light vacuum desiccator and tested within 3 days.

TGA was employed to quantify the hydrate water (H) and calcium hydroxide (CH) of different mixtures at the ages of 1, 2, 3, and 7 days. Netzsch STA 449 F3 Jupiter was utilized for the test. For each mixture, about 50 mg of paste sample that was placed in an alumina crucible was heated from 40 to 900 °C with a heating rate of 10 °C/min and under an argon environment with a flow rate of 30 ml/min.

## 5.3. RESULTS

### 5.3.1. RAM EXTRUSION RHEOLOGY

**F**IGURE 5.6(a) presents an example of the extrusion force concerning piston displacement. A pre-test zone (displacement: 0-29.5 mm) was utilized to compact the fresh mixture and transfer the material status from a static state to a dynamic state, which has been explained in [8]. It could be noticed that the piston started to touch the fresh mixture at a displacement of about 11 mm. During the displacement from 11 mm to 16 mm (piston speed: 1 mm/s), an unstable curve pattern was observed due to the existence of air bubbles and the thixotropy of the fresh mixture. The curve becomes relatively stable at the end of the pre-test zone under the piston speed of 2 mm/s. Afterwards, the piston was driven under a predefined speed (see Table 5.5). Relatively flat curves could be found in the test zone. The average upstream extrusion pressure was calculated using Eq 5.4.

Through applying the non-linear least squares regression analysis in the Originlab, Basterfield et al. model (Eq 2.6) was fitted to the test results. Both the experimental and fitted results are plotted in Figure 5.6(b). The correlation between test results and Basterfield et al. model was nearly perfect since the R-squared value of three fitted curves was about 0.99 in all cases. The rheological parameters, namely,  $\sigma_0$ ,  $k$ , and  $n$ , were determined as well. The shear yield stress of the fresh mixtures was calculated according to Eq 2.7. Figure 5.6(c) reports the obtained shear yield stress and flow consistency. Increasing the HGCC content resulted in increased flow consistency in the fresh mixture. Mixture HCC exhibited the highest shear yield stress. However, there was no apparent difference between mixtures LCC and MCC in shear yield stress.

### 5.3.2. EVALUATION OF 3D PRINTABILITY

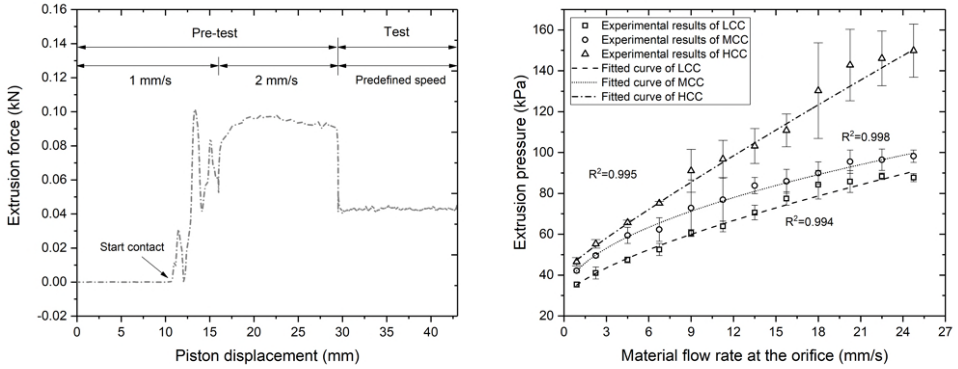
#### OPEN TIME

In this study, by using 2820 mm/min of the printing speed (material flow rate: 1.5 L/min), the open time of mixtures LCC, MCC, and HCC was noted as 80 min, 70 min, and 30 min, respectively. The open time of fresh mixtures was reduced by increasing the HGCC substitution (Figure 5.7).

#### BUILDABILITY

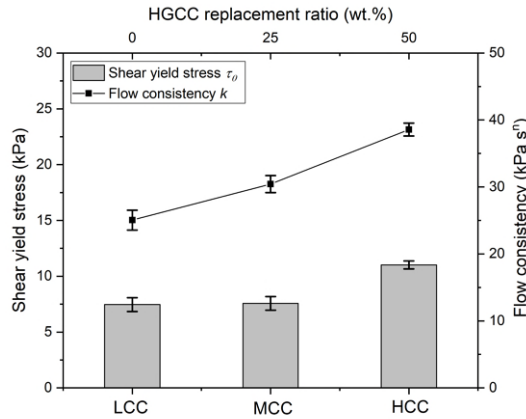
##### Method 1

Figure 5.8 presents the buildability test results by using Method 1. In this test, only mixture HCC could be used to stack 21 layers vertically without collapse. Using mixtures LCC and MCC, the printed structure could only maintain its shape until the 10<sup>th</sup> and 11<sup>th</sup> layers, respectively. The height of printed structures before the structure was finished or before failure was recorded and plotted in Figure 5.8(b). Increasing the



(a)

(b)



(c)

Figure 5.6: (a) A typical plot of the ram extrusion test; (b) Experimental results of extrusion pressure with different material flow rates at the orifice and fitted curves via using Basterfield et al. model (Eq 2.6); (c) Computed rheological parameters: shear yield stress  $\tau_0$ , and flow consistency  $k$  of mixtures LCC, MCC, and HCC.

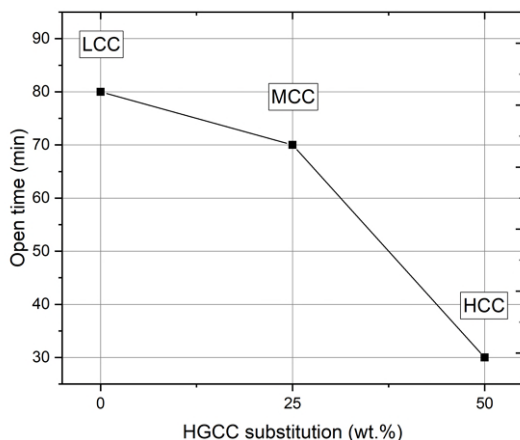


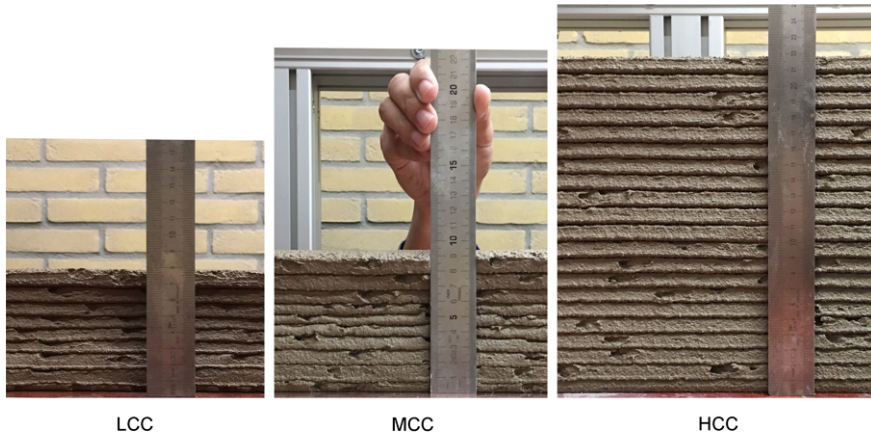
Figure 5.7: Open time varies with the HGCC substitution in calcined clay.

HGCC content could significantly improve the buildability of fresh mixture. As shown in Figure 5.9, the final collapse was induced by misalignment of the printing path. Two reasons may lead to the instability of printed structures. First, the deformation of the bottom layers gradually increased the nozzle standoff distance, which resulted in the inaccurate layer deposition. As shown in Figure 5.8(a), the 1<sup>st</sup> layer of the printed structure was severely compressed. Compared with mixture LCC, the 1<sup>st</sup> layer of the printed wall showed better shape stability by using mixtures MCC and HCC. Second, since the nozzle could not stop printing immediately after finishing one filament, it was required to remove the excess materials manually. Thus, both sides of each filament displayed uncontrolled shapes and positions in Figure 5.9. For mixtures LCC and MCC, elastic buckling failure always started from one side to the other of the printed structure (Figure 5.9). However, these constraints did not severely influence the printing process of mixture HCC. Through using Method 1, the difference in buildability between mixtures MCC and LCC was not clear.

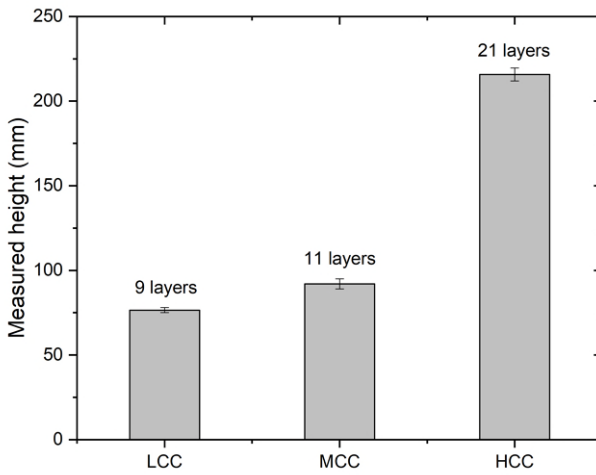
### Method 2

Figure 5.10 illustrates the maximum stacked-layer number and the corresponding height of the printed structure for different mixtures. As shown in Figures 5.10(a) and 5.12, the layer thickness is increased from the bottom to the top of the printed structure, especially mixtures LCC and MCC. Only mixture HCC could reach the designed layer number without collapse, and showed relatively even layer thickness. In comparison with Method 1, the boundary condition of the printed layer in Method 2 was more stable. The difference between mixtures LCC and MCC on buildability performance could be indicated.

Overall, the buckling failure of the printed structure may be mainly attributed to the unstable layer deposition, which was induced by the increase of nozzle standoff



(a)



(b)

Figure 5.8: Buildability test results of Method 1: (a) Buildability performance of mixtures LCC, MCC, and HCC; (b) Height and layer number of the printed object by using different mixtures (mixtures LCC and MCC: data recorded before collapse; mixture HCC: data recorded after the 21<sup>st</sup> layer).

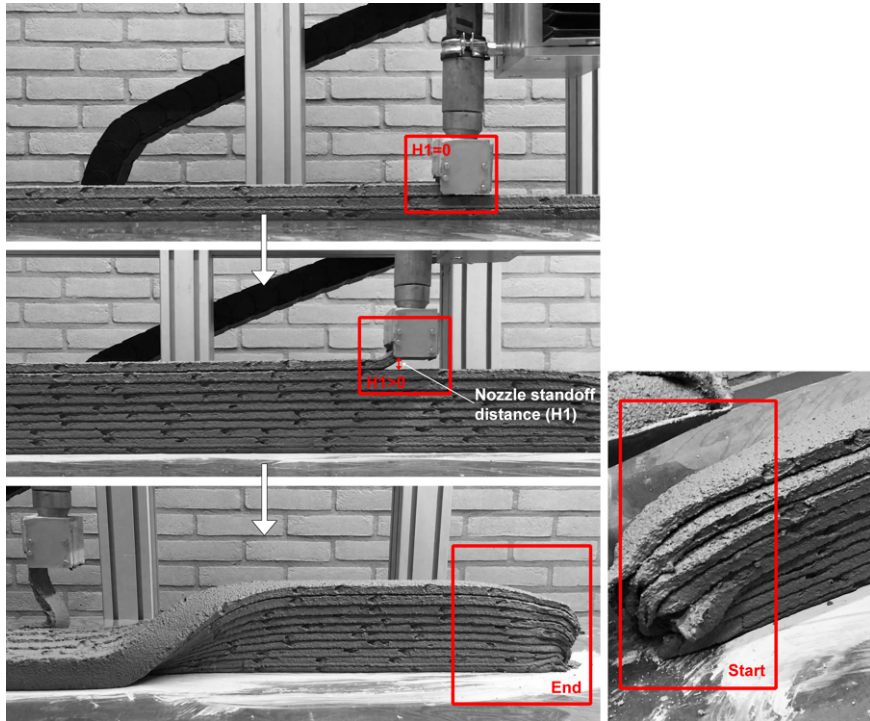
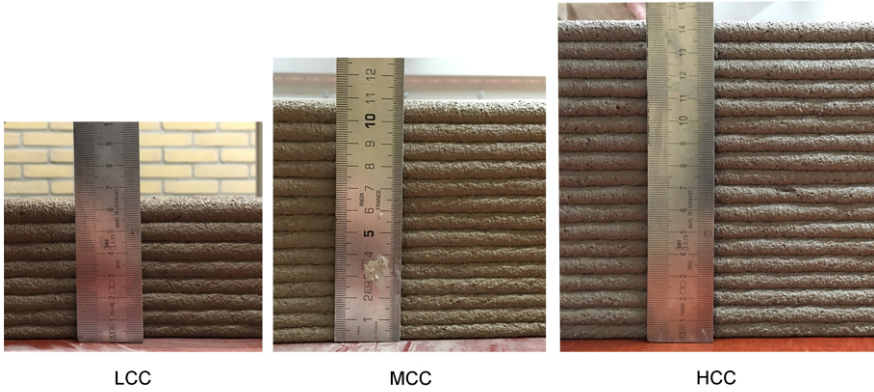


Figure 5.9: Method 1-possible reasons for collapse of the rising structure.

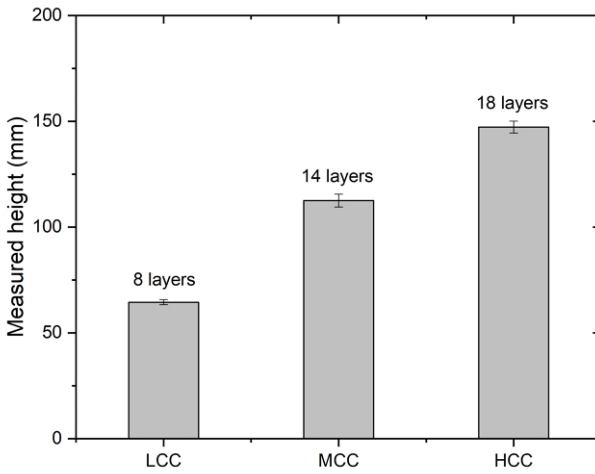
distance (Figures 5.9 and 5.11), and the reduction of layer contacted area (Figure 5.12). In Method 1, each layer was dropped onto the substrate via a hybrid down- and back-flow nozzle with a rectangle opening (nozzle 1). The contact area between layers was quite stable and constant (Figure 5.12). Since a down-flow nozzle with a round opening (nozzle 2) was employed in Method 2, the new layer was deposited on the substrate through a squeezed and compressed forming process. As mentioned in Section 3.3.2, Chapter 3, the substrate needed to sustain not only the load from the weight of the new layer but also the force from the nozzle. However, this force was not constant during the printing process. It was decreased due to the increase of nozzle standoff distance. The contact area between layers, as well as layer thickness, became more uncontrollable for mixtures with weak buildability as resulting from Method 2.

### 5.3.3. COMPRESSIVE STRENGTH

Figure 5.13 shows the compressive strength of mold-cast and 3D printed samples (except for mixture REF) at 7 days. For cast samples, mixtures containing calcined clay exhibited a much higher compressive strength than mixture REF. Increasing HGCC% in calcined clay improved the compressive strength of cast samples (7 days). The increment of strength between mixtures MCC and HCC was limited. Anisotropic properties were observed for the printed specimens. According to the experimental



(a)



(b)

Figure 5.10: Buildability test results of Method 2: (a) Buildability performance of mixtures LCC, MCC, and HCC; (b) Height and layer number of the printed object by using different mixtures (mixtures LCC and MCC: the maximum height before collapse; mixture HCC: data recorded after the 18<sup>th</sup> layer).



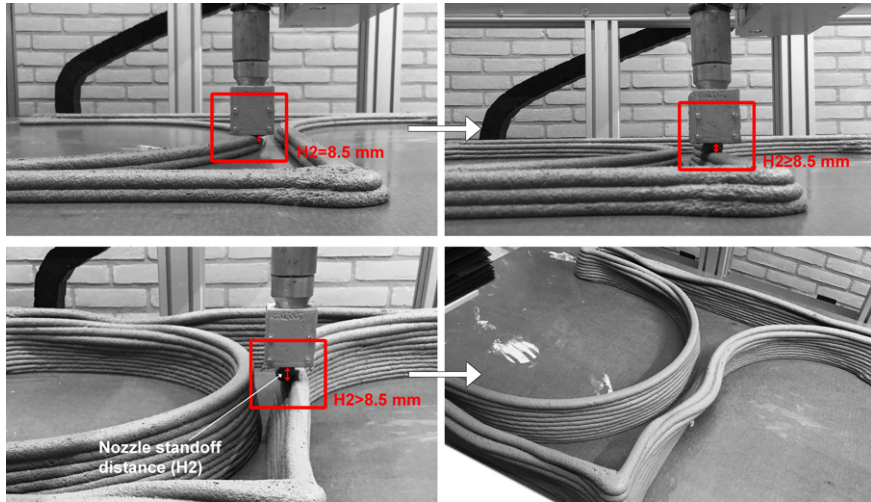


Figure 5.11: Method 2-possible reasons for collapse of the rising structure.

results, it could be found that the printed specimens displayed the highest compressive strength in loading direction Y in comparison with directions Z and X. The possible reasons have been discussed in [9–12] (see Section 4.3.5, Chapter 4). For mixtures LCC and MCC, the printed samples were stronger than cast samples in all test directions. However, printed samples of mixture HCC had lower compressive strength than its cast samples except for loading direction Y. For printed samples, mixture MCC exhibited the optimal compressive strength at 7 days. In loading directions Y and Z, mixture LCC showed higher strength than mixture HCC.

#### 5.3.4. AIR VOID CONTENT AND DISTRIBUTION

An ROI of 13 mm in height and 25 mm in diameter were obtained in each cylindrical sample. After performing image analysis via ImageJ, the 2D air void content, and the average air void diameter of each slice are computed and plotted in Figures 5.14(a) and 5.14(b). Based on the results of image analysis in Figure 5.14, for each sample, the interface region could be defined as the region in the height of 5-8 mm due to the relatively higher air void content. The regions of 0-5 mm and 8-13 mm in height could be regarded as the layer area. Figures 5.14(a) and 5.14(b) showed massive air voids with large diameters in the interface region (especially 6-7.5 mm in height) for samples HCC and MCC. Nevertheless, it was relatively difficult to distinguish the interface visually in sample LCC. Compared to samples MCC and HCC, the distribution of air voids in sample LCC was more homogeneous (please also check Figure 5.15). As shown in Figure 5.14(c), increasing HGCC% in calcined clay could significantly increase the maximum value of air void content in the interface region. Furthermore, it led to a slight increase in average air void content in both interface and layer regions.



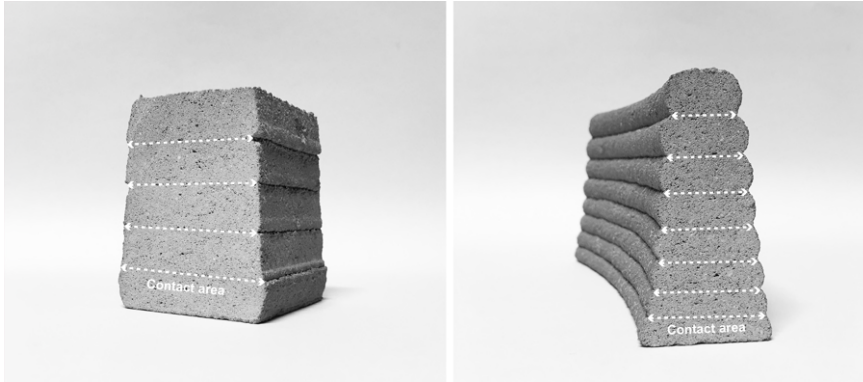


Figure 5.12: Cross-sections of printed samples by using nozzle 1 (Left) and nozzle 2 (Right). The dashed line represents the contact area between two adjacent layers.

### 5.3.5. HYDRATION KINETICS

#### Isothermal calorimetry

Figure 5.16 shows both heat flow and cumulative heat results of all studied mixtures. In Figure 5.16(a), for all curves, the first peak can be attributed to the heat released from the particle wetting, the initial dissolution of the dry components, and the formation of ettringite at an early age [13]. A dormant period was observed, followed by an acceleration period and by the main hydration peak (I). With the absence of calcined clay, mixture REF had the longest dormant time of 12 h and took near 38 h to reach the main hydration peak, for which the heat flow resulted in the lowest among the studied mixtures. For mixtures LCC, MCC, and HCC, the increase of HGCC content in calcined clay results in, (1) a reduction in the dormant period; (2) a shift of the main hydration peak to the early age; (3) an increase in the intensity of the main hydration peak. Among them, mixture HCC showed the highest chemical reactivity.

After the main hydration peak, a small shoulder (II), which was not present in mixture REF, was observed in the curves of mixtures LCC, MCC, and HCC. According to [14–17], peak (II) may be referred to as the aluminate peak. Around 36 h after the aluminate peak, a lower but broader peak (III) appeared in the curve of mixtures HCC, MCC, and LCC. The appeared time and intensity of peak (III) were also dependent on the HGCC content in calcined clay. The formation of the AFm phases, which could be attributed to the pozzolanic reaction of metakaolin with the relatively high concentration of CH in the pore solution [18], may be the reason for the appearance of peak (III). As shown in Figure 5.16(b), very low cumulative heat was released in mixture REF, while the addition of calcined clay led to a distinct increase in the cumulative heat of 7 days. For mixtures LCC, MCC, and HCC, it was evident that increasing the dosage of HGCC could significantly increase the total heat emission. Nevertheless, mixtures HCC and MCC showed very close results of the cumulative heat at 7 days.

#### Quantification of hydrate water and calcium hydroxide

Thermogravimetric (TG) curves of different mixtures at 1, 2, 3, and 7 days of curing are

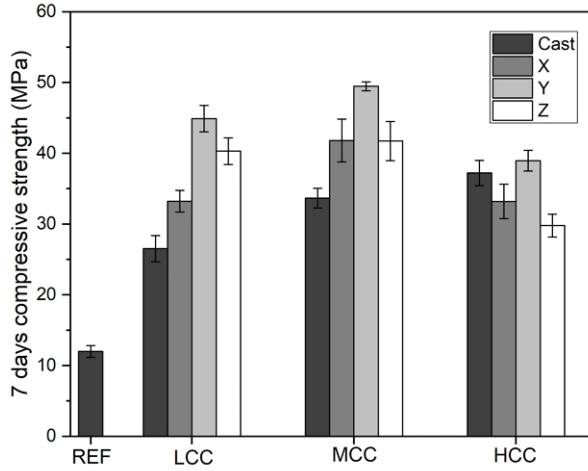


Figure 5.13: Compressive strength of both cast and printed samples from different mixtures at the age of 7 days. For test directions X, Y, and Z, the reader is referred to Figure 4.3.

illustrated in Figure 5.17(a). To identify the boundaries of different phases or groups of phases, derivative thermogravimetric (DTG) curves are plotted in Figure 5.17(a) according to TG results. The mass loss during the temperature between 40 °C and 600 °C was regarded as hydrate water (H) [7]. As mentioned by [7, 19], calcium hydroxide (CH) decomposes to calcium oxide and water between 400 °C and 500 °C. For all mixtures in this study, the breakdown of the CH phase ranged between about 420 °C and 500 °C, which can be seen in Figure 5.17(a). Peaks above 600 °C are due to the decarbonization of calcite, which is originated from the limestone filler in mixtures and the formed carbonation of CH during the curing time [20]. Therefore, the normalized amount of H and CH were expressed as a percentage of the dry sample weight at 600 °C:

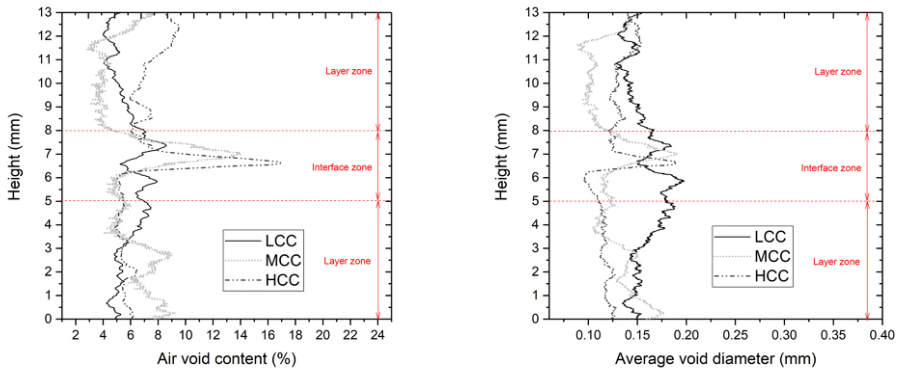
$$W_{[H_2O]} = \frac{M_{40^\circ C} - M_{600^\circ C}}{M_{600^\circ C}} \times 100(\%) \quad (5.5)$$

and

$$W_{[Ca(OH)_2]} = \frac{M_{420^\circ C} - M_{500^\circ C}}{M_{600^\circ C}} \times \frac{m_{[Ca(OH)_2]}}{m_{[H_2O]}} \times 100(\%) \quad (5.6)$$

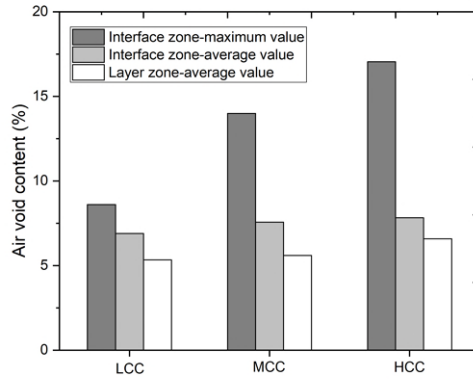
$W_{[H_2O]}$ , and  $W_{[Ca(OH)_2]}$  are the mass percentages of H and CH in mixtures, respectively;  $M_{40^\circ C}$ ,  $M_{420^\circ C}$ ,  $M_{500^\circ C}$  and  $M_{600^\circ C}$  represent the TG results at 40 °C, 420 °C, 500 °C, and 600 °C, respectively;  $m_{[Ca(OH)_2]}$  and  $m_{[H_2O]}$  stand for the molar masses of CH (74 g/mol) and water (18 g/mol), respectively. The computed results are summarized in Table 5.7.

The H and CH contents are illustrated in Figures 5.17(b) and 5.17(c). More hydrate water content has been found in mixtures containing calcined clay in comparison with



(a)

(b)



(c)

Figure 5.14: (a) 2D air void content analysis; (b) Average air void diameter analysis; (c) Air void content in the interface and layer zones; Interface zone: 5-8 mm in height of the sample. Layer zone: 0-5 mm and 8-13 mm in height of the sample.

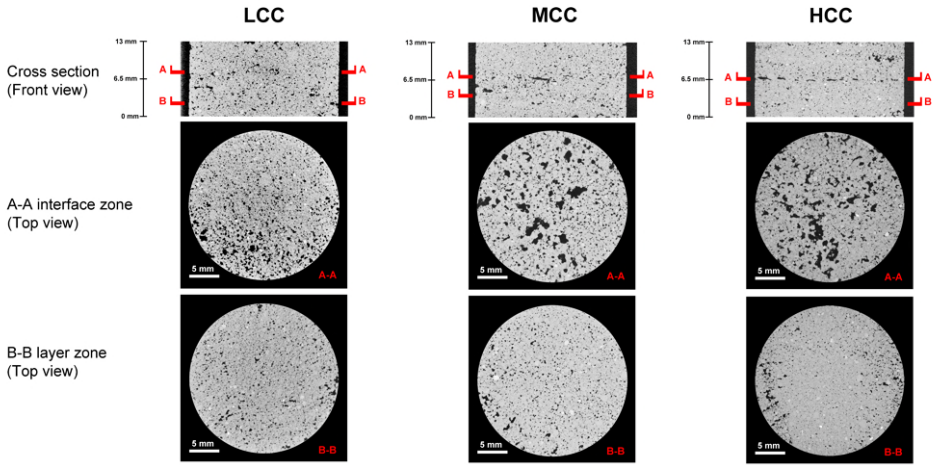


Figure 5.15: Grayscale images of different samples acquired from CT scanning.

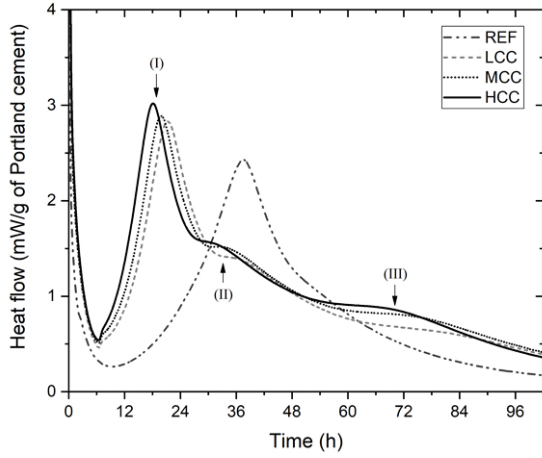
mixture REF within the first 7 days. Replacing part of LGCC by HGCC increased the H amount after 3 days of hydration slightly. At 7 days, mixtures LCC, MCC, and HCC showed similar contents of hydrate water. In comparison with mixture REF, mixtures containing calcined clay showed a much higher amount of CH on the first day of hydration. Increasing HGCC content may contribute to accelerating hydration in the first day. The CH percentage of mixtures LCC, MCC, and HCC kept an increasing trend within the first two days. Afterwards, a significant reduction in the amount of CH was observed until the material age of 7 days. The mixture with a higher HGCC% in calcined clay demonstrated a higher reduction of CH content. Mixture HCC had the lowest CH content already from the second day. However, mixture REF exhibited a much more amount of CH from the second day in contrast to the mixtures containing calcined clay. As mentioned earlier, the consumption of CH could be due to the pozzolanic reaction, which was also indicated as the AFm peak (peak III) in Figure 5.17(a). Since this reaction is still under investigation, it was not discussed further in this chapter.

## 5.4. DISCUSSION

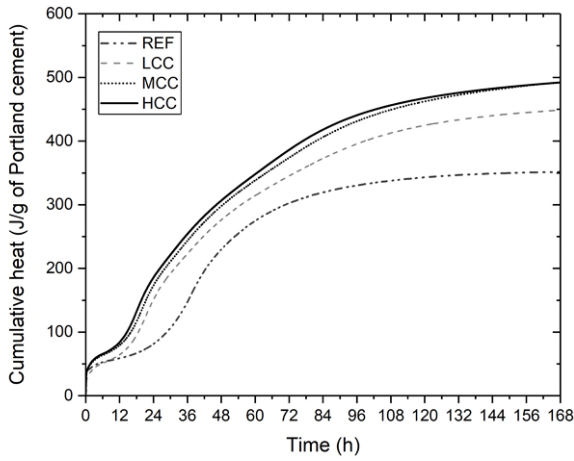
### 5.4.1. EFFECT OF INCREASING HGCC CONTENT ON 3D PRINTABILITY

In this study, both the average grain size ( $D_{v50}$ ) and SSA of LGCC are much larger than PC and LP. Partially replacing the content of LP by LGCC resulted in increased  $SSA_{total}$  of the mixture (Table 5.4). HGCC showed a slightly higher SSA than LGCC and much finer grain size when compared to other dry components (LP, PC, and LGCC). According to [21–23], at a similar water-to-solid ratio, the mean distance between the surface of particles ( $\delta$ ) could be expressed as:

$$\delta = d_{SSA} \left( \left( \frac{\phi}{\phi_m} \right)^{-\frac{1}{3}} - 1 \right) \quad (5.7)$$

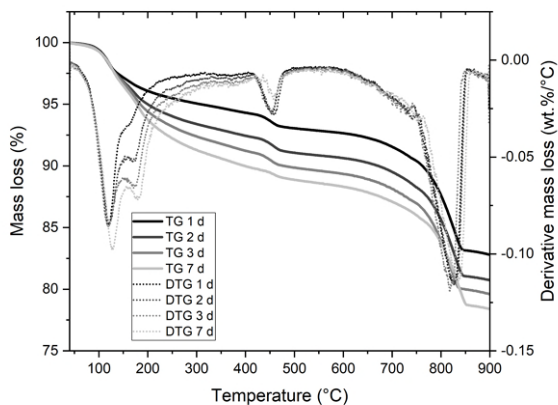


(a)

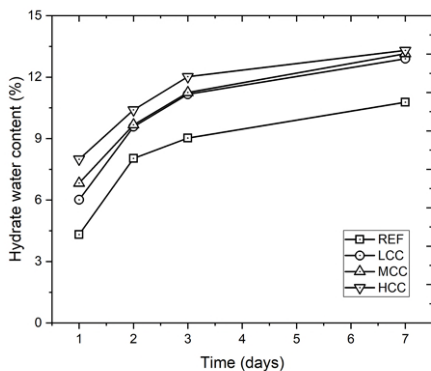


(b)

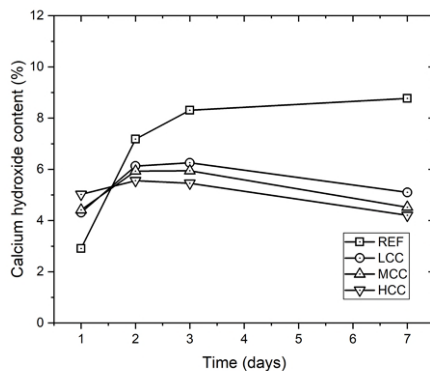
Figure 5.16: Isothermal calorimetry test results of (a) Normalized heat flow with time (4 days). (I)-main hydration peak, (II)-aluminate peak, (III)-AFm reaction peak; and (b) Normalized cumulative heat with time (7 days).



(a)



(b)



(c)

Figure 5.17: TGA at 1, 2, 3, and 7 days: (a) A typical example of TG and DTG curves (mixture HCC); (b) The normalized amount of hydrate water (H) relative to the dry sample weight at 600 °C; (c) The normalized amount of calcium hydroxide (CH) relative to the dry sample weight at 600 °C.

Table 5.7: TG test results-the normalized amount of calcium hydroxide (CH) and hydrate water (H) at 1, 2, 3, and 7 days.

Mixture	Time [days]	H [wt.%]	CH [wt.%]
REF	1	4.31	2.91
	2	8.03	7.18
	3	9.03	8.31
	7	10.77	8.77
LCC	1	6.01	4.31
	2	9.58	6.13
	3	11.16	6.25
	7	12.90	5.10
MCC	1	6.83	4.41
	2	9.67	5.93
	3	11.25	5.94
	7	13.14	4.52
HCC	1	7.99	5.02
	2	10.40	5.56
	3	12.02	5.46
	7	13.30	4.21

$$d_{SSA} = \frac{6}{SSA_{total} \times \rho} \quad (5.8)$$

where  $d_{SSA}$  represents the average diameter from the specific surface area, and  $\rho$  is the density of the binder mixture.  $\phi$  and  $\phi_m$  stand for the solid volume fraction and the maximal packing fraction of solid, respectively.  $\phi_m$  is not a well-defined parameter that depends on both the spatial distribution of particles and flow history [24]. As suggested in Berodier and Scrivener [21],  $\phi_m$  can be calculated via the model proposed by Hu and de Larrard [25].

$$\phi_m = 1 - 0.45 \left( \frac{d_{min}}{d_{max}} \right)^{0.19} \quad (5.9)$$

where  $d_{min}$  and  $d_{max}$  denote the minimum and maximum particle diameters in the mixture. Note that, according to Roussel et al. [23], the obtained result via Eq 5.9 may overestimate the value of  $\phi_m$ . As suggested in [21, 23, 24],  $\phi_m$  is assumed as 0.64 for cementitious pastes. Thus, 0.64 was used as the value of  $\phi_m$  in the case of the computed value via Eq 5.9 is larger than 0.64. The effect of admixtures and aggregate on mean interparticle distance was not taken into consideration in this study. Figure 5.18(a) indicates that increasing the  $SSA_{total}$  could significantly decrease the average interparticle distance.

The partial replacement of LGCC by HGCC in this study could change not only the chemical composition (metakaolin content), but also the physical properties of the binder, i.e., total SSA of solid, and mean interparticle distance (see Figure 5.18(a)). Since the ram extrusion test was performed at the material age of 15 min, the physical properties of the powder skeleton may dominate the extrusion rheology of fresh mixture at a constant water-to-binder ratio. An inversely proportional correlation between the mean interparticle distance and flow consistency of the fresh mixture was illustrated in Figure 5.18(b). The shear between particles was increased as the interparticle distance diminished [21]. As mentioned by Yahia et al. [26], the increase of interparticle friction induced by the increase of solid to solid contact can be one reason

for the increase of viscosity. Figure 5.18(b) also shows the relationship between mean particle distance and shear yield stress of fresh mixtures. It seemed that the shear yield stress rarely increased until the mean interparticle distance was smaller than a critical value. To my knowledge, the reason associated with this phenomenon is still not clear.

The open time under the printing speed of 2820 mm/min was reduced by increasing HGCC% in calcined clay. In this study, the fresh mixture was not printed continuously during the test, and there was a time interval (5 min) between two subsequent printing sessions. From a microscale view, cement particles may experience flocculation, and nucleation during the time interval. Non-reversible hydrate bonds may have been formed between particles, which could still be broken under the effect of sufficient external remixing or shearing force [27, 28]. Thus, it is feasible to print the fresh mixture after a short pre-pumping session (5 min) at an earlier age. Nevertheless, the chemical bonds between particles could be rebuilt again at rest [27]. A fixed remixing or shearing force from the printing system seemed insufficient to destroy all the interparticle connections with time passing. Eventually, the significant workability loss led to the termination of the test.

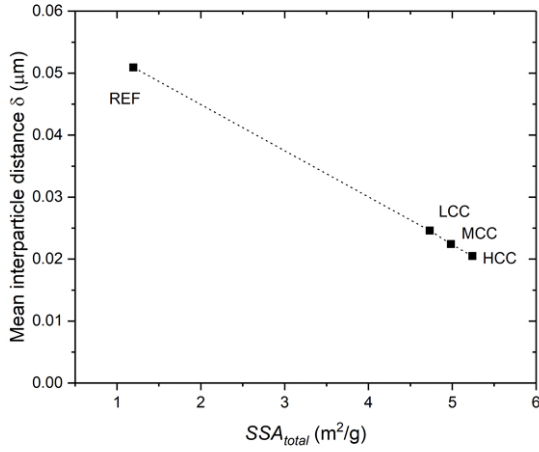
5

According to [29, 30], the buildability was dominated by the structural build-up behavior of fresh mixture at rest at a series of constant printing parameters (printing speed, time interval, printing setup, and the geometry of the printing path). From a macroscopic observation, increasing the HGCC content in calcined clay could enhance the buildability of fresh mixture, which indicated the increase of structural build-up at rest. Blending HGCC in the mixture may contribute to the enhancement of particle flocculation and increased water adsorption induced by physical characteristics of HGCC particles, i.e., the fine grain size, high specific surface area, and layered structure [31]. However, the obtained results in this study are still insufficient to explain this phenomenon.

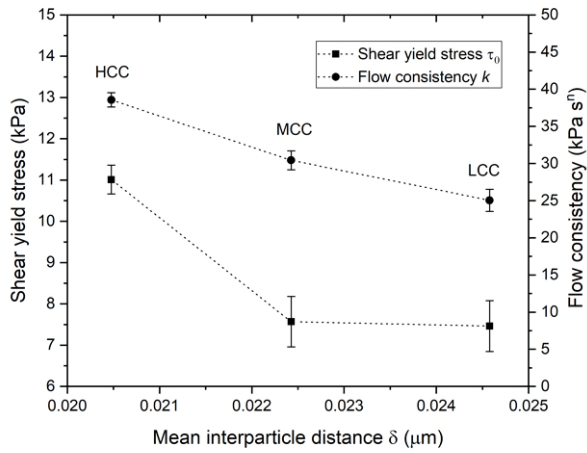
#### 5.4.2. EFFECT OF INCREASING HGCC CONTENT ON HYDRATION KINETICS

Adding calcined clay in mixtures could significantly accelerate the cement hydration (Figure 5.16(a)), and increase the content of hydration products (CH and H) after the first day (Figures 5.17(b) and 5.17(c)). For mixtures containing calcined clay, 1-day hydration was also accelerated by increasing the HGCC content. The filler effect induced by calcined clay may play the dominant role during the first day of hydration. Increasing HGCC% in calcined clay seemed to promote its filler effect further. Berodier and Scrivener [21] reported that the interparticle distance was the most critical factor in influencing the reaction rate of  $C_3S$  hydration. The relationship between the slope of the acceleration period of the main peak and the mean interparticle distance of different binder systems is presented in Figure 5.19. The acceleration rate of the main hydration peak was obtained according to [32, 33]. Figure 5.19 indicates that the acceleration rate was increased by reducing the average interparticle distance, which agreed with the findings from [21].





(a)



(b)

Figure 5.18: Relationship between: (a) Mean interparticle distance and total SSA of solid; (b) Mean interparticle distance and shear yield stress as well as flow consistency obtained in ram extrusion test.

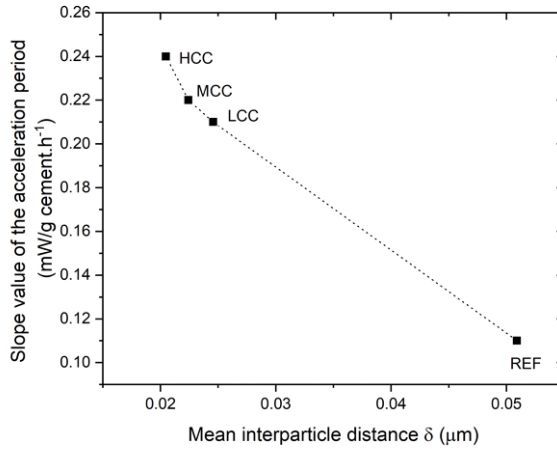


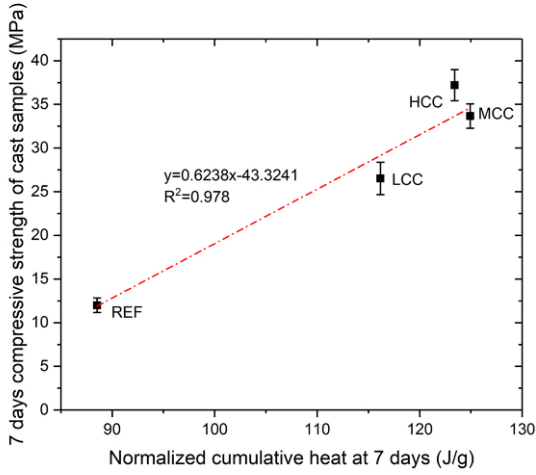
Figure 5.19: Slope value of the acceleration period as a function of the mean interparticle distance.

### 5.4.3. EFFECT OF INCREASING HGCC CONTENT ON COMPRESSIVE STRENGTH

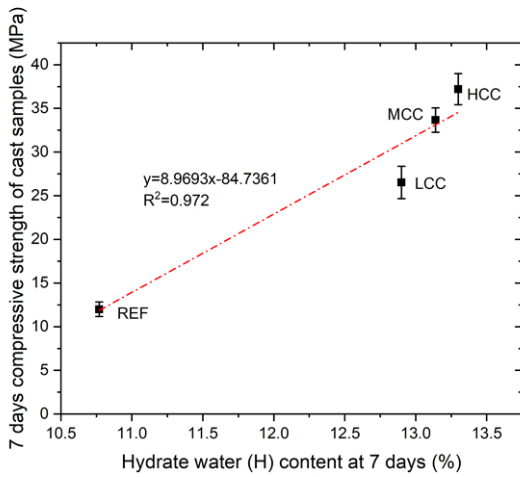
The compressive strength at 7 days was measured on both mold-cast and printed samples. According to the test results from [18], increasing the metakaolin content in calcined clay could increase the 7 days compressive strength of LC3-50 system mortar. The test results of cast samples in this chapter confirmed these findings. In this study, the only difference for different mixtures is the calcined clay composition. Here I assumed that the air void content and distribution of cast samples were similar among different mixtures. Thus, the compressive strength of cast samples might mainly rely on the hydration of cementitious materials. Positive correlations were obtained between compressive strength of cast samples and normalized cumulative heat (mixtures HCC and MCC showed very close results), as well as the hydrate water content at 7 days in Figure 5.20.

However, these correlations could not be formulated for the compressive strength of printed samples. The printed sample of mixture HCC showed the weakest compressive strength at 7 days (see Figure 5.13). Generally, for quasi-brittle materials, the increment of porosity could lead to a proportional reduction of strength [34]. Macropores, especially air voids, may dominate the mechanical performance of printed concrete. In this study, mixture HCC showed the weakest compressive strength, which may be attributed to the highest air void content at the interface (maximum value, see Figure 5.14) of its printed sample.

The possible reasons why the mixtures containing HGCC showed large and more air voids in the interface zone were summarized as follows. First, according to [27, 30], for the same time interval and printing environment conditions (ambient temperature and relative humidity), the cold-joint/weaker interface could be easily formed by using a fresh mixture with a high thixotropy/structuration rate. Thus, in this context, the high



(a)



(b)

Figure 5.20: The linear relationship between: (a) 7 days compressive strength and normalized cumulative heat at 7 days (excluding any heat within the first 12 h after mixing) obtained from isothermal calorimetry test; (b) 7 days compressive strength and hydrate water (H) content at 7 days obtained from TGA.

air void content between layers could be attributed to the high structuration rate of the fresh mixture. Second, in the case of mixtures containing HGCC (mixtures MCC and HCC), after the top layer deposition, the deformation of the substrate was smaller than that of mixture LCC due to the fast growth of material stiffness (as indicated by the high buildability). This may be attributed to the fast particle flocculation and accelerated surface drying process induced by HGCC. Consequently, many unfilled areas were kept forming large air voids between two subsequent layers, as shown in Figure 5.15.

However, in comparison to mixture LCC, the printed sample of mixture MCC exhibited stronger compressive strength, even containing a higher content of air voids at the interface region (see Figure 5.14). Therefore, the compressive strength of printed concrete should rely on both the hydration degree of cementitious materials and the air void content at the interface region.

### 5.5. CONCLUSION

THE results yielded from this study indicated the considerable effects of different grades of calcined clays on 3D printability, compressive strength, and hydration of limestone and calcined clay-based cementitious materials. The findings are summarized as follows:

- For the ram extrusion rheology, an excellent correlation between experimental results and Basterfield et al. model was obtained. Increasing HGCC% in calcined clay could modify not only the metakaolin content, but also the physical property of the fresh mixture, i.e., the increase of total specific surface area, and decrease of mean interparticle distance, which may be the primary reason for the increase of flow consistency of the fresh mixture. A steeper increase of shear yield stress was found between mixtures MCC and HCC, whereas mixture LCC showed a very close value to that of mixture MCC.
- By increasing the HGCC content, the buildability of fresh mixture was noticeably improved, whereas the open time was reduced. A possible reason was that blending HGCC in the mixture may contribute to the enhancement of particle flocculation and increased water adsorption induced by the fine grain size, high specific surface area, and layered structure of HGCC particles. However, further study is needed to validate this.
- Calcined clay addition (mixtures LCC, MCC, and HCC) resulted in the acceleration of hydration as compared to limestone (mixture REF). The 1-day hydration was enhanced due to the increase in the replacement of HGCC, which may be attributed to the reduction of the mean interparticle distance. A positive correlation between the slope value of the acceleration period and the average interparticle distance was observed.
- For the mold-cast samples, the mixture with higher dosage of HGCC displayed a stronger compressive strength at 7 days, and the hydration degree played a dominant role in the compressive strength development. The obtained results showed a linear relationship between the compressive strength of cast samples

and the normalized cumulative heat as well as the hydrate water content at 7 days.

- For the printed samples, the compressive strength at 7 days was not only dependent on the hydration degree but also on the structural build-up of fresh mixtures at rest. The results confirmed that fresh mixtures with good buildability might be vulnerable to enclose more air voids for forming cold joint/weak interface between two adjacent layers. Due to the increase of metakaolin content (HGCC%), more and larger air voids were found in the interface zone, which weakened the compressive strength of printed cementitious materials.

## REFERENCES

- [1] Y. Chen, C. R. Rodriguez, Z. Li, B. Chen, O. Çopuroğlu, and E. Schlangen, *Effect of different grade levels of calcined clays on fresh and hardened properties of ternary-blended cementitious materials for 3D printing*, *Cement and Concrete Composites* **114**, 103708 (2020).
- [2] R. Basterfield, C. Lawrence, and M. Adams, *On the interpretation of orifice extrusion data for viscoplastic materials*, *Chemical Engineering Science* **60**, 2599 (2005).
- [3] NEN-EN 196-2, *Method of testing cement - Part 2: Chemical analysis of cement*, (2013).
- [4] X. Zhou, Z. Li, M. Fan, and H. Chen, *Rheology of semi-solid fresh cement pastes and mortars in orifice extrusion*, *Cement and Concrete Composites* **37**, 304 (2013).
- [5] A. Perrot, Y. Mélinge, D. Rangeard, F. Micaelli, P. Estellé, and C. Lanos, *Use of ram extruder as a combined rheo-tribometer to study the behaviour of high yield stress fluids at low strain rate*, *Rheologica Acta* **51**, 743 (2012).
- [6] V. N. Nerella, M. Krause, and V. Mechtcherine, *Direct printing test for buildability of 3D-printable concrete considering economic viability*, *Automation in Construction* **109**, 102986 (2020).
- [7] B. Lothenbach, P. Durdzinski, and K. De Weerd, *Thermogravimetric analysis*, in *A Practical Guide to Microstructural Analysis of Cementitious Materials*, edited by K. Scrivener, R. Snellings, and B. Lothenbach (CRC press, 2016) Chap. 5, pp. 177–212.
- [8] Y. Chen, S. Chaves Figueiredo, Yalçinkaya, O. Çopuroğlu, F. Veer, and E. Schlangen, *The effect of viscosity-modifying admixture on the extrudability of limestone and calcined clay-based cementitious material for extrusion-based 3D concrete printing*, *Materials* **12**, 1374 (2019).
- [9] T. Le, S. Austin, S. Lim, R. Buswell, R. Law, A. Gibb, and T. Thorpe, *Hardened properties of high-performance printing concrete*, *Cement and Concrete Research* **42**, 558 (2012).

- [10] B. Panda, S. Chandra Paul, and M. Jen Tan, *Anisotropic mechanical performance of 3D printed fiber reinforced sustainable construction material*, *Materials Letters* **209**, 146 (2017).
- [11] B. Panda, G. B. Singh, C. Unluer, and M. J. Tan, *Synthesis and characterization of one-part geopolymers for extrusion based 3D concrete printing*, *Journal of Cleaner Production* **220**, 610 (2019).
- [12] Y. Chen, K. Jansen, H. Zhang, C. Romero Rodriguez, Y. Gan, O. Copuroglu, and E. Schlangen, *Effect of printing parameters on interlayer bond strength of 3D printed limestone calcined clay-based cementitious material: An experimental and numerical study*, *Construction and Building Materials* **262**, 120094 (2020).
- [13] P. S. de Silva and F. P. Glasser, *Hydration of cements based on metakaolin: Thermochemistry*, *Advances in Cement Research* **3**, 167 (1990).
- [14] J. W. Bullard, H. M. Jennings, R. A. Livingston, A. Nonat, G. W. Scherer, J. S. Schweitzer, K. L. Scrivener, and J. J. Thomas, *Mechanisms of cement hydration*, *Cement and Concrete Research* **41**, 1208 (2011).
- [15] Y. Chen, S. Chaves Figueiredo, Z. Li, Z. Chang, K. Jansen, O. Çopuroğlu, and E. Schlangen, *Improving printability of limestone-calcined clay-based cementitious materials by using viscosity-modifying admixture*, *Cement and Concrete Research* **132**, 106040 (2020).
- [16] D. Jansen, F. Goetz-Neunhoeffer, B. Lothenbach, and J. Neubauer, *The early hydration of Ordinary Portland Cement (OPC): An approach comparing measured heat flow with calculated heat flow from QXRD*, *Cement and Concrete Research* **42**, 134 (2012).
- [17] F. Zunino and K. Scrivener, *The influence of the filler effect on the sulfate requirement of blended cements*, *Cement and Concrete Research* **126**, 105918 (2019).
- [18] F. Avet and K. Scrivener, *Investigation of the calcined kaolinite content on the hydration of Limestone Calcined Clay Cement (LC3)*, *Cement and Concrete Research* **107**, 124 (2018).
- [19] R. Roychand, S. De Silva, D. Law, and S. Setunge, *High volume fly ash cement composite modified with nano silica, hydrated lime and set accelerator*, *Materials and Structures/Materiaux et Constructions* **49**, 1997 (2016).
- [20] M. Antoni, J. Rossen, F. Martirena, and K. Scrivener, *Cement substitution by a combination of metakaolin and limestone*, *Cement and Concrete Research* **42**, 1579 (2012).
- [21] E. Berodier and K. Scrivener, *Understanding the filler effect on the nucleation and growth of C-S-H*, *Journal of the American Ceramic Society* **97**, 3764 (2014).
- [22] F. De Larrard, *Concrete Mixture Proportioning: A Scientific Approach*, in *E & FN SPON* (CRC Press, London, 2005).

- [23] N. Roussel, A. Lemaître, R. J. Flatt, and P. Coussot, *Steady state flow of cement suspensions: A micromechanical state of the art*, Cement and Concrete Research **40**, 77 (2010).
- [24] P. Coussot, *Introduction to the rheology of complex fluids*, in *Understanding the Rheology of Concrete* (Woodhead Publishing, 2011) pp. 3–22.
- [25] C. Hu and F. de Larrard, *The rheology of fresh high-performance concrete*, Cement and Concrete Research **26**, 283 (1996).
- [26] A. Yahia, M. Tanimura, and Y. Shimoyama, *Rheological properties of highly flowable mortar containing limestone filler-effect of powder content and W/C ratio*, Cement and Concrete Research **35**, 532 (2005).
- [27] N. Roussel, *Rheological requirements for printable concretes*, Cement and Concrete Research **112**, 76 (2018).
- [28] N. Roussel, G. Ovarlez, S. Garrault, and C. Brumaud, *The origins of thixotropy of fresh cement pastes*, Cement and Concrete Research **42**, 148 (2012).
- [29] A. Perrot, D. Rangeard, and A. Pierre, *Structural built-up of cement-based materials used for 3D-printing extrusion techniques*, Materials and Structures/Materiaux et Constructions **49**, 1213 (2016).
- [30] T. Wangler, E. Lloret, L. Reiter, N. Hack, F. Gramazio, M. Kohler, M. Bernhard, B. Dillenburger, J. Buchli, N. Roussel, and R. Flatt, *Digital concrete: opportunities and challenges*, RILEM Technical Letters **1**, 67 (2016).
- [31] T. R. Muzenda, P. Hou, S. Kawashima, T. Sui, and X. Cheng, *The role of limestone and calcined clay on the rheological properties of LC3*, Cement and Concrete Composites **107**, 103516 (2020).
- [32] E. Berodier, *Impact of the Supplementary Cementitious Materials on the kinetics and microstructural development of cement hydration*, Ph.D. thesis (2015).
- [33] M. M. Costoya Fernandez, *Effect of Particle Size on the Hydration Kinetics and Microstructural Development of Tricalcium Silicat*, Ph.D. thesis, EPFL (2008).
- [34] D. Liu, B. Šavija, G. E. Smith, P. E. Flewitt, T. Lowe, and E. Schlangen, *Towards understanding the influence of porosity on mechanical and fracture behaviour of quasi-brittle materials: experiments and modelling*, International Journal of Fracture **205**, 57 (2017).





# 6

## CHARACTERIZATION OF AIR-VOID SYSTEMS IN 3D PRINTED CEMENTITIOUS MATERIALS USING OPTICAL IMAGE SCANNING AND X-RAY COMPUTED TOMOGRAPHY

*To date, far too little attention has been paid to reveal the air void characteristics in 3D printed cementitious materials. Therefore, to fill this gap, this chapter attempts to provide an example of systematically characterizing the typical air void system of 3D printed cementitious materials via different image acquisition and analysis techniques. Two printable limestone and calcined clay-based mixtures were employed to prepare the printed samples. The micrographs were acquired by using optical image scanning and X-ray computed tomography. Afterwards, air void metrics in printed cementitious materials were determined, i.e., content, distribution, size, and shape. The results revealed that most of the air voids with the diameter in the range of 10-1000  $\mu\text{m}$  were distributed evenly in the layer region of printed samples. Large air voids (1000-6000  $\mu\text{m}$ ) were enclosed mainly between the printed filaments (interface region), which resulted in the relatively higher local porosity than that of layer region. Additionally, the majority of air voids displayed irregular and elongated shapes, which could be attributed to the extrusion and layer-wise manufacturing processes in 3D printing. Finally, a comparison between optical image scanning and X-ray computed tomography was given.*

## 6.1. INTRODUCTION

OWING to the differences in fresh properties and manufacturing processes, the air void system in 3D printed cementitious materials should differ from that of the mold-cast cementitious materials. According to Aitcin [2], the viscosity of paste, the size of coarse aggregate, the consistency of fresh mixture, and the condition of vibration and compaction influence the formation of entrapped air voids in hardened concrete. As reported by [3], the viscosity of fresh mixtures for extrusion-based 3D concrete printing (3DCP) may be higher than that of mold-cast concrete to avoid water drainage and ensure the stability of the layered structure during the printing process. Also, there are no vibration and compaction processes in 3DCP. The extrusion process in 3DCP may influence the air void parameters, such as shape, size, and distribution.

For implementing 3DCP in building construction, the investigation into the mechanical performance of 3D printed cementitious materials needs to be prioritized. The strength and elasticity of hardened cementitious materials are mainly influenced by capillary pores and air voids [4, 5]. For mold-cast concrete, increasing about 1% of air voids could lead up to a 4-5% reduction in the compressive strength [6, 7]. Due to the layer-wise manufacturing processes, many interlayers were formed in a 3D printed structure. The interlayer bonding (also known as interface adhesion) is considered as a weakness of the 3D printed structure [8–10], which is attributed to the limited intermixing between two subsequent layers [11]. High amount of air voids between the layers as a typical phenomenon can be found in many 3D printed cementitious materials with a weak interface adhesion [8, 12, 13]. Under scanning electron microscope, Nerella et al. [8] observed many longitudinal cavities induced by entrapped air voids between two layers in their printed sample that showed weak mechanical performance. Similarly, others [12, 14] reported that increasing the air void content in the interlayer region could result in a severe reduction of interface adhesion. Therefore, for some 3D printed cementitious materials, air voids may play a dominant role in the interlayer bond strength. Quantitative air void characterization of 3D printed cementitious materials becomes quite essential for assessing and predicting the corresponding mechanical performance. Additionally, the air void analysis could be considered as a useful method for selecting the optimal mix design and printing parameters (e.g., time intervals between layers, nozzle standoff distances, printing speeds, and others) for 3DCP research.

The air void characterization of mold-cast concrete is typically done using both fresh and hardened cementitious materials. Ley et al. [15] proposed an approach to measure the size and spacing factor of air voids in fresh concrete. However, analysis of air voids in hardened cementitious materials appears more frequently in literature. As indicated in earlier studies [16–18], digital image acquisition and processing is a powerful tool, widely implemented to investigate the microstructure of materials. The air voids in hardened cementitious materials can be rapidly determined via stereological examination of polished sections or thin sections using an optical microscope or flatbed scanner, and quantified by 2D/1D approaches (e.g., linear-traverse method, and point-count method from ASTM C457-98 [19], as reported by [5, 6, 18, 20–23]). However, air bubbles are distributed in a 3D space of hardened cementitious materials. Only using the 2D approach could not indicate

anisotropy/heterogeneity of air voids in studied samples. X-ray computed tomography was therefore employed by many researchers [24–28] for acquiring digital images that allowed assessing the 3D heterogeneity of air void structure.

In the case of 3D printed cementitious materials, earlier studies [29, 30] have attempted to determine the air void content using X-ray computed tomography scanning and image analysis. However, to my knowledge, few researchers have been able to draw on any systematic research into characterizing air void system of 3D printed cementitious materials. On the other hand, optical microscope (or scanner) is widely available in the majority of laboratories, whereas micro-computed tomography (Micro-CT) scanner is not. Thus, it is worthwhile to explore to what extent can the air void characteristics of 3D printed cementitious materials be reliably determined using optical microscopy (or scanning) for thin- and polished-section analyses, in comparison with X-ray computed tomography.

The objective of this chapter is to systematically characterize the typical air void system of 3D printed cementitious materials via digital image analysis. Two limestone and calcined clay-based 3D printable cementitious materials with different interlayer properties that were developed in Chapter 5 were used to prepare the printed samples. Optical image scanning and X-ray computed tomography, as two distinct techniques, were employed to acquire digital images. Afterwards, binary images, containing only air voids, were segmented from the obtained images. Air voids of 3D printed cementitious materials could therefore be studied in characteristics of content, distribution, size, and shape by different approaches. Additionally, a discussion about possible reasons for air void formation in printed cementitious materials is offered. Furthermore, a comparison between the two employed methodologies, optical image scanning and X-ray computed tomography, is given.

## 6.2. MATERIALS AND METHODS

### 6.2.1. PRINTABLE MIXTURE DESIGN

TWO printable mixtures that were presented in Chapter 5 were used in the current study (see Table 6.1).

Table 6.1: Mixture proportions of printable cementitious materials (% of the binder mass).

Mixture	PC	LGCC	HGCC	LP	Water	Sand	SP	VMA
M1	40	20	20	20	150	30	2	0.24
M2	40	30	10	20	150	30	2	0.24

### 6.2.2. SAMPLE PREPARATION

A hybrid down- and back-flow based nozzle with a rectangle opening (width: 40 mm; height: 12 mm) was adopted in this study to print the filament with the rectangular cross-section. The fresh mixture was prepared by following protocols in Figure 4.1. Based on fixed printing parameters (Table 6.2), a beam that contained 5 vertically stacked layers was manufactured per mixture. The length of each layer was 900 mm. For the first 24 h after printing, the printed beam was cured under the plastic film at the

ambient environment ( $20 \pm 2$  °C, and about 55% relative humidity). After that, the sample was stored in a fog room with  $20 \pm 2$  °C, and 99% relative humidity until it was 28-day-old. The samples for air void analysis were extracted at the end of the curing.

The dimensions and extracted positions of the specimens are illustrated in Figure 6.1. Note that, each specimen contained three interlayer regions. The specimen preparation of thin sections was derived from earlier studies [31, 32]. Before polishing, the extracted prisms were impregnated by using low-viscosity epoxy with fluorescent pigment. Standard thin sections with a thickness of  $30 \mu\text{m}$  (approximately  $27 \mu\text{m}$  of cementitious material, and  $3 \mu\text{m}$  of mounting glue) were obtained via a semi-automatic thin sectioning machine. Lab-grade ethanol was utilized as coolant during processes of cutting, grinding, and polishing. For X-ray computed tomography (CT) scanning, cylindrical samples ( $\varnothing 25 \text{ mm}$ ; height: 40 mm) were drilled and sawn from the printed beam.

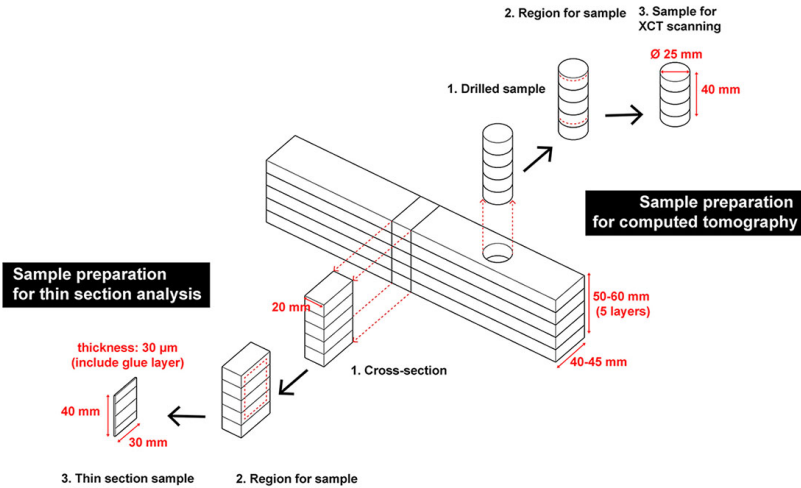


Figure 6.1: Illustration of sample preparation for thin section analysis, and X-ray computed tomography.

Table 6.2: Printing parameters.

Printing parameters	
Printing start time (Material age) [min]	15
Time interval between two layers [min]	1.5
Material flow rate [L/min]	1.7
Nozzle moving speed [mm/min]	3600
Nozzle opening [mm <sup>2</sup> ]	12 × 40
Layer thickness [mm]	10-12
Nozzle standoff distance [mm]	0

### 6.2.3. IMAGE ACQUISITION AND SEGMENTATION

### THIN SECTION

To capture images of entire thin sections, a digital film and photo scanner (Epson Perfection V800) with a resolution of up to 4800 dpi was used. A region of interest (ROI) (35 mm in length and 14.5 mm in width) was extracted from each scanned image for air void analysis (see Figure 6.2). The resolution of scanned image was  $7.2 \mu\text{m}/\text{pixel}$ . Thin sections were also studied with a Leica DM2500P optical microscope equipped with polarization and fluorescence capability. A Leica DFC310FX digital camera was implanted in the optical microscope to acquire optical micrographs of the thin sections at  $1392 \times 1040$  un-interpolated resolution. All acquired images were exported as uncompressed tagged image file format (TIFF) images. The segmentation of air voids in scanned thin sections was carried out by Trainable Weka Segmentation (TWS) plugin from a freeware image processing software ImageJ [33]. The segmentation process via the method of TWS is illustrated in Figure 6.2.

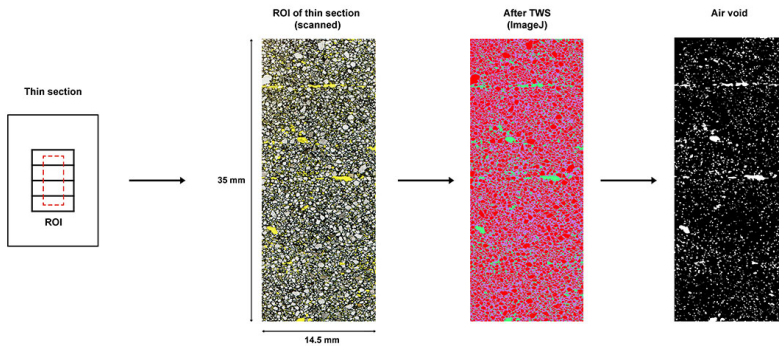


Figure 6.2: ROI of the thin section and TWS segmentation process.

### X-RAY COMPUTED TOMOGRAPHY

A Micro-CT scanner (Phoenix Nanotom) was used to obtain the microstructure of small cylindrical sample ( $\varnothing$  25 mm; height: 40 mm). By using the dedicated Phoenix Datas|x software, reconstructed slices were carried out (Details about CT scanning can be found in Section 4.2.7, Chapter 4). The resolution of obtained slices was  $27 \mu\text{m}/\text{pixel}$ . For each sample, 1297 transverse planes/cross-sections (CT-TP) and 40 longitudinal planes (CT-LP) of grayscale value (GSV) images were obtained for performing image analysis (see Figure 6.3).

ImageJ was also employed for conducting the image segmentation. However, instead of TWS, the thresholding method was adopted to segment air voids in GSV images for saving computation time. An example of image segmentation result was illustrated in Figure 6.4.

#### 6.2.4. AIR VOID CHARACTERIZATION

Air voids of 3D printed cementitious materials were investigated in terms of content, distribution, size, and shape. Different approaches to characterizing the air void systems

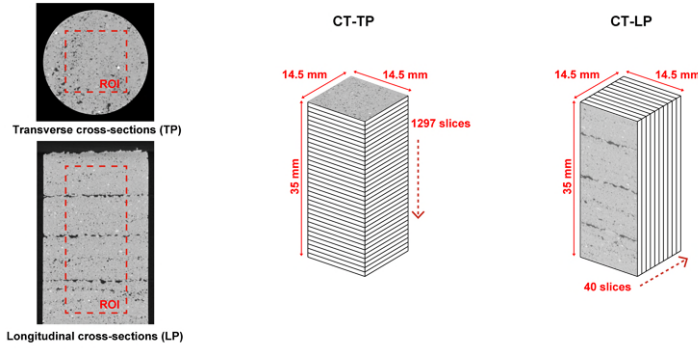


Figure 6.3: CT-TP and CT-LP GSV images extracted from the reconstructed 3D volume.

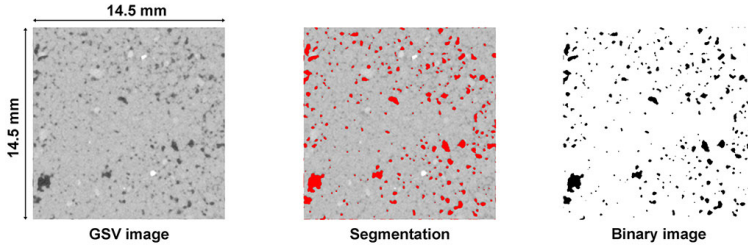


Figure 6.4: An example of air void segmentation of GSV image.

were summarized in Table 6.3. Three aspects of air void characterization were presented as follows.

#### CONTENT AND DISTRIBUTION

For TS and CT-LP images (after segmentation), the air void content and distribution of each image were computed and analyzed via a MATLAB-code. Air void pixels were counted in every linear-row per image. The local porosity ( $P_{lp}$ ) and air void content ( $V_{lp}$ ) was calculated through Eq 6.1 and Eq 6.2, respectively.

$$P_{lp} = \frac{M_{row}}{T_{row}} \quad (6.1)$$

$$V_{lp} = \frac{M_{image}}{T_{image}} \quad (6.2)$$

where  $M_{row}$  is the pixel number of air void per row, and  $T_{row}$  represents the total pixel number per row.  $M_{image}$  and  $T_{image}$  stand for the pixel number of air void and total pixel number per image, respectively. In the case of CT-TP images, the local porosity ( $P_{tp}$ ) that was equal to air void content of each transverse slice can be computed via Eq

6.3. For calculating air voids content ( $V_{tp}$ ), Eq 6.4 was used.

$$P_{tp} = \frac{M_{image}}{T_{image}} \quad (6.3)$$

$$V_{tp} = \frac{V_{air}}{V_{total}} \quad (6.4)$$

where  $V_{air}$  is the total air volume of ROI prism, and  $V_{total}$  is the volume of ROI prism. The air void volume was measured by using 3D Objects Counter plugin from ImageJ.

#### SIZE DISTRIBUTION

For some 3D printed cementitious materials with weak interlayer bondings, it has been found that the air voids in the interface region exhibited a larger average size than that of other regions (see Figure 5.14, Chapter 5). The coarse pore probably induced by merging and overlapping of entrapped air voids could weaken the mechanical performance of printed structure significantly. Thus, it is necessary to quantify the air void size distribution in this context. The area of each pore in TS and CT-LP images and the volume of each pore in the reconstructed 3D volume using CT-TP images were determined by Analyze Particles and 3D Objects Counter (ImageJ), respectively. The pore diameter was generally used to describe the pore size. 2D and 3D pore diameter ( $d_{2D}$ ,  $d_{3D}$ ) could be computed via Eq 6.5 and Eq 6.6, respectively.

$$d_{2D} = \sqrt{\frac{4Area}{\pi}} \quad (6.5)$$

$$d_{3D} = \sqrt[3]{\frac{6Volume}{\pi}} \quad (6.6)$$

Besides, to characterize the pore size along with the sample height, the average 2D air void diameter of every CT-TP image was calculated as well.

#### SHAPE PROPERTY

The morphology of air voids was observed on optical micrographs of thin sections and visualized in 3D through using CT-TP images. This is a qualitative way to illustrate the distribution and shape of air voids. Furthermore, 2D circularity and 2D aspect ratio of each pore, as given in Eq 6.7 and Eq 6.8, were used to quantify the shape properties of air voids in TS and CT-LP images. The shape of air voids is close to a perfect circle when the value of circularity is about 1. Elongated/concave pores appeared in the interface area can be directly observed in longitudinal cross-sections of printed samples (see Figure 6.5). The aspect ratio was employed to evaluate the elongation magnitude of the pore structure.

$$Circularity = \frac{4\pi A}{S^2} \quad (6.7)$$

$$Aspectratio = \frac{w}{h} \quad (6.8)$$

where  $A$ ,  $S$ ,  $w$ , and  $h$  are the area, perimeter, horizontal width, and vertical height of an air void.

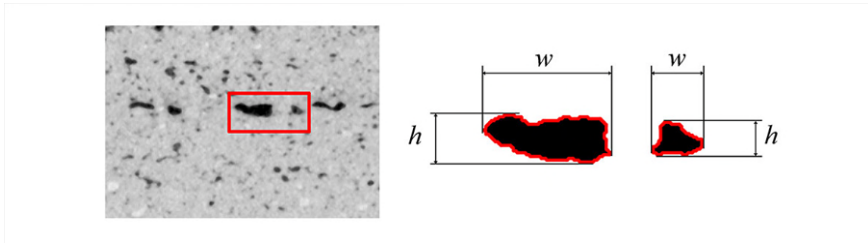


Figure 6.5: Illustration of the horizontal width and vertical height of the air void.

Table 6.3: Overview of approaches for characterizing the air void system.

Image type	Optical image scanning		X-ray computed tomography	
	Longitudinal sections (TS)	cross-sections (CT-LP) <sup>1</sup>	Longitudinal cross-sections (CT-LP)	Transverse cross-sections (CT-TP)
Slice number (per sample)	1	40	40	1297
Resolution	7.2 $\mu\text{m}/\text{pixel}$	27 $\mu\text{m}/\text{pixel}$	27 $\mu\text{m}/\text{pixel}$	27 $\mu\text{m}/\text{pixel}$
Content and distribution	$P_{lp}$ and $V_{lp}$	$P_{lp}$ and $V_{lp}$	$P_{lp}$ and $V_{lp}$	$P_{tp}$ and $V_{tp}$
Size distribution	$d_{2D}$	$d_{2D}$	$d_{2D}$	$d_{3D}$ and average $d_{2D}$ (per slice)
Morphological study	Optical micrographs		3D visualization	
Shape	2D circularity, 2D aspect ratio	2D circularity, 2D aspect ratio	Average circularity	2D (per slice)

<sup>1</sup> It is also possible to use all CT-LP images (537 slices) to reconstruct 3D volume for performing 3D analysis of air voids, which should generate the same results as using CT-TP images ( $V_{tp}$  and  $d_{3D}$ ). However, the selected CT-LP images in this study were analyzed using the same means for processing TS images to provide more possibilities of the stereological examination.

## 6.3. RESULTS AND DISCUSSION

### 6.3.1. AIR VOID CONTENT AND DISTRIBUTION

BASED on the CT-LP images, the local porosity of samples M1 and M2 is illustrated in Figure 6.6. Additionally, Figure 6.7 shows the local porosity results obtained by TS, CT-LP, and CT-TP images. In general, the air voids were not homogeneously distributed within samples M1 and M2. It could be found that the interface of the printed samples displayed relatively higher air void content compared to other regions, especially sample M1. The position of interface areas could be indicated in Figure 6.6. In comparison with sample M2, sample M1 exhibited much higher air void content in the interface, which agreed with the obtained results in Section 5.3.4, Chapter 5. Magnitude differences of the local porosity results were also observed across measurements. It can be found that less significant differences between CT-TP and CT-LP images compared with that between CT-TP and TS images. As mentioned earlier, the resolution of scanned thin sections is about 7.2  $\mu\text{m}/\text{pixel}$ , which is much smaller than that of GSV images (27  $\mu\text{m}/\text{pixel}$ ) from CT scanning (CT-LP and CT-TP images). Thus, small air bubbles with a theoretical diameter between 7.2  $\mu\text{m}$  and 27  $\mu\text{m}$  were also taken into account in TS images. Additionally, using different image segmentation methods may induce changes in porosity as well.



The results of total air void contents computed by using different images are reported in Figure 6.8. Sample M1 shows a higher void content than sample M2. However, notable differences in the total air void content obtained by using different methods were also found in Figure 6.8. In comparison with the air void content obtained from CT-TP images, a much higher air void content was predicted by TS images, and a slightly lower result was achieved by CT-LP images. Due to the 2D effects, the results measured via TS and CT-LP images may lead to the over-/under-estimation of air void content compared with CT-TP images. Besides, the above-mentioned differences between TS and CT images could also contribute to such deviations.

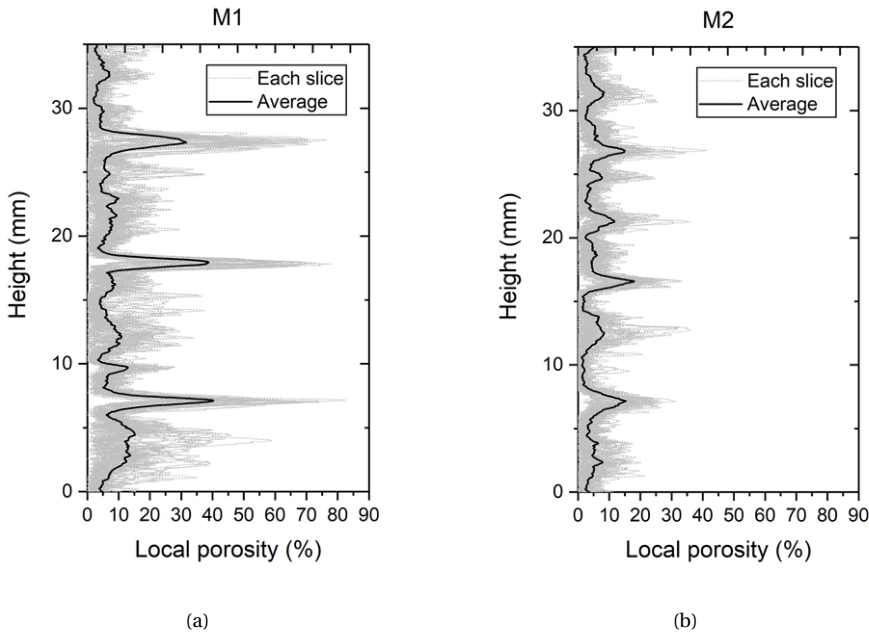
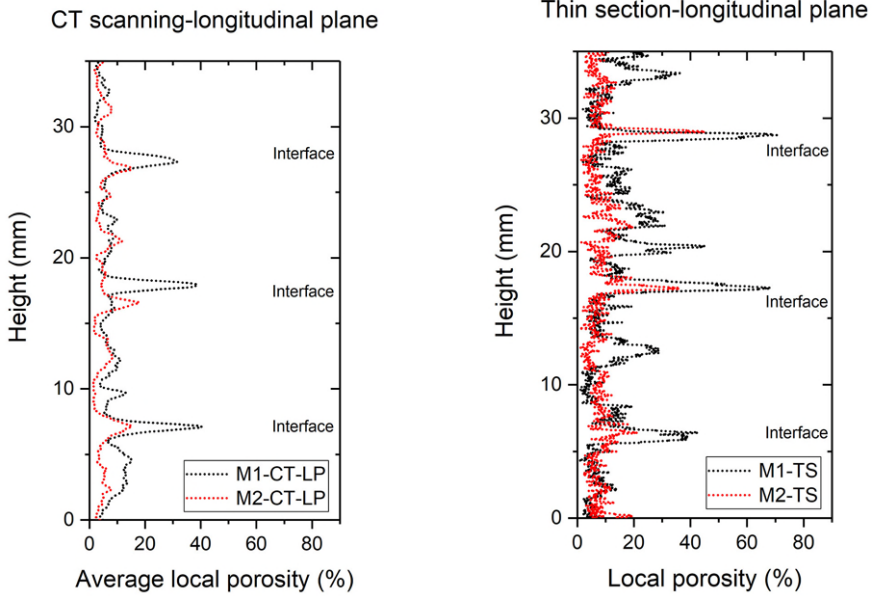


Figure 6.6: Local porosity vs. sample height of samples M1 and M2 based on 40 CT-LP images: (a) Result of sample M1; (b) Result of sample M2. The gray line is the computed result of each slice, and the black curve means the average result from 40 slices.

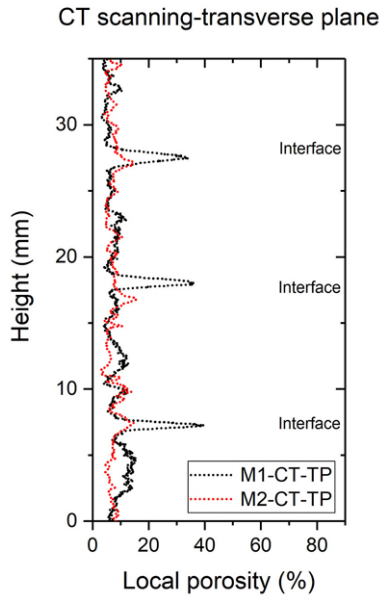
### 6.3.2. AIR VOID SIZE DISTRIBUTION

The CT-TP images for each sample are visualized in 3D, as shown in Figure 6.9. The cyan colored objects in the image represent the air voids within the sample. The air voids were segmented into two groups based on the pore diameter in CT-TP images ( $d_{3D}$  of small and medium air voids: 10-1000  $\mu\text{m}$ ;  $d_{3D}$  of large air void: 1000-6000  $\mu\text{m}$ ). As shown in Figure 6.9, most of the pores in both samples belong to small and medium air voids. The large air voids in sample M1 were mainly distributed in the interface area, whereas a relatively uniform distribution of large air voids throughout the sample was found in sample M2. Rationally, the concentrated pores in the interface area led to the



(a)

(b)



(c)

Figure 6.7: Local porosity vs. sample height of samples M1 and M2: (a) Average result of CT-LP images; (b) Result of TS images; (c) Result of CT-TP images.

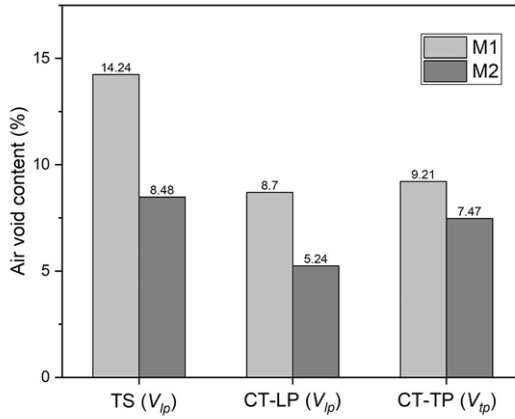


Figure 6.8: Total air void content  $V_{I_p}$  from TS images (Left); Total air void content  $V_{I_p}$  from CT-LP images (Middle); Total air void content  $V_{I_p}$  from CT-TP images (Right).

high local porosity (see Figure 6.7). Besides, Figure 6.13(a) presents the average pore diameter of air voids in each transverse cross-section from the bottom to the top of the sample. Particularly in sample M2, coarser air voids that could result in the high average pore diameter were also indicated in the layer region.

Figures 6.10 and 6.11 present the pore diameter distribution of samples M1 and M2. In general, the medium air voids (100-1000  $\mu\text{m}$ ) accounted for the highest void content across measurements. Sample M1 exhibited a higher volume of large air voids (1000-6000  $\mu\text{m}$ ) than sample M2. The relative frequency of air voids in different size groups is illustrated in Figure 6.12. Magnitude differences of the results between TS and CT (LP and TP) images could be indicated. As shown in Figure 6.12, small air voids (10-100  $\mu\text{m}$ ) possessed the largest relative frequency of overall air voids in the results obtained from TS images. However, for CT-LP and CT-TP images, most of air voids were characterized as medium air voids. As mentioned in the previous section, the differences between TS and CT (-LP and -TP) images in the image resolution and the segmentation method may induce this phenomenon.

### 6.3.3. AIR VOID SHAPE PROPERTY

#### MORPHOLOGICAL STUDY

In Figure 6.9, large air voids were mainly found in the interlayer region of sample M1. A typical example of the 3D configuration of air voids in the interface region of sample M1 (part of A-A section) is presented in Figure 6.14. The connectivity of large air voids in the interlayer was evidently observed. The vast majority of medium and large air voids exhibited irregular and anisotropic shapes, which agreed well with the findings of Van Der Putten et al. [30]. In Figure 6.15, a typical interface area of the printed sample (M1) is highlighted. Under plane polarized light (PPL) mode, epoxy impregnated air voids

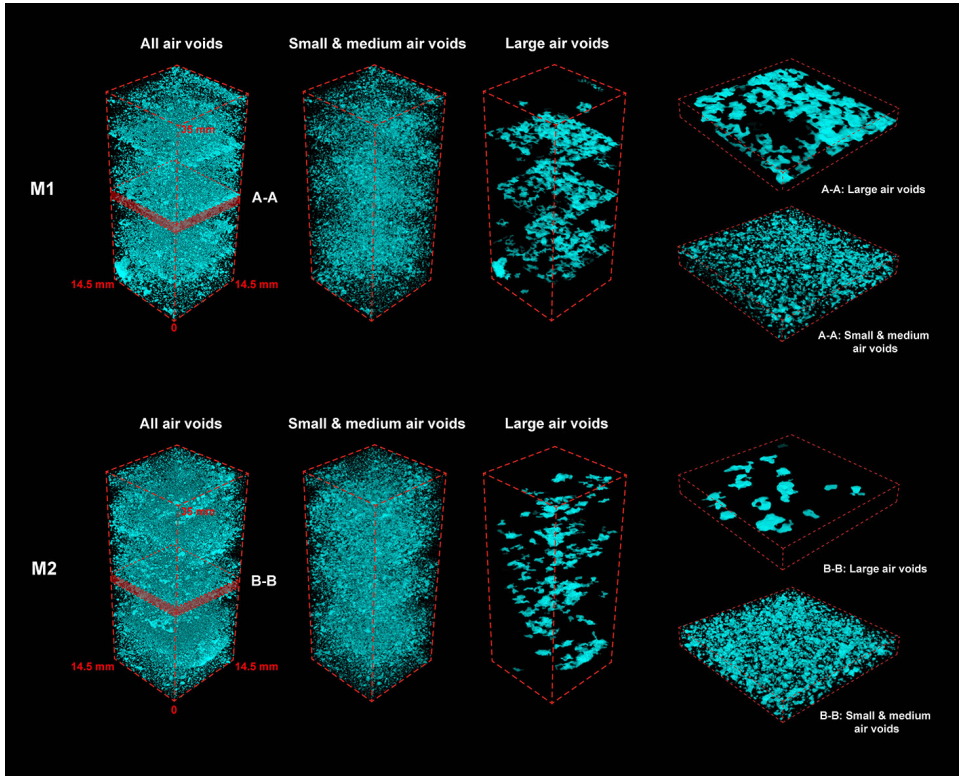


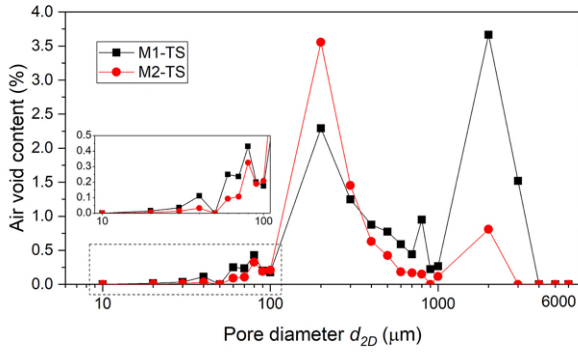
Figure 6.9: 3D visualization of the air voids in the prism ROI. A-A section: interface region of sample M1 (thickness: 2 mm); B-B section: interface region of sample M2 (thickness: 2 mm). Small and medium air voids: 10-1000  $\mu\text{m}$ ; Large air voids: 1000-6000  $\mu\text{m}$ .

display yellow color because of the fluorescent pigment. In contrast, the binder appears black, and the sand particles are bright with light gray- and/or brown-textures. Similar to the 3D configuration of the air void system, large air voids with the elongated shape were found in the interface area.

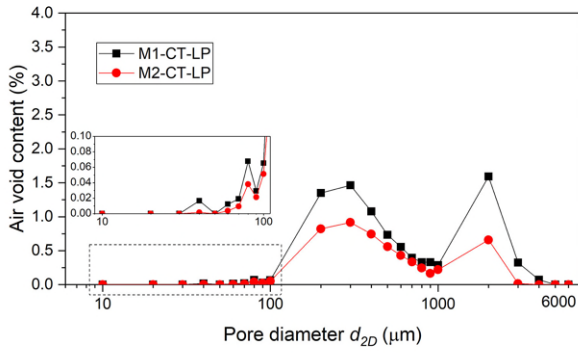
Photomicrographs of large air voids (Figure 6.16(a)), medium air voids (Figure 6.16(b)), as well as small air voids (Figures 6.16(c) and 6.16(d)) were acquired under crossed polarized light (XPL) mode to observe these air voids in thin sections further. The large air void appears to act as a ‘crack’ between two layers, whereas the medium air void may be formed by several connected ellipsoidal pores. Small air void as the minimum unit could keep the round shape in the paste. In Figure 6.16, it can be seen that all air voids were filled with crystals, most likely portlandite and/or calcite (see Figure 6.16(a)). Needle-like ettringite or portlandite crystals were observed on the surface of small air voids, as seen in Figures 6.16(c) and 6.16(d).

#### CIRCULARITY AND ASPECT RATIO

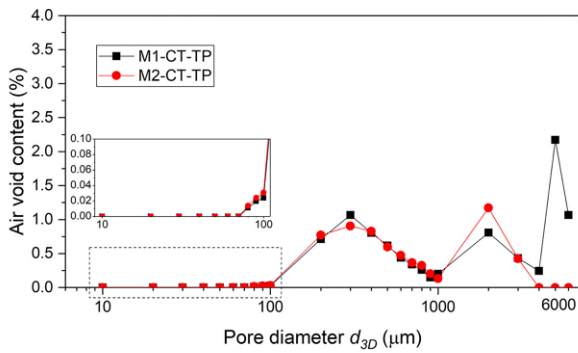
Figure 6.17 illustrates the comparison of the air void circularity distribution of different specimens, where the air void circularity distributions were obtained from TS and



(a)



(b)



(c)

Figure 6.10: Pore size distribution of samples M1 and M2: (a)  $d_{2D}$  from TS images; (b)  $d_{2D}$  from CT-LP images; (c)  $d_{3D}$  from CT-TP images.

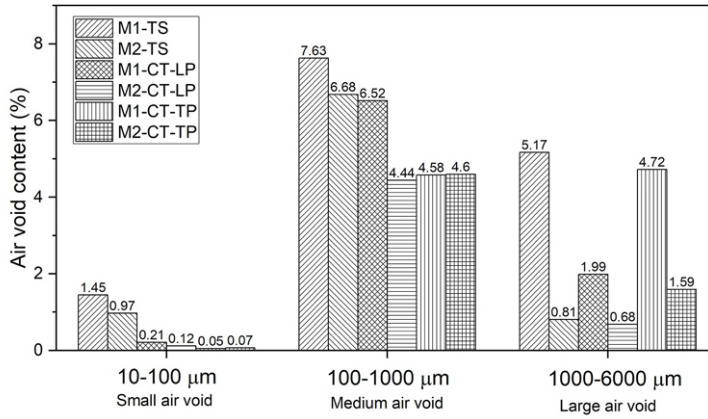


Figure 6.11: Pore size distribution of samples M1 and M2-characterized into three pore size groups.

CT-LP images, respectively. The y-axis in Figure 6.17 presents the relative frequency of the pore circularity for describing the shape property of air voids in different specimens. For each measurement, the general trend of the pore circularity distributions was similar in different specimens. Compared with sample M1, there is a higher amount of air voids with the higher values of circularity (0.9-1) in sample M2. Variations across measurements were also evident. The circularity of the maximum relative frequency, as obtained from TS images, is around 0.925-0.95, whereas this value is 1 in CT-LP images. In Figure 6.13(b), the average air void circularity in transverse cross-sections of sample M2 is slightly larger than that of sample M1 throughout the specimen. The correlation between the average circularity and the pore size is illustrated in Figure 6.18. For both samples, air voids with the small pore size showed the relatively higher average value of circularity.

The aspect ratio was also studied to investigate the orientation of air voids in the horizontal direction. Figure 6.19 illustrates the aspect ratio of air voids throughout the sample based on TS and CT-LP images. Compared with TS images (Figure 6.19(a)), the results obtained by CT-LP images could indicate the approximate interface position in Figure 6.19(b). Especially in sample M1, many air voids with large aspect ratio ( $w/h > 3$ ) were found at the sample height of about 7.2 mm, 18.1 mm, and 27.4 mm, where the high local porosity appeared in sample M1, as shown in Figure 6.7. The aspect ratio distribution of air voids is demonstrated in Figure 6.20. The general trend of aspect ratio distribution is the same for different samples by using different types of images. For both samples M1 and M2, more than 35% of air voids are in the range of 1.1-8. The aspect ratio in the range of 1.1-2 represents the largest category (except the results of CT-LP images in sample M2). In Figure 6.21, the relationship between the average aspect ratio and the pore size is reported. The average aspect ratio of small air voids in both samples was close to 1. For medium and large air voids, the aspect ratio exhibited an increasing trend with the increase of pore diameter, which was clearly indicated in Figure 6.21(b). Note that, owing to the limited image resolution, especially the images obtained using X-ray

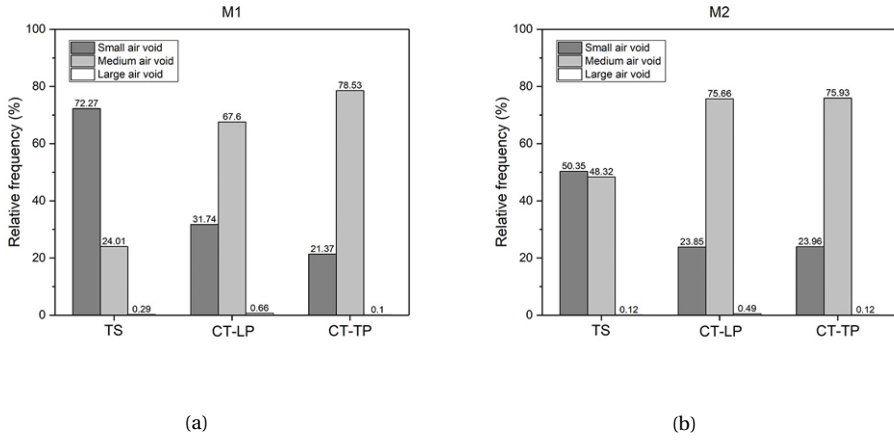


Figure 6.12: Relative frequency of air voids in three pore size groups characterized by analyzing TS, CT-LP and CT-TP images: (a) Sample M1; (b) Sample M2.

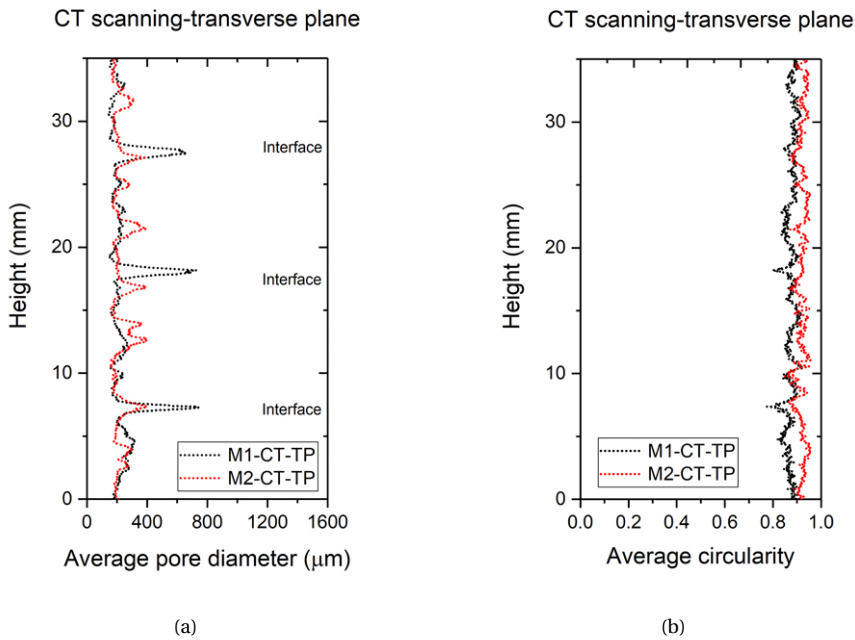


Figure 6.13: (a) The average pore diameter of air voids in each CT-TP image from the bottom to the top of the sample; (b) The average circularity of air voids in each CT-TP image from the bottom to the top of the sample.



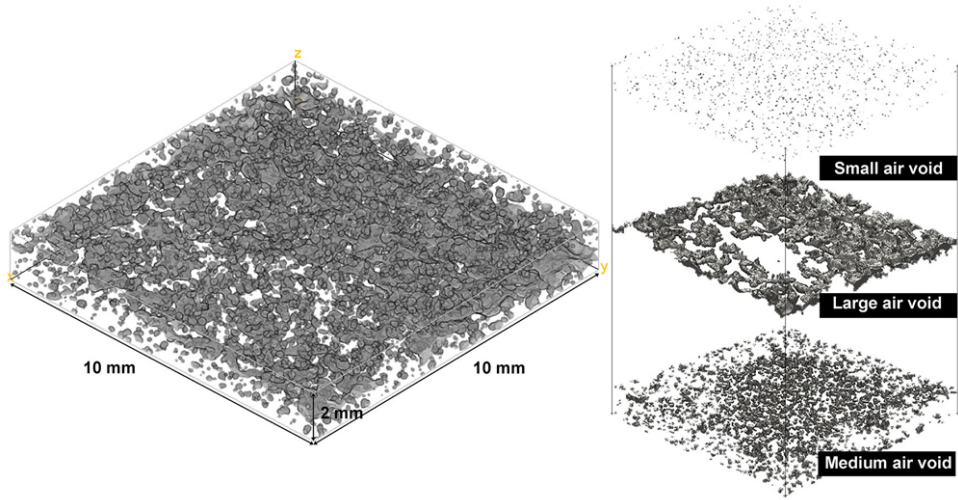


Figure 6.14: 3D configuration of the interlayer region in sample M1 (volume:  $10 \times 10 \times 2 \text{ mm}^3$ ).

computed tomography, many small air voids comprise only several pixels (in 2D), which may be insufficient to indicate their intrinsic shape properties. Thus, most of small air voids appear to be more spherical than macropores.

### 6.3.4. PERSPECTIVE AND LIMITATIONS

#### FORMATION OF AIR VOIDS IN PRINTED CEMENTITIOUS MATERIALS

Overall, the air voids in 3D printed cementitious materials showed significant differences in morphology and distribution compared with mold-cast cementitious materials in [24, 25, 28]. It could be found that small and medium air voids ( $10\text{-}1000 \mu\text{m}$ ) were primarily distributed in the printed layer, whereas most of the large air voids ( $1000\text{-}6000 \mu\text{m}$ ) appeared in the interlayer region. Since air-entraining agents were not added in the studied mixtures, the formation of small air voids ( $10\text{-}100 \mu\text{m}$ ) was possibly due to the existence of grinding aid that was used for producing Portland cement. Besides, the presence of polycarboxylate ether-based superplasticizer in mixtures may also contribute to the entrainment of such air voids [34, 35].

The fresh mixtures (both M1 and M2) displayed very high consistency during the extrusion process, as well as high stiffness and near zero-slump after deposition. Due to the high flow consistency of fresh mixtures, air bubbles were stabilized and may be evenly distributed in the matrix during the mixing process of fresh mixture preparation. Afterwards, the fresh mixture was extruded through a conveying pump. The extrusion force provided by the pump can compact the fresh mixture, which could also redistribute and reshape the air voids in the filament. Besides, the loading from upper layers seemed to compress/compact air voids in the substrate vertically. As a consequence, massive compressed, merged, and overlapped air voids with the elongated shape that showed a high value of aspect ratio in the longitudinal



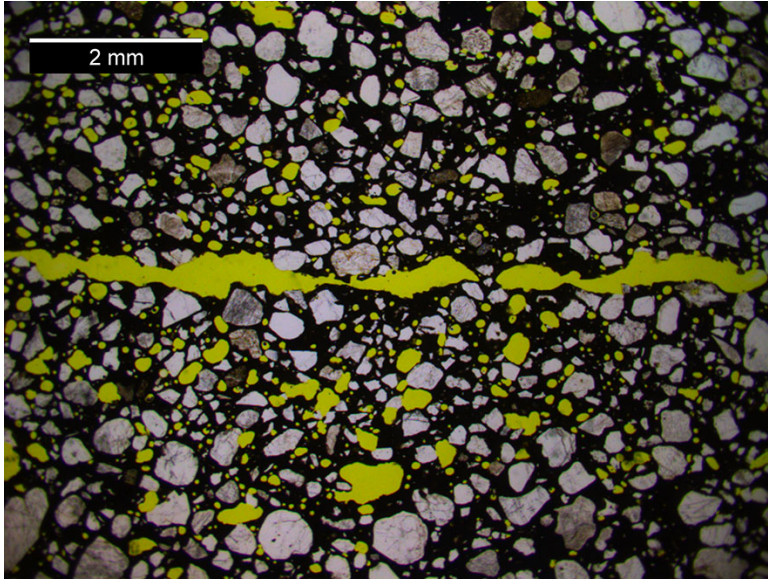


Figure 6.15: Photomicrograph of the interlayer region in sample M1 (under PPL mode). Yellow areas represent the air bubbles. Image fields:  $8.95 \times 6.69 \text{ mm}^2$ .

cross-section eventually were found in the layer regions (see Figures 6.15 and 6.16(b)). Under the extrusion pressure, the small air voids were also difficult to retain the spherical shape. Most of them displayed slight anisotropy in the 2D image (Figure 6.15) and ellipsoid shape in the 3D visualization (Figure 6.14). It should be noted that coarse air voids may be enclosed in the filament during the extruding/printing process since the vacuum de-airing system was not adopted in my extrusion system. Few large air voids were recognized in the layer of both samples M1 and M2 (see Figure 6.9).

The large air void was formed mainly in the interface area, which can be attributed to the layer-wise manufacturing process in 3DCP. Many parameters, e.g., material thixotropy, time gaps, nozzle types, and others, influenced air voids content in the interlayer region from studies [12, 13]. In this study, the printing parameters were kept identical. The only difference between the two studied mixtures was the proportions of HGCC and LGCC in calcined clay. Sample M2 containing a lower content of HGCC, showed much lower porosity in the interface region in comparison with sample M1. As reported in Section 5.4.3, Chapter 5, increasing the content of HGCC in calcined clay could enhance buildability and structural build-up behavior at rest of fresh mixtures for 3D printing. The fresh mixture with the higher thixotropy/buildability leads to enclose more large air voids in the interface.

#### COMPARISON BETWEEN OPTICAL IMAGE SCANNING AND X-RAY COMPUTED TOMOGRAPHY

The comparison between optical image scanning and X-ray computed tomography in terms of sample preparation, image acquisition, and the pros and cons is summarized in Table 6.4. The main challenge of using thin sections to characterize air void system of printed samples is the sample preparation, which is not only a time-consuming process

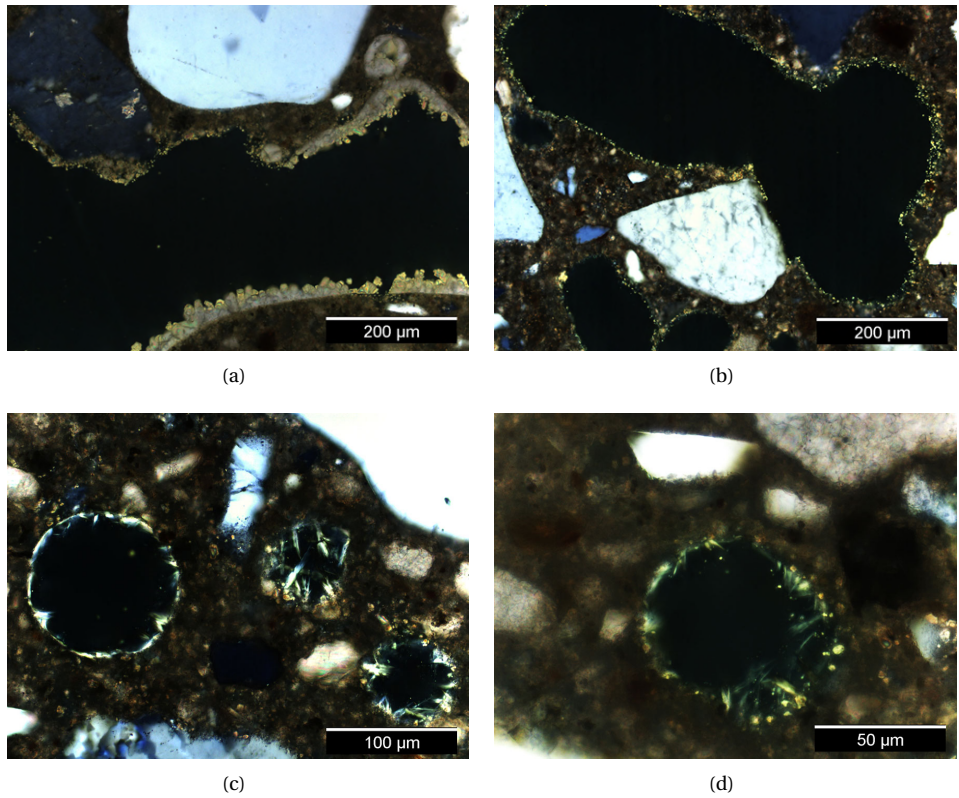


Figure 6.16: (a) Photomicrograph of the large air void (part) in the interface (under XPL mode). Image fields:  $0.70 \times 0.53 \text{ mm}^2$ ; (b) Photomicrograph of the medium air void (under XPL mode). Image fields:  $0.70 \times 0.53 \text{ mm}^2$ ; (c) Photomicrograph of the small air void (under XPL mode). Image fields:  $0.35 \times 0.27 \text{ mm}^2$ ; (d) Photomicrograph of the small air void (detail) (under XPL mode). Image fields:  $0.18 \times 0.14 \text{ mm}^2$ .

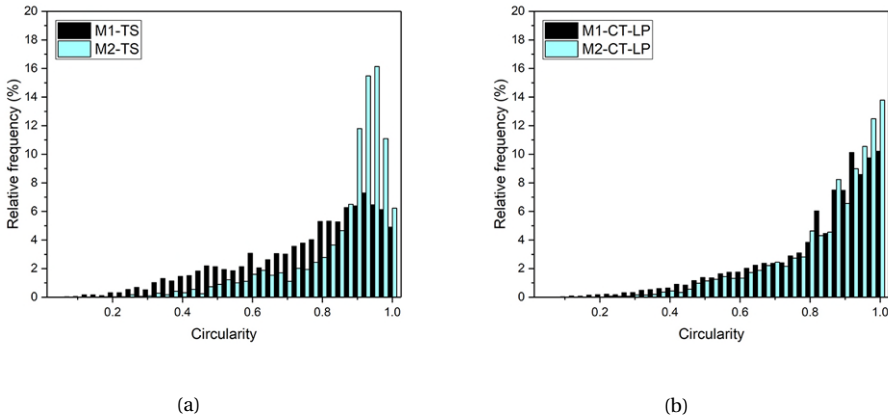
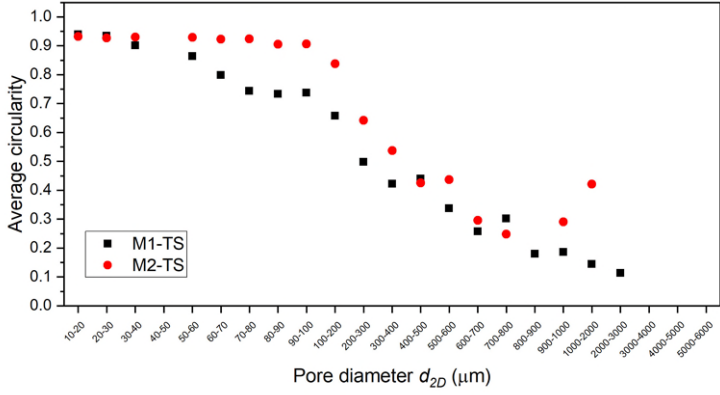


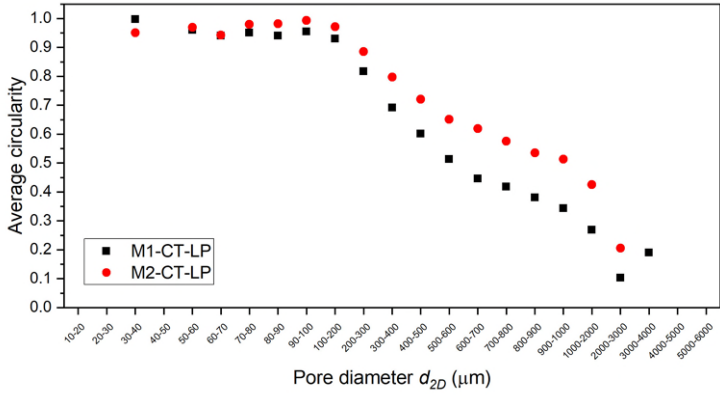
Figure 6.17: Circularity distribution of air voids measured by: (a) TS images; (b) CT-LP images.

but also a delicate work. Unlike thin sections, the cored sample in this study for CT scanning can be prepared easily. However, the accuracy of digital image analysis is mostly dependent on the resolution of images. As mentioned by Zhang et al. [36], maximum resolution of GSV images from CT scanning is limited by the dimension of the sample. The cored sample should be equal in size or larger than the necessary representative elementary volume. In contrast, it is apparently in contradiction with the fact that the resolution of  $10\ \mu\text{m}$  is needed to quantify the small air voids. In further research, multiscale samples might be used to conduct the air void characterization via CT scanning.

In comparison with CT-TP images, the limitations of using TS and CT-LP images on air void characterization should be highlighted. First, as mentioned earlier, using TS and CT-LP images may over-/under-estimated the total air void content and the local porosity along with the longitudinal cross-section of printed samples due to the 2D effects. Second, the acquired pore area in the TS and CT-LP images may not represent the actual size of air voids, which depends on the position of the cross-section (see Figure 6.22). Finally, most of the air voids in printed samples displayed elongated/concave shapes. The analysis of TS and CT-LP images can indicate the shape properties of air voids in one plane projection. In contrast, it is difficult to reveal the spatial anisotropy/heterogeneity of air voids. For further study, it is recommended to increase the dimension of the printed sample for optical microscopy/scanning. As described by ASTM C457-98 [19] and NEN-EN 480-11 [37], the concrete specimen with a field area of  $100 \times 100\ \text{mm}^2$  was required for performing air void analysis. The large specimen may require longer preparation time (e.g., cutting, polishing, and other treatments) and lead to a reduction of image resolution. In contrast, it can offer more interface regions for studying and quantifying the large air voids ( $>1000\ \mu\text{m}$ ).



(a)



(b)

Figure 6.18: Correlation between average circularity and pore size of samples M1 and M2: (a) TS images; (b) CT-LP images.

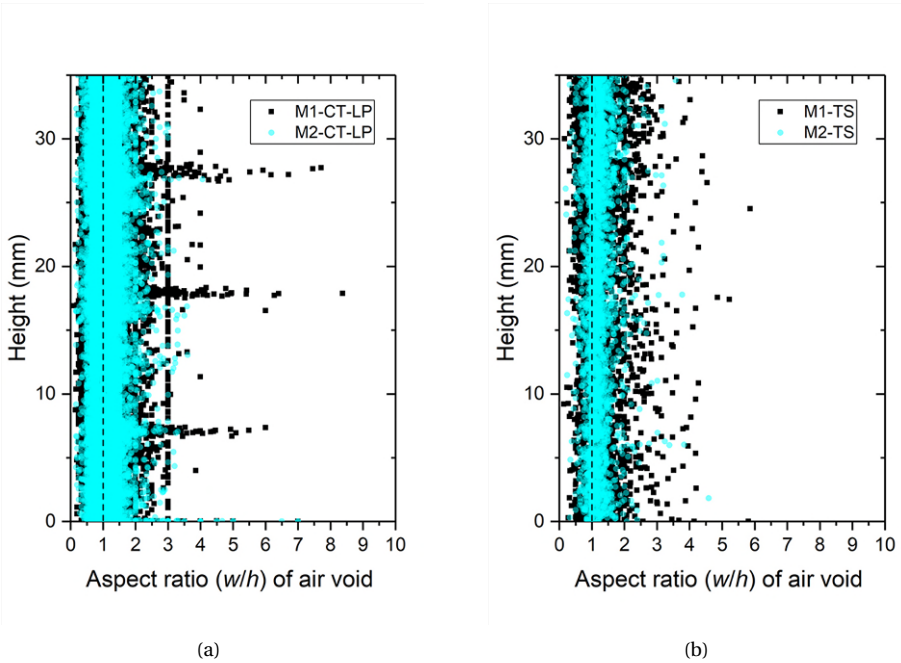


Figure 6.19: The aspect ratio of air void along with the sample height: (a) TS images; (b) CT-LP images.

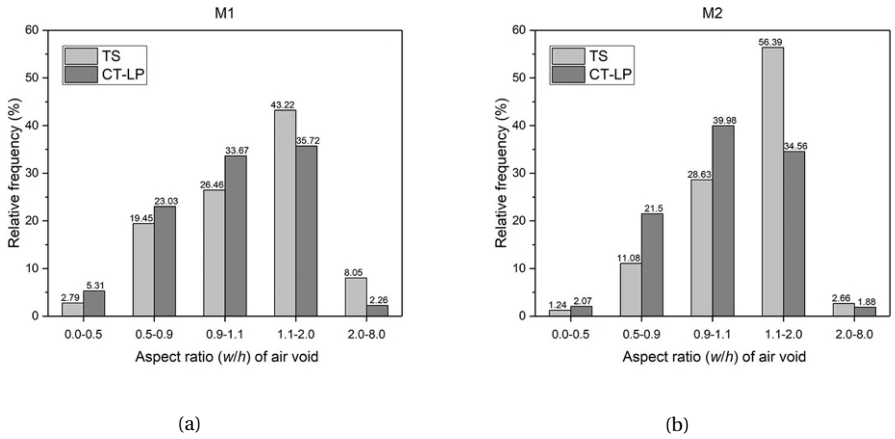
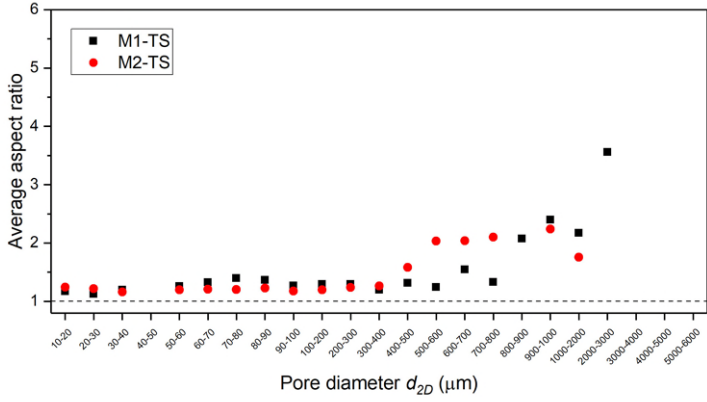
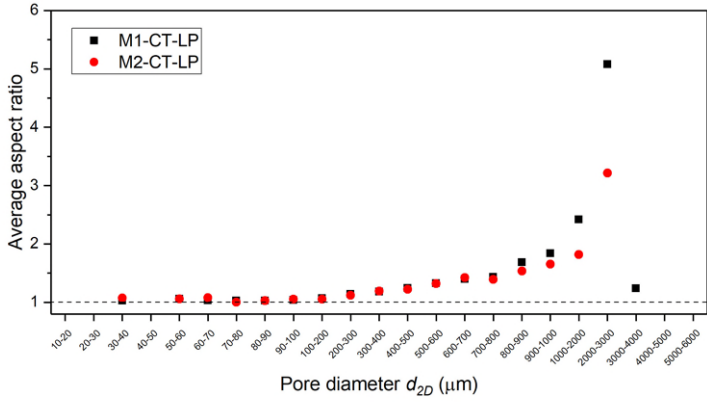


Figure 6.20: The aspect ratio distribution of air voids measured by using TS and CT-LP images: (a) Sample M1; (b) Sample M2.



(a)



(b)

Figure 6.21: Correlation between average aspect ratio and pore size of samples M1 and M2: (a) TS images; (b) CT-LP images.

Table 6.4: Comparative study of different approaches for characterizing air voids.

	Optical image scanning - thin section	X-ray computed tomography	
Image type	TS (LP)	CT-LP	CT-TP
Sample prep			
Time (per sample) <sup>1</sup>	At least 36-48 h.	At most 0.5-1 h.	
Difficulty	Difficult, it requires experienced operators.	Simple, it requires less skilled labor.	
Image acquisition			
Time (per sample) <sup>1</sup>	Less than 0.5 h.	3.5-4 h (scanning + reconstruction).	
Difficulty	Simple, it requires a specialized operator.	Simple, it requires a certified operator.	
Pros	<ol style="list-style-type: none"> <li>1) Multi-scale observation and analysis.</li> <li>2) Possible to characterize the pores with small diameters (smaller than 10 <math>\mu\text{m}</math> is possible).</li> <li>3) It is easy to segment sand grain and paste phases.</li> <li>4) Indicating the interlayer region directly.</li> </ol>	<ol style="list-style-type: none"> <li>1) A sufficient number of slices.</li> <li>2) Most of the air voids could be characterized (larger than several tens micron).</li> <li>3) Indicating the interlayer region directly.</li> </ol>	<ol style="list-style-type: none"> <li>1) 3D analysis.</li> <li>2) Illustrating anisotropy of air voids.</li> <li>3) Most of the air voids could be characterized (larger than several tens micron).</li> </ol>
Cons	<ol style="list-style-type: none"> <li>1) 2D effects.</li> <li>2) Challenges with the sample preparation.</li> <li>3) A limited number of slices.</li> </ol>	<ol style="list-style-type: none"> <li>1) Limited image resolution for big sample sizes.</li> <li>2) 2D effects.</li> <li>3) It is challenging to distinguish between sand and cement paste.</li> </ol>	<ol style="list-style-type: none"> <li>1) Limited image resolution for big sample sizes.</li> <li>2) It is challenging to distinguish between sand and cement paste.</li> <li>3) Longer processing time.</li> </ol>

<sup>1</sup> The required time for each sample mentioned in this table is based on the experiences of the author, which could provide a reference for readers.

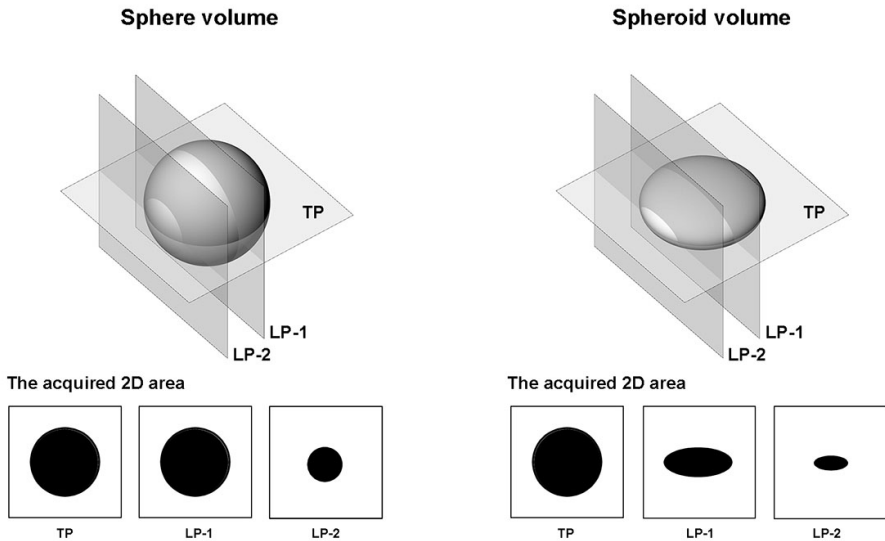


Figure 6.22: Schematic description of the cross-sections of the sphere (Left) and spheroid (Right). For the spherical voids, only once the slice from the center plane of the sphere (TP and LP-1), the acquired 2D area (diameter) can represent the size of the corresponding air void. For the other anisotropic shapes, like spheroid, all acquired 2D areas can not indicate the real size of the air void.

## 6.4. CONCLUSION

ACCORDING to the yielded results, the salient conclusions of this study can be drawn as follows:

- The results of local porosity and total air void content obtained by TS, CT-LP and CT-TP images illustrated a similar trend. Thus, material researchers could employ one of these approaches to quantify the air void content and distribution of 3D printed cementitious materials for selecting the optimal mix design and printing parameters.
- The air voids with the diameter in the range of  $10\ \mu\text{m}$  to  $1000\ \mu\text{m}$  seemed to be evenly distributed in the layer, whereas the large air voids ( $1000\text{-}6000\ \mu\text{m}$ ) were formed mainly at the interface region (several large air voids were also found in the layer region), especially in sample M1. For both samples, the medium air voids ( $100\text{-}1000\ \mu\text{m}$ ) accounted for the highest air void content across measurements. Due to the possibility of merging and overlapping, the majority of air voids exhibited irregular and elongated shapes. This could be attributed to the extrusion and layer-wise manufacturing process in 3DCP.
- Both values of the average circularity and aspect ratio of small air voids ( $10\text{-}100\ \mu\text{m}$ ) were close to 1. This might be due to the small air voids made by only few pixels, which can not sufficiently indicate their intrinsic shape properties. In the



case of medium and large air voids, the average circularity was decreased, and the average aspect ratio revealed an increasing trend with the increase of pore size.

- Thin section can be used for multi-scale analysis and observation of air voids, whereas the sample preparation is a challenge. The sample for X-ray computed tomography can be easily prepared. Nevertheless, the image resolution is limited for the sample with a relatively large size.
- In comparison with CT-TP images, the limitations of using TS and CT-LP images for air void analysis were highlighted. Due to the 2D effects, the measured results from TS and CT-LP images may lead to over-/under-estimation of local porosity and air void content. Additionally, the pore diameter obtained by TS and CT-LP images may not represent the real size of air voids. For pore morphology, the spatial anisotropy/heterogeneity of air voids may not be adequately indicated by TS and CT-LP images.

## REFERENCES

- [1] Y. Chen, O. Çopuroğlu, C. Romero Rodriguez, F. F. Mendonca Filho, and E. Schlangen, *Characterization of air-void systems in 3D printed cementitious materials using optical image scanning and X-ray computed tomography*, *Materials Characterization* **173**, 110948 (2021).
- [2] P. C. Aitcin, *Entrained air in concrete: Rheology and freezing resistance*, in *Science and Technology of Concrete Admixtures*, Vol. 17 (Elsevier Ltd, 2015) pp. 87–95.
- [3] A. Perrot, D. Rangeard, V. Nerella, and V. Mechtcherine, *Extrusion of cement-based materials - An overview*, *RILEM Technical Letters* **3**, 91 (2019).
- [4] R. Kumar and B. Bhattacharjee, *Porosity, pore size distribution and in situ strength of concrete*, *Cement and Concrete Research* **33**, 155 (2003).
- [5] E. K. Nambiar and K. Ramamurthy, *Air-void characterisation of foam concrete*, *Cement and Concrete Research* **37**, 221 (2007).
- [6] P. Choi, J. H. Yeon, and K. K. Yun, *Air-void structure, strength, and permeability of wet-mix shotcrete before and after shotcreting operation: The influences of silica fume and air-entraining agent*, *Cement and Concrete Composites* **70**, 69 (2016).
- [7] K. Mehta and P. J. M. Monteiro, *Concrete: Microstructure, Properties, and Materials*, (McGraw-Hill, New York, 2006) 3rd ed.
- [8] V. N. Nerella, S. Hempel, and V. Mechtcherine, *Effects of layer-interface properties on mechanical performance of concrete elements produced by extrusion-based 3D-printing*, *Construction and Building Materials* **205**, 586 (2019).
- [9] A. Perrot, D. Rangeard, and A. Pierre, *Structural built-up of cement-based materials used for 3D-printing extrusion techniques*, *Materials and Structures/Materiaux et Constructions* **49**, 1213 (2016).

- [10] R. J. Wolfs, F. P. Bos, and T. A. Salet, *Hardened properties of 3D printed concrete: The influence of process parameters on interlayer adhesion*, *Cement and Concrete Research* **119**, 132 (2019).
- [11] N. Roussel, *Rheological requirements for printable concretes*, *Cement and Concrete Research* **112**, 76 (2018).
- [12] Y. W. D. Tay, G. H. A. Ting, Y. Qian, B. Panda, L. He, and M. J. Tan, *Time gap effect on bond strength of 3D-printed concrete*, *Virtual and Physical Prototyping* **14**, 104 (2019).
- [13] B. Panda, N. A. N. Mohamed, S. C. Paul, G. V. Singh, M. J. Tan, and B. Šavija, *The effect of material fresh properties and process parameters on buildability and interlayer adhesion of 3D printed concrete*, *Materials* **12**, 2149 (2019).
- [14] Z. Geng, W. She, W. Zuo, K. Lyu, H. Pan, Y. Zhang, and C. Miao, *Layer-interface properties in 3D printed concrete : Dual hierarchical structure and micromechanical characterization*, *Cement and Concrete Research* **138**, 106220 (2020).
- [15] M. T. Ley, D. Welchel, J. Peery, and J. LeFlore, *Determining the air-void distribution in fresh concrete with the Sequential Air Method*, *Construction and Building Materials* **150**, 723 (2017).
- [16] J. L. Chermant, L. Chermant, M. Coster, A. S. Dequiedt, and C. Redon, *Some fields of applications of automatic image analysis in civil engineering*, *Cement and Concrete Composites* **23**, 157 (2001).
- [17] M. Coster and J. L. Chermant, *Image analysis and mathematical morphology for civil engineering materials*, *Cement and Concrete Composites* **23**, 133 (2001).
- [18] N. Marinoni, A. Pavese, M. Foi, and L. Trombino, *Characterisation of mortar morphology in thin sections by digital image processing*, *Cement and Concrete Research* **35**, 1613 (2005).
- [19] ASTM C457-98, *Standard Test Method for Microscopical Determination of Parameters of the Air-Void System in Hardened Concrete*, (1998).
- [20] K. K. Aligizaki and P. D. Cady, *Air content and size distribution of air voids in hardened cement pastes using the section-analysis method*, *Cement and Concrete Research* **29**, 273 (1999).
- [21] K. Peterson, J. Carlson, L. Sutter, and T. Van Dam, *Methods for threshold optimization for images collected from contrast enhanced concrete surfaces for air-void system characterization*, *Materials Characterization* **60**, 710 (2009).
- [22] R. Pleau, M. Pigeon, and J. L. Laurencot, *Some findings on the usefulness of image analysis for determining the characteristics of the air-void system on hardened concrete*, *Cement and Concrete Composites* **23**, 237 (2001).

- [23] M. Wyrzykowski, R. Kiesewetter, B. Münch, R. Baumann, and P. Lura, *Pore structure of mortars with cellulose ether additions - Study of the air-void structure*, Cement and Concrete Composites **62**, 117 (2015).
- [24] S. Y. Chung, P. Sikora, T. Rucinska, D. Stephan, and M. Abd Elrahman, *Comparison of the pore size distributions of concretes with different air-entraining admixture dosages using 2D and 3D imaging approaches*, Materials Characterization **162**, 110182 (2020).
- [25] T. Kim and J. Olek, *Effects of sample preparation and interpretation of thermogravimetric curves on calcium hydroxide in hydrated pastes and mortars*, Transportation Research Record **2290**, 10 (2012).
- [26] A. Koenig, *Analysis of air voids in cementitious materials using micro X-ray computed tomography ( $\mu$ XCT)*, Construction and Building Materials **244**, 118313 (2020).
- [27] G. Sokhansefat, M. Moradian, M. Finnell, A. Behravan, M. T. Ley, C. Lucero, and J. Weiss, *Using X-ray computed tomography to investigate mortar subjected to freeze-thaw cycles*, Cement and Concrete Composites **108**, 103520 (2020).
- [28] T. S. Yun, K. Y. Kim, J. Choo, and D. H. Kang, *Quantifying the distribution of paste-void spacing of hardened cement paste using X-ray computed tomography*, Materials Characterization **73**, 137 (2012).
- [29] H. Lee, J.-H. J. Kim, J.-H. Moon, W.-W. Kim, and E.-A. Seo, *Correlation between pore characteristics and tensile bond strength of additive manufactured mortar using X-ray computed tomography*, Construction and Building Materials **226**, 712 (2019).
- [30] J. Van Der Putten, M. Deprez, V. Cnudde, G. De Schutter, and K. Van Tittelboom, *Microstructural characterization of 3D printed cementitious materials*, Materials **12**, 2993 (2019).
- [31] S. Chaves Figueiredo, O. Çopuroğlu, and E. Schlangen, *Effect of viscosity modifier admixture on Portland cement paste hydration and microstructure*, Construction and Building Materials **212**, 818 (2019).
- [32] O. Çopuroğlu, *Revealing the dark side of portlandite clusters in cement paste by circular polarization microscopy*, Materials **9**, 176 (2016).
- [33] I. Arganda-Carreras, V. Kaynig, C. Rueden, K. W. Eliceiri, J. Schindelin, A. Cardona, and H. S. Seung, *Trainable Weka Segmentation: A machine learning tool for microscopy pixel classification*, Bioinformatics **33**, 2424 (2017).
- [34] R. Gagné, *Air entraining agents*, in *Science and Technology of Concrete Admixtures* (Elsevier Ltd, 2015) pp. 379–391.
- [35] P. C. Nkinamubanzi, S. Mantellato, and R. J. Flatt, *Superplasticizers in practice*, in *Science and Technology of Concrete Admixtures* (Elsevier Ltd, 2015) pp. 353–377.

- [36] M. Zhang, Y. He, G. Ye, D. A. Lange, and K. V. Breugel, *Computational investigation on mass diffusivity in Portland cement paste based on X-ray computed microtomography ( $\mu$ CT) image*, *Construction and Building Materials* **27**, 472 (2012).
- [37] NEN-EN 480-11: 2005, *Admixtures for concrete, mortar and grout - Test methods - Part 11: Determination of air void characteristics in hardened concrete*, (2005).

# 7

## EFFECT OF PRINTING PARAMETERS ON INTERLAYER BOND STRENGTH OF 3D PRINTED LIMESTONE-CALCINED CLAY-BASED CEMENTITIOUS MATERIALS

*This chapter presents an experimental and numerical study to investigate the impacts of different printing parameters on the interlayer bond strength of the 3D printed limestone and calcined clay-based cementitious materials. All samples were manufactured by a lab-scale 3D printer equipped with a hybrid back- and down-flow nozzle (rectangular opening). The uniaxial tensile test was employed to quantify the interface adhesion of printed specimens. Moreover, the grayscale value image of microstructure, as well as the air void content and distribution of the printed specimens were acquired by X-ray computed tomography and characterized by image analysis. The experimental results showed that extending the time interval between construction of two layers could decrease the bond strength, whereas only increasing the nozzle standoff distance exhibited limited effects on that. The weak bond strength could be attributed to the high local porosity at the interface of the specimen. Additionally, numerical simulations of the uniaxial tensile test were conducted using a 2D lattice fracture model, which can predict the bond strength of printed specimens for different void contents in the interface layer.*

---

Parts of this chapter were published in *Construction and Building Materials* **262**, 120094 (2020) [1].  
Numerical simulation was conducted by Dr. Hongzhi Zhang.

## 7.1. INTRODUCTION

MOST of the recent studies [2–4] attempted to explore the mechanism of interface formation induced by different printing parameters. Performing uniaxial tensile test [2, 4–8] is a direct way to obtain the bond strength between two layers. However, for printed cementitious materials, the details of the uniaxial tensile tests are not so commonly reported in the literature, i.e., the complete load and displacement curve including pre- and post-peak properties. In general, there is a lack of knowledge regarding fracture mechanics within the context of 3D printed cementitious materials.

Lattice fracture model, as a mechanical modeling approach, is widely used to explain the fracture behavior of cementitious materials since the simulated crack patterns and tensile strengths are very close to those observed in experiments [9, 10]. Earlier studies [11–13] employed the discrete lattice fracture model to predict and model the fracture process of the digital specimen in a mechanical test, e.g., compression, flexural, splitting, and uniaxial tensile strength. The digital specimen, mimicking the cementitious material (the input of material mesostructure), can be constructed by using different techniques, e.g., X-ray computed tomography [11, 13, 14], nanoindentation [15], and others [16, 17].

The printing parameters, including short-time intervals and nozzle standoff distances, seemed extremely critical for a single batch material in practice. This chapter aims to investigate the effect of these printing parameters on the interlayer bond strength of 3D printed limestone-calcined clay-based cementitious materials. The printed specimens were tested in the uniaxial tension under a non-rotational boundary condition for obtaining the complete load and displacement curve (containing the softening branch). Furthermore, X-ray computed tomography scanning was used for acquiring the digital material structure. Based on the obtained digital material structure, the air void (also known as macropores) content and distribution were measured and analyzed as well. Finally, numerical simulations of the experiments were conducted using a 2D lattice fracture model.

## 7.2. MATERIALS

A printable mixture proposed in Chapter 5 was used in this study (see Table 7.1).

Table 7.1: Mixture proportions of printable cementitious materials (% of the binder mass).

	PC	LGCC	HGCC	LP	Water	Sand	SP	VMA
Mixture	40	30	10	20	150	30	2	0.24

## 7.3. EXPERIMENTAL TESTS

### 7.3.1. SAMPLE PREPARATION

A hybrid down- and back-flow nozzle was utilized in this study (Figure 4.6). The nozzle with a rectangle-opening of  $40 \times 13.5 \text{ mm}^2$  could provide a large contact surface area between two layers, which may ensure printing stability. The moving speed of the nozzle was set as 3600 mm/min with respect to a material flow rate of 1.9 L/min. Samples were printed and prepared under the same ambient condition of  $20 \pm 2 \text{ }^\circ\text{C}$  and about 55% RH.

All printed objects with the designed dimensions of 800 mm in length, 25-27 mm in height, and 40 mm in width consisted of two layers (only one filament for each layer). Two printing parameters were investigated in this study: the time interval between two adjacent layers, as well as the height between the bottom of the nozzle and the substrate (nozzle standoff distance).

#### TIME INTERVAL

In this study, the default printing speed was 3600 mm/min. Thus, assuming the object has the identical layers (the same path length of each layer) from the bottom to the top, 20 s, 1 min, and 10 min of time intervals may represent three scenarios in Figure 7.1(a): objects with path length of 1200 mm, 3600 mm, and 36000 mm for each layer, respectively. In this test series, the nozzle standoff distance was kept as 0 mm. The first layer was exposed to the ambient environment without any cover, and the second layer was laid after a time interval of 20 s, 1 min, and 10 min, respectively (see Figure 7.1).

#### NOZZLE STANDOFF DISTANCE

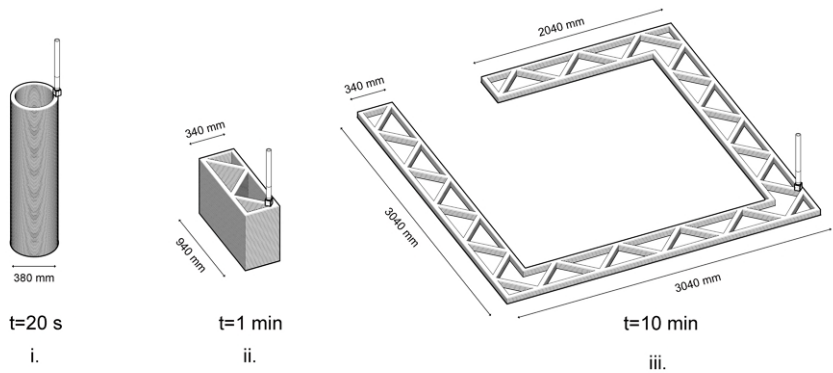
The nozzle was featured as a hybrid back- and down-flow. According to my preliminary printing tests (see Figure 7.2(a)), nozzle standoff distance greater than 10 mm led to inaccurate positioning of the layers. Therefore, as shown in Figure 7.1(b), three different nozzle standoff distances 0, 5, and 10 mm were selected to make the second layer. 0 mm was the default value, and 10 mm was the maximum tolerance value. For each trial, the time gap between the two adjacent layers was controlled as 1 min in this test series.

#### MOLD-CAST SPECIMEN

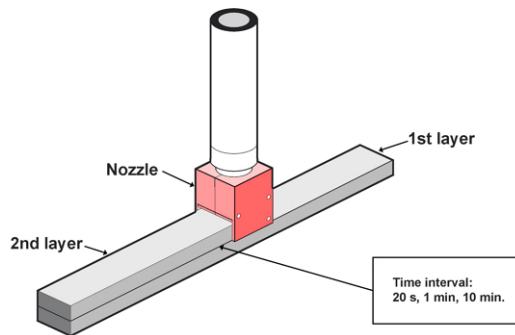
Cast samples with dimensions of  $160 \times 40 \times 40 \text{ mm}^3$  were also prepared and tested. Fresh mixtures were filled into the mold manually. No compaction was applied. Both cast and printed samples were stored under the plastic film for the first 24 h. Afterwards, all samples were cured and stored in a fog room ( $20 \pm 2 \text{ }^\circ\text{C}$ , and 99% RH) before conducting the tests.

#### 7.3.2. UNIAXIAL TENSILE TEST

Uniaxial tensile test was performed to determine the bond strength of printed and cast samples. One day before testing, three specimens (Figures 7.3(a) and 7.3(b)) with 20 mm of length, 20 mm of width, and 24 mm of height were sawn from the printed and mold-cast objects by using a cutting machine. To ensure the printed sample failed at the interface zone, a notch with a depth of 5 mm and a height of 3 mm was made on four sides of the sample at the interlayer (Figure 7.3(b)). The notches were also made on the cast samples at the same position. Uniaxial tensile tests were conducted on a servo-hydraulic Instron 8872 machine. Before implementing the test, the frontal surface of specimens was painted white by using acrylic paint. Afterwards, evenly distributed black dots were randomly made with a permanent marker for employing digital image correlation (DIC). The prepared specimens were glued between two non-rotating platens via using a rapid hardening adhesive to keep the same deformation along the four sides of the specimen (Figure 7.3(c)). The test was controlled by the average value of two linear variable differential transducers (LVDTs) at



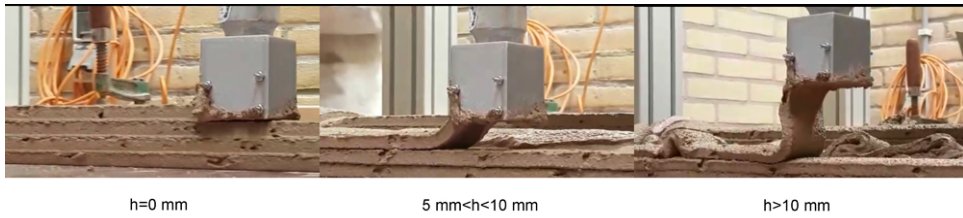
(a)



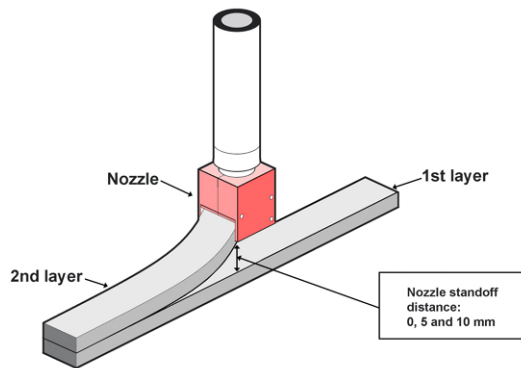
(b)

Figure 7.1: (a) Three scenarios: i. A small object with 1200 mm of path length for each layer (Time interval-20 s); ii. A medium object with 3600 mm of path length for each layer (Time interval-1 min); iii. A large object with 36000 mm of path length for each layer (Time interval-10 min). (b) Schematic diagram of the printing process by different time intervals between two layers.





(a)



(b)

Figure 7.2: (a) Increasing the nozzle standoff distance  $h$  could lead to the inaccurate layer deposition; (b) Schematic diagram of the printing process by different nozzle standoff distances between two layers.

loading speed of  $0.01 \mu\text{m/s}$ . A Canon camera model EOS 6D equipped with a Tamron aspherical 28–75 mm lens was utilized to acquire images during the test process. DIC of each test was analyzed by an open-source software Ncorr2 [18].

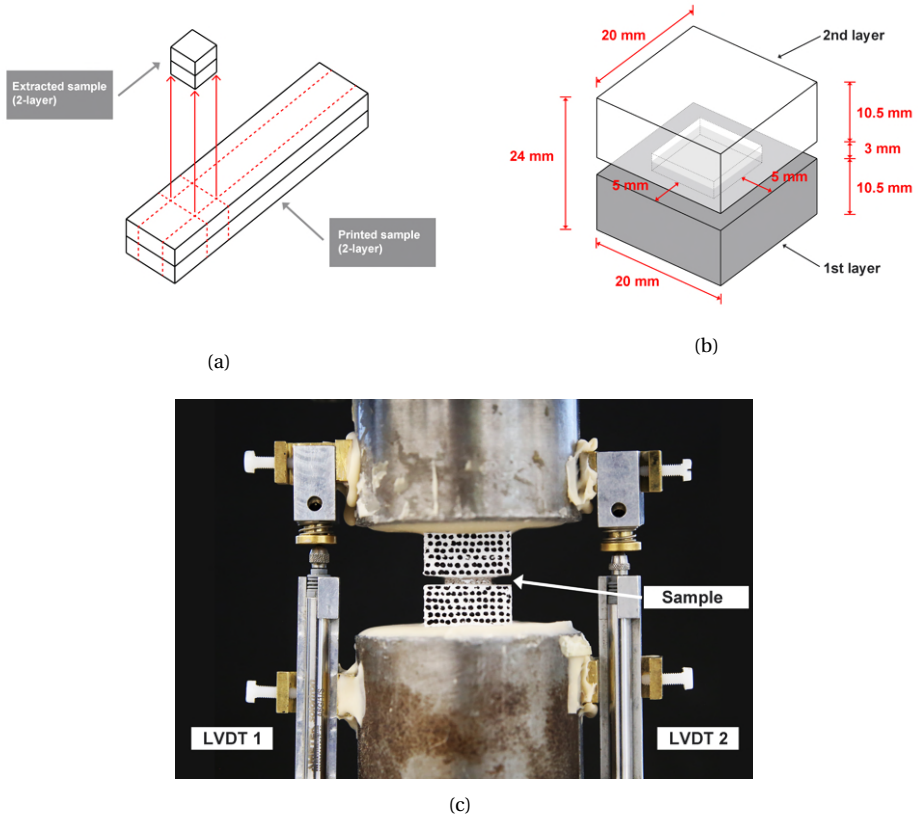


Figure 7.3: (a) Extracting the specimen from the printed sample; (b) Illustration of the specimen for performing uniaxial tensile test; (c) A photograph of the uniaxial tensile test setup.

### 7.3.3. X-RAY COMPUTED TOMOGRAPHY

In this study, X-ray computed tomography (CT) scanning was used to acquire the grayscale-based digital microstructure of the printed and cast specimens for air void analysis and specimen digitalization for modeling. In Figure 7.4, cylindrical samples with a circular cross-section of 25 mm diameter and 25–27 mm height were drilled from both printed and cast objects (at the material age of 7 days). After CT scanning, grayscale value (GSV) images with a resolution of  $50 \mu\text{m}/\text{pixel}$  were acquired (Details about CT scanning can be found in Section 4.2.7, Chapter 4).

For each specimen, 40 longitudinal cross-sections of GSV images were extracted from the reconstructed 3D volume (see Figure 7.5). For segmenting the air voids, the so-called tangent-slope method [19, 20] (illustrated in Figure 7.6) was applied to the

cumulative histogram. It should be noted that only pores larger than the X-ray CT resolution ( $50\ \mu\text{m}$ ) can be detected in this manner. The air void content and distribution of each segmented binary image could be determined through a MATLAB-code.

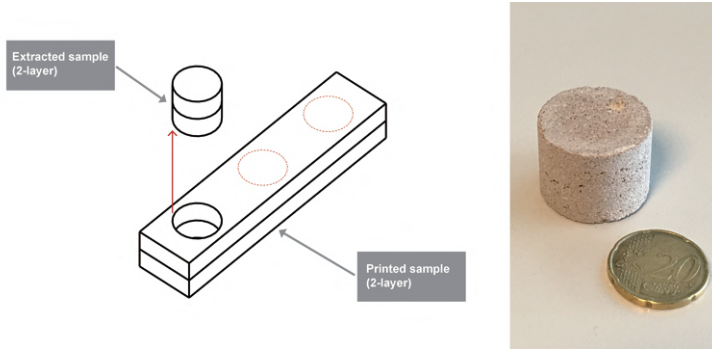


Figure 7.4: Extracting specimens from the printed sample (Left); A photograph of the cored specimen for CT scanning (Right).

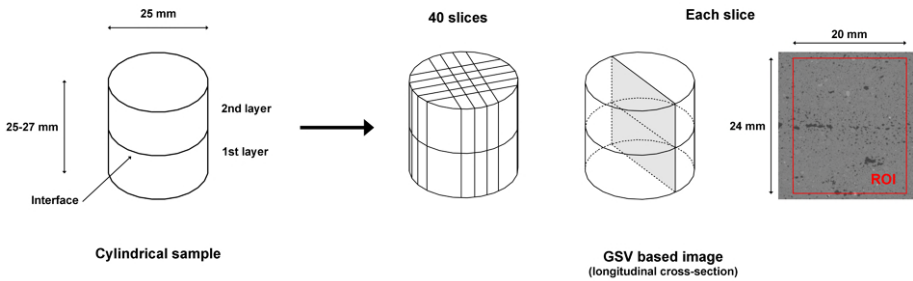


Figure 7.5: The process of acquiring GSV based images for air void analysis and modeling.

## 7.4. MODELING

**D**UE to its simplicity and efficiency, the discrete lattice model has been widely used to simulate the mechanical properties of cementitious materials, at both microscale [14, 20, 21] and mesoscale [22, 23]. The model uses a lattice of Timoshenko beam elements to discretize the material domain. All the elements have a linear elastic behavior (note that it is possible to assign a ductile constitutive law of the local element, as shown in [10]). Cracks are generated by removing the element in which stress exceeds its strength under a specific boundary condition. In the case of heterogeneous materials, the heterogeneity is easily introduced by overlapping the digitalized material structure on the lattice and assigning different local mechanical properties to the elements according to their positions.

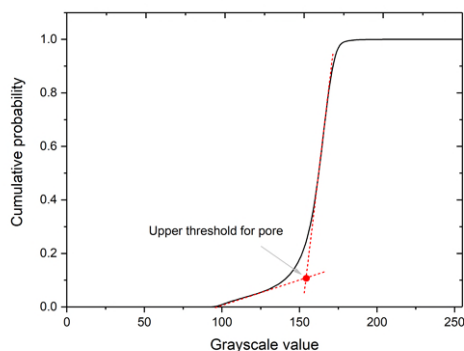


Figure 7.6: Schematic explanation of the approach used to segment the air voids.

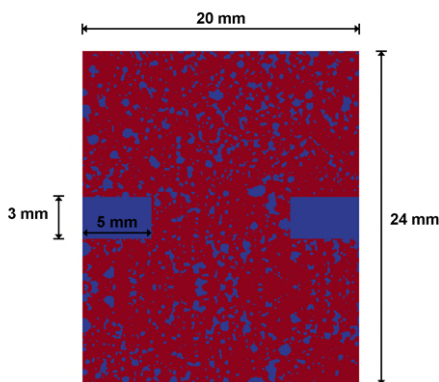


Figure 7.7: The notched digital specimen (cast specimen) used for the fracture and deformation analysis.

In the current study, the segmented 2D material structure with a height of 24 mm and a length of 20 mm ( $480 \times 400 \text{ pixel}^2$ ) was used to build a series of 2D models. Two notches (with the size of 3 mm in height and 5 mm in length) were created in the meshes at mid-height (see Figure 7.7). As shown in Figure 7.8, a quadrangular grid of square cells was first defined, in which a node was then randomly positioned within a concentric sub-cell. According to a previous study [24], a ratio of 0.5 between the length of the cell and sub-cell can introduce the geometry disorder in the digital cementitious material while avoiding significant variations in the length of elements. Therefore, this ratio was consistently adopted herein. Delaunay triangulation was performed on the set of the defined notes, on the basis of which nodes in adjacent Voronoi cells are connected by the beam elements. This mesh configuration results in a Poisson's ratio of 0.18 [25], which is realistic for cementitious materials [26].

At the investigated length scale, the 2D material structure was considered as a

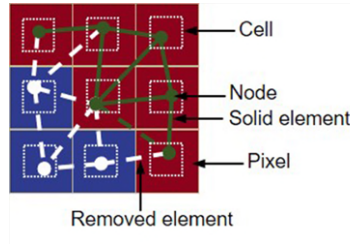


Figure 7.8: Schematic illustration of the 2D mesh generation.

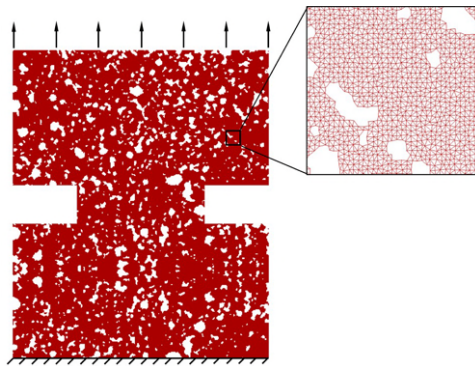


Figure 7.9: The boundary condition of the computational uniaxial tension test.

two-phase structure, i.e., solid and pore phases. As shown in Figure 7.8, the element that has one/two nodes located in the pore or notch area was then removed from the system as the initial flaw embedded in the material. As a simplification, all the elements located in the solid phase are assumed having the same mechanical properties, i.e., elastic modulus and tensile strength (Note that no local compressive failure is needed to simulate fracture performance of such material under uniaxial tension [24]). Those two mechanical properties were assumed to correspond with those of the mold-cast samples to investigate the influence of the pore structure on the global mechanical performance of the specimens and further explain the experimental observations. The computational uniaxial tension test was achieved by applying uniform displacement of the nodes on one side and blocking the degrees of freedom of the nodes in the opposite side (see Figure 7.9). It is worth to mention that in order to simulate the boundary constraints between the steel plates and specimen in the experiments, lateral deformation and rotation of the nodes at the boundaries were fixed. In order to consider the variation of the 2D material structure, for each case, 3 simulations were carried out on the basis of 2D slices extracted from different locations (see Figure 7.5).

## 7.5. RESULTS AND DISCUSSION

### 7.5.1. UNIAXIAL TENSILE STRENGTH

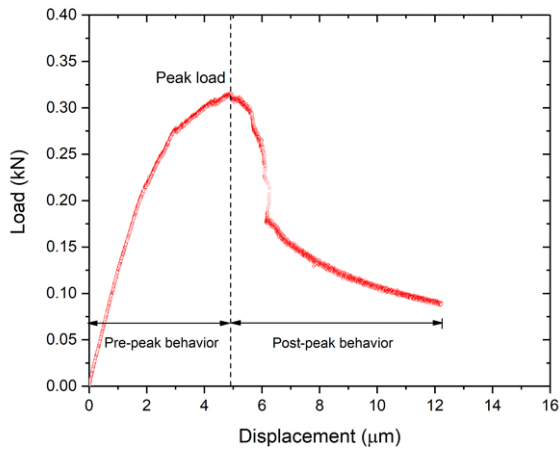
ALL load and displacement curves of the uniaxial tension tests are given in Figure 7.11. The displacement of each test was the average value of two LVDTs. All specimens showed brittle behavior in tension. A similar pattern of the load and displacement curve was observed. As shown in Figure 7.10(a), the load initially increased quasi-linearly with increasing vertical displacement until reaching the peak load. Except for the specimens with a 10 min time gap (in Figure 7.11(c)), the peak load corresponded to a displacement of 4-5  $\mu\text{m}$ . After the peak load, a load decrease was observed as deformations grow. In Figure 7.10(b), the color close to red in the DIC image represented the region suffering high deformation and containing cracks. It could be found that two cracks nucleated from both notch tips, and then continued propagating. Finally, both cracks formed at the interface. The peak load in this test could be regarded as the ultimate interlayer bond force of the specimen. The peak force of each curve from Figure 7.11 was collected and divided by the cross-section area ( $10 \times 10 \text{ mm}^2$ ) to compute the uniaxial tensile bond strength. The calculated results were presented in Figure 7.12.

### 7.5.2. AIR VOID CONTENT AND DISTRIBUTION

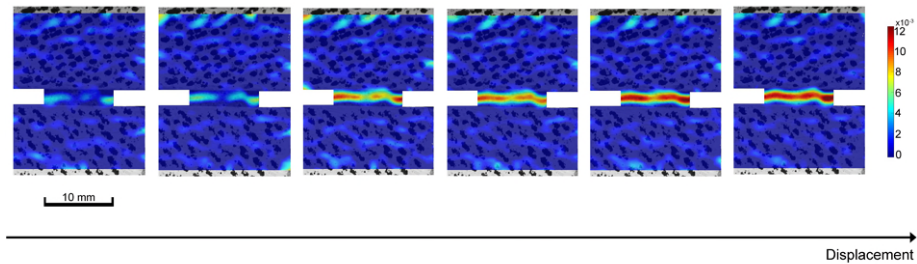
The air void content and distribution of each GSV image is presented in Figure 7.13. The term porosity could be referred to as air void content in this context. It could be found that the porosity in the middle zone of the printed specimens was higher than in other areas, which was due to the presence of the interface. In contrast to the printed sample, the air void distribution of the cast sample was more homogeneous. For the printed sample, the interlayer zone could be located mid-height of the sample, with the height ranging from 10.5 mm to 13.5 mm. It was also the region to make notches. In general, for a quasi-brittle material, the mechanical properties are inversely proportional to the porosity [27]. Since the crack is localized in the interlayer zone, the strength of the specimens is mainly determined by the porosity within this area. The total porosity in the interlayer zone is therefore investigated and plotted in Figure 7.14(a). However, as shown in Figure 7.14(a), the results of the total porosity in the interlayer zone were very close between different specimens, except for the 10 min and cast cases. Both of them displayed higher porosity than others. As reported by Lee et al. [28], the total fraction of pores in the interlayer may not directly affect the bond strength of printed samples. Compared with the total porosity in the interlayer zone, the maximum value of local porosity seems to be a more critical factor to dominate the bond strength (see Figure 7.14(b)).

#### TIME INTERVAL

In Figure 7.14(b), the maximum value of local porosity in the interlayer zone increased with the increase of time interval, which is in good agreement with the interlayer bond strength in the previous section. The specimen with a 20 s of time interval shows the minimum value of average local porosity at the interface (Figure 7.14(b)) among all specimens, which seems to be the main reason for its highest bond strength in Figure 7.12. Extending the time interval between two layers may lead to a high concentration of macropores distributed along the interface, which is a possible reason for the higher



(a)



(b)

Figure 7.10: An example: (a) A typical load and displacement curve of the uniaxial tensile test; (b) The corresponding DIC analysis of the specimen.

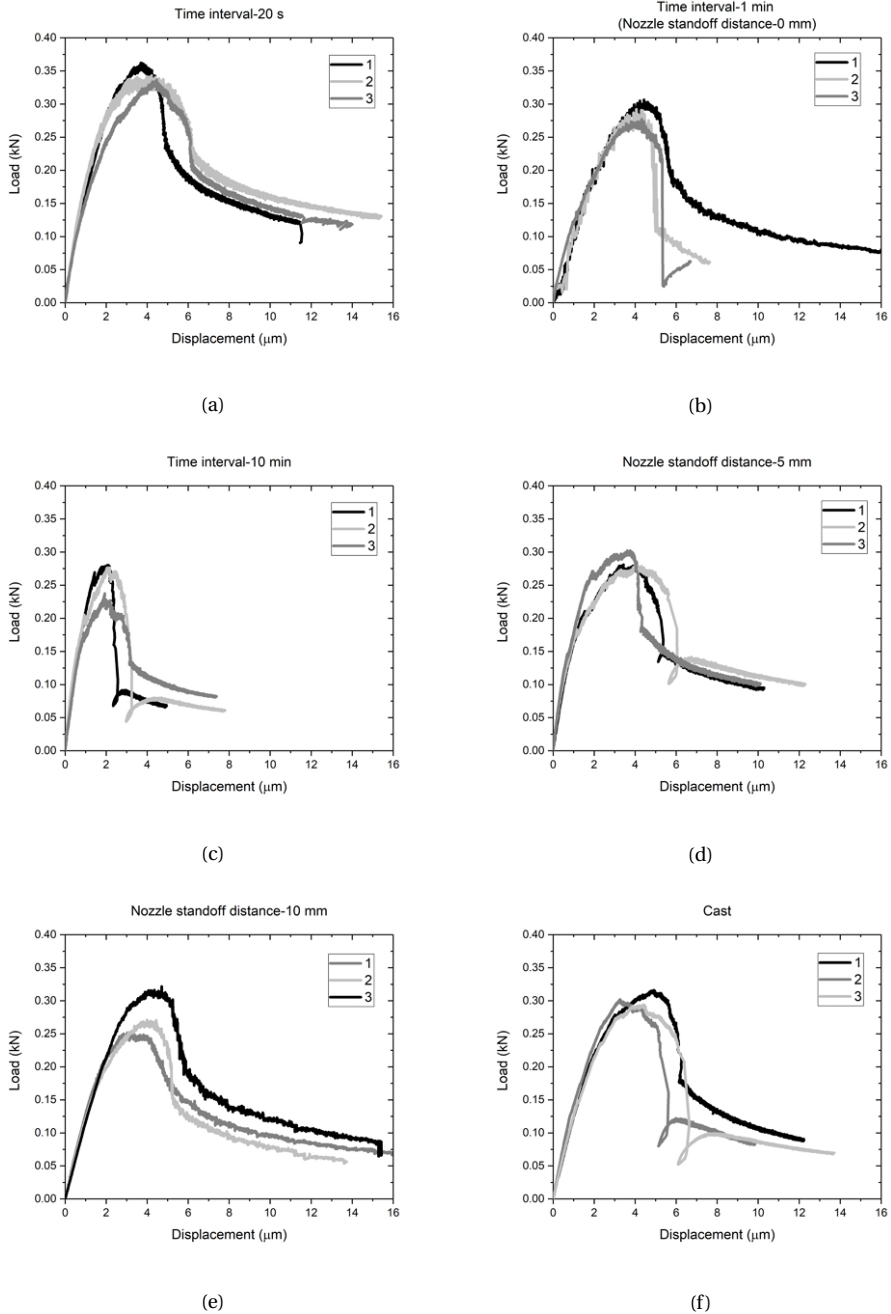


Figure 7.11: Load vs. displacement curves of uniaxial tensile tests at the material age of 7 days: (a) Time interval-20 s; (b) Time interval-1 min (also known as nozzle standoff distance-0 mm); (c) Time interval-10 min; (d) Nozzle standoff distance-5 mm; (e) Nozzle standoff distance-10 mm; (f) Cast.



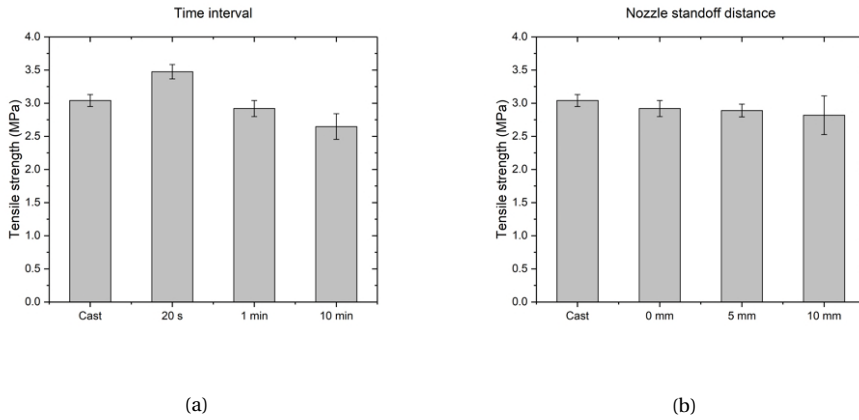


Figure 7.12: Uniaxial tensile strength results at the material age of 7 days: (a) Different time intervals; (b) Different nozzle standoff distances.

maximum value of local porosity in the interlayer zone of sample 10 min. As shown in Figure 7.15, the extruded layer exhibited a rough top surface. For a short-time gap (20 s and 1 min in this study), the stress from the upper layer could result in a slight deformation of the bottom layer. Since the substrate has a relatively lower surface tension, the load induced by the weight of the top layer might rearrange the orientation of the top surface of the substrate (bottom layer), and it might increase the interacted bond area between two layers [2]. However, after 10 min, the deformation of the substrate (after depositing the top layer) may be decreased due to the growth of material stiffness that is attributed to the cement particle flocculation and nucleation, as well as water loss induced surface drying process. The surface tension of the bottom layer was also increased. It results in less amount of interacted bond areas between the old and new layers. Many unfilled areas were kept forming the ‘wide’ macropores between two layers. This is also evident in Figure 7.16. In comparison with other samples, sample 10 min showed massive macropores that have large pore widths (>2 mm). Most of those macropores distributed at the sample height of 12–13 mm. Consequently, for sample 10 min, the maximum value of local porosity was also found in this height range (see Figure 7.13). Therefore, extending the time interval could increase the number of ‘wide’ macropores at the interface area, which increased the value of local porosity.

#### NOZZLE STANDOFF DISTANCE

The samples made with different nozzle standoff distances showed a close result of the maximum value of local porosity in the interlayer zone in Figure 7.14(b). As mentioned earlier, the dropped layer process, because of the increased nozzle height, could increase the possibility of inaccurate layer deposition, which may reduce the contact area between two adjacent layers. The variable contact pressures and surface areas between two layers induced by the inaccurate layer deposition could result in the high scatter of the test results [29] (see Figure 7.2(a)). Therefore, it is essential to keep the

nozzle standoff distance within a valid range during the printing process. A real-time height measurement device and a feedback system that were reported by Wolfs et al. [30] could be employed for an inline control of the nozzle standoff distance in practice.

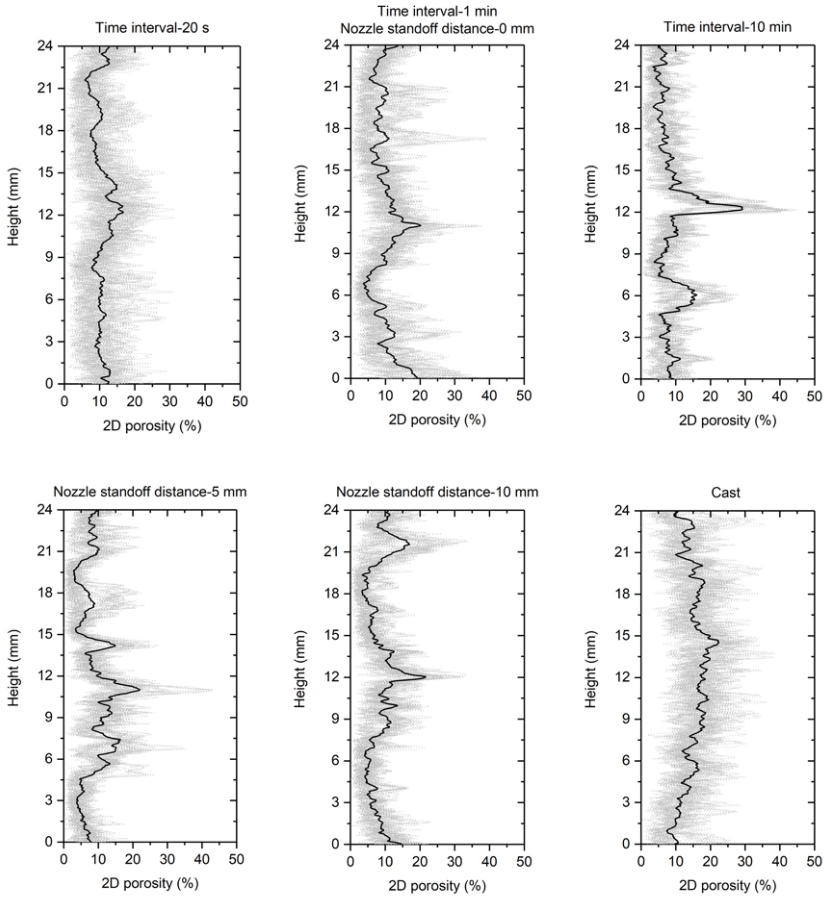
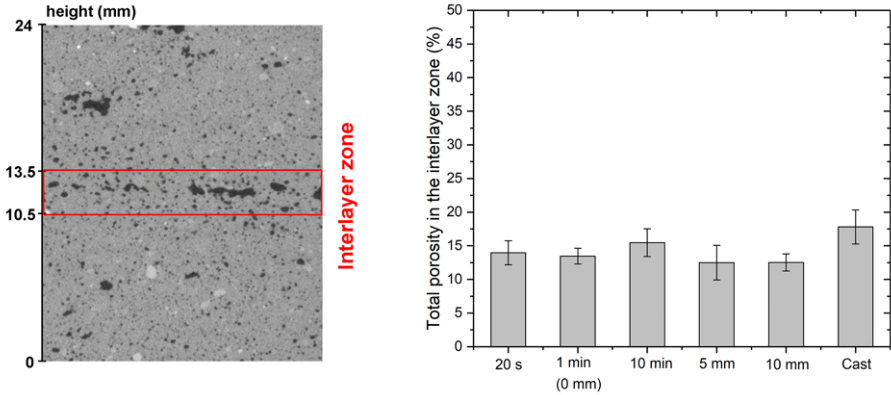


Figure 7.13: Air void content and distribution (local porosity) of different samples made with various printing parameters. The gray line represents the individual computed result. The black line indicates the average relation.

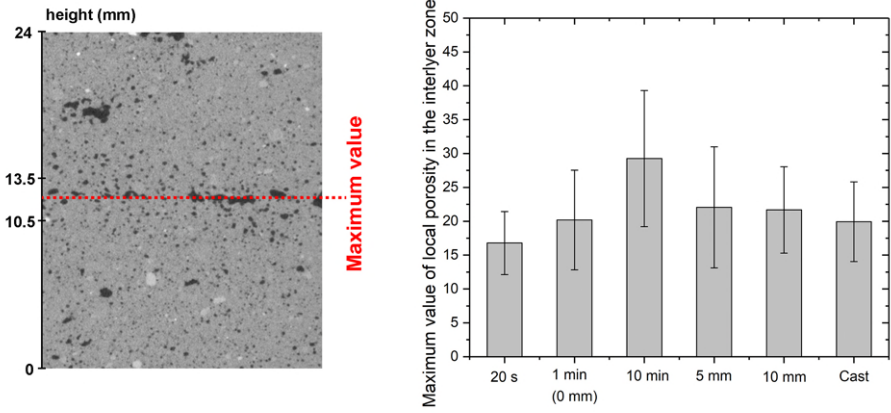
### 7.5.3. MODELING RESULTS

#### CALIBRATION

Through a trial-and-error process, the input elastic modulus and tensile strength of the lattice element have been determined as 25 GPa and 9 MPa, respectively. As shown in Figure 7.17, with the aforementioned parameters, the modeling results of cast samples show reasonable agreement with the experimental results in terms of the pre-peak part,



(a)



(b)

Figure 7.14: (a) Total porosity in the interlayer zone; (b) The maximum value of local porosity in the interlayer zone. Interlayer zone: 10.5–13.5 mm in the height of the sample.

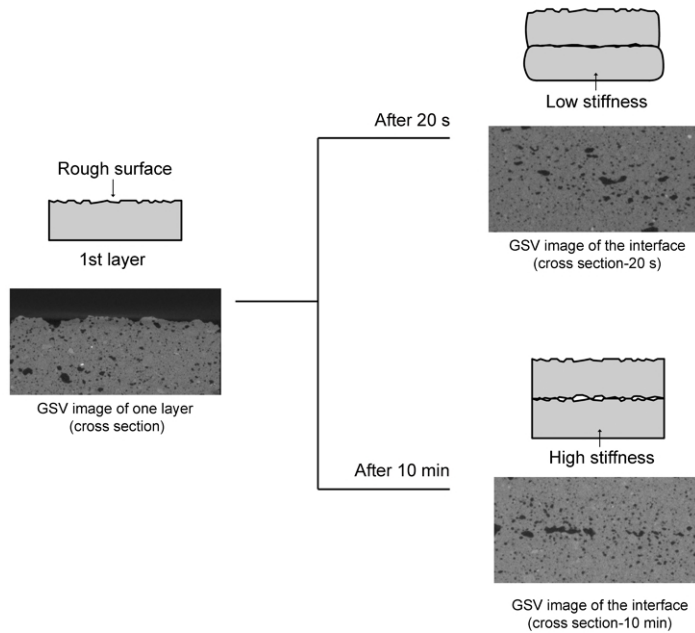


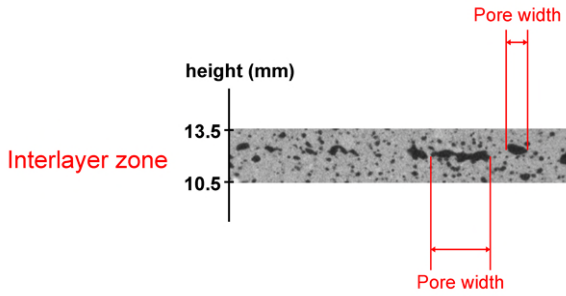
Figure 7.15: Illustration of the influences of extending the time interval on air void formation at the interface.

especially the tensile strength. The crack is localized in the middle area of the sample. However, a brittle post-peak behavior is observed in the simulation. This is mainly attributed to the fact that the constitutive relation of the local elements is assumed as elastic-brittle. As pointed by Zhang et al. [31], the strain-softening behavior at the microscale must be considered in the mesoscale model for quantitative prediction of fracture behavior of cementitious composites. Additionally, as a 2D model was used in the current study, the crack cannot propagate out-of-plane. This also contributes to the brittle post-peak behavior. Possible solutions would be deriving the local elastoplastic constitutive relations from experiments or simulations at a lower scale (i.e., microscale) as performed in [10, 20, 31–33]. Nevertheless, the purpose of this study is to show the potential of the mesoscale model and not to have an ‘exact’ match.

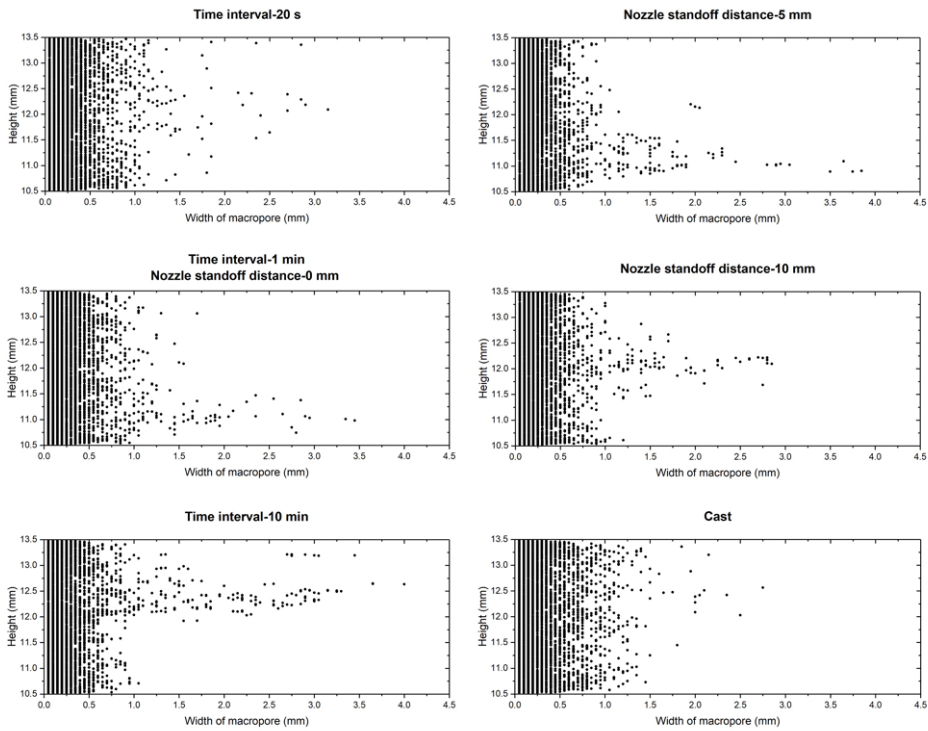
#### MODELING RESULTS OF PRINTED SAMPLES

The mechanical properties of the material made from different parameters were investigated by the 2D lattice fracture model. Figure 7.18 shows the simulated load-displacement curves by keeping the input but varying the 2D material structure (the segmented binary image). A variation appeared between different 2D material structures due to the heterogeneous nature of the cementitious material.

Figures 7.19 and 7.20 show the fracture pattern of the simulated specimens. All the cracks are localized in the middle part of the sample, where the notches are presented. It is in accordance with the experimental observation (see Figure 7.10(b)). Besides, it

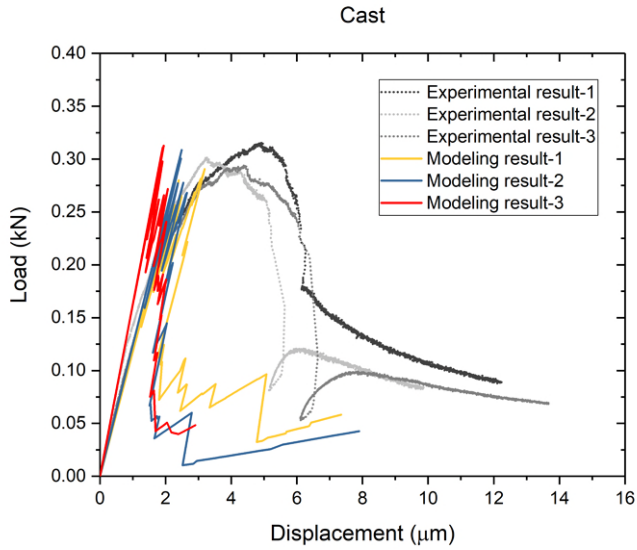


(a)

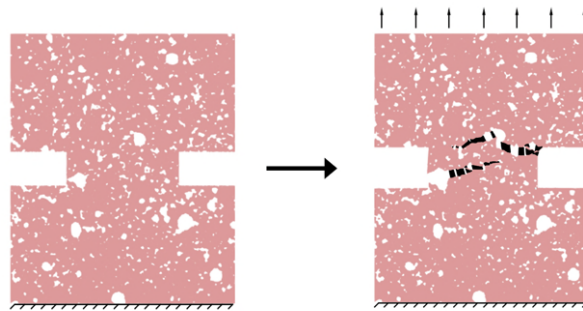


(b)

Figure 7.16: (a) Illustration of pore width determination; (b) Pore width distribution of different samples (results of 40 cross-sections for each sample were plotted) in the interlayer zone (10.5-13.5 mm in height).



(a)



Cast sample

(b)

Figure 7.17: (a) The simulated load vs. displacement curves of the cast specimens; (b) The simulated crack pattern (Left: initial specimen; Right: fractured specimen). Pink area-cementitious material; White area-air void; Black area-crack opening.

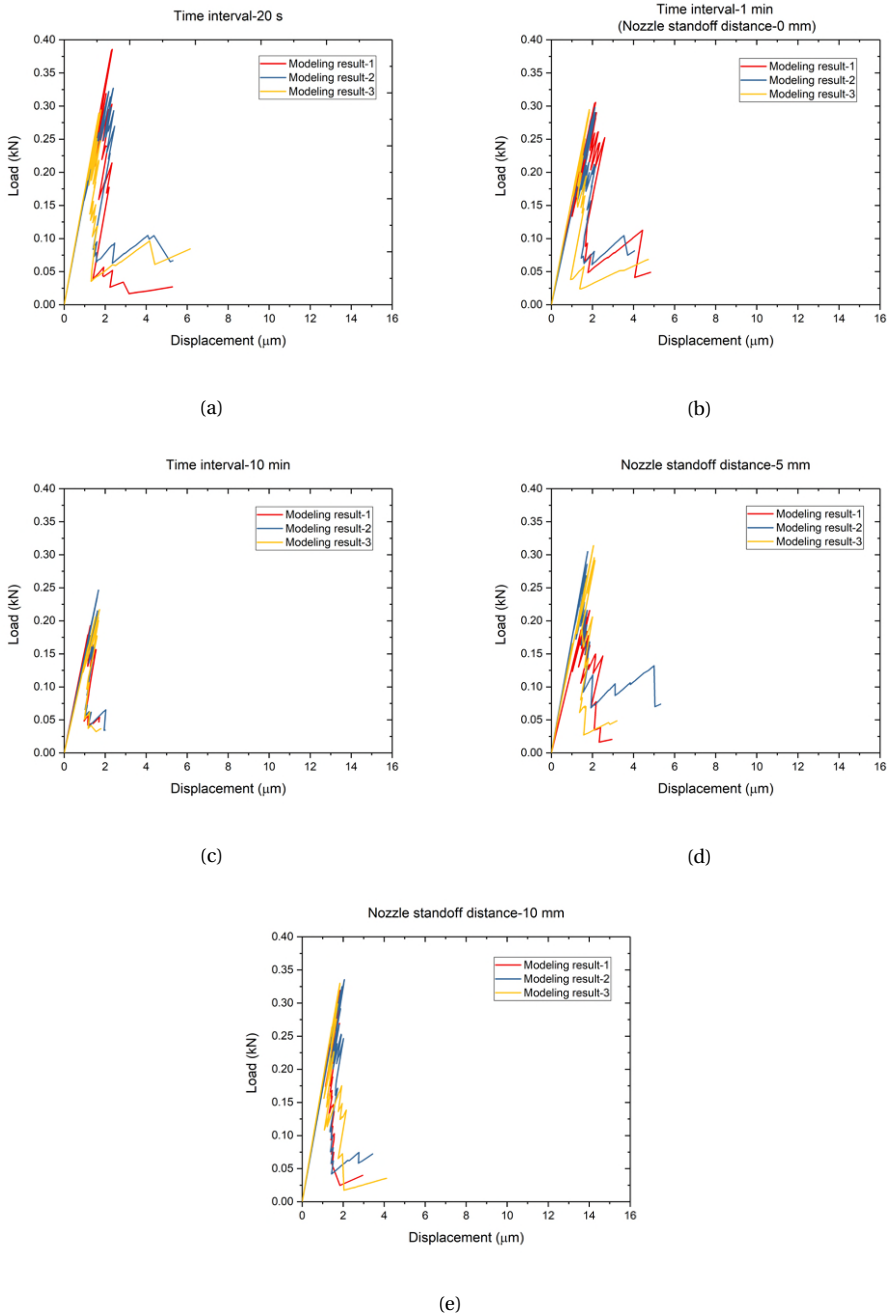
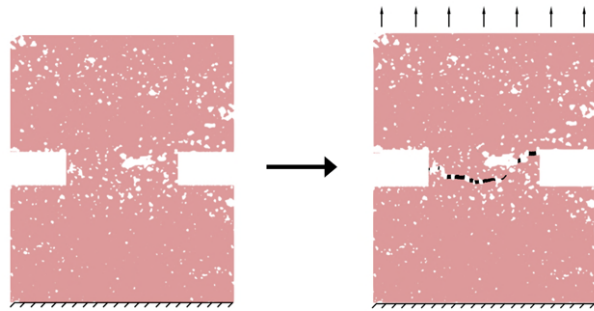
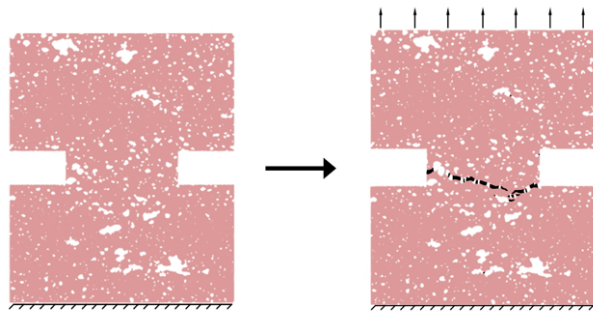


Figure 7.18: Simulated load vs. displacement curves of uniaxial tension tests: (a) Time interval-20 s; (b) Time interval-1 min (also known as nozzle standoff distance-0 mm); (c) Time interval-10 min; (d) Nozzle standoff distance-5 mm; (e) Nozzle standoff distance-10 mm.



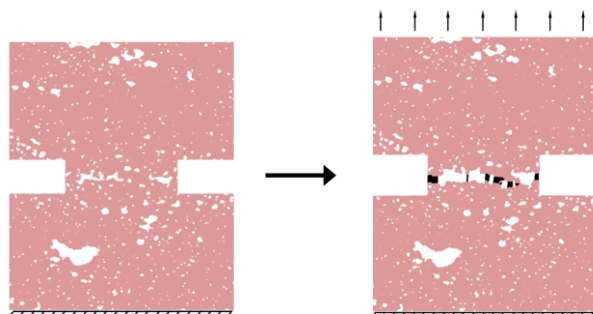
Time interval-20 s

(a)



Time interval-1 min  
(Nozzle standoff distance-10 mm)

(b)

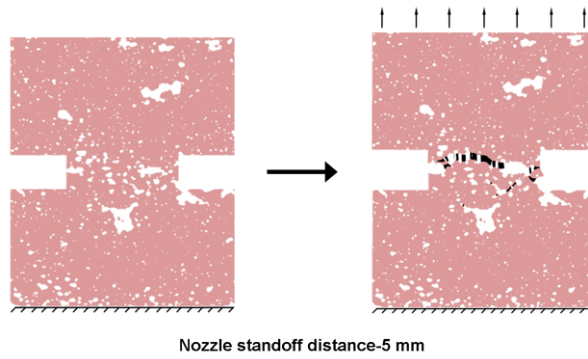


Time interval-10 min

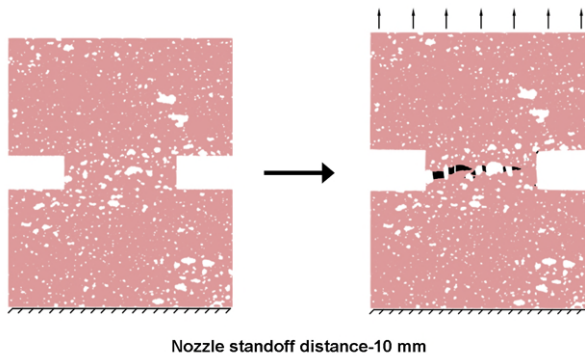
(c)

Figure 7.19: The simulated fracture patterns for different printed specimens (Left: initial specimen; Right: fractured specimen): (a) Time interval-20 s; (b) Time interval-1 min (also known as nozzle standoff distance-0 mm); (c) Time interval-10 min. Pink area-cementitious material; White area-air void; Black area-crack opening.





(a)



(b)

Figure 7.20: The simulated fracture patterns for different printed specimens (Left: initial specimen; Right: fractured specimen): (a) Nozzle standoff distance-5 mm; (b) Nozzle standoff distance-10 mm. Pink area-cementitious material; White area-air void; Black area-crack opening.

can be observed that there is a tendency for cracks to propagate along the air voids, and this tendency becomes more evident in the simulated specimen with 10 min time interval. Thus, it confirmed that the local porosity in this area played a dominant role in the interlayer bond strength. Figure 7.21 shows a comparison between the predicted tensile strength and experimental results. In general, the predicted results correspond well with the experiments. The only exception is specimen 10 mm due to the heterogeneous nature of the cementitious material. The predicted result is higher than the experimental result but still the error is less than 15%. Therefore, the 2D model in this study can give reasonable predictions and catch the trend of the strength variation along with the material structure.

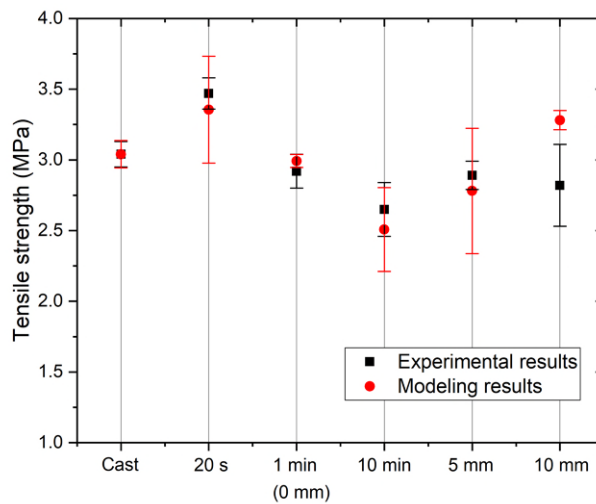


Figure 7.21: Comparison between the modeling and experimental results.

## 7.6. CONCLUSION

THE following conclusions could be drawn in this chapter:

- The specimen with a 20 s of time interval showed the highest interlayer bond strength compared to that of other specimens, which may be attributed to its lowest local porosity at the interface. As the increment of the time interval (from 1 min to 10 min), the interlayer bond strength of printed specimens was reduced at most 13% in comparison with the cast specimens. The reduction in bond strength with prolonging the time interval was due to the increase of local porosity, which was attributed to the increased number of ‘wide’ macropores (pore width > 2 mm) in the interlayer zone.
- By increasing the nozzle standoff distance, limited effects on bond strength in the

interlayer zone have been observed. The possibility of inaccurate layer deposition was increased by increasing the nozzle height, which increased the scatter of uniaxial tensile test results.

- The predicted results of bond strength from the 2D lattice fracture model corresponded well with the experimental results of the uniaxial tensile test. In the model, the local strength of the elements is not changed when the time interval between the layers increases. Since the predicted strength is similar between experiment and model, it can be concluded that the effect of short time intervals (20 s - 10 min) has no (or minimal) influence on the bonding of the material. The strength seems to be only influenced by the local porosity. If the time interval would increase further, the bonding between the materials is probably also affected.
- Due to the limitation of the 2D lattice fracture model, it is worthwhile to employ a 3D lattice fracture model to obtain more insights in the fracture mechanics of 3D printed cementitious materials in further study.

## REFERENCES

- [1] Y. Chen, K. Jansen, H. Zhang, C. Romero Rodriguez, Y. Gan, O. Copuroglu, and E. Schlangen, *Effect of printing parameters on interlayer bond strength of 3D printed limestone calcined clay-based cementitious material: An experimental and numerical study*, *Construction and Building Materials* **262**, 120094 (2020).
- [2] Y. W. D. Tay, G. H. A. Ting, Y. Qian, B. Panda, L. He, and M. J. Tan, *Time gap effect on bond strength of 3D-printed concrete*, *Virtual and Physical Prototyping* **14**, 104 (2019).
- [3] E. Keita, H. Bessaies-Bey, W. Zuo, P. Belin, and N. Roussel, *Weak bond strength between successive layers in extrusion-based additive manufacturing: measurement and physical origin*, *Cement and Concrete Research* **123**, 105787 (2019).
- [4] B. Panda, S. C. Paul, N. A. N. Mohamed, Y. W. D. Tay, and M. J. Tan, *Measurement of tensile bond strength of 3D printed geopolymers mortar*, *Measurement: Journal of the International Measurement Confederation* **113**, 108 (2018).
- [5] T. Le, S. Austin, S. Lim, R. Buswell, R. Law, A. Gibb, and T. Thorpe, *Hardened properties of high-performance printing concrete*, *Cement and Concrete Research* **42**, 558 (2012).
- [6] T. Marchment, J. G. Sanjayan, and B. Nematollahi, *Interlayer Strength of 3D Printed Concrete : Influencing Factors and Method of Enhancing*, in *3D Concrete Printing Technology* (Elsevier Inc., 2019) pp. 241–264.
- [7] J. G. Sanjayan, B. Nematollahi, M. Xia, and T. Marchment, *Effect of surface moisture on inter-layer strength of 3D printed concrete*, *Construction and Building Materials* **172**, 468 (2018).

- [8] J. Van Der Putten, M. Deprez, V. Cnudde, G. De Schutter, and K. Van Tittelboom, *Microstructural characterization of 3D printed cementitious materials*, *Materials* **12**, 2993 (2019).
- [9] E. Schlangen, *Experimental and Numerical Analysis of Fracture Processes in Concrete*, Ph.D. thesis, Delft University of Technology (1993).
- [10] H. Zhang, B. Šavija, S. C. Figueiredo, and E. Schlangen, *Experimentally validated multi-scale modelling scheme of deformation and fracture of cement paste*, *Cement and Concrete Research* **102**, 175 (2017).
- [11] B. Šavija, H. Zhang, and E. Schlangen, *Micromechanical testing and modelling of blast furnace slag cement pastes*, *Construction and Building Materials* **239**, 117841 (2020).
- [12] H. Zhang, Y. Gan, Y. Xu, S. Zhang, E. Schlangen, and B. Šavija, *Experimentally informed fracture modelling of interfacial transition zone at micro-scale*, *Cement and Concrete Composites* **104**, 103383 (2019).
- [13] H. Zhang, B. Šavija, and E. Schlangen, *Combined experimental and numerical study on micro-cube indentation splitting test of cement paste*, *Engineering Fracture Mechanics* **199**, 773 (2018).
- [14] H. Zhang, B. Šavija, and E. Schlangen, *Towards understanding stochastic fracture performance of cement paste at micro length scale based on numerical simulation*, *Construction and Building Materials* **183**, 189 (2018).
- [15] M. Luković, B. Šavija, H. Dong, E. Schlangen, and G. Ye, *Micromechanical Study of the Interface Properties in Concrete Repair Systems*, *Journal of Advanced Concrete Technology* **12**, 320 (2014).
- [16] B. Šavija, M. Luković, J. Pacheco, and E. Schlangen, *Cracking of the concrete cover due to reinforcement corrosion: A two-dimensional lattice model study*, *Construction and Building Materials* **44**, 626 (2013).
- [17] Z. Qian, E. Schlangen, G. Ye, and K. van Breugel, *Modeling framework for fracture in multiscale cement-based material structures*, *Materials* **10** (2017).
- [18] J. Blaber, B. Adair, and A. Antoniou, *Ncorr: Open-source 2D digital image correlation Matlab software*, *Experimental Mechanics* **55**, 1105 (2015).
- [19] K. L. Scrivener, *Backscattered electron imaging of cementitious microstructures: Understanding and quantification*, *Cement and Concrete Composites* **26**, 935 (2004).
- [20] H. Zhang, B. Šavija, S. C. Figueiredo, M. Lukovic, and E. Schlangen, *Microscale testing and modelling of cement paste as basis for multi-scale modelling*, *Materials* **9** (2016).

- [21] H. Zhang, Y. Xu, Y. Gan, Z. Chang, E. Schlangen, and B. Šavija, *Combined experimental and numerical study of uniaxial compression failure of hardened cement paste at micrometre length scale*, *Cement and Concrete Research* **126** (2019).
- [22] B. Šavija, J. Pacheco, and E. Schlangen, *Lattice modeling of chloride diffusion in sound and cracked concrete*, *Cement and Concrete Composites* **42**, 30 (2013).
- [23] H. Zhang, B. Šavija, Y. Xu, and E. Schlangen, *Size effect on splitting strength of hardened cement paste: Experimental and numerical study*, *Cement and Concrete Composites* (2018).
- [24] E. Schlangen and E. J. Garboczi, *Fracture simulations of concrete using lattice models: computational aspects*, *Engineering Fracture Mechanics* **57**, 319 (1997).
- [25] H. Zhang, B. Šavija, M. Luković, and E. Schlangen, *Experimentally informed micromechanical modelling of cement paste: An approach coupling X-ray computed tomography and statistical nanoindentation*, *Composites Part B: Engineering* **157**, 109 (2019).
- [26] K. Mehta and P. J. M. Monteiro, *Concrete: Microstructure, Properties, and Materials*, (McGraw-Hill, New York, 2006) 3rd ed.
- [27] D. Liu, B. Šavija, G. E. Smith, P. E. Flewitt, T. Lowe, and E. Schlangen, *Towards understanding the influence of porosity on mechanical and fracture behaviour of quasi-brittle materials: experiments and modelling*, *International Journal of Fracture* **205**, 57 (2017).
- [28] H. Lee, J.-H. J. Kim, J.-H. Moon, W.-W. Kim, and E.-A. Seo, *Correlation between pore characteristics and tensile bond strength of additive manufactured mortar using X-ray computed tomography*, *Construction and Building Materials* **226**, 712 (2019).
- [29] R. J. Wolfs, F. P. Bos, and T. A. Salet, *Hardened properties of 3D printed concrete: The influence of process parameters on interlayer adhesion*, *Cement and Concrete Research* **119**, 132 (2019).
- [30] R. J. M. Wolfs, F. P. Bos, E. C. F. van Strien, and T. A. M. Salet, *A real-time height measurement and feedback system for 3D concrete printing*, in *High Tech Concrete: Where Technology and Engineering Meet*, edited by D. Hordijk and M. Luković (2018) pp. 2474–2483.
- [31] H. Zhang, Y. Xu, Y. Gan, E. Schlangen, and B. Šavija, *Experimentally validated meso-scale fracture modelling of mortar using output from micromechanical models*, *Cement and Concrete Composites* **110**, 103567 (2020).
- [32] L. Y. Lv, H. Zhang, E. Schlangen, Z. Yang, and F. Xing, *Experimental and numerical study of crack behaviour for capsule-based self-healing cementitious materials*, *Construction and Building Materials* **156**, 219 (2017).
- [33] H. Zhang, Y. Xu, Y. Gan, Z. Chang, E. Schlangen, and B. Šavija, *Microstructure informed micromechanical modelling of hydrated cement paste: Techniques and challenges*, *Construction and Building Materials* **251**, 118983 (2020).



# III

## DISCUSSION AND CONCLUSION





# 8

## CHALLENGES AND OPPORTUNITIES FOR IMPLEMENTING 3D CONCRETE PRINTING IN BUILDING CONSTRUCTION

*The objective of this chapter is to discuss the challenges and opportunities of implementing 3D concrete printing in building and infrastructure construction, considering its technical, sustainability, and economic potentials. Most of the raised points in this chapter are common issues of 3D concrete printing industry.*

## 8.1. INTRODUCTION

THE developed 3D printable cementitious materials in this thesis can manufacture a lab-scale prototype (see Figure 8.1). However, it may still be a long way to widely use such materials in practice since most of the techniques related to extrusion-based 3D concrete printing (3DCP) are currently under development. This chapter aims to discuss the concerns, barriers, and state-of-the-art solutions for using 3DCP in building and infrastructure construction. Technical challenges concerning, i.e., on-site printing, reinforcement placement, standardization, and durability, were initially summarized. In addition, discussions about manufacturing calcined clay sustainably and economically, and fabricating complex-geometric/topology optimized structure elements were given.

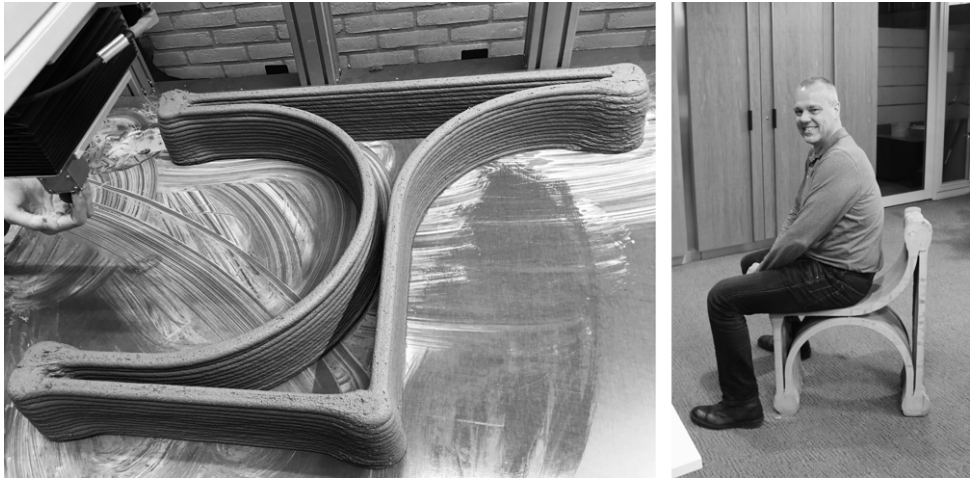


Figure 8.1: A lab-scale prototype was fabricated by using a limestone-calcined clay-based cementitious material developed in this thesis.

## 8.2. TECHNICAL CHALLENGES

### 8.2.1. ON-SITE PRINTING

DU E to the absence of formwork, curing of 3D printed cementitious materials at a very early age (during printing) remains a critical issue for researchers [3]. Difficulties in printing environment control may lead to rapid water loss from the deposited materials. This can lead to the weak adhesion between layers [4–6] and severe plastic shrinkage cracks (see Figure 8.2), which affect the final mechanical performance and durability of the printed cementitious materials. For improving the early-age plastic shrinkage, the increase of internal curing using saturated lightweight aggregate or chemical admixtures (e.g., shrinkage reducing agents) have been proposed as a solution by [7].

Water evaporation induced by dry air, wind and/or high ambient temperature during printing should be prevented [4]. Using a curing compound might be a solution, but the impact on bond strength must be considered. Performing 3DCP construction in

a temporarily controlled environment could also be a favorable solution. For example, Apis Cor did 3DCP construction in a temperature-controlled tent to control water loss during the printing process [7]. Other challenges of on-site 3DCP, i.e., transportation and assembly of the printing system, process-induced effects, and construction management, need to be thoroughly considered [8].



Figure 8.2: Drying plastic shrinkage induced cracks on the printed cementitious materials, adapted from [3].

### 8.2.2. REINFORCEMENT PLACEMENT

Structural safety seems to be a significant concern towards rapidly developing and spreading 3DCP [9]. Being quasi-brittle, concrete is weak in tension and shows poor ductility. Steel reinforcement is the most common way to solve this problem in conventional concrete. However, it is quite difficult to lay steel reinforcement automatically and directly in the 3DCP process [10, 11]. Many approaches have been introduced for reinforced 3DCP, which are summarized in Table 8.1.

#### Steel rebar reinforcement (manual)

As shown in Figure 8.3(a), printing concrete formwork, placing steel rebars, and pouring fresh concrete is currently one of the most generic and applicable strategies for 3DCP to make load-bearing structural components. However, this method limits many potential advantages of 3DCP [12]. Besides, an external reinforcement system can also be applied in fabricating 3D printed concrete structures (see Figure 8.3(b)), according to [13]. A structural component is divided into several segments that are printed separately. Afterwards, these printed segments are connected and assembled into the final element along with a unique steel reinforcement system.

#### Mesh reinforcement

As shown in Figure 8.3(c), the mesh reinforcement is pre-installed, and the fresh cementitious materials are deposited through two nozzles on either side of the pre-installed mesh reinforcement. This method was firstly presented by a Chinese construction company Huashang Tengda ltd and was improved by Marchment and Sanjayan [14]. Instead of a large-scale pre-installed steel mesh, which mostly limited

the design freedom, the authors [14] embedded multiple short meshes during printing. By employing a novel nozzle, a mesh segment is introduced vertically while the deposition of material layers. The small mesh reinforcements are also lapped in the interlayer for enhancing the bond strength (see Figure 8.3(d)).

### **Fiber reinforcement**

Bos et al. [9] pointed out that fiber-reinforced cementitious materials with adequate tensile strength and elasticity could be developed for additive manufacturing. As they mentioned, two challenges remain to impede the use of fiber reinforcement in 3DCP. First, blockage, segregation, and uneven distributions (in quantity and orientation) are not avoided even only with 1-3 vol.% of fibers in the printable concrete. Second, how can we ensure that fibers can effectively pass-through between filaments? To date, many attempts [15–21] using different types of fibers have been made to develop 3D printable fiber-reinforced cementitious materials. However, solving such problems, especially the second one, by the current 3DCP process is still challenging.

### **Cable reinforcement**

The use of cable reinforcement based on the idea from [22] as a more advanced concept is initially proposed by studies [12, 23]. An entrainment device that can embed various types of metal cables during printing has been developed and used by the 3DCP research group at TU Eindhoven since 2017. In their tests, significant post-crack failure strength and deformation capacity of steel cable-reinforced concrete have been obtained [12]. This technique was successfully employed to build the first 3DCP bicycle bridge in Gemert, Netherlands [24]. Similar approaches and experimental tests of 3D printed cementitious materials with cable reinforcement are reported by [25, 26] recently. Carbon-cable is also feasible to be employed in this technique [27]. Nonetheless, as with fiber reinforcement, cable reinforcement cannot increase the layer-to-layer interface tensile strength of printed concrete.

### **Penetration of steel reinforcement**

Penetrating steel reinforcement, such as nails, screws, deformed and helical bars, is used to enhance the vertical layer-to-layer bonding of the printed structure (see [28–30]). This technique is defined as a layer penetration reinforcing method (LPRM) by Marchment and Sanjayan [29, 31]. They stated that a fixed number of layers is printed initially, and the pre-cut reinforcement is vertically penetrated in the deposited fresh layers afterwards. A secondary robot or a specific attachment of printhead is employed to place steel bars automatically. However, the automated penetration system is still under investigation currently. In works [28–30], the steel reinforcement is manually inserted into the fresh layers. Using this method, Marchment and Sanjayan [29] found that both deformed and helical bars could enhance the flexural strength of the printed sample with reinforcement. The slippage of reinforcements is regarded as the failure mechanism of all tested samples. Thus, the bond between the inserted bars and cementitious materials may play the dominant role. Perrot et al. [30] pointed out that nails with a rough surface are recommended for achieving a good bond with cementitious materials. They also reported that the penetration force of nails is

influenced by the rheological behaviors of the printed cementitious materials, including both initial yield stress and structuration rate.

Table 8.1: A summary of the available reinforcement approaches for 3DCP

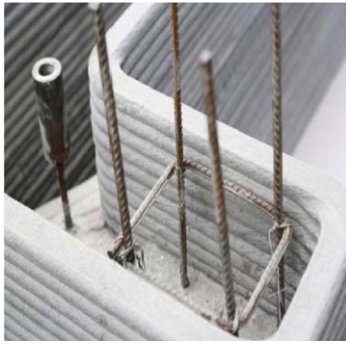
Type	Material	Illustration	Reference
Steel rebar reinforcement (manual)	Steel rebars.	See Figures 8.3(a) and 8.3(b).	[13, 24]
Mesh reinforcement	Steel meshes.	See Figures 8.3(c) and 8.3(d).	[14]
Fiber reinforcement	Steel, carbon, basalt, polyvinyl-alcohol, polypropylene, glass, and other fibers.	See Figure 8.4(a).	[15–21]
Cable reinforcement	Steel, carbon, and other cables (or chains).	See Figure 8.4(b).	[23, 25, 27, 35]
Penetration of steel reinforcement	Nails, screws, steel rebars.	See Figures 8.4(c) and 8.4(d).	[28–31, 34]

### 8.2.3. STANDARDIZATION

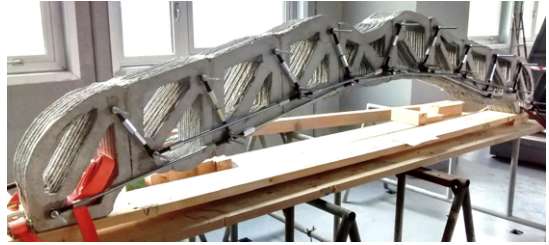
There are no standards, norms or guidelines specifically available for printable concrete [9, 36, 37]. 3DCP is an emerging technique for concrete fabrication. Current research efforts are built on the experiments from only a limited number of academic institutions. For the use of 3DCP in building and construction sector, standards for material making and testing, manufacturing process, and structural design are highly demanded [9, 36]. Although there is no standard or guideline in the material section, several specific test methods are designed to evaluate fresh and hardened properties of 3D printable cementitious materials (see Section 2.4, Chapter 2). With the rapid development of 3DCP, the existing test methods will be improved, and more predictable processes will be designed. Standards for printable concrete will be released in the future. Additionally, as mentioned by Wolfs [38], the ‘design by testing’ approach can be applied in the case of using the large-scale printed structural component in practice. The legal framework of ‘design by testing’ approach is provided by Eurocode [39]. For a proper understanding of scale effects and structural properties, large scale testing of 3D printed structural elements is adopted (see Figure 8.5).

### 8.2.4. DURABILITY

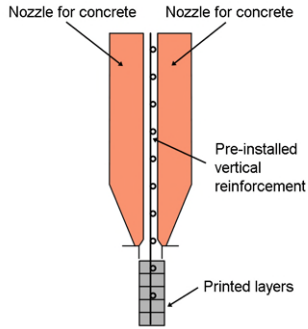
The durability of 3D printed concrete elements is also a concern to impede the implementation of 3DCP in building construction. However, durability aspects have not yet been prioritized in the current studies of 3DCP. For implementing 3D printed concrete components in practice, more attention should be paid to the long-term performance of printed concrete. The reasons are given as follows. First, detrimental effects on concrete and reinforcement performances induced by the addition of chemical admixtures, e.g., accelerator, retarder, and viscosity modifying admixture, need to be studied [40]. Second, the interlayer of printed structure with a high porosity leads to not only weak bonding strength but also high water permeability and chloride



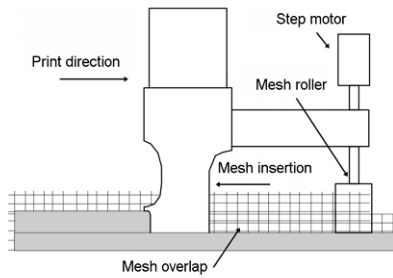
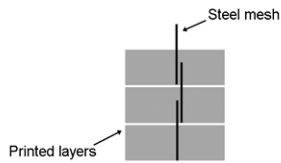
(a)



(b)



(c)



(d)

Figure 8.3: (a) Steel reinforcement and 3D printed concrete formwork by Winsun, adapted from [32]; (b) External steel reinforcement system connected with 3D printed concrete segments, adapted from [13]; (c) Pre-installed mesh reinforcement method by Huashang Tengda ltd, adapted from [14]; (d) Mesh insertion and embedment method, adapted from [14].



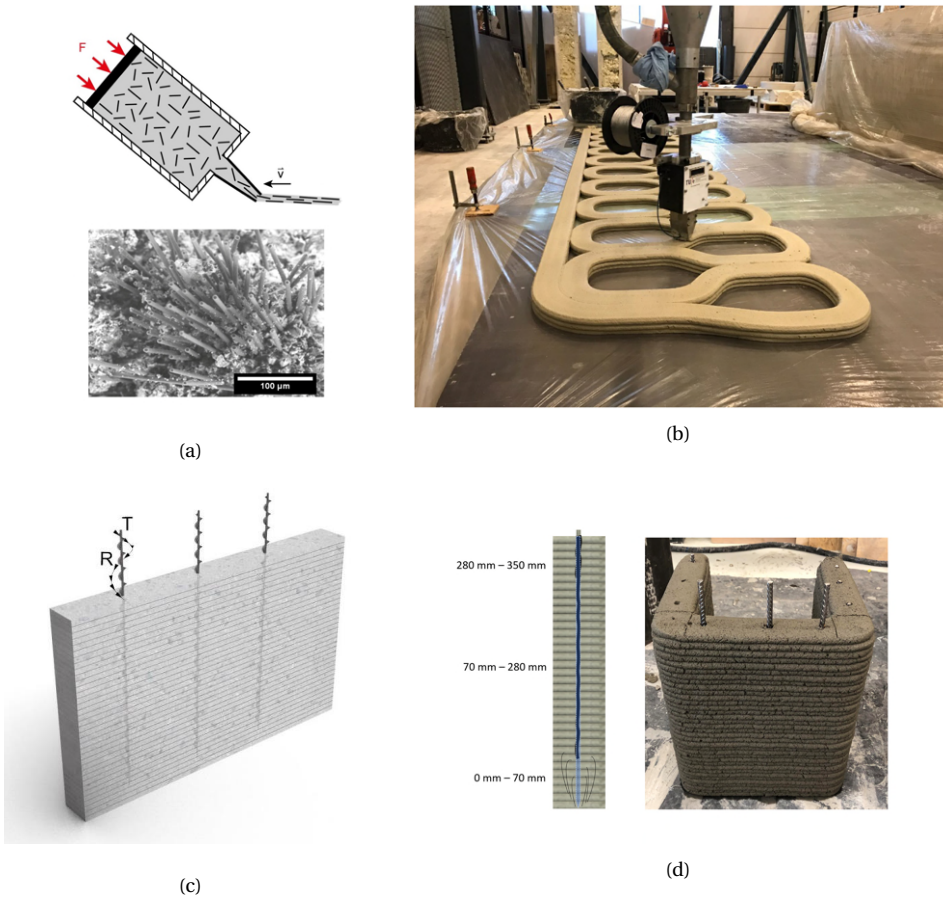


Figure 8.4: (a) 3D printed cementitious materials with fiber reinforcement, adapted from [17]; (b) 3D printed cementitious materials with cable reinforcement, adapted from [33]; (c) Illustration of screw reinforcement for 3D printed cementitious materials, adapted from [34]; (d) 3D printed cementitious materials reinforced by penetrated steel rebars, adapted from [31].



Figure 8.5: The test setup for large-scale 3D printed structural elements in TU Eindhoven, adapted from [38].

penetration levels [40–42]. Third, owing to the high content of binding materials (especially Portland cement) in available 3DCP recipes, shrinkage and creep of large-scale 3D printed concrete should be investigated. Other durability issues related to material compositions and environmental conditions, i.e., carbonation, and freeze-thawing degradation, should be considered regarding the material composition, specific function, and requirement of printed concrete elements.

### 8.3. ENVIRONMENTAL AND ECONOMIC POTENTIALS

#### 8.3.1. FLASH CALCINATION OF CLAY

As mentioned in Chapter 2, the production of calcined clay is also a process that consumes energy and emits CO<sub>2</sub>. There are three stages to manufacturing calcined clay or metakaolin on an industrial scale, including the initial grinding/selection, rotary kiln calcination, and the grinding of calcined materials. More recently, flash calcination (see Figure 8.6), as a more advanced method, is employed to produce metakaolin [43]. A comparison between rotary kiln and flash calcination processes is given in Table 8.2. It could be found that the calcination time of flash calcination method is much shorter than that of rotary kiln. The heating temperature in the flash calcination process is increased by about 150–500 °C, whereas the total energy consumption is reduced compared to rotary kiln calcination. Because of the rapid release of water vapor, calcined clay produced by flash calcination displays a bit higher specific surface area (SSA) and reactivity than that made by rotary calcination [44, 45]. However, contrary results were reported by [43, 46]. The authors found that flash metakaolin showed a higher circularity and lower SSA than rotary-kiln metakaolin. The chemical and mineral properties of metakaolin are not modified by using different calcination methods. The different findings in various studies may be attributed to the different raw materials and calcined procedures.

From a sustainable point of view, flash calcination seems to be the optimal option for producing calcined clay. However, it is worth noting that the initial investment of this technique is about twice of the retrofitted kiln [47]. Besides, the optimal flash calcination process for achieving the metakaolin with the ideal physical properties (fineness, SSA,



Table 8.2: Comparison between rotary kiln and flash calcination processes [43, 47].

	Rotary kiln calcination	Flash calcination
Calciner	The specific rotary kiln for producing metakaolin. Or a retrofitted calciner based on a clinker kiln (examples in Cuba).	The optimized flash calciner with a high initial investment.
Calcination temperature	700-850 °C	1000-1200 °C
Calcined time	3-5 h.	A few tenths of a second (heated to reach 700 °C and quickly cooled to 100 °C).
Grinding after calcination	Yes (due to the agglomeration).	No (insufficient time to agglomerate).
Energy consumption	3235 MJ/t. (Equal to 43% of clinker production in Cuba).	2775 MJ/t. (Equal to 37% of clinker production in Cuba).

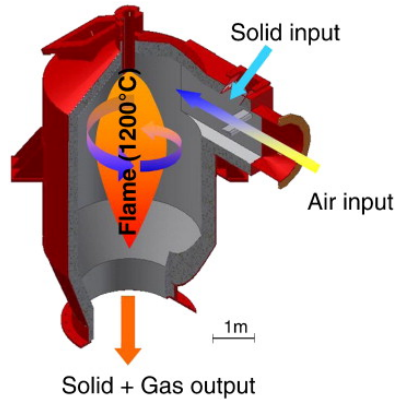


Figure 8.6: Illustration of the working mechanism of a flash calciner, adapted from [43].

and morphology of particles) is still under investigation [48].

### 8.3.2. PRINT IN A SMART AND EFFICIENT WAY

3DCP can be used to manufacture customized/complex geometric elements directly, which is an enormous advantage over conventional concrete construction. As reported by [40], using the mold-cast method is difficult to produce a concrete structure with complex geometry economically, which requires the employment of wasteful, one-time-use molds. In contrast, 3DCP does not need any formwork principally. The unit cost of digital fabrication (3DCP in this context) shows a very flat curve with increased complexity in Figure 8.7. The authors also believed that continued research and development of additive manufacturing could significantly enhance the cost-efficiency of components with low complexities and the demand of highly complex building components.

Lim et al. [49] identified that the 3D model could be optimized for strength before concrete printing, and thus the final print only requires the minimum amount of

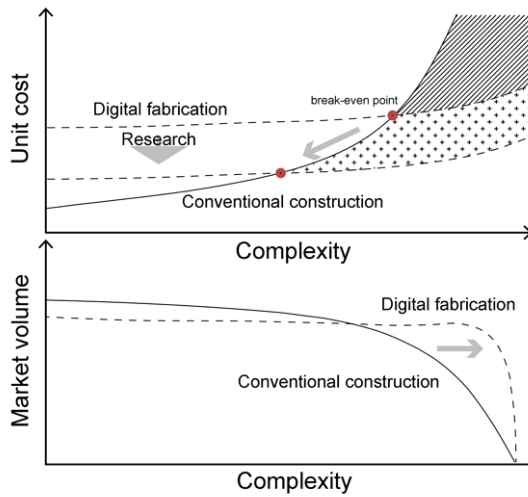


Figure 8.7: In both graphs, the dashed and solid curves represent digital fabrication and conventional construction, respectively. Top: Unit cost vs. complexity of building component. After the break-even point, using additive manufacturing shows great economic potential. Under the driving force of research, the break-even point can be shifted to the left. Bottom: Market volume vs. complexity of building component. With the development of digital fabrication, the demand for higher complexities is increasing. Adapted from [40].

concrete. According to Tay et al. [10], topology optimization and finite element analysis can be utilized to generate optimized designs for 3DCP elements. Combined with topology-optimized structural design methods, 3DCP becomes a more functional and sustainable fabrication method in practice. About 50% of environmental impacts can be reduced by employing additive manufacturing of concrete with structural optimization in comparison with conventional construction [50].

As shown in Figure 8.8, a lab-scale post-tensioned concrete girder with a 4 m span was fabricated by connecting several 3D printed concrete segments at Ghent University. In this case, the concrete distribution, shape, and curvature of the post-tension cable are optimized using topology optimization techniques. Compared with a T-section girder with the similar size and deflection (under the same load), more than 20 vol.% of concrete materials are saved in the optimized concrete girder [51, 52]. Note that 3D printed concrete segments can be regarded as permanent formwork in this project. The internal cavity of these printed components is filled by grout, which is the same as the method adopted in the 3DCP bicycle bridge in Gemert [51].

However, the advantages of 3DCP are strongly limited by the printing capability of the system. Structures like arch, vault, and dome shapes, are a bottleneck challenging the current 3DCP technique. Perkins and Skitmore [54] offered one method for 3D printing to handle those special structures by simultaneously printing another material in the void, creating a kind of scaffold. The supporting parts can be removed once they are no longer required. The method is quite like the printing flow of Fused Deposition Modeling (FDM). Two types of materials for printing and supporting, respectively, are

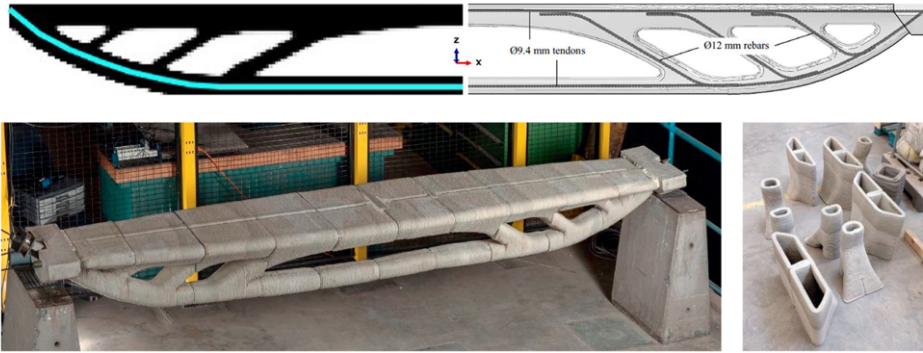


Figure 8.8: A lab-scale 3D printed and post-tensioned concrete girder constructed at Ghent University, adapted from [51, 52].

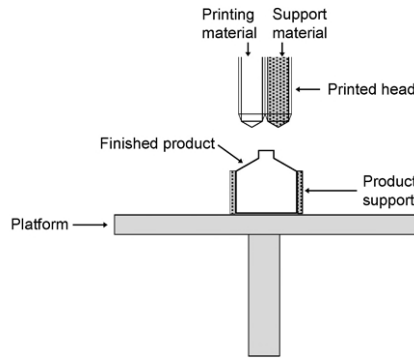
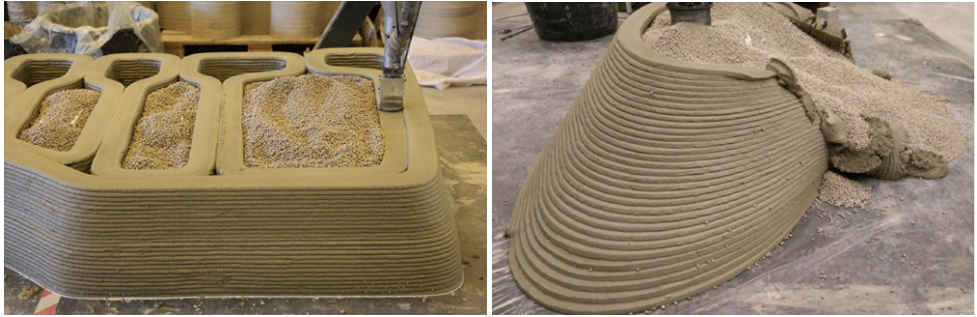


Figure 8.9: Illustration of the working mechanism of FDM, adapted from [53].

extruded through two nozzles separately (see Figure 8.9). The support material is applied to print a support structure to avoid collapsing of the printed structure. Subsequently, the support structure will be removed [53]. This idea has also been demonstrated by [49, 55, 56]. Lim et al. [55] utilized a gypsum-based material as support material, for it is low strength and can be easily removed as well as 100% recycled. Besides, as mentioned by Wolfs [38], the coarse lightweight filler can also be employed as the temporary support material to provide the support of layers in vertical and horizontal directions during 3DCP (see Figure 8.10). Nonetheless, more maintenance, cleaning, and control are required for operating such a support structure [49].

Inspired by masonry strategies for constructing cantilevers, vaults, and domes hundreds of years ago, attempts to build cantilevers using 3DCP without any temporary support were made by [57]. The authors identified the parameters (i.e., support, initial brick stress state, and layer continuity) that dominate the structural stability of cantilevers in masonry construction and then shifted these parameters into 3DCP for reproducing such structures. Also, they proposed the guidelines for designing printable



(a)

(b)

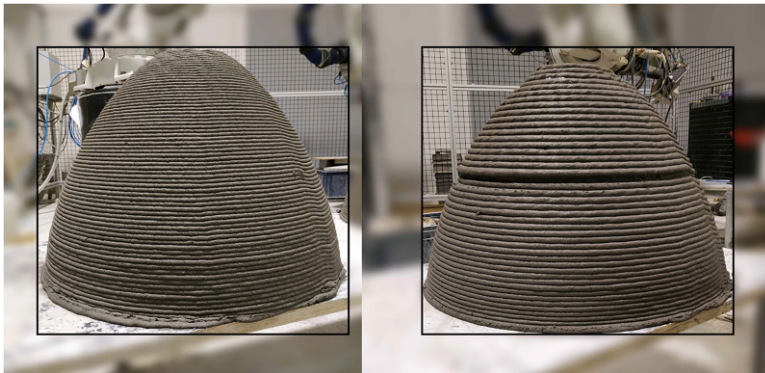
Figure 8.10: Examples of using the temporary support material during printing: (a) A normal trial; (b) A failed trial. Adapted from [38].

geometries and for generating the optimal printing toolpath considered fresh-state behaviors of materials (yield stress, structuration rate, and others). To validate the identified constraints, the designed domes and Nubian vaults have been successfully printed based on the generated printing toolpaths, as seen from Figure 8.11.

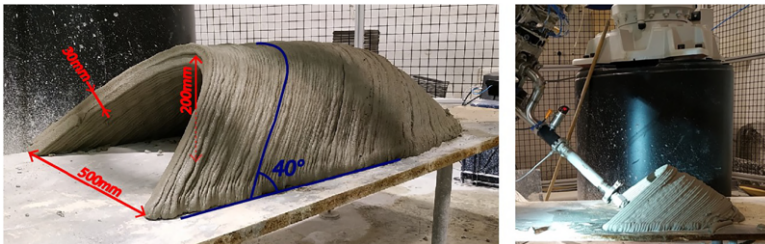
#### 8.4. CONCLUSION

THIS chapter discussed the challenges and opportunities of implementing 3DCP in building and infrastructure construction, considering its technical, sustainability, and economic potentials. The following points could be summarized:

- On-site printing: the curing of printed cementitious materials is strongly influenced by the ambient temperature and humidity, and seems to be a main constraint to impede the on-site printing.
- Reinforcement: the proposed reinforcement methods for 3DCP include steel rebar reinforcement (manual), mesh reinforcement, fiber reinforcement, cable reinforcement, and penetration of steel reinforcement. Among of them, only the penetration reinforcing method and mesh reinforcement could effectively enhance the interlayer bonding of printed structures.
- Standard: the norm for printable concrete is currently unavailable. In the material sector, specific test methods are designed to evaluate fresh and hardened properties of 3D printable cementitious materials. In the aspect of structural design, the ‘design by testing’ approach can be employed.
- Durability: the durability issues related to the effects of chemical admixtures, the interlayer with high porosity, high content of binding materials, and other factors need to be considered in practice.
- Calcined clay: using flash calcination may be the most sustainable way to produce calcined clay. However, the high initial investment of this technique should be



(a)



(b)

Figure 8.11: (a) 3D printed domes (Left: constant layer thickness; Right: variable layer thickness); (b) An example of a 3D printed Nubian vault. Adapted from [57].

considered.

- Complex geometric structure: the fabrication of geometrically-complex/topology optimized concrete components in a sustainable and cost-efficient way is one of the primary advantages of using 3DCP compared to the conventional mold-cast method. Many strategies, i.e., printed formwork, temporary support, optimization of printing geometry and toolpath, can be employed to improve the printing capability of the current system.

## REFERENCES

- [1] Y. Chen, F. Veer, and O. Çopuroğlu, *A critical review of 3D concrete printing as a low CO<sub>2</sub> concrete approach*, *Heron* **62**, 167 (2017).
- [2] Y. Chen, S. Chaves Figueiredo, Z. Li, Z. Chang, K. Jansen, O. Çopuroğlu, and E. Schlangen, *Improving printability of limestone-calcined clay-based cementitious materials by using viscosity-modifying admixture*, *Cement and Concrete Research* **132**, 106040 (2020).
- [3] G. De Schutter, K. Lesage, V. Mechtcherine, V. N. Nerella, G. Habert, and I. Agusti-Juan, *Vision of 3D printing with concrete — Technical, economic and environmental potentials*, *Cement and Concrete Research* **112**, 25 (2018).
- [4] E. Keita, H. Bessaies-Bey, W. Zuo, P. Belin, and N. Roussel, *Weak bond strength between successive layers in extrusion-based additive manufacturing: measurement and physical origin*, *Cement and Concrete Research* **123**, 105787 (2019).
- [5] J. G. Sanjayan, B. Nematollahi, M. Xia, and T. Marchment, *Effect of surface moisture on inter-layer strength of 3D printed concrete*, *Construction and Building Materials* **172**, 468 (2018).
- [6] R. J. Wolfs, F. P. Bos, and T. A. Salet, *Hardened properties of 3D printed concrete: The influence of process parameters on interlayer adhesion*, *Cement and Concrete Research* **119**, 132 (2019).
- [7] D. Marchon, S. Kawashima, H. Bessaies-Bey, S. Mantellato, and S. Ng, *Hydration and rheology control of concrete for digital fabrication: Potential admixtures and cement chemistry*, *Cement and Concrete Research* **112**, 96 (2018).
- [8] V. Mechtcherine, V. N. Nerella, F. Will, M. Näther, J. Otto, and M. Krause, *Large-scale digital concrete construction – CONPrint3D concept for on-site, monolithic 3D-printing*, *Automation in Construction* **107**, 102933 (2019).
- [9] F. Bos, R. Wolfs, Z. Ahmed, and T. Salet, *Additive manufacturing of concrete in construction: Potentials and challenges of 3D concrete printing*, *Virtual and Physical Prototyping* **11**, 209 (2016).
- [10] Y. W. D. Tay, B. Panda, S. C. Paul, N. A. Noor Mohamed, M. J. Tan, and K. F. Leong, *3D printing trends in building and construction industry: a review*, *Virtual and Physical Prototyping* **12**, 261 (2017).



- [11] T. Wangler, E. Lloret, L. Reiter, N. Hack, F. Gramazio, M. Kohler, M. Bernhard, B. Dillenburger, J. Buchli, N. Roussel, and R. Flatt, *Digital concrete: opportunities and challenges*, RILEM Technical Letters **1**, 67 (2016).
- [12] T. A. Salet, F. P. Bos, R. J. Wolfs, and Z. Y. Ahmed, *3D concrete printing - A structural engineering perspective*, in *High Tech Concrete: Where Technology and Engineering Meet - Proceedings of the 2017 fib Symposium*, edited by D. Hordijk and M. Luković (2017) pp. xliii–lvii.
- [13] D. Asprone, F. Auricchio, C. Menna, and V. Mercuri, *3D printing of reinforced concrete elements: Technology and design approach*, *Construction and Building Materials* **165**, 218 (2018).
- [14] T. Marchment and J. Sanjayan, *Mesh reinforcing method for 3D Concrete Printing*, *Automation in Construction* **109**, 102992 (2020).
- [15] A. R. Arunothayan, B. Nematollahi, R. Ranade, S. H. Bong, and J. Sanjayan, *Development of 3D-printable ultra-high performance fiber-reinforced concrete for digital construction*, *Construction and Building Materials* **257**, 119546 (2020).
- [16] S. Chaves Figueiredo, C. Romero Rodríguez, Z. Y. Ahmed, D. H. Bos, Y. Xu, T. M. Salet, O. Çopuroğlu, E. Schlangen, and F. P. Bos, *An approach to develop printable strain hardening cementitious composites*, *Materials and Design* **169**, 107651 (2019).
- [17] M. Hambach and D. Volkmer, *Properties of 3D-printed fiber-reinforced Portland cement paste*, *Cement and Concrete Composites* **79**, 62 (2017).
- [18] V. Li, F. Bos, K. Yu, W. McGee, T. Y. Ng, S. C. Figueiredo, K. Nefs, V. Mechtcherine, V. N. Nerella, J. Pan, G. van Zijl, and J. Kruger, *On the emergence of 3D printable Engineered, Strain Hardening Cementitious Composites (ECC/SHCC)*, *Cement and Concrete Research* **132**, 106038 (2020).
- [19] G. Ma, Z. Li, L. Wang, F. Wang, and J. Sanjayan, *Mechanical anisotropy of aligned fiber reinforced composite for extrusion-based 3D printing*, *Construction and Building Materials* **202**, 770 (2019).
- [20] B. Nematollahi, M. Xia, P. Vijay, and J. G. Sanjayan, *Properties of Extrusion-Based 3D Printable Geopolymers for Digital Construction Applications*, in *3D Concrete Printing Technology* (Elsevier Inc., 2019) pp. 371–388.
- [21] P. Shakor, S. Nejadi, S. Sutjipto, G. Paul, and N. Gowripalan, *Effects of deposition velocity in the presence/absence of E6-glass fibre on extrusion-based 3D printed mortar*, *Additive Manufacturing* **32**, 101069 (2020).
- [22] B. Khoshnevis, D. Hwang, K.-T. Yao, and Z. Yeh, *Mega-scale fabrication by contour crafting*, *International Journal of Industrial and Systems Engineering* **1**, 301 (2006).
- [23] F. P. Bos, Z. Y. Ahmed, E. R. Jutinov, and T. A. Salet, *Experimental exploration of metal cable as reinforcement in 3D printed concrete*, *Materials* **10** (2017).

- [24] T. A. Salet, Z. Y. Ahmed, F. P. Bos, and H. L. Laagland, *Design of a 3D printed concrete bridge by testing\**, *Virtual and Physical Prototyping* **13**, 222 (2018).
- [25] Z. Li, L. Wang, G. Ma, J. Sanjayan, and D. Feng, *Strength and ductility enhancement of 3D printing structure reinforced by embedding continuous micro-cables*, *Construction and Building Materials* **264**, 120196 (2020).
- [26] G. Ma, Z. Li, L. Wang, and G. Bai, *Micro-cable reinforced geopolymer composite for extrusion-based 3D printing*, *Materials Letters* **235**, 144 (2019).
- [27] V. Mechtcherine, A. Michel, M. Liebscher, and T. Schmeier, *Extrusion-Based Additive Manufacturing with Carbon Reinforced Concrete : Concept and Feasibility Study*, *Materials* **13**, 2568 (2020).
- [28] B. Baz, G. Aouad, and S. Remond, *Effect of the printing method and mortar's workability on pull-out strength of 3D printed elements*, *Construction and Building Materials* **230**, 117002 (2020).
- [29] T. Marchment and J. Sanjayan, *Penetration Reinforcing Method for 3D Concrete Printing*, in *Second RILEM International Conference on Concrete and Digital Fabrication – Digital Concrete 2020*, Vol. 109, edited by F. Bos, S. Lucas, R. Wolfs, and T. Salet (2020) pp. 680–690.
- [30] A. Perrot, Y. Jacquet, D. Rängeard, E. Courteille, and M. Sonebi, *Nailing of Layers: A Promising Way to Reinforce Concrete 3D Printing Structures*, *Materials* **13**, 1518 (2020).
- [31] T. Marchment and J. Sanjayan, *Bond properties of reinforcing bar penetrations in 3D concrete printing*, *Automation in Construction* **120**, 103394 (2020).
- [32] V. Mechtcherine, J. Grafe, V. N. Nerella, E. Spaniol, M. Hertel, and U. Füssel, *3D-printed steel reinforcement for digital concrete construction – Manufacture, mechanical properties and bond behaviour*, *Construction and Building Materials* **179**, 125 (2018).
- [33] D. Asprone, C. Menna, F. P. Bos, T. A. Salet, J. Mata-Falcón, and W. Kaufmann, *Rethinking reinforcement for digital fabrication with concrete*, *Cement and Concrete Research* **112**, 111 (2018).
- [34] L. Hass and F. Bos, *Bending and Pull-Out Tests on a Novel Screw Type Reinforcement for Extrusion-Based 3D Printed Concrete*, in *Second RILEM International Conference on Concrete and Digital Fabrication – Digital Concrete 2020.*, Vol. 28, edited by F. Bos, S. Lucas, R. Wolfs, and T. Salet (2020) pp. 632–645.
- [35] J. H. Lim, B. Panda, and Q.-c. Pham, *Improving flexural characteristics of 3D printed geopolymer composites with in-process steel cable reinforcement*, *Construction and Building Materials* **178**, 32 (2018).



- [36] B. Panda, S. C. Paul, L. J. Hui, Y. W. D. Tay, and M. J. Tan, *Additive manufacturing of geopolymer for sustainable built environment*, *Journal of Cleaner Production* **167**, 281 (2017).
- [37] B. Panda, S. Chandra Paul, and M. Jen Tan, *Anisotropic mechanical performance of 3D printed fiber reinforced sustainable construction material*, *Materials Letters* **209**, 146 (2017).
- [38] R. Wolfs, *Experimental characterization and numerical modelling of 3D printed concrete*, Ph.D. thesis, Eindhoven University of Technology (2019).
- [39] Eurocode, *NEN-EN 1992 - Design of concrete structures*, (2004).
- [40] T. Wangler, N. Roussel, F. P. Bos, T. A. Salet, and R. J. Flatt, *Digital concrete: A review*, *Cement and Concrete Research* **123**, 105780 (2019).
- [41] V. N. Nerella, S. Hempel, and V. Mechtcherine, *Effects of layer-interface properties on mechanical performance of concrete elements produced by extrusion-based 3D-printing*, *Construction and Building Materials* **205**, 586 (2019).
- [42] J. Van Der Putten, M. De Volder, P. Van den Heede, G. De Schutter, and K. Van Tittelboom, *3D Printing of Concrete: The Influence on Chloride Penetration*, in *Second RILEM International Conference on Concrete and Digital Fabrication – Digital Concrete 2020*, Vol. 28, edited by F. Bos, S. Lucas, R. Wolfs, and T. Salet (2020) pp. 500–507.
- [43] R. San Nicolas, M. Cyr, and G. Escadeillas, *Characteristics and applications of flash metakaolins*, *Applied Clay Science* **83-84**, 253 (2013).
- [44] K. Scrivener, F. Martirena, S. Bishnoi, and S. Maity, *Calcined clay limestone cements (LC3)*, *Cement and Concrete Research* **114**, 49 (2018).
- [45] F. A. Zunino Sommariva, *Limestone calcined clay cements ( LC3 ): raw material processing , sulfate balance and hydration kinetics*, Ph.D. thesis, EPFL (2020).
- [46] M. Claverie, F. Martin, J. P. Tardy, M. Cyr, P. De Parseval, O. Grauby, and C. Le Roux, *Structural and chemical changes in kaolinite caused by flash calcination: Formation of spherical particles*, *Applied Clay Science* **114**, 247 (2015).
- [47] S. Sánchez Berriel, A. Favier, E. Rosa Domínguez, I. R. Sánchez MacHado, U. Heierli, K. Scrivener, F. Martirena Hernández, and G. Habert, *Assessing the environmental and economic potential of Limestone Calcined Clay Cement in Cuba*, *Journal of Cleaner Production* **124**, 361 (2016).
- [48] A. Z. Khalifa, Cizer, Y. Pontikes, A. Heath, P. Patureau, S. A. Bernal, and A. T. Marsh, *Advances in alkali-activation of clay minerals*, *Cement and Concrete Research* **132**, 106050 (2020).
- [49] S. Lim, R. A. Buswell, T. T. Le, S. A. Austin, A. G. Gibb, and T. Thorpe, *Developments in construction-scale additive manufacturing processes*, *Automation in Construction* **21**, 262 (2012).

- [50] I. Agustí-Juan and G. Habert, *Environmental design guidelines for digital fabrication*, *Journal of Cleaner Production* **142**, 2780 (2017).
- [51] C. Menna, J. Mata-Falcón, F. P. Bos, G. Vantighem, L. Ferrara, D. Asprone, T. Salet, and W. Kaufmann, *Opportunities and challenges for structural engineering of digitally fabricated concrete*, *Cement and Concrete Research* **133**, 106079 (2020).
- [52] G. Vantighem, W. De Corte, E. Shakour, and O. Amir, *3D printing of a post-tensioned concrete girder designed by topology optimization*, *Automation in Construction* **112**, 103084 (2020).
- [53] P. Wu, J. Wang, and X. Wang, *A critical review of the use of 3-D printing in the construction industry*, *Automation in Construction* **68**, 21 (2016).
- [54] I. Perkins and M. Skitmore, *Three-dimensional printing in the construction industry: A review*, *International Journal of Construction Management* **15**, 1 (2015).
- [55] S. Lim, T. Le, J. Webster, R. Buswell, S. Austin, A. Gibb, and T. Thorpe, *Fabricating construction components using layer manufacturing technology*, in *Global Innovation in Construction Conference 2009 (GICC'09)* (2009).
- [56] R. Duballet, O. Baverel, and J. Dirrenberger, *Classification of building systems for concrete 3D printing*, *Automation in Construction* **83**, 247 (2017).
- [57] P. Carneau, R. Mesnil, N. Roussel, and O. Baverel, *Additive manufacturing of cantilever - From masonry to concrete 3D printing*, *Automation in Construction* **116**, 103184 (2020).

# 9

## CONCLUSIONS AND RECOMMENDATIONS

*In this chapter, retrospection, conclusions and findings of this Ph.D. thesis are summarized and discussed. Additionally, suggestions are given for possible further work.*

## 9.1. RETROSPECTION

THE main goal of this thesis was to develop sustainable cementitious materials for extrusion-based 3D concrete printing (3DCP) by using the ternary blend of limestone, calcined clay, and Portland cement (PC). Pumpability, extrudability, open time, and buildability are widely accepted criteria for a cementitious material to be 3D printable. When the 3D printing setup and printing parameters are kept identical, these engineering features are dominated by the rheological and thixotropic properties of fresh mixture that depend on the binder composition, the type and gradation of aggregate, the water to binder ratio, the binder to aggregate ratio as well as the type and dosage of admixture. It would be too complicated to study all material parameters for developing printable mixtures. Thus, considering the research necessity and feasibility, three main material parameters, i.e., different replacement levels of PC by limestone and calcined clay, different dosages of viscosity modifying admixture (VMA), and different grade levels of calcined clays, were selected for investigation. Moreover, the layer adhesiveness/interlayer bonding is believed to be a weakness in a printed structure. A high air void content at the interface is observed in many printed specimens with a weak interlayer bonding. The characterization of air voids in printed cementitious materials is therefore required. Besides, the interlayer bonding between two adjacent layers is strongly influenced by the printing parameters, e.g., time intervals and nozzle standoff distances, which should be investigated as well. In this thesis, the following attempts were made to achieve the research objectives.

Chapter 3 investigated the effects of different PC replacement levels by blends of calcined clay and limestone on 3D printability, stiffness evolution, and early-age hydration. For developing the printable mixtures, slump, slump flow, and water retention tests were employed. Afterwards, inline printing methods (definition: see footnote in Section 2.4.1), i.e., extrudability window and buildability tests, were conducted to evaluate the printability of the developed mixtures. For determining the impacts on stiffness evolution within the first 3 hours (the critical period for printing a large component), initial setting time and the total specific surface area at 1 h and 3 h were measured. Additionally, the influences on early-age hydration and strength development were quantified.

In Chapters 4 and 5, the effects of different dosages of VMA and different grade levels of calcined clays on fresh-state behaviors, 3D printability, and hardened properties of limestone-calcined clay-based cementitious materials were investigated. For assessing the abovementioned material properties, both offline (definition: see footnote in Section 2.5) (flowability, ram extrusion and green strength) and inline (extrudability, open time, and buildability) tests were executed to quantify the fresh properties and 3D printability of studied mixtures. Meanwhile, the impacts on the hydration, mechanical performance, and air void content of printed samples were determined using isothermal calorimetry, compressive strength (7 days) testing, and X-ray computed tomography scanning.

In Chapter 6, a systematic characterization of the typical air void system of 3D printed cementitious materials via digital image analysis was given. Two limestone and calcined clay-based 3D printable cementitious materials with different interlayer properties developed in Chapter 5 were used to prepare the printed samples. Optical

image scanning and X-ray computed tomography were employed to acquire digital images for determining air voids characteristics of printed cementitious materials, i.e., content, distribution, size, and shape. In addition, possible reasons for air void formation in printed cementitious materials, and the pros and cons of two employed methodologies were discussed.

Chapter 7 studied the impacts of different printing parameters, including time intervals, and nozzle standoff distances, on interlayer bonding of a limestone calcined clay-based 3D printed cementitious material. The printed specimens that contained two layers were tested in the uniaxial tension under a non-rotational boundary condition for obtaining the interlayer bond strength. The air void content and distribution of different printed specimens were characterized using X-ray computed tomography and digital image analysis. Finally, a 2D lattice model was employed to simulate the uniaxial tensile test of printed samples containing different air void contents at the interface.

Chapter 8 discussed the concerns, barriers, and state-of-the-art solutions for implementing 3DCP in building construction.

## 9.2. CONCLUSIONS

### 9.2.1. GENERAL PRINCIPLES OF 3D CONCRETE PRINTING

GENERAL conclusions for the development of 3D printable cementitious materials were summarized as follows:

- *Three critical stages are considered for thoroughly determining 3D printability of fresh cementitious materials.*

**Stage 1. Flow under shearing.** In the beginning, the fresh mixture should exhibit proper flowability and pumpability under a constant shear force provided by the pump. However, due to the stiffness evolution and ongoing hydration of cementitious materials, the workability of fresh mixture changes with time. Open time is, therefore, required to be quantified at this stage. Besides, slump flow, ram extrusion, pumpability, and extrudability tests can be conducted to quantify the material properties. Accordingly, the suitable printing speed and material flow rate are obtained regarding the rheology of studied mixtures and the capability of printing setup.

**Stage 2. Layer stacking within the open time.** After extrusion, the deposited material swiftness from a dynamic status to a static status. Due to the thixotropy, the deposited layer immediately emerges with certain yield stress that could retain its shape with the limited deformation under the load from upper layers; even the material is still within the open time. The buildability test is suitable to be applied in this stage. Consequently, the ideal layer thickness and vertical building rate for avoiding the printed structure collapsing are determined.

**Stage 3. Green strength/stiffness evolution.** To fabricate a large concrete component, 3-4 h continuous printing appears to be required. The deposited layers should show a high structural build-up to ensure structural stability during this period. Green strength test can be used to effectively monitor the very early-age strength development of studied mixtures, especially after their initial

set. As an output, the maximum layer number/printed structure height for one printing session can be predicted concerning the predefined printing parameters.

- *Offline methods are more efficient and appropriate than inline printing characterizations at the initial stage of new material development.*

Most of material engineering properties, i.e., pumpability, extrudability, and buildability, need to be examined by using the specific inline test methods. However, such tests are accompanied by massive time and material consumption, as well as intensive labor works, even under a lab-scale. Additionally, at the initial stage of new material development, large quantities of trial-error-based processes are highly demanded. Thus, offline characterizations of fresh mixtures are suggested to be employed before inline printing validation. In the present study, offline methods, such as slump, slump flow, ram extrusion, green strength, and Vicat penetration (setting time) tests, were applied, which could not only efficiently characterize the fresh-state behaviors of studied mixtures but also provide indicators for developing similar materials in further study. Nevertheless, it is worth noting that not all the aforementioned offline methods are useful for all types of printable cementitious materials.

- *The development of printable cementitious materials cannot be seen as independent from printing setup, process, and end application.*

Except for the rheology of fresh cementitious materials, the printability is related to the printing speed (nozzle moving speed and material flow rate), object size (toolpath length), object geometry, time gap between layers, nozzle standoff distance, the start printing time, and ambient condition (temperature and humidity). Besides, a cementitious material is printable using one 3DCP setup, whereas it might be invalid or show different behaviors using others. For printable cementitious materials, the 3DCP setup and printing process define the upper and lower bounds. Thus, the printability of a developed cementitious material in this context should be regarded as a relative result. All these printing parameters belong to the boundary conditions, which need to be clarified.

### 9.2.2. MAIN CONCLUSIONS OF THE THESIS

Main concluding remarks of the thesis were drawn and highlighted as follows:

- Physical and/or chemical characteristics of supplementary cementitious materials (calcined clay), i.e., morphology, fineness, specific surface area, and the content and type of reactive phases, strongly influence 3D printing. As discussed in Chapters 3 and 5, the addition of calcined clay can improve buildability and green strength/stiffness development with time, increase water and superplasticizer demands, reduce flowability and extrudability. These effects are further enhanced by either increasing the proportion of calcined clay in the binder or increasing the dosage of metakaolin in calcined clay. The aforesaid phenomena can link to the reduction of water film thickness and mean particle distance, the increase of friction between particles, and the consumption of superplasticizer, which appears to be attributed to the layered structure, high

content of reactive aluminate, and high specific surface area of calcined clay. Since calcined clays provided by different suppliers may exhibit various material features, systematically raw material characterization is essential before the use in cementitious materials.

- The dosage of VMA is a critical factor in influencing the fresh and hardened properties of limestone and calcined clay-based cementitious materials. Increasing the VMA dosage (from 0.14% to 0.48% of the binder mass in Chapter 4) can increase the extrusion pressure, buildability, and green strength within the first 2.5 h. However, increasing the amount of VMA in the mixture can reduce the flowability and open time as well as delay the cement hydration.
- For many 3D printed cementitious materials with a weak layer adhesiveness, a high amount of air voids between the layers as a typical phenomenon can be found. In the printed samples (see Chapter 6), the air voids with the diameter in the range of 10  $\mu\text{m}$  to 1000  $\mu\text{m}$  seemed to be evenly distributed in the layer, whereas the large air voids (1000-6000  $\mu\text{m}$ ) were formed mainly at the interface region. Additionally, due to the possibility of merging and overlapping, the majority of air voids exhibited irregular and elongated shapes. This could be attributed to the extrusion and layer-wise manufacturing process in 3DCP.
- Optical image scanning and X-ray computed tomography can be effectively employed to characterize the air-void system of 3D printed cementitious materials. Thin/polished section can be used for multi-scale analysis and observation of air voids, whereas the sample preparation is a challenge. The sample for X-ray computed tomography can be easily prepared. Nevertheless, the image resolution is limited for the sample with a relatively large size.
- In the present study, air void content at the interface is believed as a dominant factor adversely affecting interlayer bond strength. Both material properties and printing processes influence the formation of air voids between two layers. In Chapters 4, 5, 6, the fresh mixtures with superior buildability and fast green strength development showed a high value of local porosity at the interface when printing parameters were kept constant. In contrast, as mentioned in Chapter 7, if using the same material, extending the time interval between the construction of two layers led to a significant increase of local porosity in the interlayer zone, whereas only increasing the nozzle standoff distance showed limited influences on that.

### 9.3. RECOMMENDATIONS FOR FURTHER STUDY

**I**N this thesis, attempts have been made to characterize the fresh and hardened properties of limestone-calcined clay-based 3D printable cementitious materials. Many issues were tackled, whereas others were left for further investigation.

- The present work showed that the addition of calcined clay could significantly influence the fresh and hardened properties of studied mixtures. Such effects are

generally ascribed to the features of calcined clay, i.e., layered microstructure, fine particle size, high specific surface area, and high content of reactive aluminate phases. However, it is still a lack of study to reveal the mechanism about how these material characteristics of calcined clay influence 3D printing, stiffness development, structural build-up as well as hydration of studied mixtures. Many relevant hypotheses were proposed in Chapters 3 and 5, which need to be validated in further work.

- Investigating the effect of other material parameters, i.e., aggregate to binder mass ratio ( $A/B$ ), water to binder mass ratio, and types of superplasticizers and VMAs on 3D printing of limestone-calcined clay-based cementitious materials. Among them, increasing  $A/B$  could further reduce PC content in printable mixtures, which is also a strategy for developing sustainable 3DCP, as mentioned in Chapter 2. Besides, inorganic VMAs, such as micro-/nano-silica, nano-clay, nano-alumina, and graphene oxide, have great potential to be used in 3D printable limestone-calcined clay-based cementitious materials. Inorganic VMAs display minor or even zero inhibition on cement hydration compared to cellulose-derivative VMAs.
- Investigating the effect of other printing parameters, i.e., nozzle types, and printing environmental conditions, on interlayer properties (bond strength and air void content). The nozzle variables include the flow direction (e.g., down-flow, back-flow, or hybrid of back- and down-flow), the size and geometry of the nozzle opening (e.g., round or rectangle). The down-flow nozzle (for both round and rectangle openings) may enhance the interlayer bond strength of the printed sample, mostly when the nozzle standoff distance is smaller than the width of the nozzle opening. This is because the nozzle may add extra force to the deposited substrate. Besides, exposing the substrate under the drying environment can lead to many severe issues, for instance, drying shrinkage induced cracking and the cold joint between layers. Thus, protecting the layer from drying during the printing process becomes critical in this context.
- Investigating the effect of pumping/extrusion process on green strength development, hydration, and hardened properties of limestone-calcined clay-based cementitious materials. In this thesis, mold-cast samples were employed in the green strength test, which overlooks the influences induced by the pumping/extrusion process. As observed in Chapter 3, the pumping/extrusion process could increase the temperature and decrease the initial setting time of fresh mixtures, caused by the friction between the printing setup (pump, hose, and nozzle) and fresh cementitious materials. Such effects may accelerate green strength development and cement hydration. Also, the extrusion/pumping process can influence the shape, size, content, and distribution of air voids affecting the mechanical performance of both very early- and later-age specimens.
- Modifying the developed limestone-calcined clay-based cementitious materials to adapt to the printing strategy of set-on-demand. Extrusion of high or sufficiently



stiff material as the most common printing strategy was employed in this thesis. However, as discussed in Chapter 2, set-on-demand printing seems to be more appropriate for implementing 3DCP in large-scale concrete construction.

- Extending research into the directions related to volume stability (shrinkage and creep) and durability (e.g., carbonation, sulfate attack, chloride penetration, freeze-thawing, and others) of 3D printed cementitious materials. This study focused on the fresh-state behaviors, 3D printing, hydration (within 7 days), and mechanical performance (within 28 days) of limestone-calcined clay-based cementitious materials. For engineering practice, the long-term performance of such printed cementitious materials should be considered. It is essential to evaluate the abovementioned properties of printed samples under different specific conditions and to find ways to deal with the possible issues in the future.



# ACKNOWLEDGMENTS

At the end of this thesis, I would like to express my gratitude to the people who have helped and supported me over the past 4 years. Without you, my supervisors, colleagues, friends and family, this journey should be much more difficult than I thought.

First of all, an extraordinary acknowledgment goes to China Scholarship Council for funding this research.

I would like to thank my promotor Prof. Erik Schlangen, for giving me the opportunity to be a member of Microlab three years ago. His guidance, support, and comments motivated me to find the “answers” for my research. Discussions with Erik are always pleasant to me. His sense of humor never lets you feel nervous and stressed. I want to keep his insightful suggestions in mind, which can always inspire me to find a way to tackle difficulties. My sincere appreciation goes to my co-promotor Dr. Oğuzhan Çopuroğlu, who gave me 100% support during my Ph.D. Without his help in scientific writing and presenting, I cannot grow from a student to a researcher. In our discussions, we could always find many ideas related to my research topic. I am very grateful for his suggestions in our first meeting. Since then, I firmly decided to choose 3D concrete printing as my Ph.D. research topic. I also want to deliver my gratitude to my second promotor Dr. Fred Veer for offering me the chance to start a Ph.D. life at Delft University of Technology and introducing Erik and Oğuzhan to me. Fred is always friendly, patient and highly efficient for all my asking.

Meanwhile, I would like to thank all my doctoral committee members, Prof. Yamei Zhang, Prof. Theo Salet, Prof. Ulrich Knaack, and Prof. Bert Sluys for taking the time and effort to read the preliminary version of this thesis, propose comments and attend my Ph.D. defense.

Special appreciation goes to Branko Šavija and Stefan Chaves Figueiredo. Branko shared a lot of valuable advice and ideas with me. Stefan helped me conduct experimental tests and shared many research experiences when I was a rookie at Microlab. I would also like to thank my officemates Yidong Gan and Yask Kulshreshtha. It is a great pleasure to share my research and life with you. Additionally, I want to give many thanks to Anne Linde van Overmeir, who helped me translate my summary in this thesis from English to Dutch.

I want to take a moment to express my gratitude to Hua Dong, Tianshi Lu, Zhiwei Qian, Xu Ma, Hongzhi Zhang, Zhenming Li, Shi Xu, Ze Chang (Lu Cheng), Shan He, Yu Zhang and Zhi Wan. Thank you for helping and supporting me in this challenging experience. A special appreciation goes to Dr. Guang Ye; thanks for organizing parties for the Chinese festivals (Mid-Autumn Festival) and sharing Chinese food with us. My gratitude also goes to Claudia Romero Rodríguez, Fernando França de Mendonça Filho, Yading Xu, Marija Nedeljković, Patrick Holthuizen, Emanuele Rossi, Martin Megalla, and Bianca Fraga Silva. Thanks for the friendship, the lunchtime, coffee break, parties and all the great times we have shared.

I am very grateful to those who helped me carry out my experiments in Microlab: Arjan Thijssen for his help in ESEM and XCT scanning, John van den Berg for his help in TGA, Koen Jansen (MSc) for his help in 3D printing and Ton Blom for his kind support and help in material preparation. Special thanks to Maiko van Leeuwen (Taibangla!) for his help in many experiments. Moreover, we have a lot of fun times together (volleyball activities, parties, and games). Furthermore, our secretary Jacqueline van Unen-Berghenengouwen, Jaap Meijer and former secretary Claire de Bruin are also highly appreciated for their kind help on various daily issues.

Appreciation goes to all the other colleagues of Microlab: Xuliang Hou (Ying Yang), Jiayi Chen (Wenqin Shi), Bei Wu, Hao Huang, Zhipei Chen, Shizhe Zhang, Boyu Chen, Xuhui Liang, Zhiyuan Xu, Yun Chen, Yitao Huang, Chen Liu, Minfei Liang, Kuba Pawlowicz, Albina Kostiuhenko, Bart Hendrix, Jeannette van den Bos, Mladena Luković, Henk Jonkers, Renee Mors, Irving Alfredo Flores Beltran, Luiz Miranda de Lima Junior, Ameya Kamat, Shozab Mustafa and Damian Palin. I would also like to thank the help and friendship from all former colleagues: Xiaowei Ouyang, Yibing Zuo, Wenjuan Lyu, Peng Gao, Yong Zhang, Leyang Lu, Xingliang Yao, Dawei Gu, Marija Krstic, Çağlar Yalçinkaya and Josef Kveton.

I am also very thankful to all friends that I met in Delft. My gratitude goes to Boyuan Zhang, Qingpeng Li, Wang Pan, Yi Xia, Langzi Chang, Mrs. Bo Song and Chenjie Yu. Appreciate your help and support, especially in the first year of my Ph.D.

Finally, I want to express my gratitude to my wife, parents and parents-in-law, for their unconditional and endless love, support, tolerance and encouragement.

Yu Chen  
Delft, July 2021

# CURRICULUM VITÆ

## Yu CHEN

04-07-1990                      Born in Jilin, China.

### EDUCATION

Mar 2017–2021                      Ph.D. candidate in 3D concrete printing  
Delft University of Technology, the Netherlands

*Thesis:*                                      Investigation of limestone-calcined clay-  
based cementitious materials for sustainable  
3D concrete printing

*Promotor:*                                      Prof. dr. ir. E. Schlangen  
Dr. ir. F. A. Veer

*Copromotor:*                                      Dr. O. Çopuroğlu

Sep 2014–Dec 2015                      Postgraduate in Architecture Design (Master of Architecture in Design)  
University of Nottingham, the United Kingdom

Sep 2009–July 2014                      Undergraduate in Architecture (Bachelor of Architecture)  
Xi'an University of Architecture and Technology, China



# LIST OF PUBLICATIONS

## JOURNAL PUBLICATIONS

1. **Y. Chen**, F. Veer, O. Çopuroğlu, *A critical review of 3D concrete printing as a low CO<sub>2</sub> concrete approach*, [Heron](#) **62**, 3 (2017).
2. **Y. Chen**, S. Chaves Figueiredo, Ç. Yalçinkaya, O. Çopuroğlu, F. Veer, E. Schlangen, *The effect of viscosity-modifying admixture on the extrudability of limestone and calcined clay-based cementitious material for extrusion-based 3D concrete printing*, [Materials](#) **12**, 1374 (2019).
3. **Y. Chen**, Z. Li, S. Chaves Figueiredo, O. Çopuroğlu, F. Veer, E. Schlangen, *Limestone and calcined clay-based sustainable cementitious materials for 3D concrete printing: a fundamental study of extrudability and early-age strength development*, [Applied Sciences](#) **9**, 1809 (2019).
4. **Y. Chen**, S. Chaves Figueiredo, Z. Li, Z. Chang, K. Jansen, O. Çopuroğlu, E. Schlangen, *Improving printability of limestone-calcined clay-based cementitious materials by using viscosity-modifying admixture*, [Cement and Concrete Research](#) **132**, 106040 (2020).
5. **Y. Chen**, C. Romero Rodriguez, Z. Li, B. Chen, O. Çopuroğlu, E. Schlangen, *Effect of different grade levels of calcined clays on fresh and hardened properties of ternary-blended cementitious materials for 3D printing*, [Cement and Concrete Composites](#) **114**, 103708 (2020).
6. **Y. Chen**, K. Jansen, H. Zhang, C. Romero Rodriguez, Y. Gan, O. Çopuroğlu, E. Schlangen, *Effect of printing parameters on interlayer bond strength of 3D printed limestone-calcined clay-based cementitious materials: An experimental and numerical study*, [Construction and Building Materials](#) **262**, 120094 (2020).
7. **Y. Chen**, O. Çopuroğlu, C. Romero Rodriguez, F.F. Mendonça Filho, E. Schlangen, *Characterization of air-void systems in limestone-calcined clay-based 3D printed cementitious materials using optical image scanning and X-ray computed tomography*, [Materials Characterization](#) **173**, 110948 (2021).
8. **Y. Chen**, S. He, Y. Zhang, Z. Wan, O. Çopuroğlu, E. Schlangen, *3D printing of calcined clay-limestone-based cementitious materials*, **under review**.
9. **Y. Chen**, S. He, Y. Gan, O. Çopuroğlu, F. Veer, E. Schlangen, *A review of printing strategies, sustainable cementitious materials and characterization methods in the context of extrusion-based 3D concrete printing*, **under review**.
10. Y. Gan, M. Vandamme, H. Zhang, **Y. Chen**, K. van Breugel, E. Schlangen, B. Šavija, *Micro-cantilever testing on the short-term creep behaviour of cement paste at micro-scale*, [Cement and Concrete Research](#) **134**, 106105 (2020).

11. Z. Chang, Y. Xu, **Y. Chen**, Y. Gan, E. Schlangen, B. Šavija, *A discrete lattice model for assessment of buildability performance of 3D-printed concrete*, [Computer-Aided Civil and Infrastructure Engineering](#) **36**, 638-655 (2021).



## CONFERENCE PROCEEDINGS

1. **Y. Chen**, F. Veer, O. Çopuroğlu, E. Schlangen, *Feasibility of using low CO<sub>2</sub> concrete alternatives in extrusion-based 3D concrete printing*, First RILEM International Conference on Concrete and Digital Fabrication – Digital Concrete, Zürich, Switzerland, 269-276 (2018).
2. **Y. Chen**, Ç. Yalçinkaya, O. Çopuroğlu, E. Schlangen, *The Effect Of Viscosity Modifier Agent On The Early Age Strength Of The Limestone And Calcined Clay-Based Sustainable And 3D Printable Cementitious Material*, Proceedings of the 10th International Concrete Congress, İzmir, Turkey, 242-250 (2019).
3. **Y. Chen**, S. Chaves Figueiredo, Ç. Yalçinkaya, O. Çopuroğlu, E. Schlangen, *Extrudability tests of the limestone and calcined clay based 3D printable cementitious mixtures by using ram extruder*, Rheology and Processing of Construction Materials (RheoCon2), Dresden, Germany (2019).

ISBN 978-94-6421-404-8



9 789464 214048

 **TU Delft**